Angle-resolved photoemission studies of quantum materials

Jonathan A. Sobota

Stanford Institute for Materials and Energy Sciences, SLAC National Accelerator Laboratory, 2575 Sand Hill Road, Menlo Park, California 94025, USA

Yu He

Department of Applied Physics, Yale University, New Haven, Connecticut 06511, USA, Department of Physics, University of California, Berkeley, California 94720, USA, and Stanford Institute for Materials and Energy Sciences, SLAC National Accelerator Laboratory, 2575 Sand Hill Road, Menlo Park, California 94025, USA

Zhi-Xun Shen

Stanford Institute for Materials and Energy Sciences, SLAC National Accelerator Laboratory, 2575 Sand Hill Road, Menlo Park, California 94025, USA and Geballe Laboratory for Advanced Materials, Departments of Physics and Applied Physics, Stanford University, Stanford, California 94305, USA

(published 26 May 2021)

The physics of quantum materials is dictated by many-body interactions and mathematical concepts such as symmetry and topology that have transformed our understanding of matter. Angle-resolved photoemission spectroscopy (ARPES), which directly probes the electronic structure in momentum space, has played a central role in the discovery, characterization, and understanding of quantum materials ranging from strongly correlated states of matter to those exhibiting nontrivial topology. Over the past two decades, ARPES as a technique has matured dramatically with ever-improving resolution and continued expansion into the space, time, and spin domains. Simultaneously, the capability to synthesize new materials and apply nonthermal tuning parameters *in situ* has unlocked new dimensions in the study of all quantum materials. These developments are reviewed, and the scientific contributions they have enabled in contemporary quantum materials research are surveyed.

CONTENTS

I. INTRODUCTION

Quantum many-body and relativistic effects are at the heart of modern condensed matter physics: new organizing principles emerge from the collective behavior of a large number of constituents with coupled degrees of freedom. In general a solid-state system can be modeled by a Hamiltonian H with its associated eigenvalues and eigenstates. In the simple case where the behavior is dictated by the electron kinetic energy and crystal potential H_0, the system is well described by the quantum theory of electronic band structure, where the electron wave functions $\psi_{\mathbf{k}}(\mathbf{r})$ are Bloch states with eigenvalues $\epsilon_{\mathbf{k}}$ representing the electronic band dispersion with respect to wave vector $\mathbf{k}$ (Ashcroft and Mermin, 1976). Despite the remarkable success of this theory, as evidenced by the semiconductor revolution it spawned in the middle of the last century (Sze and Ng, 2006), for most many-body problems in condensed matter physics such a description is insufficient and/or unsatisfactory. This is because for strongly interacting electron systems, Hamiltonian terms such as $H_{e\text{-}e}$ and $H_{e\text{-ph}}$ couple electrons to other electrons or to phonons, respectively, and thereby invalidate an independent-electron description (Pines and Nozières, 1966; Mahan, 2000). This often leads to surprising phenomena such as high-temperature superconductivity in the cuprates (Bednorz and Müller, 1988) and iron pnictides (Kamihara et al., 2006, 2008). In other cases, interactions such as spin-orbit coupling H_{SOC} encode the electron wave functions with topological properties that are not evident solely from the energy-momentum dispersion $\epsilon_{\mathbf{k}}$ and require analysis of the geometric phase of $\psi_{\mathbf{k}}(\mathbf{r})$ for a complete understanding (Hasan and Kane, 2010; Qi and Zhang, 2011; Haldane, 2017). These properties are unusually robust with respect to perturbations, as exemplified by quantized edge conduction in materials exhibiting quantum Hall effects (Klitzing, Dorda, and Pepper, 1980; Thouless et al., 1982; Konig et al., 2007; C.-Z. Chang et al., 2013; Fei et al., 2017). The union of these material families have come to be known as *quantum materials*. Figure 1 presents an overview of the quantum material families within the scope of this review.

Fermionic quasiparticles are instrumental for describing the rich physics of quantum materials. One of the most descriptive quantities is the *single-particle spectral function*, which is experimentally accessible with momentum resolution using angle-resolved photoemission spectroscopy (ARPES) (Smith and Traum, 1975; Himpsel and Eastman, 1978; Kampf and Schrieffer, 1990; Smith and Kevan, 1991; Damascelli, Hussain, and Shen, 2003; Hüfner, 2003; Plummer and Eberhardt, 2007). ARPES is based on the photoelectric effect, in which light is used to liberate electrons from a material such that their preemission energy and momentum distributions can be determined (see Fig. 1, top-left panel). Since these are the same electrons participating in the many-body physics governed by H, a wealth of information can be gleaned from these energy-momentum maps, as elaborated on in Fig. 2. In the case of weakly interacting electrons, the ARPES intensity simply follows the electronic band structure, with the energy-momentum dependence reflecting the band dispersion $\epsilon_{\mathbf{k}}$. From this information alone is it is possible to extract fundamental properties such as the electron velocities and Fermi surface geometry (Himpsel and Eastman, 1980). The more profound impact of ARPES is due to its ability to detect, quantify, and disentangle the various microscopic contributions to H and their combined impact, including those invalidating the independent-electron description. As shown schematically in the middle row of Fig. 2, electron-phonon interactions (Balasubramanian et al., 1998; Hengsberger et al., 1999; Valla, Fedorov, Johnson, and Hulbert, 1999; Lanzara et al., 2001), electron-electron interactions (Pines and Nozières, 1966), and spin-orbit coupling (LaShell, McDougall, and
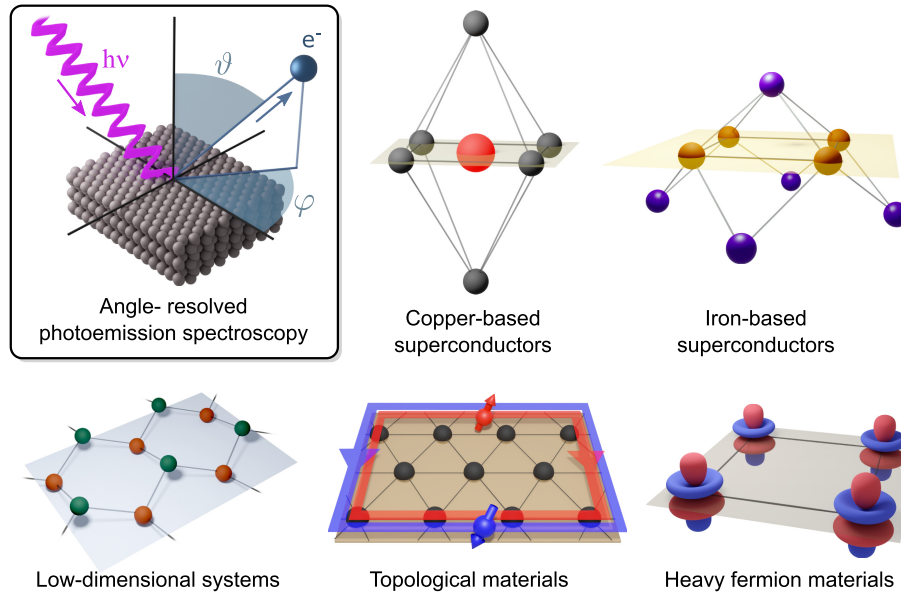
FIG. 1.   Top-left panel: schematic of angle-resolved photoemission spectroscopy (ARPES). Photons of energy $h\nu$ are used to photoemit electrons into vacuum, where their kinetic energies and emission angles are resolved. Other panels: the scope of quantum materials studied by ARPES, corresponding to sections in this review (heavy fermion materials are representative of the materials discussed in Sec. VIII).

Jensen, 1996) each have distinct signatures in the ARPES spectra, visible as renormalized and/or split dispersions with respect to the noninteracting bands. The amalgamation of these interactions results in the unique physics of quantum materials. The bottom row of Fig. 2 shows schematic ARPES spectra representative of many quantum materials, including topological states of matter, superconductors, charge density wave systems, and Mott insulators.

ARPES owes much of its utility to the fact that the photoelectric cross section is at least 5 orders of magnitude higher than other processes such as inelastic light and neutron scattering (Yeh and Lindau, 1985; Thompson and Vaughan, 2001). The pace of scientific progress has been further accelerated by overcoming technical challenges throughout the past half century. The evolution of the state of the art over this period is illustrated by Fig. 3. The top row shows representative ARPES spectra of a cuprate superconductor; it is readily seen that the resolution and hence information content of the spectra has increased dramatically. At the same time, efforts have expanded to improve diverse metrics such as spin detection efficiency and spatial and temporal resolutions. Many of these technical developments were catalyzed by the cuprate problem and the advent of third generation synchrotron light sources (Damascelli, Hussain, and Shen, 2003) and have kept apace with the discovery of new families of quantum materials, with the impact evidenced by the steadily increasing number of publications [Fig. 3(e)].[1] These developments are summarized in Fig. 3(f), where the crucial role of the light source is highlighted, evidencing the reciprocal stimulation of scientific and technique developments. Other notable developments include advanced synthesis techniques, tunable sample environments, versatile light sources, and

novel spectrometers with efficient multichannel detection capable of resolving multiple quantum numbers of the photoemitted electrons.

The goal of this review is to highlight the advances and future opportunities in quantum materials research unlocked by these ARPES developments, with an emphasis on activities since earlier reviews (Damascelli, Hussain, and Shen, 2003; Lynch and Olson, 2005; Plummer and Eberhardt, 2007; Himpsel and Lindau, 2009). In Sec. II we begin with an elementary discussion on the principles of ARPES, then describe state-of-the-art experimental methods in Sec. III. We then focus on four families of quantum materials (see Fig. 1): cuprate superconductors (Sec. IV), iron-based superconductors (Sec. V), low-dimensional materials (Sec. VI), and topological materials (Sec. VII). Section VIII provides a review of ARPES studies on other quantum material families with interesting transport properties, correlation effects, and/or topological properties. We conclude with a discussion and outlook (Sec. IX).

II. ANGLE-RESOLVED PHOTOEMISSION SPECTROSCOPY

A. General description

ARPES is based on the photoelectric effect, in which a photon impinges on a material and is absorbed by an electron, which then escapes from the material (Cardona and Ley, 1978; Hüfner, 2003). The utility of ARPES as a spectroscopic tool derives from the fact that one can exploit the kinematics of the photoemission process to deduce the binding energy E_B and crystal momentum $\hbar\mathbf{k}$ of the electron before it was emitted from the material. A generic ARPES measurement consists of a single-crystal sample irradiated by monochromatic light of energy $h\nu$, resulting in photoemission of electrons in all
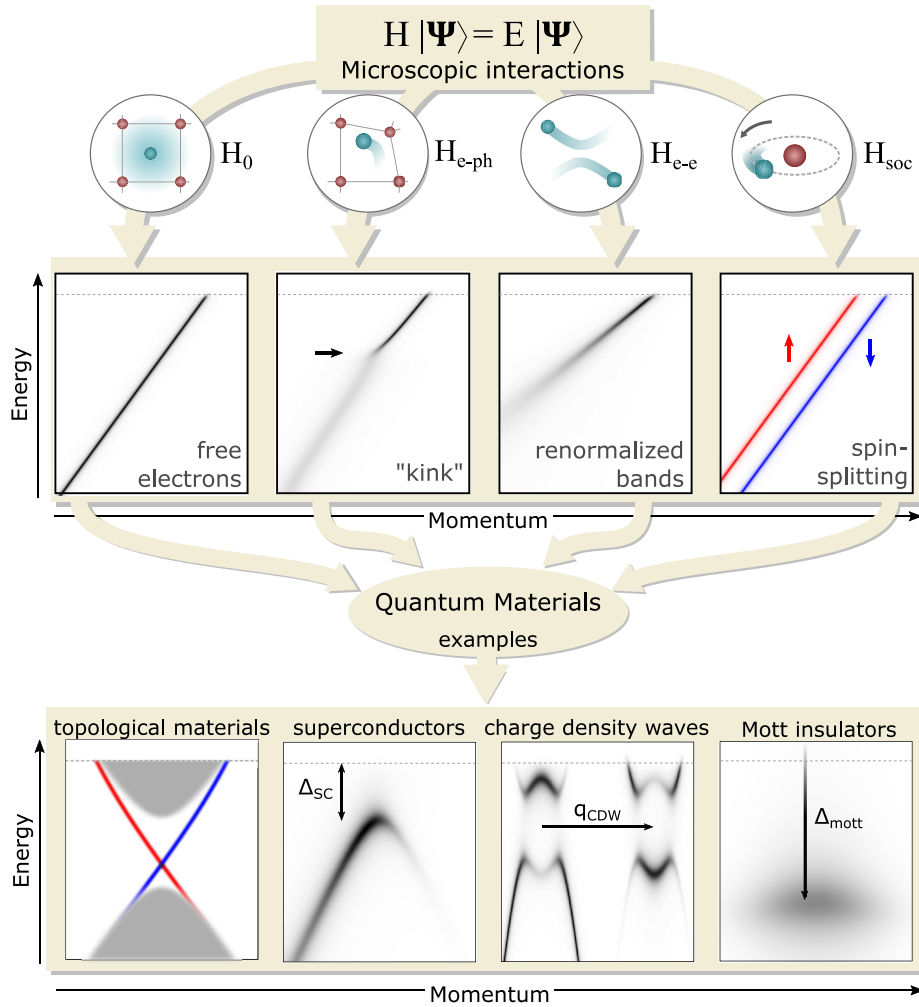
FIG. 2. Schematic depiction of microscopic interactions and their distinct signatures in an ARPES spectrum. Starting with a crystal potential H_0, the ARPES spectrum reflects the band structure of independent electrons. Electron-phonon coupling $H_{e\text{-ph}}$ introduces a "kink" in the band dispersion, with an increased peak width below the kink energy. Electron-electron coupling $H_{e\text{-}e}$ leads to an energy-dependent peak width and a renormalized band velocity. Finally, spin-orbit coupling H_{SOC} can split spin or orbital degeneracy. Together these interactions give rise to the physics of quantum materials, including topological materials (with spin-polarized surface states), superconductors (with superconducting gap Δ_{SC}), charge density waves (with folding wave vector q_{CDW}), and Mott insulators (with Mott gap Δ_{Mott}).

possible directions. A fraction of these electrons are collected using a photoemission spectrometer (Sec. III.C) that records the kinetic energy E_{kin} and emission angles (ϑ, φ) of each detected electron. Here ϑ is the polar angle with respect to the surface normal, and φ is the azimuthal angle typically defined with respect to the experimental geometry or crystal axis; see Fig. 1. Note that E_{kin} is defined with respect to the sample's vacuum level E_{vac}. Based on energy and momentum conservation, one can then derive the following relationships[2] between the preemission and postemission electronic states:

$$E_{kin} = h\nu - \phi - E_B, \qquad (1)$$

$$\hbar \mathbf{k}_{\parallel} = \sqrt{2mE_{kin}} \sin(\vartheta), \qquad (2)$$

where ϕ is the sample surface work function and $\hbar \mathbf{k}_{\parallel}$ is the crystal momentum of the electron parallel to the surface in the extended zone scheme. E_{kin} is the photoelectron kinetic energy and E_B is the binding energy of the electron prior to emission.[3] Because of the discrete in-plane periodicity of the crystal structure, $\mathbf{k}_{\parallel}$ is conserved throughout the photoemission process (modulo an in-plane reciprocal lattice vector $\mathbf{G}_{\parallel}$). The orthogonal component $\mathbf{k}_{\perp}$ is not conserved during transmission through the surface but can be deduced under certain assumptions (Sec. II.B).

The energetics of the photoemission process are depicted in Fig. 4. Rather than directly report E_{kin}, which is dependent on $h\nu$, ARPES data are typically plotted with respect to $E - E_F = -E_B$, where E_F is the sample's Fermi level (see

---

[2]In writing Eq. (2), we have neglected the momentum of the photon since it is negligible in the ultraviolet range, although it must be considered in the soft- and hard-x-ray regimes (Fadley, 2005).

[3]Ultimately, the detected kinetic energy is determined by the work function of the analyzer ϕ_A rather than that of the sample, as shown in Fig. 4.
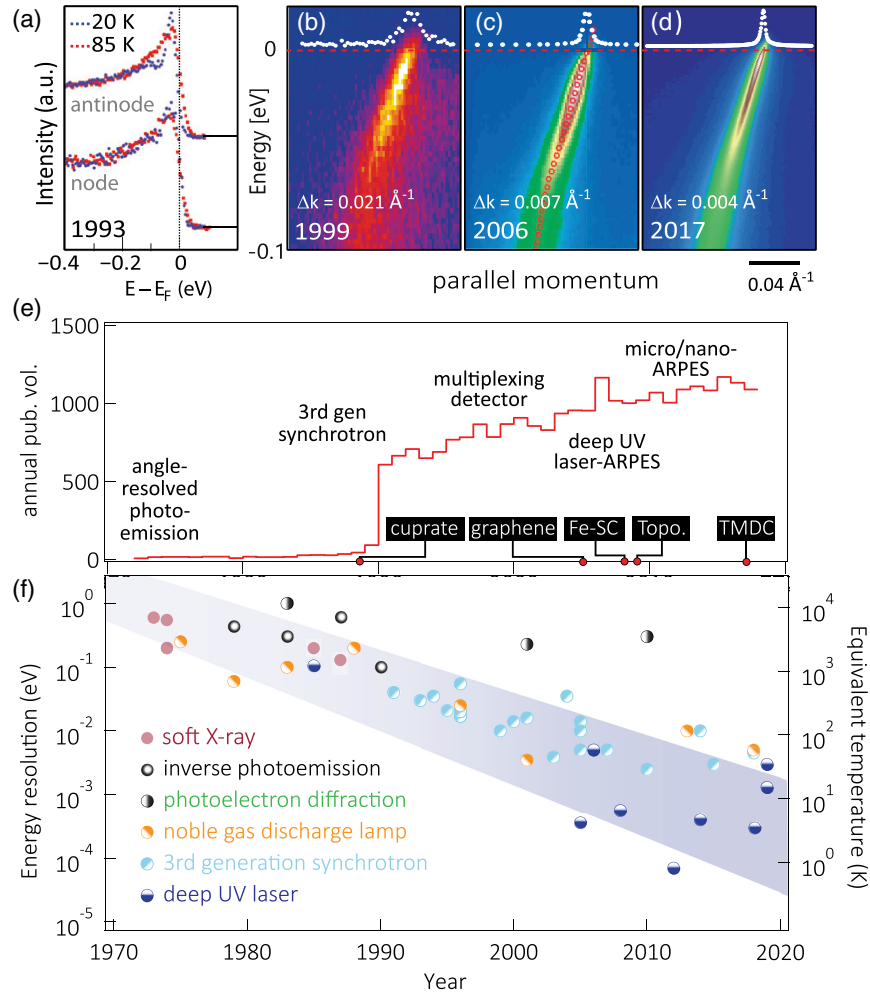
FIG. 3. State of the art in ARPES over time. (a)–(d) Improvement in energy and momentum resolution, as exhibited by the spectral function along diagonal Cu-Cu direction in cuprates. Data in (d) additionally benefited from an improvement in spatial resolution to overcome surface mosaicity. Adapted from Shen *et al.*, 1993, Valla, Fedorov, Johnson, Wells *et al.*, 1999c, Koralek *et al.*, 2006, and Iwasawa *et al.*, 2017. (e) Approximate number of publications per year utilizing photoemission as determined by the Web of Science. Note the steady rise with the introduction of new materials and techniques over the past 30 years. The discontinuity around 1990 coincides with the development of third generation synchrotrons but may also contain changes in record keeping methodology. (f) Energy resolution sampled from representative publications showing an overall near-exponential improvement enabled in large part by new light sources. Different light sources are color coded differently.

Sec. III.A for experimental details), to emphasize initial-state properties.

Formally, the photoemission process can be described by the transition probability w_{fi} of an N-electron initial state $|\Psi_i^N\rangle$ to an excited final state $|\Psi_f^N\rangle$, which can be given by Fermi's golden rule:

$$w_{fi} = \frac{2\pi}{\hbar} |\langle \Psi_f^N | H_{int} | \Psi_i^N \rangle|^2 \delta(E_f^N - E_i^N - h\nu), \qquad (3)$$

where E_i^N and E_f^N are the initial- and final-state energies of the N-electron system. H_{int} is a perturbative Hamiltonian describing the electron-photon interaction

$$H_{int} = \frac{1}{2m}\left(\mathbf{p} + \frac{e}{c}\mathbf{A}\right)^2 - e\Phi - \frac{\mathbf{p}^2}{2m}$$
$$\approx \frac{e}{2mc}(\mathbf{A}\cdot\mathbf{p} + \mathbf{p}\cdot\mathbf{A}) \approx \frac{e}{mc}\mathbf{A}\cdot\mathbf{p}, \qquad (4)$$

where $\mathbf{p}$ is the electron momentum operator and $\mathbf{A}$ and Φ are the electromagnetic vector and scalar potentials. On the second line, we enforce the Weyl gauge in which the scalar potential $\Phi = 0$. The first approximation step also disregards two-photon processes $\mathbf{A}^2$. The second approximation step holds when $\mathbf{A}$ is constant over atomic dimensions such that $[\mathbf{A}, \mathbf{p}] \sim \mathbf{\nabla} \cdot \mathbf{A} = 0$; see Sec. II.C for a comment on the limitations of this so-called dipole approximation.[4] Note that

---

[4]Alternatively, one may adopt the Coulomb gauge and enforce $\mathbf{\nabla} \cdot \mathbf{A} = 0$. In this case, scalar potential $\Phi \neq 0$. Only when there is no free charge ρ can the Coulomb and the Weyl gauges be simultaneously satisfied. This condition is also known as the radiation gauge, which can be seen via

$$\frac{\rho}{\varepsilon_0} = \mathbf{\nabla} \cdot \mathbf{E} = -\nabla\Phi - \partial_t(\mathbf{\nabla} \cdot \mathbf{A}) \xRightarrow[\text{gauge}]{\text{radiation}} 0.$$
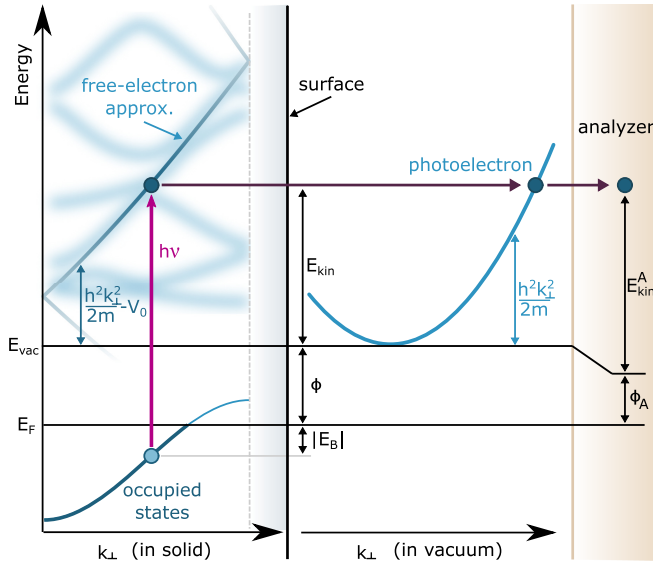
FIG. 4. Kinematics of the photoemission process in the three-step model. An electron is excited from an initial state with binding energy $|E_B|$ below E_F to a final state above E_{vac}, with $\mathbf{k}_\perp$ conserved. The final state is often approximated by a free-electron dispersion offset by an inner potential V_0, shown here in a reduced zone scheme. After transmission through the surface barrier, the photoelectron has kinetic energy $E_{kin} = h\nu - \phi - |E_B|$, where ϕ is the sample work function. $\mathbf{k}_\perp$ is not conserved during transmission through the sample surface, while $\mathbf{k}_\parallel$ is conserved throughout the entire photoemission process. Note that the detected kinetic energy E_{kin}^A is referenced to the vacuum level in the analyzer, which is determined by the analyzer work function ϕ_A.

the golden rule formalism is valid only for weak perturbations; for sufficiently intense peak fields such as those achieved in ultrafast pulses, the perturbation expansion must include higher-order terms to describe nonlinear effects such as multiphoton absorption (Lambropoulos, 1974).

Equation (3) can be described by the *one-step model*, in which photon absorption, electron excitation, and electron detection are treated as a single coherent process (Mahan, 1970; Feibelman and Eastman, 1974; Minár *et al.*, 2011). Here the final state of the photoelectron is a time-reversed LEED state, where the wave function rapidly decays into the bulk and matches a free-electron plane wave form outside the surface (Hopkinson, Pendry, and Titterington, 1980; Karkare *et al.*, 2017). Pragmatically it is often more convenient to use the *three-step model*, which phenomenologically divides the photoemission process into three steps (Berglund and Spicer, 1964): (1) The photon drives a direct optical transition for an electron in the bulk of the material. This step contains the information on the intrinsic electronic structure of the material. (2) The electron propagates to the surface. This process is described in terms of an effective mean free path λ_{MFP} imposed by both elastic and inelastic scattering processes. (3) The electron is transmitted through the surface barrier, with the electron ultimately occupying a free-electron plane wave state in the vacuum extending to the detector. The three-step model has the advantage of being more tractable since the different steps in the photoemission process are somewhat decoupled; however, in many cases the full

one-step formalism may be required to fully explain spectral intensities and matrix element effects (Lindroos, 1982; Minár *et al.*, 2011); see Sec. II.D.

To develop intuition for the photoemission process, we begin with the simple case of noninteracting electrons. The more general treatment of many-body systems, which is required to describe correlated states, is covered in Sec. II.F and by Damascelli, Hussain, and Shen (2003). As a consequence of the noninteracting condition, the N-electron initial and final states can both be trivially factorized:

$$|\Psi_f^N\rangle = \mathcal{A}|\phi_f^\mathbf{k}\rangle \otimes |\Psi_f^{N-1}\rangle, \tag{5}$$

$$|\Psi_i^N\rangle = \mathcal{A}|\phi_i^\mathbf{k}\rangle \otimes |\Psi_i^{N-1}\rangle, \tag{6}$$

where $\mathcal{A}$ is an antisymmetry operator enforcing the Pauli principle. $|\phi_i^\mathbf{k}\rangle$ and $|\phi_f^\mathbf{k}\rangle$ are the wave functions of the electron before and after absorbing a photon, and they both have the same wave vector $\mathbf{k}$ due to momentum conservation. We denote their energies as $\epsilon_\mathbf{k}$ and ϵ_f. $|\Psi_i^{N-1}\rangle$ and $|\Psi_f^{N-1}\rangle$ are the initial- and final-state wave functions of the remaining $(N-1)$-electron system. The noninteracting limit allows for a dramatic simplification since the $(N-1)$-electron system is unaffected by the removal of one electron, and thus $|\Psi_i^{N-1}\rangle = |\Psi_f^{N-1}\rangle$.

We can now calculate the total photocurrent $I = \sum_{i,f} w_{fi}$ by plugging these approximations into Eq. (3). To cast this into an intuitive form, we assume that at most a single transition $(i \to f)$ occurs at each $\mathbf{k}$. Then we have

$$I_{i \to f}(\mathbf{k}, \epsilon_f) \propto |M_{f,i}^\mathbf{k}|^2 \delta(\epsilon_f - \epsilon_\mathbf{k} - h\nu), \tag{7}$$

$$M_{f,i}^\mathbf{k} \equiv \langle \phi_f^\mathbf{k} | H_{int} | \phi_i^\mathbf{k} \rangle. \tag{8}$$

$M_{f,i}$ is the one-electron dipole matrix element, described in Sec. II.D. These equations are the central result of this section: the ARPES spectrum of a noninteracting system is a sharp peak that traces the electronic band dispersion $\epsilon_\mathbf{k}$, with its intensity modulated by the dipole matrix element. This result establishes the capability of ARPES to be used as a band-mapping technique. We stress that this simple picture will be modified in the presence of interactions, as described in Sec. II.F. Before we delve into this formalism, we explore the consequences of steps (2) and (3) of the three-step model, as well as the significance of the matrix elements and photoelectron spin.

B. Final state and $k_\perp$ determination

Although all components of $\mathbf{k}$ are conserved during photon absorption (first step of the three-step model), only the surface-parallel component $\mathbf{k}_\parallel$ is conserved when the electron transmits through the surface (third step). However, it is possible to recover the orthogonal component $\mathbf{k}_{\perp\,solid}$ if it is assumed that the final-state dispersion of the photoelectron within the crystal can be parametrized using a free-electron dispersion offset by a potential V_0: $\epsilon_f = \hbar^2 \mathbf{k}_{solid}^2 / 2m - V_0$; see Fig. 4 (Pendry, 1969; Himpsel and Eastman, 1978; Chiang *et al.*, 1979, 1980; Bartynski *et al.*, 1986). V_0, also known as

the inner potential, has been related to the average effective potential experienced by electrons in the solid (Pendry, 1969; Saldin and Spence, 1994), although it is now typically treated as a phenomenological parameter. Assuming that the photoelectron suffers no inelastic collisions at the surface, its final-state energy in the solid can be equated with the kinetic energy in vacuum $E_{\mathrm{kin}} = \hbar^2 \mathbf{k}_{\mathrm{vac}}^2/2m$. We see that the inner potential accounts for the discontinuity in $\mathbf{k}_\perp$ at the surface: $\hbar^2 \mathbf{k}_{\perp\mathrm{vac}}^2/2m = \hbar^2 \mathbf{k}_{\perp\mathrm{solid}}^2/2m - V_0$. This leads to

$$\hbar \mathbf{k}_{\perp\mathrm{solid}} = \sqrt{2m[E_{\mathrm{kin}}\cos^2(\vartheta) + V_0]}. \qquad (9)$$

Since E_{kin} varies with $h\nu$, Eq. (9) establishes a strategy for using a tunable light source to determine the $\mathbf{k}_{\perp\mathrm{solid}}$ dispersion. V_0 is *a priori* unknown but can be determined experimentally by combining Eq. (1) with the known momentum periodicity in $\mathbf{k}_{\perp\mathrm{solid}}$:

$$E_B(\mathbf{k}_{||}, \mathbf{k}_{\perp\mathrm{solid}}) = E_B(\mathbf{k}_{||}, \mathbf{k}_{\perp\mathrm{solid}} + n\mathbf{G}_\perp), \qquad (10)$$

where $\mathbf{G}_\perp$ is the out-of-plane reciprocal lattice vector and n is any integer. Note that two-dimensional electronic states do not disperse with $\mathbf{k}_\perp$; therefore, $h\nu$-dependent measurements are routinely employed to distinguish surface- from bulk-derived states.

Finally, we note that the free-electron final-state approximation does not hold in general, especially with low-$h\nu$ light sources. The structure of the final states can indeed modulate the intensity of the ARPES spectrum, a fact that must be kept in mind with the increased use of low-$h\nu$ sources in recent years (Miller *et al.*, 2015; Xiong *et al.*, 2017).

C. Surface sensitivity, resolution, and $\mathbf{k}_{||}$ range

The photoelectron signal is attenuated from the surface by the inelastic mean free path of electrons in the solid λ_{MFP}, which is a strong function of kinetic energy but weakly material dependent, with a minimum <1 nm at 20–100 eV (Seah and Dench, 1979). This implies that ARPES performed with ultraviolet light sources is highly surface sensitive, with the majority of the signal originating from the top few atomic layers. The sample surface must be atomically flat and clean to obtain information relevant to the bulk physics; see Sec. III.D.

Other factors impacting the ARPES signal include resolution effects, which can be both intrinsic and extrinsic. An important intrinsic contribution to the $\mathbf{k}_\perp$ resolution is given by the lifetime of the final state, which is finite due to the scattering processes associated with λ_{MFP}; see Sec. II.F for a more rigorous description of lifetime effects in photoemission. This can be expressed as a position-momentum uncertainty relation: $\Delta\mathbf{k}_\perp \approx \hbar/\lambda_{\mathrm{MFP}}$. For typical $h\nu$ this implies $\mathbf{k}_\perp$ broadening up to ~ 0.1 Å^{-1}, which can be a significant fraction of the Brillouin zone for layered materials (Feibelman and Eastman, 1974; Strocov, 2003). Another intrinsic factor is the breakdown of the dipole approximation $\mathbf{\nabla} \cdot \mathbf{A} = 0$. In fact, there is an abrupt change in the dielectric function at the surface leading to $\mathbf{A}$ strongly varying on an atomic scale, which can impart momentum to the photoelectron and act as a source of uncertainty in $\mathbf{k}_\perp$ (Levinson,

Plummer, and Feibelman, 1979; Miller, McMahon, and Chiang, 1996; Zabolotnyy, 2007b).

Extrinsic factors impacting resolution include sample and surface quality, which can broaden the momentum resolution due to elastic scattering and by introducing angular uncertainty. Another important factor is the experimental energy resolution, which includes the bandwidth of the light source as well as the resolution of the photoelectron spectrometer: $(\Delta E_{\mathrm{tot}})^2 = (h\Delta\nu)^2 + (\Delta E_{\mathrm{spec}})^2$. The momentum resolution has negligible contributions from $h\Delta\nu$ and is largely determined by the angular resolution of the spectrometer $\Delta\vartheta$:

$$\hbar\Delta\mathbf{k}_{||} = \sqrt{2mE_{\mathrm{kin}}}\cos(\vartheta)\Delta\vartheta. \qquad (11)$$

Another factor impacting experimental resolution is the *space-charge effect*, which occurs when the density of photoelectrons is high enough that the Coulomb repulsion between electrons in vacuum cannot be ignored (Zhou, Wannberg *et al.*, 2005; Hellmann *et al.*, 2009). Space charging leads to an energetic shift and broadening of the ARPES spectra. It is a more severe problem with pulsed light sources, especially those with lower repetition rates, due to the fact that the electrons are more likely to be emitted within the same interval in time.

Finally, we note that $h\nu$ determines the range of accessible states in both energy and momentum. The deepest E_B that can be probed is $E_B^{\mathrm{max}} = h\nu - \phi$, while the largest $\mathbf{k}_{||}$ is given by $\hbar\mathbf{k}_{||}^{\mathrm{max}} = \sqrt{2m(h\nu - \phi)}$.

D. Matrix element effects

The dipole matrix element $M_{f,i}^{\mathbf{k}}$ was previously introduced as a factor modulating the photoemission intensity within the three-step model and under the dipole and noninteracting electron approximations. The dipole-transition matrix element has profound consequences for the ability of ARPES to extract microscopic information about the wave function of the initial state $|\phi_i^{\mathbf{k}}\rangle$. For pedagogical discussions, see Karkare *et al.* (2017) and Moser (2017) and references therein. Although evaluating the matrix element in general can be complicated due to detailed measurement geometry and orbital hybridization (Day *et al.*, 2019), in many cases symmetry or conservation laws provide clear predictions. For example, when the electron is photoemitted on a mirror symmetry plane of the sample, the parity of $|\phi_i^{\mathbf{k}}\rangle$ can be deduced by measuring the photoemission intensity for various linear polarization geometries. This concept can be generalized to determine the orbital character of bands throughout the Brillouin zone (Zhang *et al.*, 2012; King *et al.*, 2014; Matt *et al.*, 2018; Day *et al.*, 2019; Yi *et al.*, 2019). The use of linearly polarized light to discern orbital character is often referred to as *linear dichroism*.

Another common application of matrix elements is to analyze the contrast in the ARPES spectrum generated between left- and right-handed circularly polarized light, known as circular dichroism in the angular distribution of photoelectrons (Schneider and Kirschner, 1995). This technique can be sensitive to the time-reversal symmetry of electronic states, with recent applications to the spin- and

orbital-angular momenta of states in topological insulators (Wang, Hsieh *et al.*, 2011; Park *et al.*, 2012), as well as the chirality and Berry phases of Dirac electrons in graphitic materials (Wang, Hsieh *et al.*, 2011; Park *et al.*, 2012). However, we caution that straightforward interpretation can be hindered by final-state effects as well as the contribution of $\nabla \cdot \mathbf{A} \neq 0$ terms, which can lead to geometry and $h\nu$ dependence of the circular-dichroism signal (Jung *et al.*, 2011; Gierz *et al.*, 2012; Mirhosseini and Henk, 2012; Scholz *et al.*, 2013; Sánchez-Barriga *et al.*, 2014; C.-Z. Xu *et al.*, 2015). Furthermore, circular dichroism is generically expected if the experiment is not carefully aligned to the sample's mirror plane. For example, circular dichroism in cuprates (Kaminski *et al.*, 2002) has been largely understood in the context of reflection-symmetry-breaking superstructure, without invoking any phenomena that break time-reversal symmetry (Borisenko *et al.*, 2004; Arpiainen, Bansil, and Lindroos, 2009).

E. Photoelectron spin

When time-reversal symmetry ($\epsilon_{\mathbf{k},\uparrow} = \epsilon_{-\mathbf{k},\downarrow}$) and inversion symmetry ($\epsilon_{\mathbf{k},\uparrow} = \epsilon_{-\mathbf{k},\uparrow}$) are both present, all electronic states are spin degenerate: $\epsilon_{\mathbf{k},\uparrow} = \epsilon_{\mathbf{k},\downarrow}$. This means that spin-polarized states may be expected in magnetic materials and in materials with strong spin-orbit coupling and broken inversion symmetry. Because of the increasingly mainstream role of spin-resolved ARPES in quantum materials research, it is worth discussing other factors contributing to the spin of a photoelectron. Here we mention two important considerations: matrix elements and the depth dependence of photoemission. For more comprehensive reviews see Kessler (1985), Kirschner (1985), Osterwalder (2006), and Heinzmann and Dil (2012).

Although the matrix element is often regarded as a higher-order concern for ARPES, it is indispensable when determining the spin of a photoelectron (Kessler, 1985). Light-polarization dependence of the photoelectron spin is ubiquitous in spin-orbit coupled systems due to the fact that the initial state is a linear superposition of different spin states: $|\phi\rangle = \sum_\alpha c_{\alpha,\uparrow}|\alpha, \uparrow\rangle + c_{\alpha,\downarrow}|\alpha, \downarrow\rangle$, where α refers to the orbital part of the wave function. The light polarization, together with the spatial symmetry of the orbitals, determines which components of the wave function are photoemitted (Sec. II.D). This can result in spin-polarized photoelectrons even from unpolarized states, as is well known for circularly polarized light in GaAs (Pierce and Meier, 1976). More recently, light polarization has been shown to control the direction of spin polarization of photoelectrons from topological insulator surface states (Sec. VII.B.1) (Jozwiak *et al.*, 2013; Sánchez-Barriga *et al.*, 2014; Xie *et al.*, 2014; Zhu *et al.*, 2014). Furthermore, spin-polarized electrons can be photoemitted even from unpolarized initial states with unpolarized light due to spin-orbit interactions in the final state (Kirschner, 1985; Heinzmann and Dil, 2012). Such effects are typically $h\nu$ dependent (Irmer *et al.*, 1995); see also Jozwiak *et al.* (2011) and references therein. For these reasons, one is cautioned not to take spin-polarized electrons as unambiguous evidence of novel physics, such as topological surface states.

Another important factor concerns the depth with respect to the surface from which the electrons originate. The finite mean free path implies that the photoemission signal is weighted strongly toward atomic layers closest to the surface. This has been invoked to explain measurements of "hidden spin polarization," in which the polarization originates from local inversion symmetry breaking within a unit cell despite the entirety of the unit cell being inversion symmetric (Riley *et al.*, 2014; X. Zhang *et al.*, 2014; Gotlieb *et al.*, 2018). At the same time, the photoelectrons originating from different depths can quantum mechanically interfere, leading to spin polarizations that depend sensitively on geometry and $h\nu$ (Zhu, Veenstra *et al.*, 2013).

Although complex, these effects endow spin-resolved ARPES with unique capabilities in unraveling the spatial and orbital structure of the initial-state wave function. However, they do imply that systematic measurements (as a function of $\mathbf{k}_{||}$, light polarization, and $h\nu$) with well-defined geometries are required to draw physically meaningful conclusions. A comparison with fully relativistic one-step photoemission calculations can be particularly helpful for interpreting the data (Braun, 1996; Minár *et al.*, 2011; Mirhosseini and Henk, 2012; Scholz *et al.*, 2013).

F. Photoemission from a many-body system

We adopt the approach of Damascelli, Hussain, and Shen (2003), which follows from two equivalent treatments of photoemission in a many-body system: multiple scattering (Mahan, 1970; Bardyszewski and Hedin, 1985) and quadratic-response (Schaich and Ashcroft, 1971; Caroli *et al.*, 1973) theories. The main difference from our treatment in Sec. II.A is that for an interacting system the many-body final and initial states cannot be trivially factorized as in Eqs. (5) and (6). Nevertheless, these forms may be cautiously taken as approximations under certain conditions, which we now elaborate on.

We can approximate the removal of the electron as an instantaneous process, known as the *sudden approximation*. In this limit the photoelectron has high final-state energy and no time to interact with the ($N - 1$)-electron system, thereby justifying the factorization in Eq. (5). The sudden creation of a hole can be associated with bosonic excitations such as phonons, plasmons, and electron-hole pairs that lead to satellite peaks on the low-energy side of the main photoemission peak (Åberg, 1967; Brisk and Baker, 1975; Citrin, Wertheim, and Baer, 1977). These are known as *intrinsic losses*, to be distinguished from *extrinsic losses*, which the photoelectron may suffer during transit or even after its transit out of the material (Joynt, 1999; Hedin and Lee, 2002; Rameau *et al.*, 2011). It has become commonplace for most ARPES measurements to be analyzed within the sudden approximation (Koralek *et al.*, 2006), although we caution that a rigorous justification at low $h\nu$ has not been established to date.

Turning now to the initial state, we may utilize the factorization in Eq. (6) by treating interactions in a mean-field approximation (as in Hartree-Fock theory). We then arrive at the most significant deviation from the independent-electron picture: the ($N - 1$)-electron system can no longer be regarded as unchanged due to electron removal, $|\Psi_i^{N-1}\rangle \neq |\Psi_f^{N-1}\rangle$.

Instead, under the sudden approximation, the $(N - 1)$-electron final state can be left in any number of excited states with eigenfunctions $|\Psi_m^{N-1}\rangle$ and energies E_m^{N-1}. The total transition probability is then a sum over excited states:

$$\sum_{f,i} |M_{f,i}^{\mathbf{k}}|^2 \sum_m |\langle \Psi_m^{N-1}|\Psi_i^{N-1}\rangle|^2 \delta(\epsilon_f + E_m^{N-1} - E_i^N - h\nu). \quad (12)$$

$|\langle \Psi_m^{N-1}|\Psi_i^{N-1}\rangle|^2$ is the probability that the removal of an electron from state i will leave the $(N - 1)$-electron system in the excited eigenstate m. For strongly correlated materials, $|\Psi_i^{N-1}\rangle$ will overlap with many eigenstates, leading to rich spectra including satellites and broadened spectral peaks. These deviations from the noninteracting picture establish the basis for ARPES to investigate many-body effects in strongly correlated electron systems. Within the Green's function formalism (Mahan, 2000), one may write the following single-electron removal spectral function $A^-(\mathbf{k}, \omega)$:

$$A^-(\mathbf{k}, \omega) = \sum_m |\langle \Psi_m^{N-1}|c_{\mathbf{k}}|\Psi_i^N\rangle|^2 \delta(\omega - E_m^{N-1} + E_i^N). \quad (13)$$

Physically, $A^-(\mathbf{k}, \omega)$ is the probability of the remaining $(N - 1)$-electron system changing in energy by ω after removal of an electron with wave vector $\mathbf{k}$. $A^-(\mathbf{k}, \omega)$ is related to the full spectral function $A(\mathbf{k}, \omega)$ by $A^-(\mathbf{k}, \omega) = A(\mathbf{k}, \omega)f(\omega)$, where $f(\omega)$ is the Fermi-Dirac distribution. By comparing Eqs. (12) and (13), we are motivated to write the photoemission intensity as

$$I(\mathbf{k}, \omega) = I_0(\mathbf{k}, h\nu, \mathbf{A})f(\omega)A(\mathbf{k}, \omega). \quad (14)$$

This is the central result of this section: under the sudden approximation (and in the absence of extrinsic losses), the photoemission signal is proportional to the single-particle spectral function. The factor of $f(\omega)$ accounts for the fact that photoemission can occur only from occupied electronic states, which enters through a thermal ensemble average when evaluating the right-hand side of Eq. (13). In practice, this limits application of ARPES to states below the Fermi level. The prefactor $I_0(\mathbf{k}, h\nu, \mathbf{A})$ accounts for intensity modulations related to matrix element effects. This relation is frequently used in modern ARPES experiments (Ding *et al.*, 1995; Randeria *et al.*, 1995; Damascelli, Hussain, and Shen, 2003).

Note that the spectral function (regardless of the correlations) obeys sum rules due to particle number and energy conservation (Randeria *et al.*, 1995; Norman *et al.*, 2000; Hüfner, 2003).

The spectral function is related to the retarded Green's function $G(\mathbf{k}, \omega) = 1/[\omega - \epsilon_{\mathbf{k}} - \Sigma(\mathbf{k}, \omega)]$ by $A(\mathbf{k}, \omega) = -(1/\pi)\text{Im}G(\mathbf{k}, \omega)$ (Mahan, 2000). Here interactions are taken into account via the *proper self-energy* $\Sigma(\mathbf{k}, \omega) = \Sigma'(\mathbf{k}, \omega) + i\Sigma''(\mathbf{k}, \omega)$, in terms of which the spectral function is given by

$$A(\mathbf{k}, \omega) = -\frac{1}{\pi}\frac{\Sigma''(\mathbf{k}, \omega)}{[\omega - \epsilon_{\mathbf{k}} - \Sigma'(\mathbf{k}, \omega)]^2 + [\Sigma''(\mathbf{k}, \omega)]^2}. \quad (15)$$

It can be seen that $\Sigma'(\mathbf{k}, \omega)$ offsets the electron band energy $\epsilon_{\mathbf{k}}$, while $\Sigma''(\mathbf{k}, \omega)$ broadens the spectral peak. Physically, the

imaginary part of the self-energy represents the single-particle scattering rate, which dictates the lifetime and therefore the energy width of each state.[5] Note that for a noninteracting system $\Sigma(\mathbf{k}, \omega) = 0$ and $A(\mathbf{k}, \omega) = \delta(\omega - \epsilon_{\mathbf{k}})$, which is consistent with Eq. (7). For weakly interacting electrons $\Sigma(\mathbf{k}, \omega)$ can be expanded to first order about $\epsilon_{\mathbf{k}}$, leading to

$$A(\mathbf{k}, \omega) = Z_{\mathbf{k}}\frac{\Gamma_{\mathbf{k}}/\pi}{(\omega - \epsilon_{\mathbf{k}})^2 + \Gamma_{\mathbf{k}}^2} + A_{\text{inc}}(\mathbf{k}, \omega), \quad (16)$$

where $Z_{\mathbf{k}} = (1 - \partial\Sigma'/\partial\omega)^{-1}$, $\epsilon_{\mathbf{k}} = Z_{\mathbf{k}}(\epsilon_{\mathbf{k}} + \Sigma')$, and $\Gamma_{\mathbf{k}} = Z_{\mathbf{k}}|\Sigma''|$ and the self-energy and derivatives are evaluated at $\omega = \epsilon_{\mathbf{k}}$. This description is valid near the Fermi surface with the conditions $|\Sigma''| \ll \epsilon_{\mathbf{k}}$ for small ω and $|\mathbf{k} - \mathbf{k}_F|$. Consistent with the predictions of Fermi liquid theory, the concept of a *quasiparticle* survives, as represented by the first term of Eq. (16), although with a reduced spectral weight $Z_{\mathbf{k}}$ (also called the coherence factor). A_{inc} is known as the incoherent part of the spectral function. It represents the error introduced by the first-order approximation of $\Sigma(\mathbf{k}, \omega)$ and must be included to satisfy the sum rule. This formalism has to be slightly modified when applied to superconductors, where charge carriers are annihilated in pairs; see Sec. III.A.

III. EXPERIMENTAL METHODS

A. Data analysis techniques and conventions

Figure 5 lays out the typical workflow of basic data reduction steps from the raw detector image to the electron energy-momentum spectra, as well as a partial collection of subsequent model-based analyses. The raw camera images often undergo different image processing procedures to remove pixel-to-pixel efficiency variations (Strocov *et al.*, 2014). Then detector nonlinearity has to be corrected so that the recorded intensity is proportional to the true electron counts (Reber *et al.*, 2014; Y. He *et al.*, 2016). For detailed analyses such as Fermi-function division and spectral weight analyses, discrete structures in the energy spectrum of the light source also have to be deconvolved iteratively.

The measured E_{kin} must be converted to the intrinsic energy $E - E_F = -E_B$, entailing a rigid shift of the energy axis of the measured spectrum. In principle the magnitude of this shift is given by $\phi_A - h\nu$, where ϕ_A is the analyzer work function; see Fig. 4. However, empirically it is more accurate to determine the E_F reference by fitting a Fermi-Dirac distribution to the spectrum of a polycrystalline metal that is electrically connected to the sample (thus ensuring that they share the same E_F). To account for lensing effects which may occur in the analyzer, this correction must often be performed separately on each angle channel of the detector. Finally, knowing the kinetic energy and emission angles $(E_{\text{kin}}, \vartheta_x, \vartheta_y)$, energy-momentum conservation laws [Eqs. (1) and (2)] may be

---

[5]It is important to differentiate the single-particle scattering rate, which measures single-particle excitation lifetime, from the transport scattering rate defined in the Boltzmann equation (Ashcroft and Mermin, 1976) and the depopulation lifetime in pump-probe experiments (S.-L. Yang *et al.*, 2015; Kemper, Abdurazakov, and Freericks, 2018).
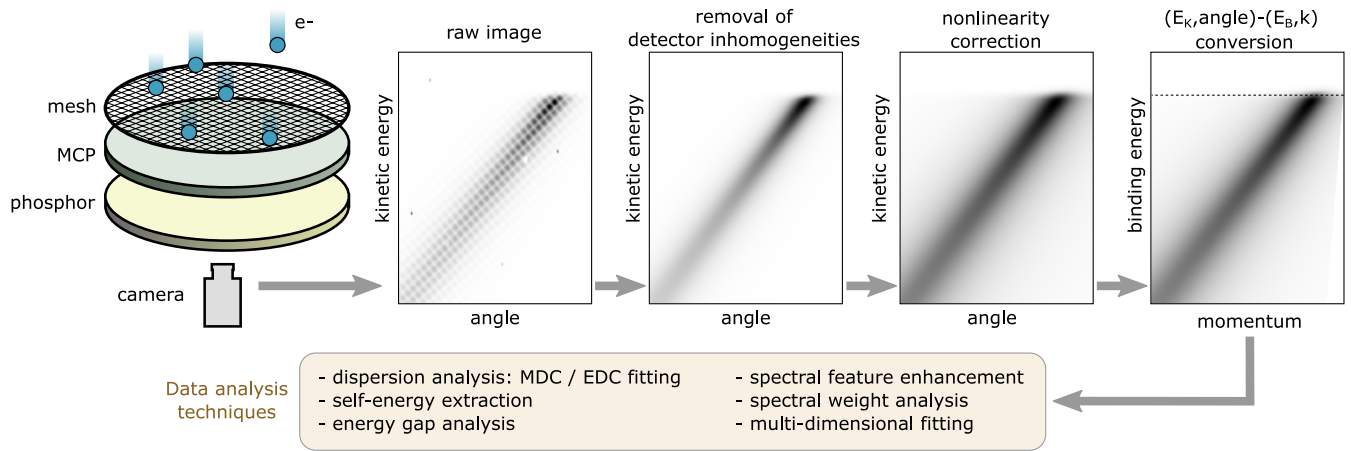
FIG. 5. Working flowchart from detector image to energy-momentum spectrum for modern ARPES with multiplexing detectors. Electron events are amplified in a multichannel plate (MCP) detector and imaged on a phosphor screen using a camera. In many implementations, a wire mesh is used to establish a uniform electric field but leaves an imprint on the raw data that must be removed. Various methods exist for removing the grid pattern during acquisition (so-called dithering or swept modes) or during postprocessing. In this flowchart, the effect of the mesh and detector inhomogeneity are exaggerated for clarity; see the text for more details of the subsequent analysis steps.

applied to compute the parallel momentum of electrons $\mathbf{k}_{\parallel}$ (Ishida and Shin, 2018; Iwasawa et al., 2018). Note that when the sample work function differs from that of the analyzer ($\phi \neq \phi_A$) one should additionally consider the effect of the electric field between the sample and analyzer (Hengsberger et al., 2008).

The photoemission intensity is most commonly displayed as an *energy-momentum cut*, as shown in Fig. 6(a). Much spectral information can then be extracted depending on the data quality and scope of models (Fig. 5). One-dimensional plots of the intensity versus $\mathbf{k}_{\parallel}$ or versus energy are known as momentum distribution curves (MDCs) or energy distribution curves (EDCs), respectively (Mahan, 1970; Schaich and
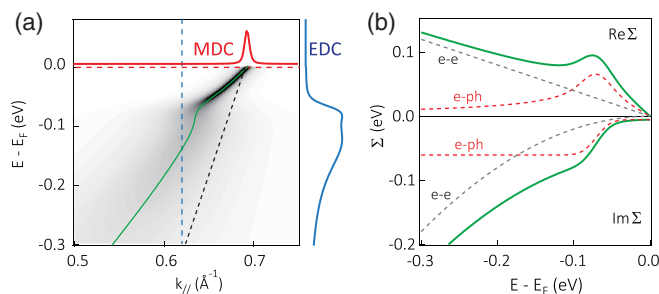
FIG. 6. Dispersion extraction and self-energy analysis in AR-PES. (a) Cut showing the photoemission intensity as a function of energy and momentum. The momentum distribution curve (MDC) and energy distribution curve (EDC) at the red and blue dashed lines are shown above and to the right, respectively. The green line is an MDC fitted dispersion. The black dashed line is the noninteracting bare-band dispersion used in the simulation. (b) Using MDC (shown here) or EDC fitting analysis, it is possible to extract Σ' and Σ'' (green lines on the top and bottom panels, respectively). From a modeling of their energy dependence, they may be further decomposed into contributions such as those from electron-electron (e-e) and electron-phonon (e-ph) scattering (dashed lines).

Ashcroft, 1971; Valla, Fedorov, Johnson, Wells et al., 1999c). The band dispersion can be approximately obtained by fitting to the peak of the MDCs or EDCs, although in general these procedures will not yield identical results due to the energy and momentum dependence of both the electron self-energy and the dipole-transition matrix element (Norman et al., 2001). Figure 6(a) highlights a complex EDC line shape (blue line) due to the energy-dependent electron-phonon self-energy. To extract interaction effects, a common approach is to map the fitting results onto Eq. (15) by approximating $\Sigma(\omega)$ to be $k_{\parallel}$ independent (only for the momentum along the cut) and reasonably guessing the background line shape (Valla, Fedorov, Johnson, and Hulbert, 1999). $\Sigma''(\omega)$ can be identified with the product of the energy-dependent peak momentum width $\Delta k_{\parallel}$ with the bare-band velocity $\partial\epsilon_{\mathbf{k}}/\partial\mathbf{k}$. Extraction of the self-energy can be nuanced since the bare-band dispersion $\epsilon_{\mathbf{k}}$ [the black dashed line in Fig. 6(a)] is in general unknown and must be empirically estimated from the data (Kordyuk et al., 2005). After $\Sigma'(\omega)$ and $\Sigma''(\omega)$ are extracted, modeling can be applied to decompose them into contributions from different interaction mechanisms, such as electron-electron and electron-phonon scattering [Fig. 6(b)], or even to achieve the reconstruction of the anomalous self-energy in the superconducting state (Bok et al., 2010, 2016), and the Eliashberg function in electron-phonon coupled systems (Shi et al., 2004; Zhou et al., 2005; Iwasawa et al., 2013). This modeling can be constrained by invoking the Kramers-Kronig relationship between $\Sigma'(\omega)$ and $\Sigma''(\omega)$ (Norman et al., 1999), although this relation relies heavily on assumptions made for the unoccupied side of the dispersion.

Often particle-hole symmetry $\Sigma(\omega) = \Sigma(-\omega)$ may be assumed (albeit not necessarily justified) for two-dimensional spectral function fittings (Meevasana et al., 2008; Li, Zhou et al., 2018). Assuming an energy-independent dipole-transition matrix element, its momentum dependence may also be extracted in this process (Meevasana et al., 2008). There are more complex models and data analysis methods,
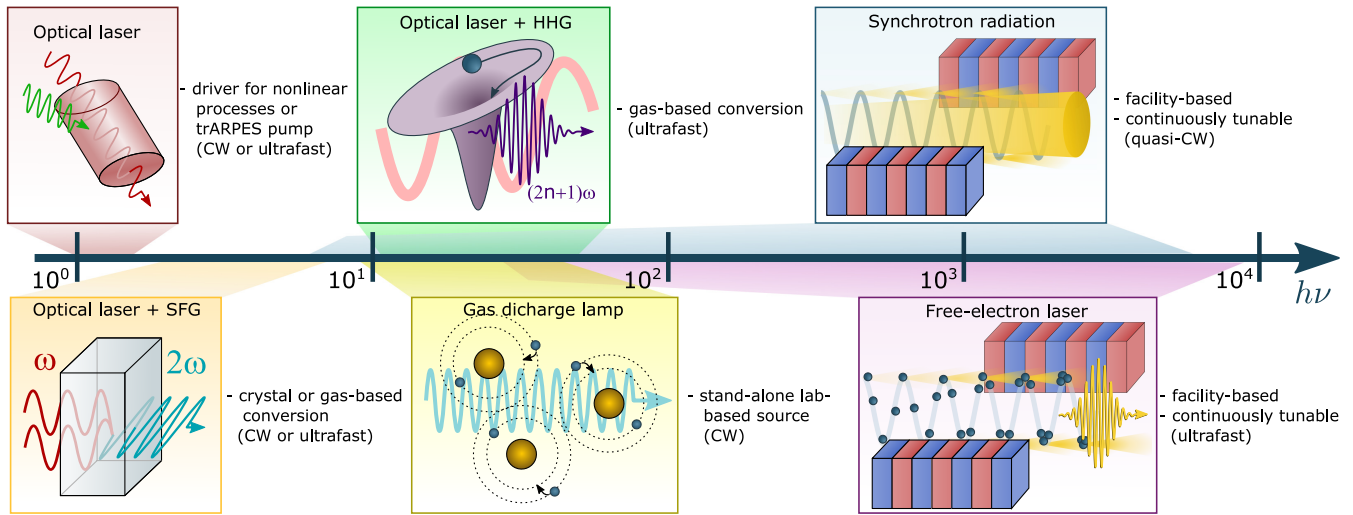
FIG. 7. Light sources for ARPES and their main characteristics and typical photon energy ranges.

including the tomographic density of states method for impurity scattering removal (Reber *et al.*, 2012), marginal Fermi liquid and power law liquid self-energy model fit (Leong *et al.*, 2017; Reber *et al.*, 2019), spectral weight moment analysis for energetic evaluation (Kondo *et al.*, 2009, 2011; Hashimoto *et al.*, 2015), critical scaling of the spectral function (Wang *et al.*, 2009), and phenomenological self-energy-based superconducting gap fitting (Franz and Millis, 1998; Norman *et al.*, 1998; Kordyuk *et al.*, 2003).

Given its frequent occurrence in the literature, of particular importance is superconducting gap fitting. In this case, the pairing interaction imprints on both the normal self-energy $\Sigma(\mathbf{k}, \omega)$ and the *anomalous self-energy* $\phi(\mathbf{k}, \omega)$ (Gor'kov, 1958; Nambu, 1960). Then ARPES probes the imaginary part of the retarded diagonal component of the Nambu Gor'kov Green's function, which indirectly reflects the superconducting pairing via the energy gap. In the case of pairing mediated by exchange of low-energy bosons, the anomalous self-energy is related to the superconducting gap $\Delta(\mathbf{k}, \omega)$ by $\Delta(\mathbf{k}, \omega) = \phi(\mathbf{k}, \omega)/Z_{\mathbf{k}}$. One commonly used low-energy phenomenological model to extract the superconducting spectral gap was proposed by Norman *et al.* (1998), in which the energy dependence of the quasiparticle scattering rate is neglected in most cases. Practically, for energy gaps comparable to the energy resolution, or in spectra that intrinsically lack coherent quasiparticles, model fitting should be treated with extreme caution, as the noise, resolution, and scattering effects can easily create an illusion of gap closure (Vishik, 2018; He *et al.*, 2020). For situations with clear coherent peaks on the gap edge, one should exercise caution when applying techniques that implicitly enforce particle-hole symmetry (such as symmetrization with respect to the Fermi level). Historically, the shift of the Fermi edge midpoint has been taken as a measure of the energy gap to overcome the lack of superconducting quasiparticle and resolution. This method is vulnerable to momentum misalignment with respect to $\mathbf{k}_F$ and strongly energy-dependent low-energy spectral intensity and therefore should be treated as a qualitative indicator of gaps. In some cases, partially momentum-integrated spectra are used to extract superconducting gap via

the Dynes fit (Dynes, Narayanamurti, and Garno, 1978; Reber *et al.*, 2012), although the requirement for an energy- and momentum-independent self-energy can be challenging to justify.

To qualitatively enhance dispersive features in the presence of strong background, a common approach is to take a second derivative of the data (along either the energy or momentum axis) or apply contrast-enhancing algorithms including maximum curvature (P. Zhang *et al.*, 2011), minimum gradient (He, Wang, and Shen, 2017), and superresolution neural network methods (Peng *et al.*, 2020). These techniques are not guaranteed to faithfully retain the original quantitative spectral information.

B. Light sources

The light source (Fig. 7) is a key factor establishing the capabilities of an ARPES experimental setup. The photon energy $h\nu$ determines the photoelectron escape depth, as well as the range and resolution of both $\mathbf{k}_\perp$ (Sec. II.B) and $\mathbf{k}_\parallel$ (Sec. II.C). In practice, higher $h\nu$ sources are often chosen for new material characterizations due to their large energy-momentum coverage. Laser light sources typically offer lower $h\nu$ but have relatively high flux and can provide either narrow or broad bandwidth. Lower $h\nu$ also implies better momentum resolution at a given detector angular resolution [Eq. (11)]. Narrow-band lasers are frequently used where high resolution, energy stability, and statistics are paramount, whereas broadband lasers are employed for time-resolved ARPES (trARPES). Continuously $h\nu$ tunable sources such as synchrotrons are highly desirable for $\mathbf{k}_\perp$ mapping in 3D materials and the identification of 2D surface states. Gas discharge lamps provide lab-based options for high-energy-resolution measurements, albeit with the drawbacks of relatively large beam size, tight sample geometry, and difficult polarization control. ARPES at free-electron lasers is currently a niche technique, but due to its broadly tunable $h\nu$ and ultrafast pulses it may play an important role for trARPES in the future.

We now describe each of these sources in greater detail.
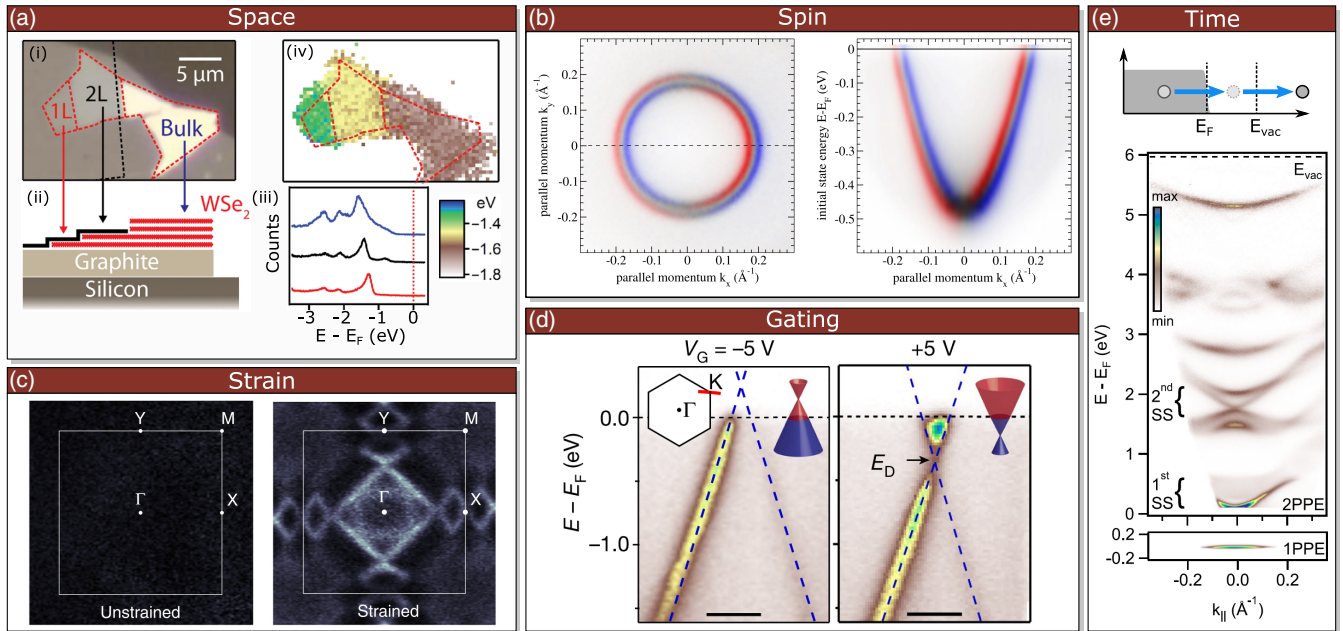
FIG. 8. Specialized ARPES techniques. (a) Spatially resolved ARPES with a 0.6 μm spot size. (i) Optical image and (ii) schematic cross section of an exfoliated WSe_2 flake with monolayer, bilayer, and bulk regions capped with monolayer graphene. (iii) EDCs from the three spatial regions and (iv) spatial map of the peak energy demonstrating the ability of μ-ARPES to map heterostructured samples. Adapted from Wilson et al., 2017. (b) Spin-resolved ARPES spectra from the Au(111) surface state demonstrating the efficiency of a state-of-the-art 2D imaging-type spin detector. From Tusche, Krasyuk, and Kirschner, 2015. (c) Fermi surface maps for strained and unstrained $Ca_{2-x}Pr_xRuO_4$ demonstrating an insulator-to-metal transition via nonthermal tuning knobs. From Riccò et al., 2018. (d) ARPES cuts at the K point of graphene using in situ electrostatic gating to shift the chemical potential. Adapted from Nguyen et al., 2019. (e) Measurement of a second topological surface state above E_F in Bi_2Se_3 demonstrating the ability of trARPES to measure unoccupied states. Adapted from Sobota et al., 2013b.

1. Synchrotron radiation

The greatest advantage of sychrotron radiation is that $h\nu$ is continuously and easily tunable by adjusting the undulator and monochromator, and user facilities are available spanning from vacuum ultraviolet (VUV) to hard-x-ray wavelengths. The overwhelming majority of ARPES work is performed in the VUV range due to its much higher cross section (Yeh and Lindau, 1985; Thompson and Vaughan, 2001) and superior resolution for a given resolving power. One advantage of the hard-x-ray regime (>2 keV) is that λ_{MFP} can exceed 10 nm, thus achieving higher bulk sensitivity; see Sec. III.F (Gray et al., 2011; Fadley, 2013). Modern undulators also offer full linear and circular polarization control (Xi et al., 2013; Hand et al., 2016). The repetition rate is set by the bunch spacing in the storage ring and is typically of the order of hundreds of megahertz with pulse durations ~10–100 ps.

While most beam lines operate with a spot size of $10 \sim 100$ μm, there is an increasing movement toward micro- and nano-ARPES measurements to avoid averaging over inhomogeneous samples (Mino et al., 2018), with spots down to 120 nm (Cattelan and Fox, 2018; Yao et al., 2018; Iwasawa et al., 2019; Kastl et al., 2019). The utility of these techniques is demonstrated in Fig. 8(a), where an exfoliated WSe_2 flake consisting of micron-scale regions of different thicknesses is spatially mapped using ARPES (Wilson et al., 2017). Concurrently, synchrotron facilities worldwide are heavily investing in improving beam coherence, enabling decades higher brightness approaching diffraction-limited

measurement conditions (Eriksson, van der Veen, and Quittmann, 2014; Maesaka, 2015).

2. Laser sources

UV laser sources offer extraordinary photon flux, energy stability, and excellent energy-momentum resolutions. Different schemes are employed to generate ultraviolet from infrared laser sources: for example, multiple stages of second-harmonic generation (SHG) in nonlinear optical crystals can achieve $h\nu$ up to 6 (Koralek et al., 2007) or 7 eV (Kiss et al., 2008; Liu et al., 2008). Higher $h\nu$ up to 9.3 (Cilento et al., 2016) or 11 eV (Berntsen, Götberg, and Tjernberg, 2011; Y. He et al., 2016) can be achieved by sum-frequency generation (SFG) in a noble gas. Beyond that, $h\nu$ up to ~100 eV can be achieved by high harmonic generation (HHG) in gas (Haight and Peale, 1994; Zhou et al., 2018).

The bandwidth is initially set by the laser source and is related to the pulse duration through their Fourier relationship. Quasi-continuous-wave lasers are preferred for achieving sub-meV bandwidth for high energy resolution (Kiss et al., 2008; Liu et al., 2008), while >18 meV bandwidth is required for sub–100 fs pulses for trARPES. Depending on the mechanism, frequency conversion can either reduce or increase the bandwidth (Gauthier et al., 2020); a notable example of the latter is HHG, which has been used to generate 11 fs pulses for trARPES (Rohde et al., 2016). The repetition rate is typically 1 kHz $\sim$ 100 MHz depending on the nature of the laser source and subsequent amplification stages. By placing focusing

optics near the sample position, spot sizes <5 μm have been achieved (Iwasawa *et al.*, 2017; Cucchi *et al.*, 2019). For UV wavelengths, full polarization control is possible using polarizers and wave plates. Zhou *et al.* (2018) provided a recent review of laser-based ARPES.

3. Free-electron lasers

A free-electron laser (FEL) produces high-intensity femtosecond-scale pulses with $h\nu \approx 100$ eV ~ 10 keV that goes beyond typical tabletop HHG wavelengths (Bonifacio, Pellegrini, and Narducci, 1984; Huang and Kim, 2007). With coverage of the soft- and hard-x-ray regimes, FELs are in principle extraordinarily flexible sources for trARPES, but the high photon energy and pulsed timing structure have made space-charge effects challenging to overcome (Pietzsch *et al.*, 2008; Hellmann *et al.*, 2012; Oloff *et al.*, 2014). Gains can be made by using higher efficiency analyzers (Kutnyakhov *et al.*, 2020), with dramatic improvement promised by the next generation of FEL sources to achieve repetition rates of up to ~1 MHz (Oloff *et al.*, 2016; Rossbach, Schneider, and Wurth, 2019). The scarcity of available FEL beam time is another practical challenge when utilizing these sources.

4. Gas discharge lamps

Gas discharge lamps are commercially available and routinely employed in laboratories. Although the emission is intrinsically narrow (≤ 1 meV), a monochromator is used to choose between different discharge lines. Most commonly the He Iα emission at 21.22 eV is used, supplemented by He IIα (40.81 eV), Ne Iα (16.85 eV), and Ar I (11.62 eV) emissions. The radiation is intrinsically continuous wave and unpolarized, although partial polarization control may be realized via a specially designed grating system. Typical spot sizes are ~1 mm, although sizes down to ~200 μm are achievable with short focal-length capillaries and apertures.

C. Photoelectron spectrometers

A photoelectron spectrometer uses electrostatic elements to manipulate the trajectory and energy of electrons and impinge them onto a detector. Modern spectrometers feature lensing elements that can be operated to record either the angular or spatial distribution of electrons, as shown in Fig. 9(a), where the angular mode is used for ARPES measurements. The detector then records the energetic and angular distributions of the photoelectrons.

The detector typically consists of a multichannel plate (MCP), which amplifies the signal while maintaining the spatial distribution of the incident electrons. Most commonly, the MCP output is impinged onto a phosphor from which the resulting luminescence can be read into a computer using a CCD camera; see Fig. 5(a). This scheme allows multiple events to be recorded in parallel (Gelius *et al.*, 1990) but has the disadvantage that the count rate response can exhibit nonlinearities (Reber *et al.*, 2014). Another approach is the use of a delay-line detector, which individually analyzes each event from the MCP output and thus features a linear response.
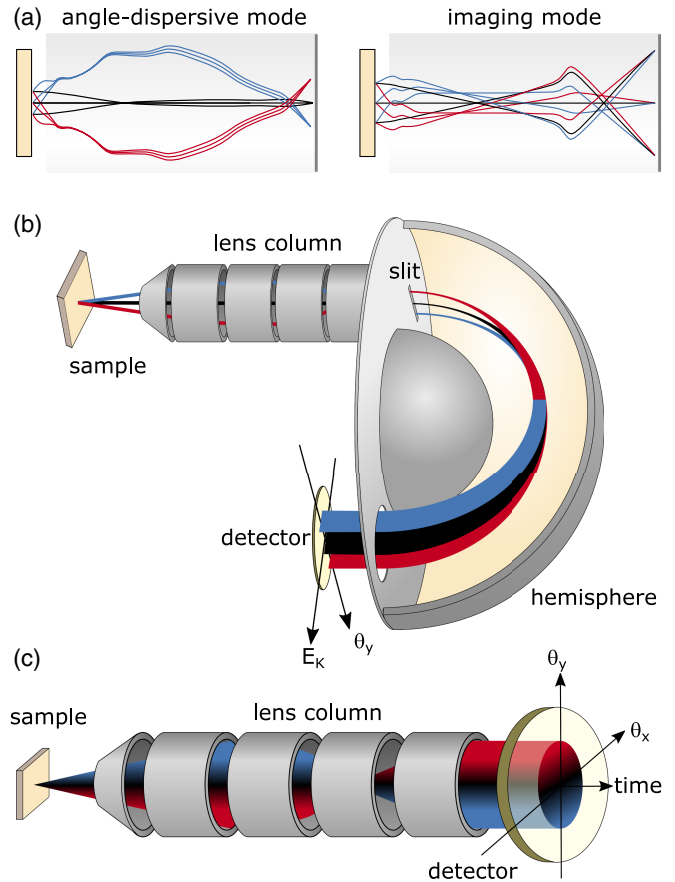
FIG. 9. Photoelectron spectrometers for ARPES. (a) Simplified depiction of lens modes for a modern analyzer. In angle-dispersive mode, electrons of the same emission angle (denoted by color) arrive at the same spatial position on the detector plane. In imaging mode, the real-space position of the electrons is mapped onto the detector, independent of emission angle. See Wannberg (2009) for quantitative calculations. (b) Hemispherical analyzer. For ARPES, the lens column is operated in angle-dispersive mode to map the angular distribution of electrons onto the entrance slit of a hemispherical deflector. A two-dimensional detector records the distribution of electrons as a function of emission angle ϑ_y and kinetic energy E_{kin}. (c) Angle-resolved time-of-flight detector. The lens column images the angular distribution of electrons onto a two-dimensional detector with time resolution, which records the emission angles (ϑ_x, ϑ_y) and photoelectron flight times.

We now survey the most commonly used photoelectron energy analyzers, as well as auxiliary techniques such as spin polarimetry.

1. Hemispherical analyzers

The hemispherical analyzer has been the workhorse of the ARPES community for the past two decades (Fellner-Feldegg *et al.*, 1974; Wannberg, 2009), as it is highly versatile (compatible with both pulsed and continuous radiation, at energies from eV to keV) and offers high angle and energy resolutions with moderate throughput. A schematic of a generic hemispherical analyzer is shown in Fig. 9(b). It consists of an input lens column, followed by a hemispherical

deflector and finally a two-dimensional electron detector. The lens column images the angular distribution of the electrons onto a slit at the entrance of the hemispherical deflector. The deflector consists of two concentric hemispherical electrodes with different electrostatic potentials, resulting in a radial electric field that causes the electrons to undergo elliptical orbits. Thus, electrons with different kinetic energies are dispersed along the radial dimension onto the detector. At the same time, the electron position orthogonal to this axis is determined by its emission angle within the window accepted by the slit. The detector therefore records the two-dimensional photocurrent distribution with respect to (E_{kin}, ϑ_y) (Mårtensson et al., 1994). Energy resolutions of the order of 1 meV are routinely obtained, although under pristine conditions sub–100 μeV resolution has been reported (Okazaki et al., 2012; Shimojima, Okazaki, and Shin, 2015). Typical acceptance angles are $\pm 15°$, with resolutions down to $\sim 0.1°$. For mapping the angular distribution orthogonal to the slit, conventionally the sample is rotated with respect to an axis parallel to the slit. However, state-of-the-art spectrometers now incorporate deflection electrodes within their lens columns, making it possible to electrostatically raster the electron beam within the accepted solid angle and thereby map a portion of the two-dimensional emission cone without any mechanical rotation (Ishida and Shin, 2018).

2. Time-of-flight spectrometers

Time-of-flight (TOF) spectrometers are based on the principle that an electron's kinetic energy can be determined by measuring the duration between its time of photoemission and its time of incidence on the detector. The light source must have short pulses and the detector itself must have suitable temporal resolution. Another crucial consideration is the repetition rate: if the period between photoemission events is too short, the slowest photoelectrons in the current cycle will be overtaken by the fastest photoelectrons from the subsequent cycle, leading to ambiguity in the interpretation of the signal. Based on these considerations, suitable pulse durations and repetition rates are $\lesssim 100$ ps and $\lesssim 1$ MHz (Ovsyannikov et al., 2013), making TOF spectroscopy suitable for many laser sources, including those configured for pump-probe measurements, but unsuitable for synchrotrons unless the storage ring is operated in a reduced-bunch mode. TOF spectrometers can achieve low background noise levels because they are intrinsically gated to the pulsed timing structure of the light source. Another attractive feature of TOF spectroscopy is that both axes of the area detector can be used to image the angular distribution of electrons, as shown in Fig. 9(c) (Wannberg, 2009; Ovsyannikov et al., 2013). This allows for higher overall throughput than a hemispherical analyzer, and the collected data constitute a three-dimensional cube with respect to $(E_{kin}, \vartheta_x, \vartheta_y)$ containing both angular directions (typically within $\pm 15°$).

3. Momentum microscopes

In recent years there has been a growth of ARPES instrumentation based on photoemission electron microscopy (PEEM) focusing optics, also known as momentum microscopes. An extraction voltage is applied to the front lens element, allowing the spectrometer to collect the complete $\pm 90°$ cone of photoemitted electrons. Energy resolution can be obtained using a retarding field (as in typical PEEM) (Kotsugi et al., 2003), TOF analysis (Schönhense et al., 2001), or dispersive energy filtering in a double hemispherical analyzer configuration, which increases the energy resolution and reduces the spherical aberrations introduced by a single hemisphere (Krömker et al., 2008). The use of PEEM optics allows the spectrometer to be operated in either spatial-imaging or momentum-imaging modes (Barrett et al., 2013). One of the most attractive advantages of momentum microscopes is the high collection efficiency, especially when operated with a TOF detector, since there are no slits or apertures to reduce the throughput, so that virtually all photoemission events are recorded. This efficiency is particularly beneficial for spin polarimetry (Tusche, Krasyuk, and Kirschner, 2015). One current challenge of momentum microscopy is that it is implemented in a limited number of groups and requires specialized expertise to operate. Moreover, it has yet to be demonstrated that it can routinely achieve sub–10 meV resolution.

4. Spin polarimetry

The widespread application of spin-resolved ARPES has been hampered by the low efficiency of spin polarimeters. Conventional spin filtering is performed using a Mott detector, in which high-energy (>10 keV) electrons are scattered off a heavy-element target such as Au or Th; see Fig. 10(a). The spin-orbit interaction results in a spin-dependent spatial asymmetry of the reflected electrons, which is measured by a pair of detectors and used to deduce the spin polarization of the incoming electrons (Gay and Dunning, 1992).
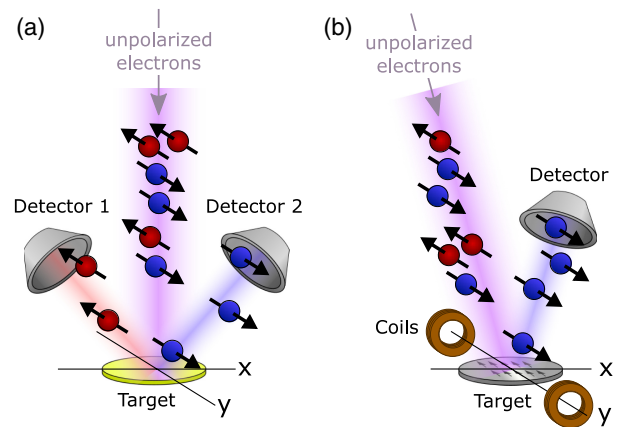
FIG. 10. Common spin polarimetry techniques. (a) Mott scattering employs the spin-orbit interaction between the incoming electrons and heavy nuclei in the scattering target. In the geometry shown here, detectors placed at $\pm x$ will detect contrast attributed to the y component of the electron spin. A pair of detectors can be placed at $\pm y$ to simultaneously detect the x component (not shown). (b) VLEED scattering employs the exchange interaction between the incoming electrons and a ferromagnetic scattering target. The measurement is sensitive to the spin component parallel to the magnetization of the target. Contrast is obtained by flipping the magnetization using Helmholtz coils.

Alternatively, detectors based on very low-energy electron diffraction (VLEED) from a ferromagnetic material have also been developed. VLEED detectors exploit the spin-dependent reflection probability due to the exchange-split band structure of the ferromagnetic scattering target; see Fig. 10(b). The spin polarization is deduced by repeating the measurement with opposite magnetization directions of the target (Hillebrecht *et al.*, 2002).

Spin polarimetry yields no direct information on the electron energy and momentum, so these techniques must be coupled with one of the previously described spectroscopic techniques. The most common approach is to install the polarimeter after the exit plane of a hemispherical analyzer, with an aperture in between that admits only a single energy and momentum channel (Dil, 2009). Recently multichannel approaches have been explored to dramatically boost the collection efficiency. This has been accomplished by coupling VLEED scattering with TOF analysis to collect a 1D spectrum versus E_{kin} (Jozwiak *et al.*, 2010). More recent approaches collect a 2D scattered image (E_{kin}, ϑ_y) with spin resolution achieved via VLEED (Ji *et al.*, 2016) or spin-polarized LEED scattering processes, as demonstrated in Fig. 8(b) (Tusche, Krasyuk, and Kirschner, 2015). Combination of 2D scattering with TOF analysis enables full 3D ($E_{kin}, \vartheta_x, \vartheta_y$) spin polarimetry (Elmers *et al.*, 2016). Schönhense, Medjanik, and Elmers (2015), Suga and Tusche (2015) and Okuda (2017) provided in-depth discussions of these emerging technologies.

D. Sample synthesis and measurement environment

While conventional systems routinely achieve ~10 K, sample temperatures below 1 K have been demonstrated using ^{3}He and elaborate thermal radiation shielding (Borisenko *et al.*, 2010). ARPES measurements must be performed in an ultrahigh vacuum chamber with magnetic shielding in order to reach ≤100 nT at the measurement position.

Because of the surface sensitivity at ultraviolet wavelengths (Sec. II.C), ARPES also requires atomically clean sample surfaces to obtain information relevant to the bulk. Preparation procedures entail surface treatment such as sputtering and annealing or, when natural cleavage planes exist, the crystal can be mechanically fractured *in situ* to expose a fresh surface. After preparation, the surface must be maintained at pressures of the order of 1×10^{-11} torr. At these pressures, residual gas molecules will form a monolayer on the fresh surface over a timescale of approximately 1 d (Hofmann, 2013). Another approach is to synthesize the materials *in situ* using molecular beam epitaxy. This high level of control over material synthesis has been instrumental for studies of monolayer superconductivity, 2D materials, and topological films. An additional useful aspect of MBE is that mismatched lattice constants can introduce biaxial strain.

Magnetic field, pressure, and gate voltage are challenging to integrate with ARPES due to the fact that photoelectrons must propagate through an obstruction-free, field-free vacuum. Nevertheless, in recent years there have been interesting developments in tuning the sample environment for ARPES measurements. Tensile or compressive strain can also be applied to single crystals via uniaxial mechanical deformation

by in-plane clamping or, in a more controlled fashion, using piezoelectric stacks together with a strain gauge (Pfau *et al.*, 2019). A separate approach entails bending the crystal (Chang, Khalsa *et al.*, 2013), which has been used to drive insulator-to-metal transitions [shown in Fig. 8(c)] (Riccò *et al.*, 2018). Finally, strain can be applied by exploiting the differential thermal contraction between dissimilar materials in the sample holder (Sunko *et al.*, 2019). Electrical perturbations are increasingly being explored, such as sample current-dependent ARPES, which requires not only screening of stray electrical fields but also consideration of the associated magnetic fields (Kaminski *et al.*, 2016). Measurements can also be performed in equilibrium but electrostatically modified conditions. A common approach is to transfer electrons by *in situ* deposition of alkali atoms such as potassium, which can be used to tune the near-surface doping (Hossain *et al.*, 2008). Recently electrostatic gating with a graphite back gate was implemented in an ARPES setup and used to directly image the carrier density-dependent electronic structure in graphene [shown in Fig. 8(d)], as well as band gap renormalization in transition metal dichalcogenides (Nguyen *et al.*, 2019). Electrostatic bias can also be applied to increase the effective acceptance-cone angle of the analyzer (Yamane *et al.*, 2019).

E. Time-resolved ARPES

trARPES plays a central role in characterizing the nonequilibrium properties of quantum materials (Bovensiepen and Kirchmann, 2012; Smallwood, Kaindl, and Lanzara, 2016; Zhou *et al.*, 2018). trARPES is performed in a pump-probe configuration using an ultrafast laser system: the pump pulse excites a sample out of equilibrium, and the probe pulse generates a photoemission signal from the transient system, as shown in Fig. 11(a). The ARPES spectrum is recorded as a function of pump-probe time delay. Although Ti:sapphire lasers have been the workhorse of the ultrafast field for decades, Yb-based lasers have recently become competitive for trARPES due to their ability to generate >100 μJ pulses at repetition rates approaching 1 MHz (Boschini *et al.*, 2014; Lorek *et al.*, 2014; Reutzel, Li, and Petek, 2019; Y. Liu *et al.*, 2020). At the same time, soft- and hard-x-ray FELs will bring trARPES to previously unexplored regimes (Sec. III.B.3).

Here we introduce the four pump-induced excitations relevant to most experiments. (1) As shown in Fig. 11(b), absorption of pump photons results in optical dipole transitions from occupied to unoccupied electronic states, with subsequent relaxation governed by intrinsic scattering processes (Fauster and Steinmann, 1995; Haight, 1995; Petek and Ogawa, 1997; Weinelt, 2002; Echenique *et al.*, 2004). This process forms the basis for two-photon photoemission spectroscopy and allows ARPES to be extended to measure states above E_F [as shown in Fig. 8(e)] (Sobota *et al.*, 2013b) and their population dynamics. (2) When the material is in an ordered state [Fig. 11(c)], the optical excitation can perturb or even destroy the order parameter. trARPES has been extensively employed to study the dynamics of destruction and reformation of states such as charge density wave and superconducting states (Schmitt *et al.*, 2008; Hellmann *et al.*, 2010;
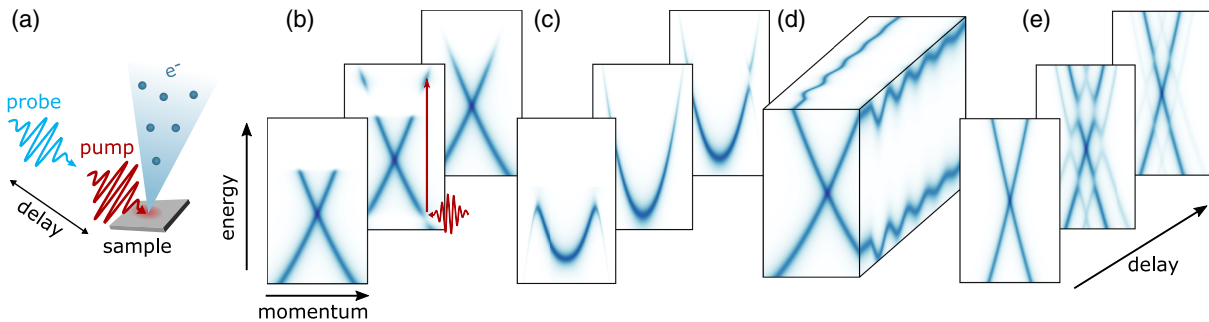
FIG. 11.   (a) Schematic of a trARPES experiment. A pump pulse optically excites the sample, and a time-delayed probe pulse generates photoelectrons that are collected by a photoelectron analyzer. (b)–(d) Sketches of the main classes of excitation phenomena, including (b) direct optical transitions and subsequent population relaxation dynamics, (c) destruction of an ordered phase followed by its recovery, (d) excitation of a coherent phonon mode associated with oscillatory binding energies, and (e) dressing of the electrons by a periodic field forming Floquet-Bloch states.

Rohwer *et al.*, 2011; Smallwood *et al.*, 2012). (3) In other scenarios, the excitation can launch a coherent mode such as a phonon via Raman processes which then manifest as an oscillatory response of the electronic structure [Fig. 11(d)] (Garrett *et al.*, 1996; Perfetti *et al.*, 2006), providing a novel approach for studying electron-phonon coupling in the time domain (Papalazarou *et al.*, 2012; Avigo *et al.*, 2013; S.-L. Yang *et al.*, 2019). (4) Finally, the electrons can be "dressed" by the periodic structure of the pump's electro-magnetic field and form Floquet-Bloch states [Fig. 11(e)] (Y. H. Wang *et al.*, 2013). These four excitation mechanisms are not mutually exclusive, and the pump photon energy $h\nu_{\text{pump}}$ is an important knob for tuning their relative contributions. Conventionally the fundamental output of a Ti: sapphire laser at 1.5 eV is used for pumping, although frequency down-conversion schemes are being explored to match $h\nu_{\text{pump}}$ to the energy scale of a particular phenomenon (Y. H. Wang *et al.*, 2013; Gierz *et al.*, 2015; Mahmood *et al.*, 2016; Reimann *et al.*, 2018).

The most common approach for probing is to generate the fourth harmonic of a Ti:sapphire laser at $h\nu_{\text{probe}} \sim 6$ eV. Higher $h\nu_{\text{probe}}$ can be achieved by HHG (Sec. III.B.2), although limitations in laser technology have conventionally restricted these approaches to lower repetition rates (~ 1 kHz). Recent developments have pushed the rates significantly higher (Nicholson *et al.*, 2018; Buss *et al.*, 2019; Puppin *et al.*, 2019; Sie *et al.*, 2019), even beyond 10 MHz (Chiang *et al.*, 2015; Mills *et al.*, 2017; Corder *et al.*, 2018). This is highly desirable for mitigating space charge, although high repetition rates are deleterious if they provide insufficient time for the sample to fully relax to equilibrium between consecutive pump pulses, leading to an elevated steady-state sample temperature (Bechtel, 1975).

Another consideration is the trade-off between spectral and temporal resolution due to their Fourier reciprocity. The spectral resolution is limited by the bandwidth of the probe pulse, while the time resolution is determined by the temporal cross-correlation of the pump and probe pulses. For a single pulse, the energy bandwidth and pulse duration ΔE and Δt (both expressed as a full width at half maximum) are related by $\Delta E \Delta t \geq 4\hbar \ln 2 \approx 1825$ meV fs, where the equality holds

only for a transform-limited Gaussian pulse. Group velocity dispersion management is required to achieve a transform-limited pulse (Trebino, 2000).

F. Other variants of ARPES

Probing surface structures and reconstructions.— Photoelectrons can be scattered and interfere with each other as they escape from the material surface, giving rise to the photoelectron diffraction effect (Liebsch, 1974; Barton *et al.*, 1985; Bachrach, 2012). This process goes beyond the three-step model and requires a full multiple scattering treatment. It can be exploited to extract surface-sensitive information such as the geometry of surface reconstruction and adsorbate-substrate arrangement (Kevan *et al.*, 1978; Woodruff *et al.*, 1978) via direct x-ray photoelectron diffraction (Osterwalder *et al.*, 2000) or angle-resolved photoemission extended fine structure (Barton *et al.*, 1983).

Probing below the surface with depth control.—X-ray standing wave photoemission is an extension of hard-x-ray photoemission, which has been used to gain additional bulk sensitivity (Dallera *et al.*, 2004; Sing *et al.*, 2009; Gray *et al.*, 2011). Of particular importance is the ability of x rays to form standing waves inside a crystalline lattice (for hard x rays) (Batterman, 1964) or artificially grown layered structures (for soft x- rays) (Yang *et al.*, 2000; Kim and Kortright, 2001). Photoemission under such conditions can not only provide layer and/or depth selectivity but also be element sensitive when the corresponding resonant x-ray energy is chosen (Gray *et al.*, 2013; Gray, 2014).

Probing unoccupied single-particle states.—Inverse photo-emission spectroscopy (IPES), also historically known as bremsstrahlung isochromat spectroscopy, is another technique (other than trARPES) that permits access to the electronic structure of unoccupied electronic states (Nijboer, 1946; Dose, 1977; Sawatzky and Allen, 1984; Dose, 1985; Himpsel, 1990). It measures the electron-addition spectral function $A^{+}(\mathbf{k}, \omega)$ by irradiating a sample with electrons and recording the resulting photon emission. It is also possible to directly inject spin-polarized electrons to probe magnetic and spin-orbit related processes (Unguris *et al.*, 1982).

The main bottleneck to its widespread application is the low cross section,[6] and consequently a compromise in achievable energy resolution (often ≥ 200 meV) (Johnson and Davenport, 1985). Another drawback in IPES is sample radiation damage due to the large dose of incident electrons ($\sim 10^{15}$ electrons/ sec), which may be partly mitigated with near-UV energy electron sources (Pillo *et al.*, 1997; Yoshida, 2012).

Probing two-particle correlations.—Double photoemission (DPE) is a process where one photon ejects two electrons simultaneously [also denoted as $(\gamma, 2e)$]. This process is forbidden in an ideal free-electron gas and becomes possible only in the presence of electron-electron interactions (Berakdar, 1998; Fominykh *et al.*, 2002). Such a trait makes valence electron DPE a direct probe of electronic correlations in solid-state systems (Gazier and Prescott, 1970; Gollisch, Schwartzenberg, and Feder, 2006; Schumann, Winkler, and Kirschner, 2009). The exchange-correlation hole (a space of low electron density surrounding a given electron due to Coulomb repulsion) can be directly measured once two ejected electrons can be traced to one single event (Schumann *et al.*, 2006; Schumann, Winkler, and Kirschner, 2007). Spin polarimetry can also be applied to further analyze the spin correlation between two photoelectrons (Morozov *et al.*, 2002; Samarin *et al.*, 2004). Recently a different type of two-photon-in-two-electron-out coincidence ARPES has been proposed to directly probe the two-particle correlation functions in solids (Su and Zhang, 2020). One interesting future avenue for applying these two-particle probes would be the direct detection of superconducting correlations in electron Cooper pairs (Kouzakov and Berakdar, 2003). However, the main challenges for current DPE-based approaches are the inherently low cross section for correlated events ($\leq 10^{-3}$ of that of single photoemission) and the requirement of low photon flux to reject the single-photon photoemission background. Detector and light source developments (Wallauer *et al.*, 2012; Chiang *et al.*, 2020; Voss *et al.*, 2020) continue to advance the state of the art.

IV. COPPER-BASED SUPERCONDUCTORS

A. Overview

As a strongly correlated single-band material that can be tuned from an insulator to a high-temperature superconductor and then to a metal via electron or hole doping, cuprates serve as the most prominent example to refine the description of correlated electronic systems (Bednorz and Müller, 1986; Anderson, 1987; Imada, Fujimori, and Tokura, 1998).

The crystal structure of a typical cuprate high-T_c superconductor can be viewed as an alternating stacking of metal-oxygen charge reservoir layers and superconducting CuO_2^{n-} layers (Fig. 12 insets), where the latter dominate the

low-energy electronic states. In hole-doped systems, each copper atom is usually caged in an oxygen octahedron or pyramid with at least one apical oxygen, forming the "T phase" (Longo and Raccah, 1973; Eisaki *et al.*, 2004). In contrast, the copper atom in electron-doped cuprates generally does not have an apical oxygen, and the charge reservoir layer is heavily buckled, forming the "T' phase" (Takagi, Uchida, and Tokura, 1989; Armitage, Fournier, and Greene, 2010).

The correlation physics of cuprates is best exemplified by the strong dependence of its physical properties on charge doping, as shown in the phase diagram (Fig. 12). Strong Coulomb repulsion on each Cu site makes undoped cuprates correlated insulators with long-range antiferromagnetic (AFM) order, despite an odd number of valence electrons for each copper. Electron and hole doping both promote intersite hopping, thus alleviating the charge localization and giving rise to a plethora of intertwined phases and crossover phenomena in the temperature-doping phase diagram (Fig. 12) (Kastner *et al.*, 1998; Armitage, Fournier, and Greene, 2010; Fradkin, Kivelson, and Tranquada, 2015). With as little as 2% hole doping or up to 15% electron doping, the long-range AFM order is destroyed, but substantial short-range AFM fluctuations extend to a much broader phase region (Keimer *et al.*, 1992; Imai *et al.*, 1993; Drachuck *et al.*, 2014). Hole doping induces a series of low-temperature phases: a spin glass region characterized by slow spin dynamics (Filipkowski, Budnick, and Tan, 1990; Julien, 2003), a dome-shaped superconducting region described mostly by d-wave gap symmetry (Hardy *et al.*, 1993; Shen *et al.*, 1993; Wollman *et al.*, 1993; Tsuei *et al.*, 1994), a valence electron charge density wave (CDW, also called "charge order") and spin stripes (Tranquada *et al.*, 1995; Abbamonte *et al.*, 2005; Ghiringhelli *et al.*, 2012; da Silva Neto *et al.*, 2016), non–Fermi-liquid charge transport (often referred to as a "strange metal") (Martin *et al.*, 1990; Batlogg *et al.*, 1994; Harris *et al.*, 1995; Ando *et al.*, 2004; Hussey *et al.*, 2011; Greene *et al.*, 2020), and eventually a more coherent metallic region (Ando *et al.*, 2000; Proust *et al.*, 2002; Vignolle *et al.*, 2008).

In addition to the ground state properties, correlation effects also manifest at high temperatures. Below a certain critical doping p_c, linear resistivity extends beyond the Mott-Ioffe-Regel limit at high temperatures (Gurvitch and Fiory, 1987; Martin *et al.*, 1990; Hwang *et al.*, 1994; Cooper *et al.*, 2009; Legros *et al.*, 2019), and the energy width of the single-particle spectrum is substantially larger than the electron binding energy and thermal energy at all temperatures above T_c (Shen and Sawatzky, 1999; Tanaka *et al.*, 2006; Kondo, Palczewski *et al.*, 2013). Another hallmark of the normal state in hole-doped cuprates is a depletion of the single-particle spectral weight near the chemical potential, crossing over at a temperature scale of T^* (the broad dash in Fig. 12). This is known as the "pseudogap" because it is not universally associated with a symmetry-broken phase.[7] We note that a quantum critical fan-type phase diagram is often used largely based on transport evidence. More recent transport

---

[6]The cross-section ratio between regular photoemission and inverse photoemission is $\sigma(IPES)/\sigma(PES) \sim \lambda_e^2/\lambda_{ph}^2$, where λ refers to the electron and photon wavelengths. At an electron energy of 10 eV (1000 eV), this ratio is $\sim 10^{-5}$ (10^{-3}). The primary reason is the low photon density of states, which limits photon creation phase space in IPES (Smith, 1988).

[7]One should exercise caution when interpreting a wide range of T^*'s measured using different techniques; see Sec. IV.B.2.
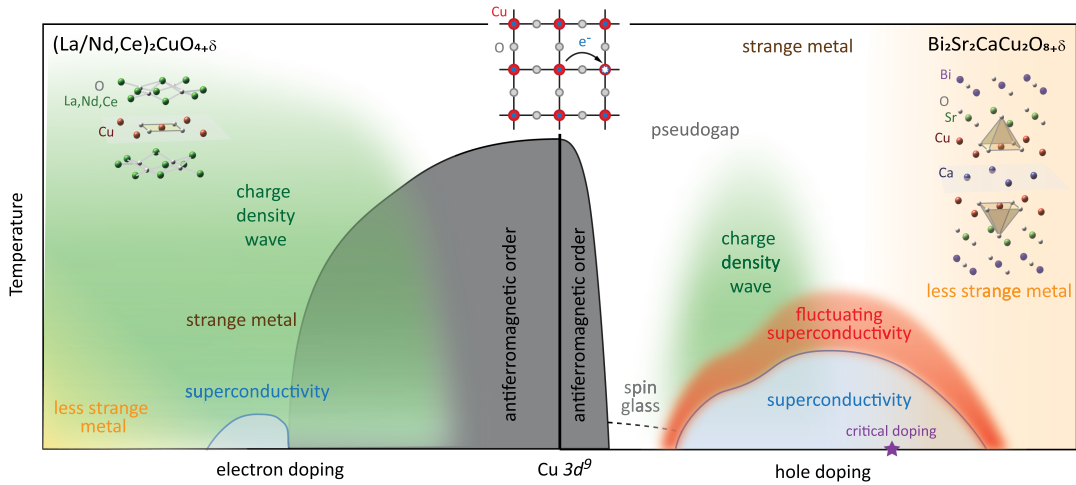
FIG. 12. Schematic temperature-doping phase diagram of electron- and hole-doped cuprate superconductors. Top-left inset: lattice arrangement for one unit cell of electron-doped cuprate $(\text{La}/\text{Nd}, \text{Ce})_2\text{CuO}_4$ ($T_c^{\max} \sim 30$ K). Top-right inset: lattice arrangement for one half unit cell of $\text{Bi}_2\text{Sr}_2\text{CaCu}_2\text{O}_{8+\delta}$ ($T_c^{\max} \sim 96$ K). Middle inset: top view of the CuO_2^{n-} plane in real space. Red circle, copper; gray circle, oxygen; blue circle, electron; white circle, doped hole; purple star, the critical doping that separates two different metallic regimes.

and single-particle measurements suggest a much less temperature-dependent boundary, which is represented here and is discussed in more detail in Sec. IV.B.3. On the electron-doped side, the phase diagram is generally similar except for a stronger AFM order and a much less temperature-dependent charge ordered region (Damascelli, Hussain, and Shen, 2003; Armitage, Fournier, and Greene, 2010; Ghiringhelli *et al.*, 2012; da Silva Neto *et al.*, 2016).

We first cover modern ARPES investigations in order of decreasing electronic energy scales: the normal state, the superconducting state, and the "zero" temperature Fermi surface ("Fermiology"). Then contributions from nonelectronic degrees of freedom are discussed in light of electron-boson coupling. The electron- and hole-doped systems are discussed based on both their unifying phenomenology and their differentiating electron-hole asymmetry.

B. Normal state

1. Doping evolution of the electronic structure

Owing to crystal-field splitting, the copper $d_{x^2-y^2}$ orbital is the highest partly filled orbital, followed by the $d_{3r^2-z^2}$ orbital [also denoted as d_{z^2}; Fig. 13(c)] (Mattheiss, 1987; Yu, Freeman, and Xu, 1987; Pickett, 1989; Damascelli, Hussain, and Shen, 2003). In one of the more three-dimensional cuprates $\text{La}_{2-x}\text{Sr}_x\text{CuO}_4$ (LSCO), polarization-dependent ARPES shows the dominance of the in-plane $d_{x^2-y^2}$ orbital component near E_F [Figs. 13(a)–13(c)], while the $d_{3r^2-z^2}$ orbital component resides mostly at higher binding energy or near the antinodal momentum [$(\pi, 0)$ point in the Brillouin zone, also known as the *antinode*] [Figs. 13(b) and 13(c)] (Matt *et al.*, 2018). Note that a dispersion of 2 eV is observed on the occupied side. Moderate to negligible k_z dispersion in different cuprates is found near the antinode, usually much smaller than the in-plane bandwidth [Figs. 13(d) and 13(e)] (Takeuchi *et al.*, 2005; Horio *et al.*, 2018; Matt *et al.*, 2018). A single-band description of superconductivity is challenged by the

vastly different T_c's among different cuprate families, which all share nominally the same CuO_2^{n-} plane. Another potential caveat to the single-band theory lies in the recently discovered heavily hole-doped cuprate superconductors with T_c's exceeding 80 K (Gauzzi *et al.*, 2016; W. Li *et al.*, 2019), where the $d_{3r^2-z^2}$ orbital content contributes more appreciably at E_F (Maier, Berlijn, and Scalapino, 2019). Varying degrees of low-energy $d_{3r^2-z^2}$ orbital content have also been proposed to account for the family dependence of T_c (Sakakibara *et al.*, 2012). For simplicity, we focus on the electronic structure associated with the $d_{x^2-y^2}$ orbital for the remainder of this section.

Strong electronic correlation inhibits double charge occupancy and promotes charge localization (Anderson, 1959; Gutzwiller, 1963; Hubbard, 1963; Kanamori, 1963; Mott, 1968). At the nominal valence Cu^{2+}, parent compound cuprates contain one electron (or, equivalently, one hole) per unit cell ("half filled") and are insulating. The copper $d_{x^2-y^2}$ orbital heavily hybridizes with the ligand oxygen p_x, p_y orbitals (see the CuO_2^{2-} sublattice in Fig. 12, upper inset), and hole carriers doped through oxygenation are postulated to form a singlet on the center copper, known as the Zhang-Rice singlet (Zhang and Rice, 1988). The system gains kinetic energy t when the hole hops between sites and pays an energy cost U when double occupancy occurs on the same site. Long-range AFM order forms on the copper sites (Imada, Fujimori, and Tokura, 1998; Lee, Nagaosa, and Wen, 2006) since the electrons gain kinetic energy by virtual intersite hopping, which is maximized when nearest-neighbor spins are anti-parallel to each other. This effective low-energy single-band approximation has enabled wide applications of the two-dimensional single-band Hubbard model to describe the behaviors of doped charge carriers in cuprates (Anderson, 1987). To effectively describe the hopping of the singlet, the Hubbard model in the large U limit may be expanded in powers of t, leading to the widely used t-J model ($J = 4t^2/U$) and its extensions (Zhang and Rice, 1988; Lee, Nagaosa, and
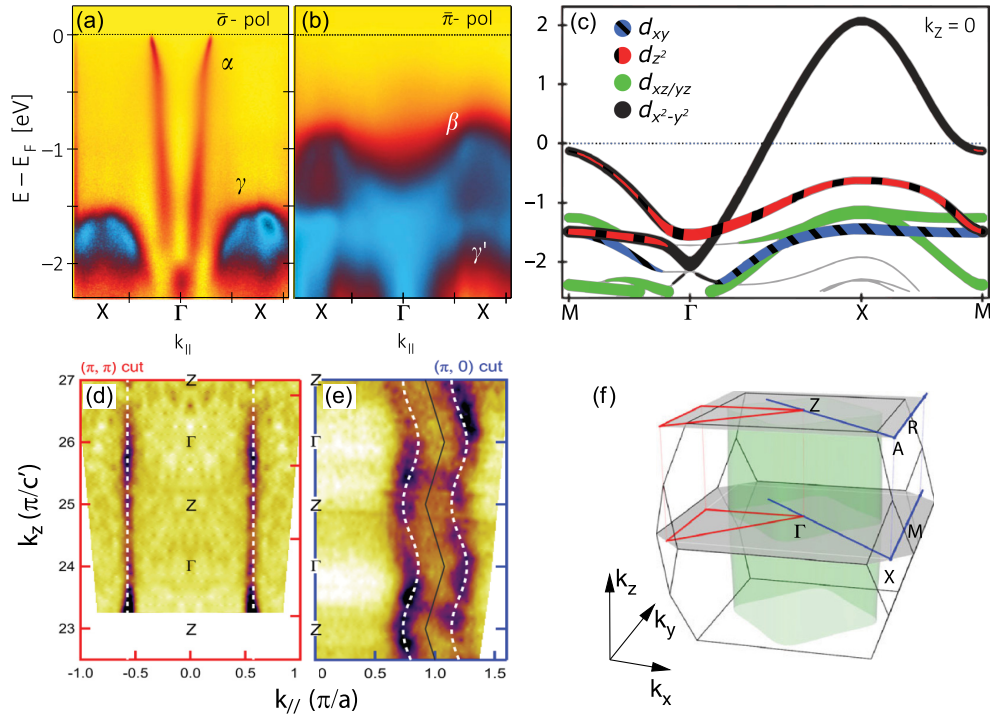
FIG. 13. Orbital contents of low-energy bands in overdoped $La_{2-x}Sr_xCuO_4$. (a) $d_{x^2-y^2}$ component selected with in-plane polarized light. (b) $d_{3r^2-z^2}$ component selected with out-of-plane polarized light. (c) DFT calculation of d-orbital contents in the low-energy bands. Adapted from Matt *et al.*, 2018. (d) k_z dispersion along nodal in-plane momenta. (e) k_z dispersion along antinodal in-plane momenta. (f) Schematic plot of the three-dimensional Brillouin zone of LSCO. Adapted from Horio *et al.*, 2018.

Wen, 2006; Spałek, 2007). In addition, multiband models have tested the validity and limitations of this single-band treatment and found that the charge transfer energy between oxygen and copper dominates the largest low-energy spectral gap (Zaanen, Sawatzky, and Allen, 1985; Emery, 1987; Varma, Schmitt-Rink, and Abrahams, 1987). In this single-band Hubbard model description, the role of the Mott gap is played by the charge transfer gap.

One hallmark of the electronic structures of cuprates is their lack of rigidity against carrier doping. The framework of cuprates' normal-state electronic structure can be viewed as an evolution from a charge transfer insulator to a metal when doped. Besides the large charge transfer gap Δ_{CT} at the 1 to 2 eV scale (sometimes referred to as the Mott gap for the previously mentioned reason), the spectral function measured by ARPES at half filling can be characterized by [Fig. 14(a)] (Wells *et al.*, 1995) (1) a dispersive feature with a bandwidth set by $\sim 2.2J \sim 300$ meV, (2) a large energy separation between $(\pi/2, \pi/2)$ and $(\pi, 0)$ spectra of about $\sim 2.2J$, and (3) the feature at $(\pi/2, \pi/2)$ being broad in energy, despite being the maximum of the valence band and thus having no electronic decay channels. While observation (1) aligns well with the predictions of the t-J model, (2) can be described only by involving higher-order hopping terms or polaron formation, indicating the importance of spin and lattice degrees of freedom (Dagotto *et al.*, 1990; Nazarenko *et al.*, 1995). Observation (3) is also difficult to explain under model calculations purely based on electronic correlations (Kohno, 2012; Wang *et al.*, 2015). Upon doping, sharp quasiparticle dispersion emerges

along Γ-X [Fig. 14(b); see also Secs. IV.B.3 and IV.B.4]; the spectral energy difference between $(\pi/2, \pi/2)$ and $(\pi, 0)$ rapidly decreases as the $(\pi, 0)$ spectrum moves toward the Fermi level [Fig. 14(b); see also Sec. IV.B.2]; and the $(\pi/2, \pi/2)$ spectrum eventually evolves into a well-defined dispersion of $8t \sim 4$ eV energy scale [Fig. 14(c)] (Ino *et al.*, 2002; Matt *et al.*, 2018). Of particular importance, the broad spectra at $(\pi, 0)$ remain $\sim J$ away from the Fermi level in underdoped systems, which is much deeper than in a simple tight-binding dispersion. This signifies the underlying Mott and possibly polaronic physics on top of which intertwined phases compete and cooperate. This large energy scale, especially at low doping [circles in Figs. 14(b)–14(e)], is what one would call the "high-energy pseudogap" (King *et al.*, 1995; Shen *et al.*, 1995; Marshall *et al.*, 1996). This gap obliterates the Fermi surface near the zone boundary, giving rise to the "Fermi arc," an incomplete segment of Fermi surface anchored around $(\pi/2, \pi/2)$ [Fig. 14(d), red lines]. Further investigations in more doped systems reveal a lower energy gap in the normal state near the antinode [solid triangles in Figs. 14(b)–14(e); see also Sec. IV.B.2] (Ding *et al.*, 1996; Loeser *et al.*, 1996; Marshall *et al.*, 1996). This low-energy gap, sometimes also referred to as the pseudogap, is likely related to various intertwined orders and their associated fluctuations. These two aspects of the pseudogap become less distinguishable with doping and manifest differently in different experiments at different temperatures (Timusk and Statt, 1999). This distinction is often not recognized in the literature and can be a source of confusion.

FIG. 14. Schematic evolution of the electronic structure in hole-doped cuprate. (a)–(c) Normal-state spectral function evolution with hole-doping along high-symmetry directions. Solid black lines, t-J model or tight-binding model band calculations. The unoccupied side is only qualitatively sketched based on Hubbard model calculations. (d) Fermi surface in underdoped and overdoped cuprates. The dashed diamond is the AFM zone boundary. (e) M point $(\pi, 0)$ and (f) nodal $\mathbf{k}_F$ near $(\pi/2, \pi/2)$ EDC evolution with hole doping. Circles, high-energy spectral feature associated with Mott physics; triangles, low-energy spectral features that are, or will evolve into, quasiparticles; black lines, half filling (HF); red lines, underdoped (UD); blue lines, overdoped (OD).

2. The pseudogap

The existence of a spectral gap above superconducting T_c (the pseudogap) refutes the conventional wisdom of a coherent metallic normal state that is required to precede a mean-field BCS superconducting transition. Early experimental indications of the pseudogap were covered in a number of previous reports and reviews (Alloul, Ohno, and Mendels, 1989; Ding et al., 1996; Loeser et al., 1996; Marshall et al., 1996; Renner et al., 1998; Campuzano et al., 1999; Fedorov et al., 1999; Timusk and Statt, 1999; Tanaka et al., 2006; Lu et al., 2012; Hashimoto et al., 2014; Keimer et al., 2015). Here we specifically discuss this phenomenon in hole-doped cuprates. For electron-doped cuprates, the spectral analog of the pseudogap is discussed in the context of the antiferromagnetic gap in Sec. IV.B.4 due to much more robust long-range AFM order.

Preformed Cooper pairing is one prominent candidate to explain the pseudogap: strong superconducting fluctuations above T_c destroy phase coherence but not the pairing (Emery and Kivelson, 1995). However, progress over the last decade suggests that the pseudogap physics far exceeds this simple picture. The fluctuating superconductivity temperature has been shown to be substantially lower than the high-energy pseudogap temperature scale T^* in many cuprate systems (see also Sec. IV.C.2) (Bilbro et al., 2011; Tallon, Storey, and Loram, 2011; Kondo, Malaeb et al., 2015). With high-resolution and high statistics photoemission, the pseudogap is identified to contain a both energetically and temperaturewise separated component from superconducting fluctuations (Fig. 15) (Lee et al., 2007; He et al., 2009; Kondo et al., 2009; Hashimoto et al., 2010, 2015; Kondo, Malaeb et al., 2015; S.-D. Chen et al., 2019).

Further evidence indicating that the pseudogap is more than simply fluctuating superconductivity comes from its temperature, momentum, and doping dependence. Below T_c, the pseudogap manifests as a superlinear deviation from the expected momentum dependence of a pure d-wave superconducting gap form near the antinode [Fig. 19(a)] (Lee et al., 2007; Vishik et al., 2012; Anzai et al., 2013). Above the fluctuating superconducting temperature but below T^*, a gapless Fermi arc forms in the nodal region [along the $(0,0)$-(π,π) direction] that grows with temperature, while the antinodal pseudogapped region gradually shrinks to zero as T^* is approached (Norman et al., 1998; Kanigel et al., 2006; Vishik et al., 2012; Kaminski et al., 2015). The different gap momentum dependences at different temperatures suggest that the pseudogap is more than a simple extension of the superconducting gap. Additionally, low-energy spectral weight analysis near the antinode shows a pronounced minimum at T_c at underdoping and optimal doping but not on the heavily overdoped side [Figs. 15(a) and 15(b)], indicating a competing relation between the pseudogap and superconductivity (Hashimoto et al., 2015). Such a distinction is also confirmed by the distinct doping dependence of the low-energy spectral weight near the node and at the antinode [Fig. 15(e)] (Tanaka et al., 2006; Kondo et al., 2009).

Moreover, the pseudogap is shown to break particle-hole symmetry, as evidenced by the misalignment between the Fermi momentum $\mathbf{k}_F$ in the normal state and the band-bending momentum $\mathbf{k}_G$ in the gapped state [Fig. 15(f)] (Hashimoto et al., 2010; He et al., 2011a). Particle-hole symmetry is inherently required for zero-sum-momentum Cooper pairing on the Fermi surface. To account for both the broad linewidth (much larger than the corresponding thermal energy) and the particle-hole asymmetry of the pseudogap, proposals based on

FIG. 15. Spectral characters of the pseudogap [red squares in (c),(d)] and its relation to superconducting quasiparticle peaks [blue dots in (c),(d)]. Temperature-dependent, Fermi-function divided antinodal spectra for (c) near-optimally doped and (d) heavily overdoped $Bi_2Sr_2CaCu_2O_{8+\delta}$. T_{AN} is the gap-closing temperature at the antinode. (a),(b) Spectral weight evolution within [0,70] meV binding energy with temperature, normalized by total spectral weight over [0,250] meV binding energy. Adapted from Hashimoto *et al.*, 2015. (e) Momentum- and doping-dependent spectral weight competition between superconducting coherent peak (down arrow) and pseudogap (up arrow) in $Bi_2Sr_2CuO_{6+\delta}$. Graduated shades correspond to the marked direction of doping. Adapted from Kondo *et al.*, 2009. (f) Particle-hole asymmetry for the pseudogap in optimally doped $Bi_2Sr_2CuO_{6+\delta}$. Adapted from Hashimoto *et al.*, 2010.

short-range AFM correlation (Rice, Yang, and Zhang, 2011) or density wave order (Chen *et al.*, 2004; Vershinin *et al.*, 2004; Lee, 2014; Hashimoto *et al.*, 2015; Hamidian *et al.*, 2016; Edkins *et al.*, 2019) saw limited success largely based on quasiparticle interference and Fermi surface measurements (see Sec. IV.D).

A more refined spectral analysis shows competition between the pseudogap and superconductivity in both temperature and momentum space [Fig. 15(e)], again indicating the potentially different nature of the high-energy pseudogap from fluctuating superconductivity (Kondo *et al.*, 2009, 2011; Hashimoto *et al.*, 2015). We caution the reader that in this strongly correlated region most of the aforementioned energy gaps lack coherent quasiparticle peaks on the gap edges and hence should not be grossly taken as an order parameter of a new phase. For example, non-Fermi-liquid self-energies such as those in the quantum critical regime have been shown to produce similarly incoherent, gapped single-particle excitation spectra around the chemical potential without breaking any additional symmetry (Wu *et al.*, 2019). These considerations lead to the postulation of pseudogap being a crossover phenomenon.

3. Emergence of quasiparticles

A long-standing puzzle on the electronic structure evolution is the apparent lack of chemical potential shift as a function of doping (Allen *et al.*, 1990). This is exemplified by the seemingly doping-independent broad spectra around 0.4–0.5 eV binding energy, which was once considered the lowest energy quasiparticle [Figs. 16(a) and 16(b)]. Systematic study of the Na-doped $Ca_2CuO_2Cl_2$ system reveals that such a broad Gaussian spectrum is likely an envelope of polaronic shakeoff satellites rather than the quasiparticle itself (Shen *et al.*, 2004). This has been proposed to come from a correlation-enhanced lattice phonon polaron near half filling (Mishchenko and Nagaosa, 2004; Rösch and Gunnarsson, 2004). In either case, the spectra along the nodal direction consist of two components, as shown in Figs. 16(a) and 16(b): a weak quasiparticle component and a stronger polaron cascade. The incoherent feature completely dominates the spectra at low doping and shows little doping dependence, yielding an apparent lack of chemical potential shift. The emergence of a quasiparticle component with low spectral weight changes the picture and provides evidence for a systematic shift of chemical potential with doping, as one would expect [shown in Fig. 16(a)]. This behavior was also seen in other experiments (Hashimoto *et al.*, 2008; Fournier *et al.*, 2010), providing a lattice-based explanation for the valence band top broadening at $(\pi/2, \pi/2)$ in the half-filled insulating phase. This also reconciles the inconsistency between the *t-J* model calculation and the exceptionally high binding energy spectrum at $(\pi, 0)$ in half-filled cuprates. Upon hole doping, the coherent spectral weight of the
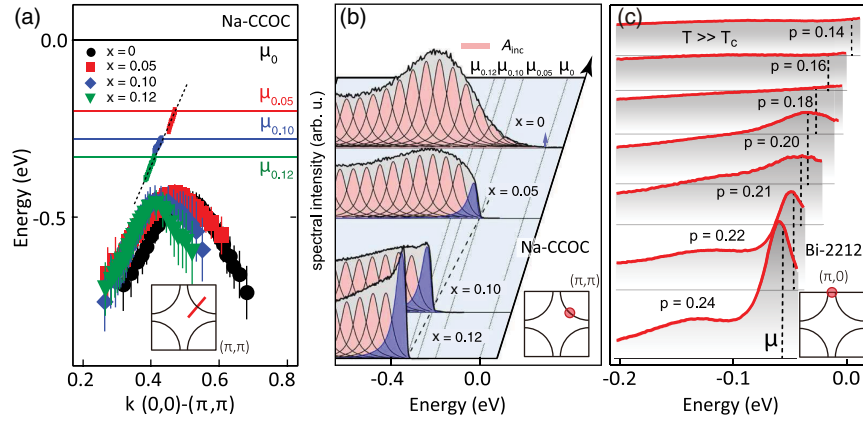
FIG. 16. Emergence of quasiparticles in different parts of momentum space with hole doping. (a),(b) Nodal quasiparticles [the straight segment of the dispersions in (a) and the purple shade in (b)] are created in $Ca_2CuO_2Cl_2$ immediately upon Na doping on Ca sites. Adapted from Shen *et al.*, 2004. (c) Doping-dependent antinodal spectra in the normal state across the critical doping in $Bi_2Sr_2CaCu_2O_{8+\delta}$. Black dashed lines indicate the chemical potentials for each doping. Adapted from Van Veenendaal, Sawatzky, and Groen, 1994, and He *et al.*, 2018a.

nodal quasiparticle quickly grows, while the weight of the polaronic shakeoff band continuously shrinks [Fig. 16(b)]. This joint manifestation of electron-electron and electron-phonon interactions is generic in cuprates, especially near half filling. Note that spin polarons are also proposed to contribute to the emergence of nodal quasiparticles near half filling (Martinez and Horsch, 1991; Wang *et al.*, 2015).

Compared to the node, the antinodal spectral coherence exhibits a much slower recovery with hole doping, as indicated in $Bi_2Sr_2CaCu_2O_{8+\delta}$ (Bi-2212). The normal-state antinodal spectrum remains highly incoherent even at optimal hole doping [Fig. 16(c)] and abruptly gains coherence only past a putative critical doping $p_c \sim 0.19$ (Chatterjee *et al.*, 2011; He *et al.*, 2018a; S.-D. Chen *et al.*, 2019). The strong coupling to the B_{1g} phonon near the antinode has been suggested to play a role in this phenomenon (Cuk *et al.*, 2004;

Devereaux *et al.*, 2004; Hashimoto *et al.*, 2015). For more discussions of the phonon contribution to the antinodal spectra, see Sec. IV.E.2.

4. AFM gap and other correlation gaps

Compared to hole doping, AFM order is more robust against electron doping (Motoyama *et al.*, 2007; Armitage, Fournier, and Greene, 2010). In electron-doped $Nd_{2-x}Ce_xCuO_4$, the highly momentum-dependent AFM gap due to (π, π) band folding can be identified at the "hot spot," where the original Fermi surface crosses the AFM zone boundary [the cut shown in the Fig. 17(b) inset] (Armitage *et al.*, 2002; He *et al.*, 2019). This magnetic gap exists even outside the long-range AFM ordered phase region and coexists with superconductivity at least up to 16% electron doping (Song *et al.*, 2012, 2017; Horio *et al.*, 2016; He *et al.*, 2019).
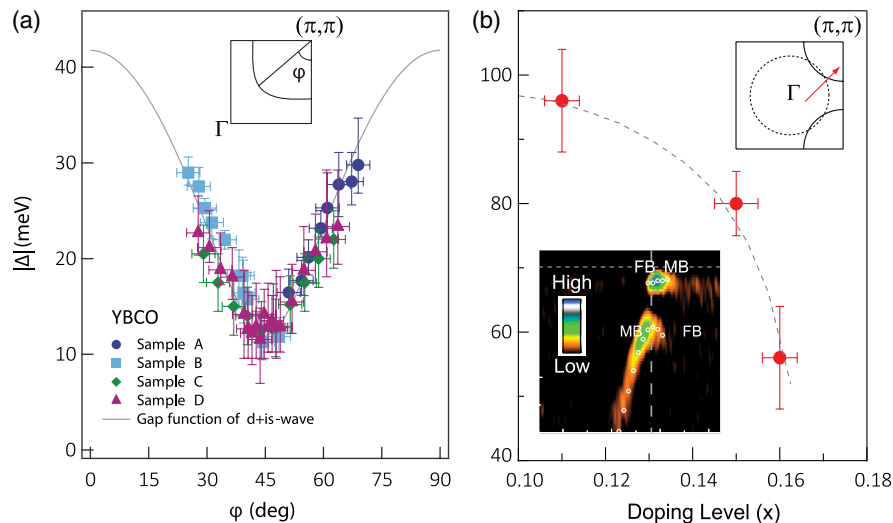
FIG. 17. Electronic correlation related energy gaps. (a) Momentum dependence of the gap near the node in underdoped YBCO. Adapted from Okawa *et al.*, 2009. (b) Energy-momentum spectra (inset) and doping dependence for the AFM gap at the AFM zone boundary in electron-doped cuprate $Nd_{2-x}Ce_xCuO_4$. Adapted from He *et al.*, 2019.

A different form of correlation-induced gap manifests on the hole-doped side. At low hole doping, the nodal spectrum is gapped by up to ~30 meV from the chemical potential regardless of the presence of superconductivity (Okawa *et al.*, 2009; Vishik *et al.*, 2012; Peng *et al.*, 2013; Razzoli *et al.*, 2013). This gap is also highly anisotropic, with its minimum along the nodal direction [Fig. 17(a)]. While proposals for the origin of this gap involve disorder and complex order parameters, the lack of well-defined quasiparticles in this deeply underdoped regime also challenges explanations in terms of a simple quasiparticle gap (Chen, Khaliullin, and Sushkov, 2009; Atkinson, Bazak, and Andersen, 2012; Lu, Xiang, and Lee, 2014). With further hole doping, this gap at the node gradually disappears before the optimal doping is reached, with the specific values being family dependent.

C. Superconducting properties

1. Momentum dependence

A single-particle energy gap is an important marker for various symmetry-broken phases. In a superconductor, the gap represents the energy required to break a Cooper pair. The gap is maximal at the normal-state Fermi momentum $\mathbf{k}_F$, where the quasiparticle becomes an equal admixture of particles and holes, and the nearby spectra satisfy

$E_{\text{hole}}(\mathbf{k}) = -E_{\text{electron}}(\mathbf{k})$, which is termed *particle-hole symmetry.* These composite excitations, known as Bogoliubov quasiparticles, have been experimentally demonstrated in a momentum-resolved way in $Bi_2Sr_2CaCu_2O_{8+\delta}$ (Matsui *et al.*, 2003; Takahashi *et al.*, 2005; Balatsky, Lee, and Shen, 2009). Cuprates have a *d*-wave superconducting order parameter that additionally breaks rotational symmetry (Shen *et al.*, 1993; Ding *et al.*, 1995; Tsuei and Kirtley, 2000; Hashimoto *et al.*, 2014), giving rise to fully gapped states along the Cu—O bonding (antinodal) direction and gapless states along the diagonal Cu—Cu (nodal) direction (Fig. 12 inset).

Recent generation laser-based ARPES and VUV synchrotron-based ARPES have mapped the $\mathbf{k}$-dependent superconducting gap $\Delta(\mathbf{k})$ in the vicinity of the node (Figs. 18 and 19) (Vishik *et al.*, 2010, 2012; Kondo, Malaeb *et al.*, 2015; Sakamoto *et al.*, 2016, 2017; Ai *et al.*, 2019). The measured $\Delta(\mathbf{k})$ can be fitted to the *d*-wave momentum form $\Delta(\mathbf{k}) = 0.5v_\Delta |\cos k_x - \cos k_y|$, where v_Δ is the *gap velocity* [the dashed lines in Figs. 19(a) and 19(b)]. Assuming zero pseudogap contribution near the node, v_Δ may be identified with the magnitude of the superconducting gap at the antinode. This is considered a plausible way to isolate the superconducting gap component even in the presence of a pseudogap around the antinode. Based on this method, v_Δ is
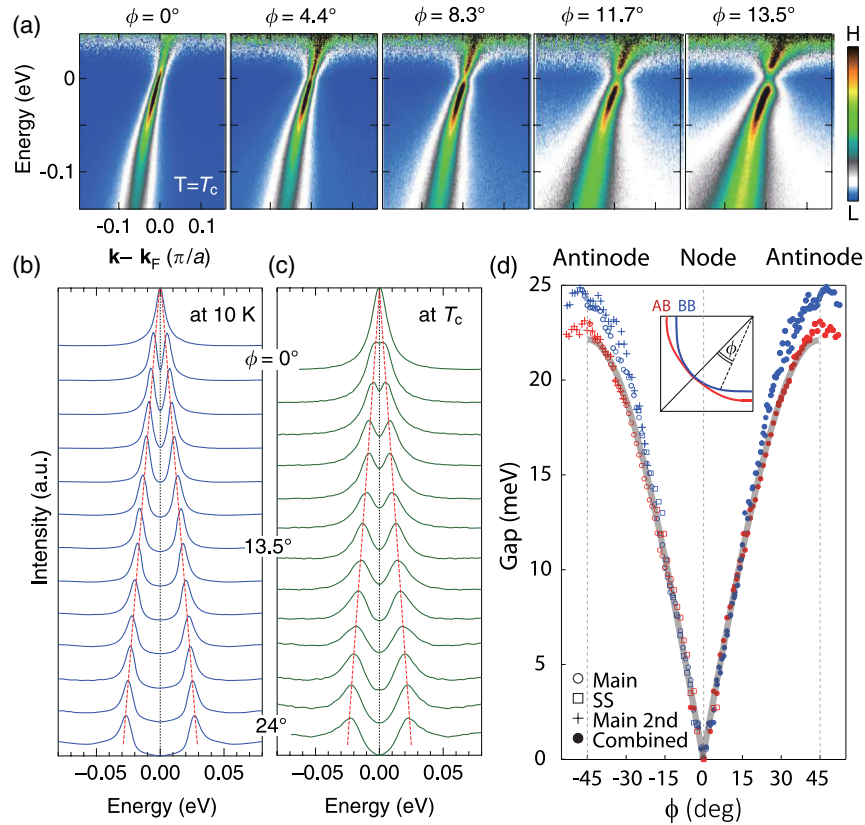
FIG. 18. High-resolution spectra near the node. (a) Fermi-function divided near-nodal cuts in optimally doped $Bi_2Sr_2CaCu_2O_8$ taken at the bulk T_c. Note the visible upper Bogoliubov quasiparticle dispersion above E_F. (b),(c) Symmetrized energy distribution curves from node to off-node direction at 10 K and the bulk $T_c = 92$ K. Note the persistent *d*-wave gap at T_c due to superconducting fluctuations. Adapted from Kondo, Malaeb *et al.*, 2015. (d) High-resolution measurement examining the *d*-wave form of the energy gaps on both the bonding and antibonding bands in overdoped Bi-2212 measured with VUV laser ARPES. AB, antibonding band; BB, bonding band; SS, superstructure; gray line, *d*-wave fit. Adapted from Ai *et al.*, 2019.

found to remain at ~40 meV over a wide range of doping ($0.07 < p < 0.19$) over which T_c changes by a factor of 2 (Vishik *et al.*, 2012; Sakamoto *et al.*, 2017; Zhong *et al.*, 2018). However, it has also been suggested that even the near-nodal region may contain pseudogap contributions especially when underdoped (Anzai *et al.*, 2013). The experimental variance in the underdoped regime [Fig. 18(c)] reflects the challenge to extract v_Δ in the absence of a full understanding of the pseudogap's potential impact toward the node. While the difference in the raw data itself is subtle, the extrapolation amplifies variations that depend sensitively on the fitting range and deviations from a simple *d*-wave form. Regardless of these nuances, the superconducting gap-to-T_c ratio ($2\Delta/k_B T_c$) near optimal doping is found to be ~10, much larger than the weak coupling BCS prediction [Fig. 19(c)]. With progressive hole doping past a critical doping p_c, this ratio precipitously drops from a large value of ~10 toward the *d*-wave BCS limit ~4.3, indicating a more weakly coupled, more BCS-like superconducting region at sufficiently high hole concentration (Vishik *et al.*, 2012; Yoshida *et al.*, 2012; He *et al.*, 2018a; Zhong *et al.*, 2018). A similar doping trend is also observed in single-layer cuprate $Bi_2(Sr, La)_2CuO_{6+\delta}$.
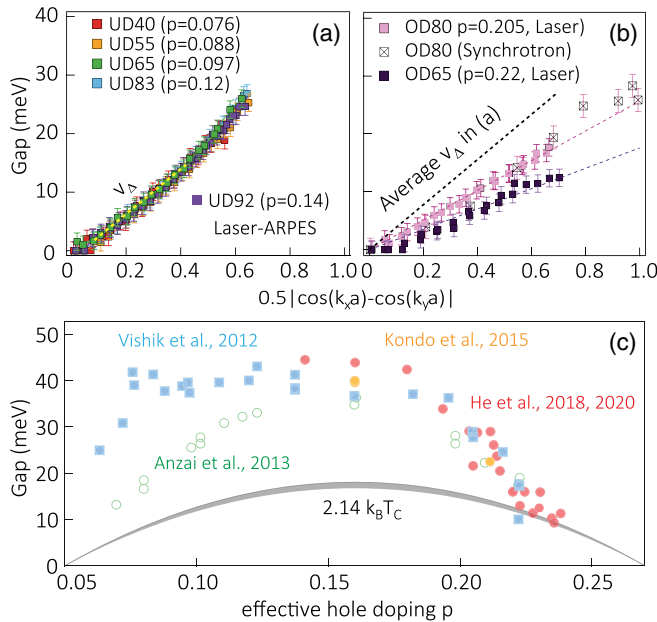
FIG. 19. Momentum- and doping-dependent superconducting gaps in $Bi_2Sr_2CaCu_2O_8$. Near-node gap $\Delta(\mathbf{k})$ measurements in (a) underdoped and (b) overdoped samples. Assuming a negligible pseudogap contribution near the node, the nodal gap velocity v_Δ may be equated with the superconducting gap at the antinode. Adapted from Vishik *et al.*, 2012. (c) Doping-dependent *d*-wave superconducting gap determined by fitting v_Δ. Superconducting T_c dome (gray crescent) is plotted against hole doping according to the empirical parabolic relation with maximum T_c between 91 and 98 K (Presland *et al.*, 1991) and is converted to energy by the weak coupling *d*-wave gap-to-T_c ratio. Data points were compiled from Vishik *et al.* (2012), Anzai *et al.* (2013), Kondo, Malaeb *et al.* (2015), and He *et al.* (2018a, 2020). The variance in the underdoped region is a combined result of deviation from simple *d*-wave gap form and different fitting momentum ranges for v_Δ.

(Bi-2201), although the gap-to-T_c ratio is consistently larger than that in $Bi_2Sr_2CaCu_2O_{8+\delta}$; see also Fig. 24(b) (Sakamoto *et al.*, 2016, 2017).

This BCS-like behavior comes together with increased metallicity. ARPES data at heavy hole doping show quadratic binding energy dependence of the nodal quasiparticle lifetime, which is broadly taken as a trait of Fermi liquid behavior (Yusof *et al.*, 2002; Kaminski *et al.*, 2003; Koitzsch, Borisenko *et al.*, 2004; J. Chang *et al.*, 2013). This interpretation should be considered cautiously given that the absolute value of the fitted self-energy is still comparable to or larger than the spectral peak binding energy.

The superconducting gap symmetry in electron-doped cuprates is more challenging to measure, mainly due to the much lower energy scales. Although *d*-wave-like near-nodal behavior has been reported (Armitage *et al.*, 2001; Horio *et al.*, 2019), the gap maximum is seen near the antiferro-magnetic zone boundary instead of the antinode (Matsui *et al.*, 2005).

2. Superconducting fluctuations

Fluctuating superconductivity above T_c (in which the pairing amplitude is nonzero but global phase coherence is absent) has been central to the discussion of the super-conductor-insulator transition, the pairing energy scale, and the dimensionality in the cuprates. High-resolution photoemission measurements on Bi-2212 have revealed substantial fluctuating superconductivity over a temperature range $\Delta T \sim (0.3 - 0.5)T_c$ above the superconducting T_c both near the node and at the antinode (Hashimoto *et al.*, 2015; Kondo, Malaeb *et al.*, 2015; S.-D. Chen *et al.*, 2019). This is in part consistent with transport and tunneling results in the $(La, Sr)_2CuO_4$ system (Božović *et al.*, 2016; P. Zhou *et al.*, 2019). In near optimally doped $Bi_2Sr_2CaCu_2O_{8+\delta}$ [Fig. 15(c)], a signature of fluctuating superconductivity (blue dots) manifests as a distinct shoulder feature inside the pseudogap (red squares) at or above T_c (pink line). A similar feature for fluctuating superconductivity also shows up as a low-energy gap right above T_c in the overdoped metallic region [Fig. 15(d), blue dots] (Hashimoto *et al.*, 2015; He *et al.*, 2018b; S.-D. Chen *et al.*, 2019). Evidence for super-conducting fluctuations is also provided by trARPES measurements of the gap dynamics (Smallwood *et al.*, 2012; Parham *et al.*, 2017; Boschini *et al.*, 2018). The relative fluctuation temperature window $\Delta T/T_c$ is barely doping dependent (Bilbro *et al.*, 2011; Tallon, Storey, and Loram, 2011; S.-D. Chen *et al.*, 2019), which agrees with the ubiquitous short antinodal superconducting correlation length of only a few lattice constants (H. Li *et al.*, 2018). Such a short correlation length may also be related to the reduced phase coherence and superfluid density even in overdoped systems that exhibit metallicity. High statistics ARPES shows an exceptionally shallow and flat antinodal band in heavily overdoped cuprates (Chuang *et al.*, 2004; Kaminski *et al.*, 2006; He *et al.*, 2020). This departure from a parabolic low-energy band structure, in combination with strong impurity scattering potential, has been associated with a reduced superfluid density (Pitaevskii and Stringari, 2016; He *et al.*, 2020).

D. Fermi surface

In a normal metal described by Fermi liquid theory, the Fermi surface is a ground state property that directly influences low-energy transport properties. The area enclosed by the closed Fermi surface measures the total carrier density and is stable against most perturbative electronic interactions, other than an attractive potential (Luttinger, 1960). However, without the notion of quasiparticles, as is the case in many underdoped to optimally doped cuprates, one questions whether the Fermi surface remains a well-defined entity. Determining the existence and the shape of the Fermi surface in cuprates has been central to addressing various correlation effects and a putative quantum critical point (the purple star in Fig. 12) (Markiewicz, 1997; Badoux *et al.*, 2016).

1. Small and large Fermi surfaces

A schematic Fermi surface evolution with both electron and hole doping is shown in Fig. 20 for a typical cuprate.[8] We begin by considering the situation at half filling: a tight-binding model gives a large Fermi surface centered around X whose area A_{FS} reflects the carrier density and is therefore exactly half of the full Brillouin zone ($A_{FS} = 1/2$) [the dashed line in Fig. 20(c)]. In reality, as discussed in Sec. IV.B.1, strong correlations modify this picture by opening a Mott gap and leading to the complete or partial removal of the Fermi surface [Fig. 20(d)].

Carrier doping leads to a reemergence of coherent spectral weight, particularly near the node. In electron-doped cuprates one must also consider the robust AFM order, which causes the Fermi surface to be folded by the AFM ordering wave vector (π, π) and gapped at the AFM zone boundary (thin-line diamond). These two effects give a small coherent nodal hole pocket and a less coherent antinodal electron pocket coexisting around optimal doping [Figs. 20(a) and 20(b)] (Armitage *et al.*, 2002; Armitage, Fournier, and Greene, 2010; Song *et al.*, 2012, 2017; He *et al.*, 2019). Note that the short quasiparticle lifetime near the antinode can make this pocket undetectable by quantum oscillations (Kartsovnik *et al.*, 2011; Breznay *et al.*, 2016; He *et al.*, 2019).

On the hole-doped side, coherent quasiparticles appear near the nodal region inside the AFM zone, while the antinodal region remains highly incoherent. However, unlike in the electron-doped case, no AFM folding is observed, leading to a construct known as the Fermi arc [Figs. 20(d) and 20(f)] (Damascelli, Hussain, and Shen, 2003; Kanigel *et al.*, 2006; Hossain *et al.*, 2008; Kondo, Malaeb *et al.*, 2015). The area of the putative nodal hole pocket (empirically calculated by assuming that the arc indeed folds across the AFM zone boundary) is given by the hole doping p. However, this estimate is of heuristic value only in the deeply underdoped region because high-resolution ARPES measurements in near-optimally doped Bi-2212 showed that the Fermi arc tip does not end on the AFM zone boundary at T_c (Kanigel *et al.*, 2006; Hashimoto *et al.*, 2011; Vishik *et al.*, 2012; Kondo, Malaeb *et al.*, 2015). Further hole doping extends the coherent

---

[8]Note that in multilayer systems multiple pockets can exist due to interlayer interactions.
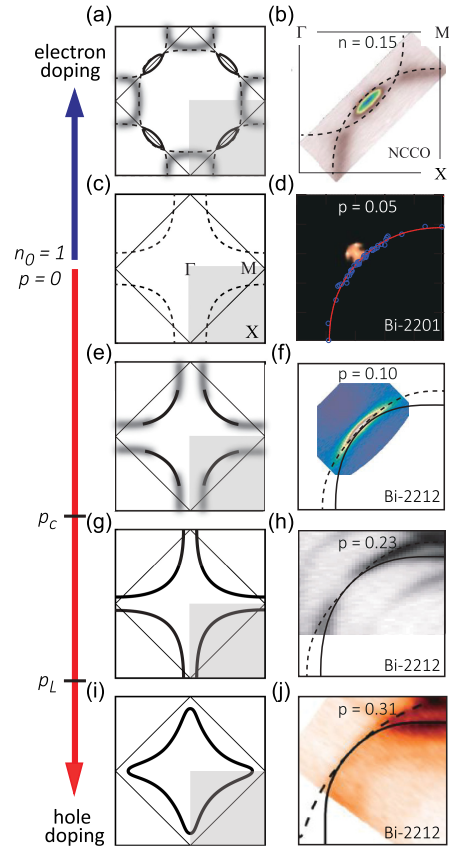
FIG. 20. Cuprate Fermi surface evolution with carrier doping. (a),(b) Schematics and experimental data on the electron-doped Fermi surface in $(\mathrm{Nd}, \mathrm{Ce})_2\mathrm{CuO}_4$ with a coherent nodal hole pocket (solid black) and a less coherent antinodal electron pocket (gray shadow). The dashed lines are Fermi surface sheets before AFM folding. The thin solid diamond is the AFM zone boundary. Adapted from Song *et al.*, 2012. (c),(d) Expected tight-binding Fermi surface and the actual Fermi surface close to half filling in $\mathrm{Bi}_2\mathrm{Sr}_2\mathrm{CuO}_{6+\delta}$. Adapted from Hashimoto *et al.*, 2008. (e),(f) Fermi "arc" in underdoped $\mathrm{Bi}_2\mathrm{Sr}_2\mathrm{CaCu}_2\mathrm{O}_{8+\delta}$ with a coherent node and incoherent antinode. Adapted from Reber *et al.*, 2012. (g),(h) Above a certain critical doping p_c the entire Fermi surface recovers coherence and connects to a single large hole pocket (He *et al.*, 2018b). The dashed and solid lines represent the anti-bonding and bonding bands in $\mathrm{Bi}_2\mathrm{Sr}_2\mathrm{CaCu}_2\mathrm{O}_{8+\delta}$, respectively. (i),(j) Further hole doping passing the van Hove point at M, undergoing a holelike to electronlike Fermi surface Lifshitz transition at p_L. Adapted from Drozdov *et al.*, 2018. The right panels are enlargements of the lower-right quadrants of the full BZs on the left.

quasiparticle toward the Brillouin zone boundary, which eventually connects to form a full hole pocket centered around X (Drozdov *et al.*, 2018; He *et al.*, 2018a; Horio *et al.*, 2018; Zhong *et al.*, 2018), and qualitative agreement with the tight-binding model is restored. This process is also accompanied by a sudden incoherent-to-coherent spectral transition at high temperatures (S.-D. Chen *et al.*, 2019).

Whether the Fermi arc is indeed one side of a small nodal pocket is contested for deeply hole-underdoped cuprates. Early photoemission experiments reported evidence for small nodal pockets in hole-underdoped cuprates (Meng *et al.*,
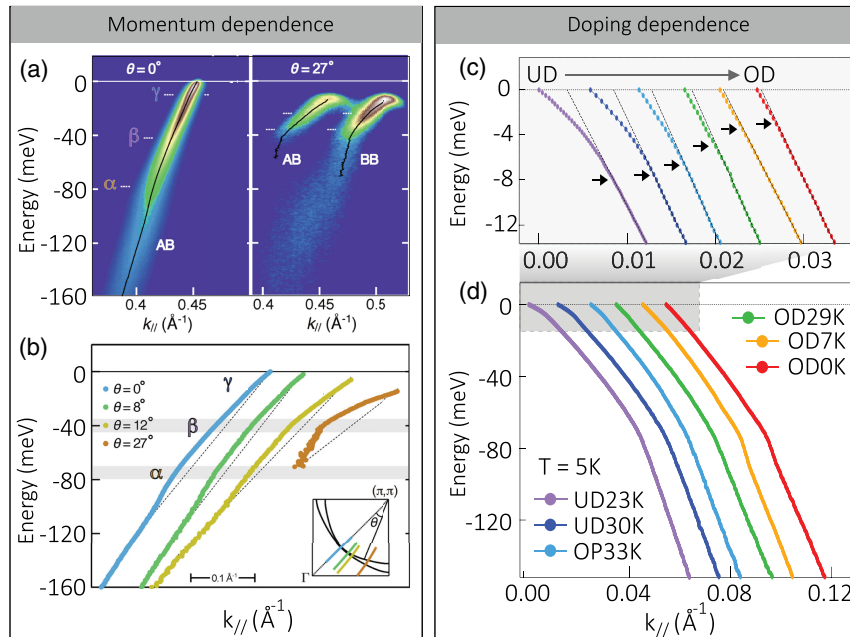
FIG. 21. Signatures of bosonic mode coupling on the nodal spectra in cuprates. (a) Mode-coupling effects on both the BB and AB in overdoped $Bi_2Sr_2CaCu_2O_{8+\delta}$ at the node and near node. (b) Extracted antibonding band dispersions from nodal to near-antinodal region. Adapted from Anzai *et al.*, 2017. (c),(d) Doping dependence of the nodal dispersion in $Bi_2Sr_2CuO_6$, with the low-energy dispersion anomalies enlarged in (c). Adapted from Kondo, Nakashima *et al.*, 2013.

2009; Razzoli *et al.*, 2010; Yang *et al.*, 2011), which were later suggested to come from structural distortions and surface reconstructions (Koitzsch *et al.*, 2004; Mans *et al.*, 2006; Nakayama *et al.*, 2006; He *et al.*, 2011b; King *et al.*, 2011a). Only recently, long-range AFM order and a small nodal pocket were unambiguously observed from the middle layers in a five-layer overall-hole-doped cuprate, prompting the discussion of disorder-induced spectral smearing and the sign of doped carriers in different layers (Kunisada *et al.*, 2020).

Fermi surface volume is related to the carrier concentration via the Luttinger theorem. When the Fermi surface is compromised by correlation effects and superconductivity, an "underlying Fermi surface" is sometimes used to empirically quantify its volume (Gros *et al.*, 2006; Sensarma, Randeria, and Trivedi, 2007). Compared to the nominal doping derived from normal-state Hall measurements (Presland *et al.*, 1991; Ando *et al.*, 2000; Balakirev *et al.*, 2003), the Fermi surface volume measured by ARPES is consistently larger over the entire superconducting doping range (Kondo *et al.*, 2004; Sakamoto *et al.*, 2016; Drozdov *et al.*, 2018; Zhong *et al.*, 2018). The highly anisotropic low-energy electronic structure and strong electron correlation effects distort the simple reciprocal relation between the Hall coefficient and the carrier density.

2. van Hove singularity

Quasi-two-dimensional cuprates like Bi-2201 and Bi-2212 possess a band structure saddle point at $(\pi, 0)$, contributing to a theoretically diverging density of states known as the van Hove singularity (vHs) (Markiewicz, 1997). Experimentally, this divergence is always broadened due to either correlation effects or k_z dispersion (Gomes *et al.*, 2007). Sufficient hole doping can lower the Fermi level through the vHs, turning the

Fermi surface from a single hole type centered around X/Y to an electron type centered around Γ [Fig. 20(i)]. This Lifshitz transition at $p = p_L$ has been proposed as another candidate for the pseudogap critical doping p_c in Bi-2212, but photoemission measurements indicate a much larger p_L than p_c in Bi-2212 (Drozdov *et al.*, 2018; He *et al.*, 2018a).[9] Moreover, the logarithmic divergence of density of states at the vHs is considered insufficient to account for the Sommerfeld coefficient divergence at p_c (Horio *et al.*, 2018; Michon *et al.*, 2019). Photoemission has also shown highly system-dependent doping for the Lifshitz transitions: $\leq 22\%$ in LSCO (Yoshida *et al.*, 2007; Hashimoto *et al.*, 2008; Razzoli *et al.*, 2010), $>26\%$ in $Tl_2Ba_2CuO_{6+\delta}$ (Platé *et al.*, 2005), ~35–40% in Bi-2201 (Kondo *et al.*, 2004), and $>30\%$ in surface self-doped $YBa_2Cu_3O_{7-\delta}$ (YBCO) (Zabolotnyy *et al.*, 2007a). In Bi-2201 and Bi-2212, this doping also coincides with the superconductor-to-metal critical transition (Kondo *et al.*, 2004; Drozdov *et al.*, 2018; Ding *et al.*, 2019).

E. Coupling between electrons and collective excitations

In conventional BCS superconductors, bosonic mode coupling provides the attractive interaction that pairs electrons (Bardeen, Cooper, and Schrieffer, 1957). The analogous "pairing glue" in high-T_c cuprates is still unknown, motivating efforts to spectroscopically characterize electron-boson

---

[9]Even though the value of p_L varies in the ARPES literature in Bi-2212, potentially limited by resolution, it is consistently higher than p_c (Chuang *et al.*, 2004; Kaminski *et al.*, 2006). Note that the doping here is calculated as an average of both the bonding and antibonding bands' Fermi surface volumes, whereas the doping on the antibonding band itself well exceeds 30%.

interactions. Lattice phonon and spin excitations are two leading candidates to account for the strong signatures of highly anisotropic mode coupling observed in ARPES (Damascelli, Hussain, and Shen, 2003).

1. Coupling near the node

With the improved energy resolution of laser-based ARPES, a cascade of dispersion anomalies (kinks) have been revealed around the nodal momentum. At 70–80 meV binding energy [feature α in Fig. 21(a)] a major dispersion kink is observed, which is usually interpreted as coupling to the oxygen in-plane breathing modes. It weakens only slightly at high temperatures, and its energy shows little momentum or family dependence (Lanzara et al., 2001; Zhou et al., 2003; Borisenko et al., 2006; Meevasana et al., 2006; Lee et al., 2008; W. Zhang et al., 2008b; Anzai et al., 2010, 2017; J. He et al., 2013; Ideta et al., 2013; Vishik et al., 2014). Laser ARPES has reported evidence of an isotope effect for this mode up to 3.4 meV (Iwasawa et al., 2008), following substantial improvement in resolution and statistics from earlier synchrotron experiments (Gweon et al., 2004; Douglas et al., 2007; Iwasawa et al., 2007). This mode is also widely seen in electron-doped cuprates, which lack an apical oxygen on top of copper (Armitage et al., 2003; Park et al., 2008). This further bolsters the in-plane nature of this phonon mode. This mode coupling has also been studied in trARPES by its imprint in the population relaxation dynamics (Graf et al., 2011; S.-L. Yang et al., 2015; Rameau et al., 2016) and pump-modulated self-energy (Rameau et al., 2014; W. Zhang et al., 2014).

An oxygen buckling B_{1g} mode with frequency of 40 meV was directly identified by Raman spectroscopy and inelastic neutron scattering to show softening across the superconducting T_c (Thomsen et al., 1988; Reznik et al., 1995). ARPES shows that the B_{1g} coupling increases moving away from the node [the kink near 40 meV in Fig. 21(b)]. In single-layer cuprates, this mode does not couple effectively due to symmetry constraints. In bilayer or trilayer cuprates, where it does couple, the kink shows a strong energy shift with the superconducting gap as the temperature goes from below to above T_c (Lee et al., 2008; Johnston et al., 2010). As a result, mode identification from kink energies usually requires detailed analysis in the superconducting state (Sandvik, Scalapino, and Bickers, 2004; Lee et al., 2008).

A mode with an even lower energy of around 10 meV (feature γ) is observed in Bi-2212 and Bi-2201. Its coupling strength weakens rapidly with hole doping [Figs. 21(c) and 21(d)], and its momentum-dependent kink energy tracks the d-wave momentum dependence of the superconducting gap below T_c (Anzai et al., 2010; Vishik et al., 2010; Kondo, Nakashima et al., 2013; Ying-Ying et al., 2013). Such a momentum-dependent form of gap shifting is interpreted as coupling to forward scattering channels ($q \approx 0$) from either low-energy phonons or out-of-plane impurities (Johnston et al., 2012; Hong et al., 2014), which may play a role in enhancing the d-wave superconductivity.

All phonon energies in cuprates have an upper bound at ~100 meV, with oxygen being the lightest composition

element. Yet several nodal dispersion anomalies exist at higher binding energies. At 100–150 meV, broad self-energy humps are seen in near-nodal spectra in Bi-2212 (Borisenko et al., 2006; W. Zhang et al., 2008b; J. He et al., 2013), some interpreted as a final-state effect specifically with low-energy laser-based photoemission (Miller et al., 2015). At 300–400 meV, a universal nodal spectral "waterfall" (near-vertical, incoherent spectral intensity) breaks the nodal dispersion, where both dipole-transition matrix element effects and intrinsic strong electronic correlation effects have been proposed to contribute [Fig. 14(c)] (Graf et al., 2007; Meevasana et al., 2008; W. Zhang et al., 2008a; Moritz, Johnston, and Devereaux, 2010; Rienks et al., 2014; Yu et al., 2020). Because of the steep quasiparticle dispersion, the nodal and near-nodal spectra can be used not only to extract the normal-state electron self-energy (Kaminski and Fretwell, 2005; Zhou et al., 2005; Zhou, Cuk et al., 2007; Meevasana et al., 2008) but also to further invert the anomalous self-energy in the superconducting state to directly reveal interactions in the pairing channel (Bok et al., 2016); see also Sec. III.A.

2. Coupling to the antinode

Unlike the dispersion anomalies near the node, mode coupling takes the form of spectral weight redistribution near the antinode partly due to the lack of sharp quasiparticle dispersions to directly intercept with. In optimally doped Bi-2212, the antinodal dispersion gradually develops a spectral weight depression at around 70 meV below the superconducting pairing temperature [Figs. 22(a) and 22(c)], reminiscent of
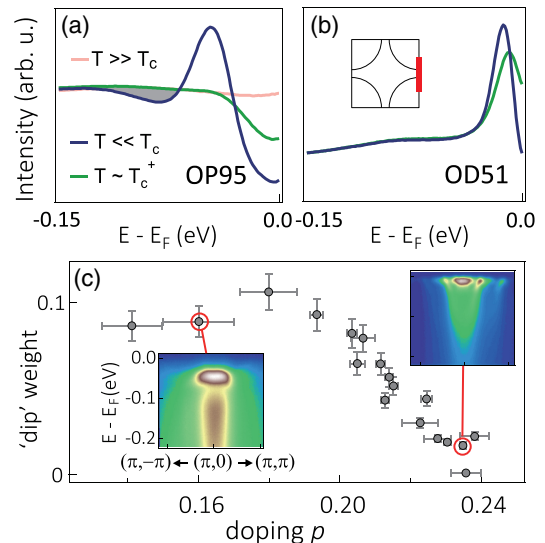
FIG. 22. Rapid change of the antinodal mode coupling across the critical doping. Parallel momentum-integrated antinodal spectra for (a) optimally doped and (b) heavily overdoped $Bi_2Sr_2CaCu_2O_{8+\delta}$ at different temperatures. The integration window is indicated by the red bar in the inset schematic Fermi surface. (c) Doping dependence of the spectral weight of the antinodal "dip" feature, reflecting the mode-coupling strength. Insets: false color plots of the antinodal spectra in the superconducting state for (a) optimally doped and (b) heavily overdoped $Bi_2Sr_2CaCu_2O_{8+\delta}$. Adapted from He et al., 2018a.

the density of states in superconducting Pb as a result of strong electron-phonon coupling (Rowell and Kopf, 1965; Dessau *et al.*, 1991; Cuk *et al.*, 2004; Devereaux *et al.*, 2004). This has been interpreted as either coupling to the oxygen B_{1g} phonon (∼36 meV in Bi-2212) or the spin-resonance mode endemic to d-wave superconductors (∼40 meV in Bi-2212), with additional spectral weight contributions from the bilayer splitting in Bi-2212 (Campuzano *et al.*, 1999; Borisenko *et al.*, 2003; Gromko *et al.*, 2003; Devereaux *et al.*, 2004; Dahm *et al.*, 2009; He *et al.*, 2018a). Dramatic change of this mode coupling is reported across the critical doping, suggesting its intimate role in the low-energy electronic structure (He *et al.*, 2018a).

3. Phonons, charge order, and superconductivity

The role of electron-phonon coupling in high-T_c superconductivity remains complex yet intriguing. Isotope substitution yields substantial change on the superfluid density but has a negligible effect on T_c (Pringle, Williams, and Tallon, 2000; Tallon *et al.*, 2005). Phonons are also known to participate in the charge order phenomenon, which directly competes with superconductivity (Blackburn *et al.*, 2013; Le Tacon *et al.*, 2014; Chaix *et al.*, 2017; He *et al.*, 2018b). The sign-changing d-wave pairing symmetry naturally favors the electronic mechanism with repulsive interaction, rather than the sign conserving breathing phonon that connects the antinodal electrons (Scalapino, 1995; Sandvik, Scalapino, and Bickers, 2004). However, small-**q** coupling phonons like the buckling B_{1g} mode and the ∼10 meV low-energy mode are predicted to enhance d-wave pairing (Bulut and Scalapino, 1996; Devereaux *et al.*, 2004; Johnston *et al.*, 2010; Li *et al.*, 2016). With doping, a fourfold change of the superconducting gap size is found to be accompanied by a simultaneous rapid change of both the electron-phonon and electron-electron interactions (He *et al.*, 2018a). This is evidenced by the strengthening of electron-phonon coupling at the antinode over the same narrow doping window in which the pseudogap suddenly appears and the superconducting gap-to-T_c ratio rapidly departs from the BCS limit (He *et al.*, 2018a, 2020; Zhong *et al.*, 2018). This indicates that these interactions turn a weaker d-wave superconductor into a stronger but more complex one. The current progress from photoemission indicates involvement of phonon coupling in the superconductivity and a potential multichannel pairing mechanism that resembles that of the monolayer FeSe/SrTiO$_3$ heterostructure (Sec. V.E.2).

F. Outlook

High-T_c cuprates will continue to receive focused interest, especially from ARPES investigation, thanks to the simplicity in its bare electronic structure and the richness in its derivative phases. Many classic questions can be addressed with versatile sample preparation methods and environment control, such as the delineation of intertwined orders and phase boundaries, the family and layer dependence of charge distribution and polarizability, quantification of carrier doping beyond the parabolic relation, and interfacial superconductivity tuning. In addition, the pursuit of the superconducting mechanism will benefit from new possibilities for breakthrough in the heavily overdoped region, where the normal state is more coherent. The nature of the superconductor-to-metal quantum phase transition at the far end of the superconducting dome will also receive more attention, which is akin to the historical development in the superconductor-to-insulator transition at low doping near the Mott limit. Last, the electron-doped cuprates (and the role of long-range AFM order and apical oxygen) will undergo more focused investigations due to the continued improvement in energy resolution. On the other hand, the search for new emergent states will continue, such as possible spin liquid near the Mott limit and the strange metal phenomena at high temperatures. Cuprate phenomenology also continues to serve as a source of inspiration for outside-the-box theoretical concepts (Zaanen *et al.*, 2015; Hartnoll, Lucas, and Sachdev, 2018).

V. IRON-BASED SUPERCONDUCTORS

A. Overview

Cuprate superconductors were the lone family of unconventional high-T_c superconductors until a new class of high-temperature superconductors was discovered in iron-based pnictide (FePn) (Kamihara *et al.*, 2006, 2008; Chen, Wu *et al.*, 2008; Rotter, Tegel, and Johrendt, 2008) and, subsequently, chalcogenide (FeCh) compounds (Hsu *et al.*, 2008). Both the transport T_c in bulk crystals and the single-particle gap-closing temperature in thin films reach above 50 K.[10] In addition to the iron-based superconductors' (FeSCs) high T_c, the interest also lies in their rich material systems, the wide range of compositional tunability, and the prospect that they can be conceptualized as the multiband counterpart of the strongly correlated single-band cuprate superconductors. The addition of Hund's coupling J_H to FeSCs of various correlation strengths U unlocks both new experimental paths and theoretical frameworks to capture even richer physics beyond single-band correlated systems [Fig. 24(c)]. There are comprehensive reviews on the materials (Johnston, 2010; Paglione and Greene, 2010; Stewart, 2011; Wang, Yang *et al.*, 2011; Chen *et al.*, 2014; Hosono *et al.*, 2018), correlation effects including the magnetism and nematicity (Dai, Hu, and Dagotto, 2012; Dagotto, 2013; Davis and Lee, 2013; Georges, de Medici, and Mravlje, 2013; Fernandes, Chubukov, and Schmalian, 2014; Dai, 2015; Fernandes and Chubukov, 2017), superconducting pairing mechanism (Hirschfeld, Korshunov, and Mazin, 2011; Chubukov, 2012; Scalapino, 2012; Bang and Stewart, 2017), and thin-film forms of FeSCs (Pustovit and Kordyuk, 2016; Lee, 2018). We focus here on the role of ARPES in advancing the understanding of FeSCs.

The Fig. 23(a) inset shows the body-centered tetragonal structure of one archetypal iron pnictide BaFe$_2$As$_2$ (Ba-122), where the alkaline earth metal layers and iron pnictogen layers sandwich each other. Significant charge transfer between these two layers results in an Fe $3d^6$ configuration from which the

---

[10]The actual T_c value on this thin-film system is still a contested topic, in part due to the difficulty of direct magnetic and transport measurements.
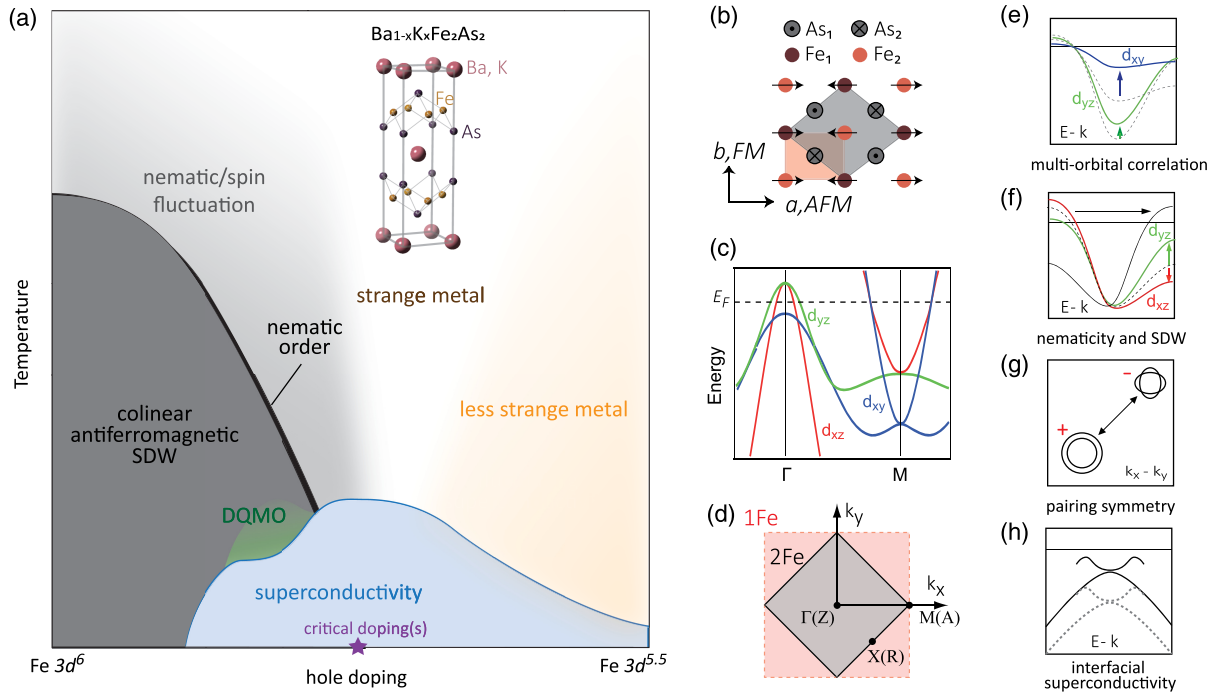
FIG. 23. (a) Schematic temperature-doping phase diagram in K-doped Ba-122 FePn system. Adapted from Kasahara *et al.*, 2010. Inset: crystal structure of parent compound Ba-122. DQMO, double-Q magnetic order. Adapted from Rotter, Tegel, and Johrendt, 2008. (b) Top view of the Fe sublattice after both the nematic order and the collinear antiferromagnetic order develop. The gray shaded diamond indicates the two-Fe unit cell when considering the As atoms alternately positioned above and below the Fe plane. The red shaded rectangle is the simplified one-Fe unit cell that ignores the As atoms. (c) Low-energy band structure along the Fe—As bond direction in a three-orbital model of a typical FeSC. (d) Typical Brillouin zone (BZ) of a FeSC projected to the FeAs plane. Symmetry labels in parentheses are projected from $k_z = \pi/c$. Red, one-Fe BZ; gray, two-Fe BZ. Schematics for (e) normal-state orbital-selective band renormalization, (f) nematicity and AFM-induced band reconstruction (neglecting d_{xy} band), (g) unconventional superconductivity with interpocket pairing. and (h) electron-phonon-coupling-induced electron shakeoff band. Adapted from Ye *et al.*, 2012, and Yi *et al.*, 2017.

multiorbital low-energy electronic states originate. Within each layer, the pnictogen and chalcogen atoms alternately pucker above and below the adjacent Fe plaquettes, creating a tetrahedral crystal field that moderately elevates the t_{2g} orbitals (d_{xy}, d_{yz}, d_{xz}) above the e_g orbitals ($d_{3r^2-z^2}$, $d_{x^2-y^2}$). Figure 23(c) shows the representative low-energy band dispersions along high-symmetry momenta, with the t_{2g} orbital contents most dominant (Lebegue, 2007; Lu *et al.*, 2008; Singh, 2008; Cvetkovic and Tesanovic, 2009). Because of the glide-plane symmetry (reflection on the Fe plane followed by a translation along the diagonal Fe-Fe direction) of the pnictogen and chalcogen atoms, each two adjacent Fe atoms are inequivalent, resulting in a two-Fe Brillouin zone [Figs. 23(b) and 23(d), gray diamond], which by symmetry operations can be "unfolded" to a one-Fe Brillouin zone [Figs. 23(b) and 23(d), red square] (Johnston, 2010). In the latter case, any derived electronic structure has to be folded back into the two-Fe zone in order to match experimental observations (Kasahara *et al.*, 2010). We caution the reader that during this virtual folding process orbital contents can change due to a glide-mirror symmetry on the Fe plane (Lin *et al.*, 2011; Brouet *et al.*, 2012). The low-energy electronic structure in FeSCs generally consists of three hole pockets centered around Γ and two electron pockets located at the

two-Fe zone corner.[11] Such a multiband low-energy electronic structure, together with the interactions therein, sets the ground for the extremely rich phases that emerge in FeSC systems.

In FeSCs, proper chemical replacement in practically any atomic site can lead to superconductivity (H. Chen *et al.*, 2009; Jiang *et al.*, 2009; Kasahara *et al.*, 2010; T. Liu *et al.*, 2010; Nandi *et al.*, 2010; Lai *et al.*, 2014; Dai *et al.*, 2015). Resembling the cuprate superconductors, but to a lesser degree (Fukuzumi *et al.*, 1996), dopants placed in the charge reservoir layer lead to more robust superconductivity than direct doping in the conduction plane (Ye *et al.*, 2014). Meanwhile, the dopants modify the electronic states via changes in not only the carrier concentration but also the Fe—As bond angle, the strength of the competing magnetic ground states, and the level of disorder (Khasanov *et al.*, 2011; Li *et al.*, 2012; R. Zhang *et al.*, 2014). Figure 23(a) shows a representative phase diagram in the K-doped $BaFe_2As_2$ system. In the stoichiometric parent compound, the system

---

[11]The symmetry notation in the Brillouin zones of FeSCs can be different, due mainly to the different c-axis stacking between the 122 and 11/111/1111 families. See Johnston (2010) for a detailed discussion.

starts off behaving like a bad metal with linear resistivity and magnetic susceptibility in the high-temperature tetragonal phase (Rotter, Tegel, and Johrendt, 2008). Upon cooling, it consecutively undergoes an orthorhombic structural distortion at $T_{\text{structure}}$ (T_s) and an antiferromagnetic transition at $T_{\text{Néel}}$ (T_N) within 1 K of each other (Huang *et al.*, 2008). The ground state is a collinear antiferromagnetic spin density wave (SDW) state with a slightly elongated a axis in which iron moments align antiferromagnetically, and a compressed b axis in which iron moments align ferromagnetically. While the orthorhombicity is smaller than 1% (Su *et al.*, 2009; Tomić *et al.*, 2013), 20%–100% in-plane electronic nematicity is observed through resisitivity measurements on detwinned single crystals (Chu *et al.*, 2010). The larger electrical resistance along the shorter, ferromagnetically ordered b axis also signifies nontrivial low-energy electronic state evolution, emphasizing the need for a direct determination of the electronic structure. Further electron or hole doping simultaneously suppresses T_s and T_N and eventually induces superconductivity (H. Chen *et al.*, 2009; Jiang *et al.*, 2009; Kasahara *et al.*, 2010; Nandi *et al.*, 2010; Parker *et al.*, 2010; Lai *et al.*, 2014). Strong nematic fluctuation and strange metal transport behaviors prevail above the superconducting dome, beneath which a critical point is suggested (Fernandes, Chubukov, and Schmalian, 2014; Si, Yu, and Abrahams, 2016; Hussey, Buhot, and Licciardello, 2018). Further electron doping toward $3d^7$ usually restores metallicity to the

normal state, while hole doping toward $3d^5$ steers toward stronger electronic correlation (Yi *et al.*, 2017). Chemical pressure (via nominal isovalent doping) and hydrostatic pressure on the iron-based parent compounds can also produce phase diagrams similar to those from heterovalent doping (Colombier *et al.*, 2009; Jiang *et al.*, 2009; Klintberg *et al.*, 2010; T. Liu *et al.*, 2010; Dong *et al.*, 2013), with an exception in the Fe(Se,S) system. There the chalcogen height from the iron plane responds differently to chemical and physical pressure (Matsuura *et al.*, 2017). This aspect does not have an as comprehensive counterpart in the cuprate phase diagram.

Although intense effort has been invested toward a unified understanding of the magnetism and superconductivity in all FeSCs, a wide distribution of family-dependent properties encumbered early efforts. In Pr /Ce/LaFeAsO$_{1-x}$F$_x$ (1111 systems), superconductivity does not coexist with the SDW phase [Fig. 24(a)] (Zhao *et al.*, 2008; Luetkens *et al.*, 2009; Rotundu *et al.*, 2009). In (Ba, K)Fe$_2$As$_2$, Ba(Fe, Co)$_2$As$_2$, and BaFe$_2$(As, P)$_2$ (Ba-122) and Co-, Ni-, and Cu-doped NaFeAs (Na-111), superconductivity and SDW coexist in the underdoped region. And the structural transition is much more separated from the AFM transition in temperature on the electron-doped side than the hole-doped side [Fig. 24(a)] (H. Chen *et al.*, 2009; Kasahara *et al.*, 2010; Nandi *et al.*, 2010; Parker *et al.*, 2010; A. Wang *et al.*, 2013). In the iron chalcogenide FeSe (11 system), despite strong AFM
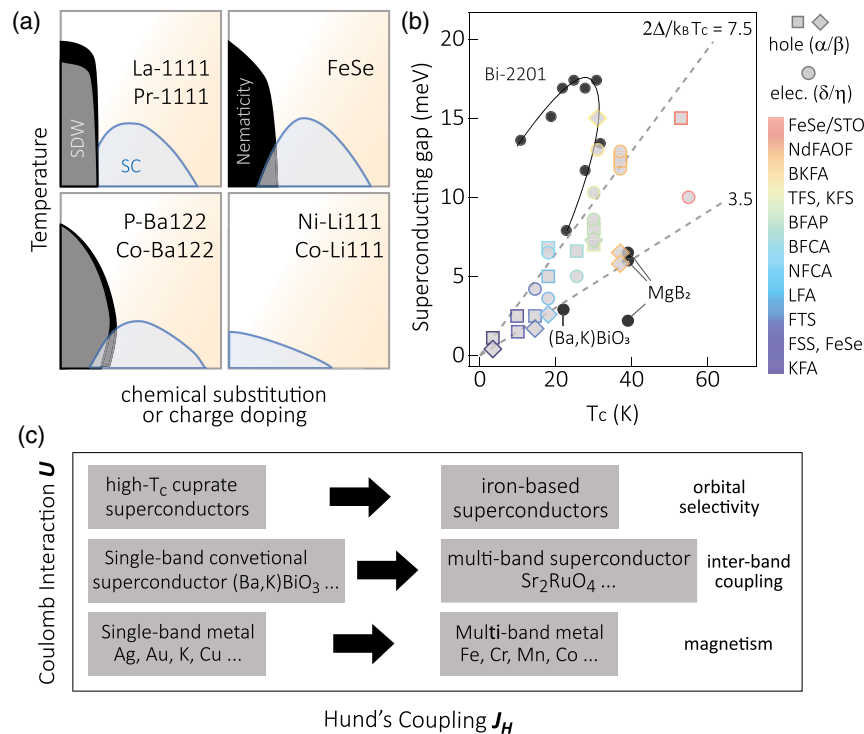
FIG. 24. Family dependence and the multiorbital nature of FeSCs. (a) Schematic temperature-doping phase diagrams for different FeSC families. Black, nematic order; gray, SDW order; blue, superconductivity; orange shade, more metallic transport. (b) Compilation of superconducting gap vs T_c for representative FeSCs (colored markers), single-layer cuprate Bi-2201 (increasing hole doping clockwise), MgB$_2$ (σ, π, and surface bands), and (Ba, K)BiO$_3$. For FeSCs, square and diamond (circle) markers represent superconducting gaps on the hole (electron) pockets. Dashed lines are reference $2\Delta/k_B T_c$ values at 3.5 (s-wave limit) and 7.5. For definitions of the compound acronyms see Yi *et al.* (2017). (c) Coulomb interaction U and Hund's coupling J_H cooperatively generate new phenomena from single-band to multiband systems.

fluctuations, only the nematic phase exists under ambient pressure [Fig. 24(a)] (Q. Wang *et al.*, 2016; Matsuura *et al.*, 2017). Adding to the peculiarity, in Co-doped LiFeAs (Li-111) both the magnetic phase and the nematic phase are absent, and the superconductivity starts right from the stoichiometric parent compound with $T_c = 18$ K [Fig. 24(a)] (Dai *et al.*, 2015). The reported superconducting gap symmetry, gap sizes, and fermiology are also widely family dependent, ranging from nodeless to nodal gap structures on different Fermi surface sheets, where the gap-to-T_c ratios for the larger gap roughly fall between the cuprates and more conventional superconductors such as MgB_2 and $(Ba, K)BiO_3$ [Fig. 24(b)]. However, it is believed that a common thread linking them all is the Hamiltonian incorporating moderate Coulomb interaction U and Hund's coupling J_H on the most dominant iron $3d$ orbitals [Fig. 24(c)] (Chubukov and Hirschfeld, 2015; Fernandes and Chubukov, 2017). As such, factoring in the vastly different correlation strengths, the doping levels, and the associated Fermi surfaces, the hope is to consistently describe the many family-dependent properties of FeSCs with a universal, minimal microscopic Hamiltonian.

ARPES played an important role in the dissection of multiple electronic degrees of freedom in FeSCs. Here we first address electronic interaction effects with decreasing energy or temperature: (1) the orbital characters and orbital-selective renormalization on the normal-state electronic structure [Fig. 23(e)], (2) the evolution of the electronic structure in the nematic and SDW states [Fig. 23(f)], (3) the pairing symmetry, pairing mechanism, and other properties of the superconducting state [Fig. 23(g)]. Finally, we discuss effects from the lattice degree of freedom, mainly the enhanced electron-phonon interaction due to strong electron correlation, and interfacial superconductivity in thin-film iron chalcogenides [Fig. 23(h)]. The discussion on possible topological superconductivity in FeChs is elaborated on in Sec. VII.B.7.

B. Normal state

1. Multiorbital character

Identification of orbital characters constitutes the first step in the investigation of electronic properties of multiband metals like the FeSCs. As introduced in Sec. V.A, the low-energy electronic structure of an FeSC most prominently features the t_{2g} d orbitals. In the high-temperature tetragonal paramagnetic normal state, the d_{xz} and d_{yz} orbital components near Γ rotate into each other under 90° rotation, forming two hole pockets near the Brillouin zone center with alternating orbital contents. The d_{xy}-dominant band forms a hole pocket at the one-Fe Brillouin zone (BZ) corner, which in reality folds into the two-Fe BZ center.[12] In the meantime, together with the d_{xy} orbital, the d_{xz}- and d_{yz}-dominant bands form elliptical electron pockets at the two-Fe zone corner with alternating orbital components along the Fermi surface. Figures 25(a)–25(d) showcase the orbital content composition on the Fermi

pockets in the normal state of NaFeAs (Zhang *et al.*, 2012). To delineate different orbital components in each band, different combinations of crystal orientation and incident photon polarization are employed to take advantage of the dipole-transition matrix element in the photoemission process [Figs. 25(c) and 25(d)] (Lu *et al.*, 2008; Yi *et al.*, 2011; Brouet *et al.*, 2012; X.-P. Wang *et al.*, 2012a; Zhang *et al.*, 2012; Watson *et al.*, 2015) (Sec. II.D).

The family-dependent normal-state electronic structures reveal a close link between the iron pnictogen or iron chalcogen atomic arrangements and electronic correlation strengths. Figure 25(e) shows the schematic measured band dispersions along the Γ-M direction in $SrFe_2P_2$, NaFeAs, and $FeSe_xTe_{1-x}$, which reflect increasing electronic correlations (Yi *et al.*, 2017). Indeed, reports of strong coupling phenomena such as polaron formation exist in the $Fe_{1.02}Te$ system (Liu *et al.*, 2013). The $d_{xz/yz}$ band renormalization is shown to correlate with the iron pnictogen or iron chalcogen bond length [Fig. 25(g)] and monotonically increase as Fe filling approaches $3d^5$ over a wide range of FeSC families (Yi *et al.*, 2017).

2. Orbital-selective Mott transitions

Because of interorbital Hund's coupling, the effect of electronic correlation U on the d_{xy} orbital is relatively independent of that on other d orbitals (Haule and Kotliar, 2009; Georges, de Medici, and Mravlje, 2013). This enables orbital-selective band renormalization and Mott transitions that affect d_{xy} orbital contents more than the rest (Si, Yu, and Abrahams, 2016). Figure 25(h) shows that, as a function of iron pnictogen or iron chalcogen bond angle, the d_{xy}-dominant band is more renormalized than the $d_{yz/xz}$-dominant band, especially in the iron chalcogenides (Brouet *et al.*, 2016; Yi *et al.*, 2017). Moreover, temperature-dependent studies found an orbital-selective coherent-to-incoherent crossover on the d_{xy} orbital at high temperature, similar to that in other complex oxides [Fig. 25(f)] (Neupane *et al.*, 2009; Yi *et al.*, 2013; Yi *et al.*, 2015; Miao *et al.*, 2016; Niu *et al.*, 2016; Pu *et al.*, 2016). Such selective multiorbital correlation has a profound impact on various low-temperature phases, as discussed later.

C. Electronic nematicity and magnetic order

In underdoped $BaFe_2As_2$, cooling from the tetragonal normal state drives the system into a structural orthorhombic and an electronic nematic phase (Avci *et al.*, 2012). At around the same temperature, the system establishes a collinear antiferromagnetic order. Hence, one major early endeavor regarding the electronic nematicity was determining whether it is lattice (structure) driven, spin (magnetic) driven, or orbital (charge) driven (Fernandes, Chubukov, and Schmalian, 2014).

Small structural orthorhombicity leads to twin domains that are locally $\pi/2$ rotated with respect to each other. With a typical domain size on the micron level (Chu *et al.*, 2010; Tanatar *et al.*, 2010), early ARPES with an $\sim$100 μm beam spot size inadvertently probed an admixture of electronic structures from both domains, adding to the complexity

---

[12]In certain systems with strong d_{xy} orbital renormalization or electron doping, some of the zone center hole pockets can be eliminated.
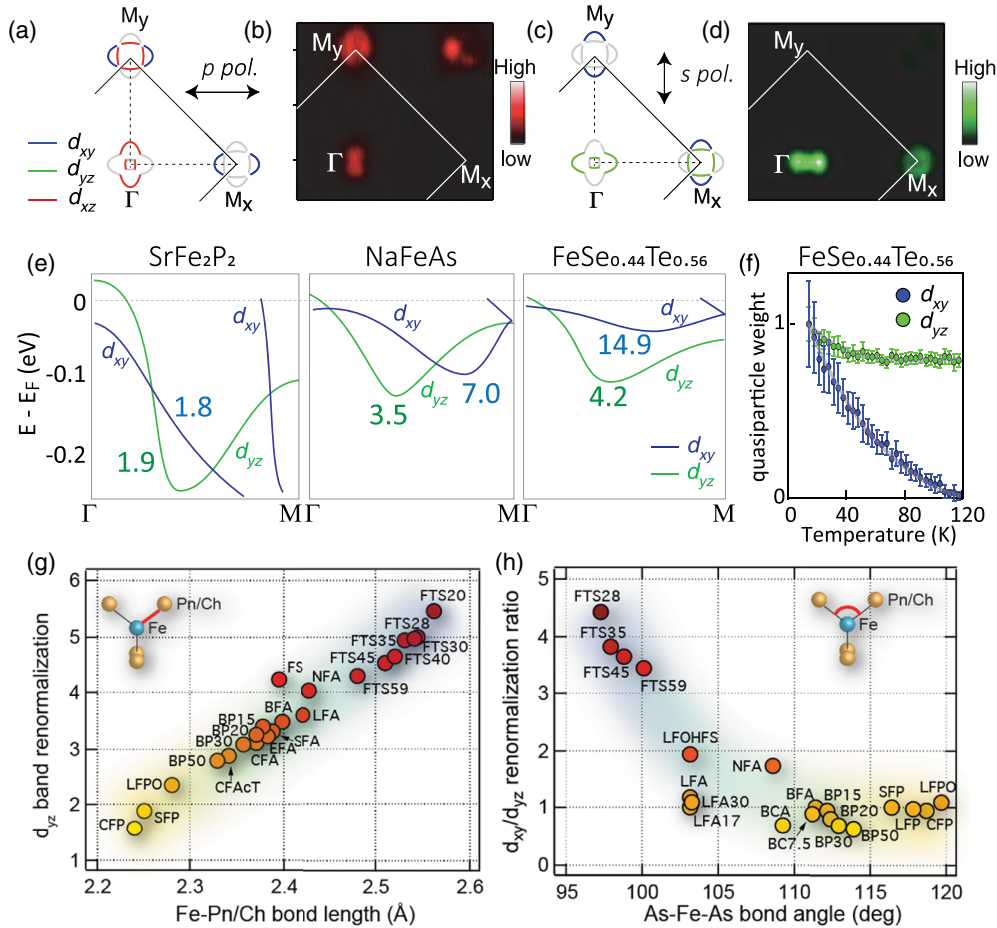
FIG. 25. Low-energy electronic band structure, Fermi surface, and correlation effects in the normal state of FeSCs. (a),(c) Schematic and (b),(d) measured Fermi surfaces in the normal state of NaFeAs. Different experimental geometries are employed to highlight different orbital components based on the dipole-transition matrix element effect. Light gray indicates where all intensities are suppressed. Adapted from Zhang *et al.*, 2012. (e) Normal-state d_{yz} (green) and d_{xy} (blue) orbital-dominated bands across different families with different correlation strengths. The bands are sketched according to experimental data. The numbers represent the renormalization factors on top of local-density approximation calculated band dispersions. Adapted from Yi *et al.*, 2017. (f) Orbital-selective quasiparticle decoherence at high temperatures in FeTe$_{0.56}$Se$_{0.44}$. Adapted from Yi *et al.*, 2015. (g) The d_{yz} orbital renormalization factor positively correlates with the iron chalcogen or iron pnictogen bond lengths. (h) Relative renormalization strength between d_{xy} and d_{yz} orbital-dominated bands as a function of the iron pnictogen bond angles of different FeSCs. The acronyms represent different FeSC families and are fully indexed by Yi *et al.* (2017).

(G. Liu *et al.*, 2009; Yi *et al.*, 2009). Uniaxial stress was later applied *in situ* to detwin the sample (Chu *et al.*, 2010), revealing a 30–120 meV band shift between the otherwise degenerate d_{yz} and d_{xz} components near the zone boundary in the nematic phase (Y. Kim *et al.*, 2011; Yi *et al.*, 2011; Zhang *et al.*, 2012; Shimojima *et al.*, 2014; Watson *et al.*, 2019). Figure 26(a) shows this band shift in detwinned BaFe$_2$As$_2$ along two orthorgonal crystal axes below T_s. The nematic energy also scales monotonically with T_s across different FeSC systems [Fig. 26(c), left panel].[13] A density-functional theory (DFT) calculation shows that such a large nematic splitting energy scale cannot be accounted for by the <1%

orthorhombic lattice distortion (Yi *et al.*, 2011), disfavoring the lattice-driven scenario for the electronic nematicity. Moreover, piezoresistance measurements indicate diverging electronic nematic susceptibility approaching the structural transition temperature and further indicates that the structural transition is a consequence of, rather than the cause of, strong electronic nematicity (Chu *et al.*, 2012).

In the meantime, the resolution of either orbital or spin origin for the electronic nematicity has been considered system dependent. In the orbital-driven scenario, the rising d_{yz} orbital along the AFM direction and the sinking d_{xz} orbital along the FM direction cause different electron fillings, resulting in a ferro-orbital order (Lee, Yin, and Ku, 2009; Lv, Wu, and Phillips, 2009; Böhmer *et al.*, 2015). This scenario is particularly relevant in bulk FeSe, where only the nematic order exists, and band splitting is observed (Nakayama *et al.*, 2014; Shimojima *et al.*, 2014; Baek *et al.*,

---

[13]The original plot interpreted the band shift as the SDW gap, but the band shift was later realized to come from the electronic nematicity (Tan *et al.*, 2013; Yi *et al.*, 2019).
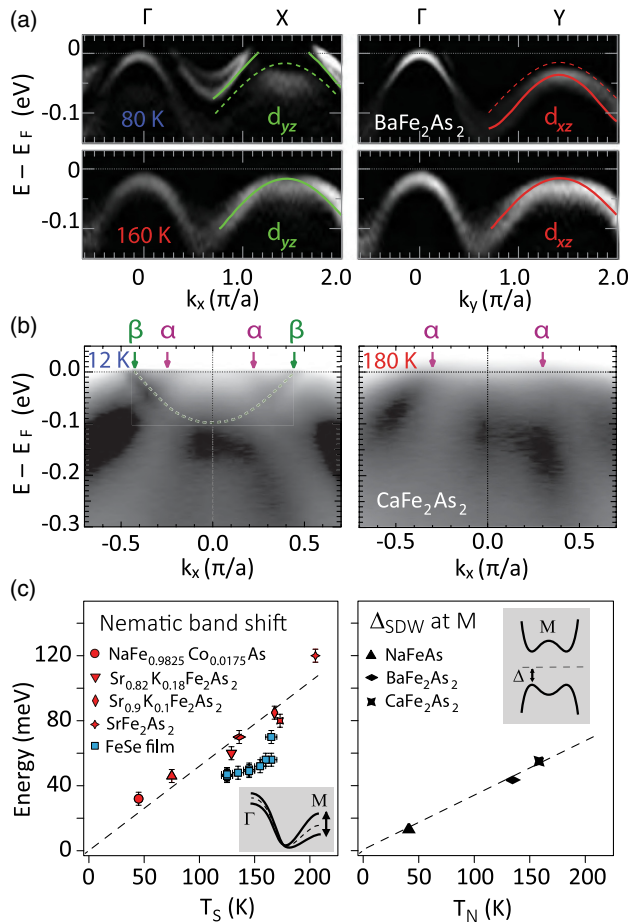
FIG. 26. Band reconstructions associated with the nematic order and collinear antiferromagnetic order in underdoped FeSCs. (a) Nematic-order-induced band shift along two high-symmetry cuts in $BaFe_2As_2$ at 80 and 160 K ($T_N \sim 138$ K). Adapted from Yi *et al.*, 2011. (b) Energy-momentum cut along Γ-M in the SDW state. Note the electron pocket folded from the zone corner (green arrows). Adapted from (Kondo *et al.*, 2010). (c) Nematic band shift energy scale and the SDW gap size at the M point plotted against their respective transition temperatures across various FeSCs. Adapted from Tan *et al.*, 2013, and Yi *et al.*, 2017.

2015; Suzuki *et al.*, 2015; Watson *et al.*, 2015; Zhang *et al.*, 2015). However, simple ferro-orbital ordering implies a constant band shift over the entire **k** space due to its localized nature (Kontani, Saito, and Onari, 2011). This contradicts the highly **k**-dependent anisotropic band shift observed in most FeSCs, which suggests nematic bond order (Suzuki *et al.*, 2015; Y. Zhang *et al.*, 2016; Pfau *et al.*, 2019). In the meantime, in doped Ba-122 systems, magnetic fluctuation is shown to scale with the orthorhombic fluctuation (Fernandes *et al.*, 2013), and the uniform magnetic susceptibility exhibits in-plane anisotropy (Kasahara *et al.*, 2012), alluding to a spin-driven nematic transition (Avci *et al.*, 2014). In this case, spin-orbit coupling carries the anisotropy from magnetic fluctuations to break the lattice rotational symmetry at the same or even slightly higher temperatures (Xu, Müller, and Sachdev, 2008; Fernandes, Chubukov, and Schmalian, 2014). Indeed at the Γ point, a sizable spin-orbit splitting of otherwise symmetry-protected $d_{xz/yz}$ degeneracy has been

observed in many FeSC compounds (Brouet *et al.*, 2012; Johnson *et al.*, 2015; Suzuki *et al.*, 2015; Borisenko *et al.*, 2016; Day *et al.*, 2018).

While the nematic transition breaks the rotational symmetry and anisotropically shifts energy bands, the SDW transition breaks the translational symmetry, folds Γ (M_y) and M_x (Γ') points into each other, and opens up energy gaps wherever bands cross and symmetry protection is absent [Fig. 26(b)] (Kondo *et al.*, 2010; M. Yi *et al.*, 2014). The detailed band reconstruction schemes were summarized in previous reviews by Ran *et al.* (2009), Shimojima *et al.* (2010), Zhang *et al.* (2012), and Yi *et al.* (2017). Here we emphasize that the C_2 symmetry from the nematic phase and the orbital dependence are evident in the SDW gap anisotropy: it is often the largest on d_{xy} crossings, followed by d_{yz} and d_{xz} segments (Richard *et al.*, 2010; M. Yi *et al.*, 2014, 2017). The emergence of the antiferromagnetic order can be viewed from both the itinerant perspective (Fermi surface nesting) and the localized perspective (local moment superexchange) (Davis and Lee, 2013; Si, Yu, and Abrahams, 2016; Fernandes and Chubukov, 2017). In the former, the family dependence is rooted in the different Fermi surface topology due to different electron filling and low-energy band structure, whereas in the latter the more strongly renormalized bands lose more coherent spectral weight to form localized magnetic moments. As with the nematic energy scale, the SDW gap energy also scales with the ordering temperature across different FeSC families [Fig. 26(c), right panel].

D. Superconducting properties

Compared to cuprates, the superconducting transitions in bulk FeSC compounds are much more mean-field-like due to higher carrier density, smaller pairing energy, and better three dimensionality (Chen, Tesanovic *et al.*, 2008; Hardy *et al.*, 2010). Scanning tunneling spectroscopy, ARPES, transport, and thermodynamic measurements report multigap behavior in the superconducting state of FeSC compounds (Stewart, 2011; Kuzmicheva *et al.*, 2014). The superconducting $2\Delta/T_c$ ratio (of the larger gap) varies from family to family, ranging from an intermediate to weak coupling BCS limit (Kuzmicheva *et al.*, 2014). A BCS-BEC crossover was proposed to occur on the extremely shallow and small Γ hole pocket in $FeSe_{1-x}Te_x$, where the Fermi energy can be tuned to match the superconducting gap size by doping (Lubashevsky *et al.*, 2012; Shibauchi, Carrington, and Matsuda, 2014; Rinott *et al.*, 2017). However, little associated thermodynamic evidence has been observed so far.

The pairing symmetry in FeSCs is highly system dependent, partly due to the family-dependent Fermi surface shapes and a vast distribution of (next-)nearest-neighbor exchange interaction strengths (Fig. 27) (C. Liu *et al.*, 2011; Davis and Lee, 2013; Si, Yu, and Abrahams, 2016). Benefiting from advances in both high-resolution synchrotron-based and laser-based ARPES, the momentum structure of the superconducting gap amplitude on different Fermi surface sheets can be determined with sub-meV resolution (Okazaki *et al.*, 2012). The most commonly discussed pairing symmetry is $s^\pm$-wave pairing in systems with both hole and electron pockets [Fig. 27(b), left panel]. In this scenario, the Γ hole pockets
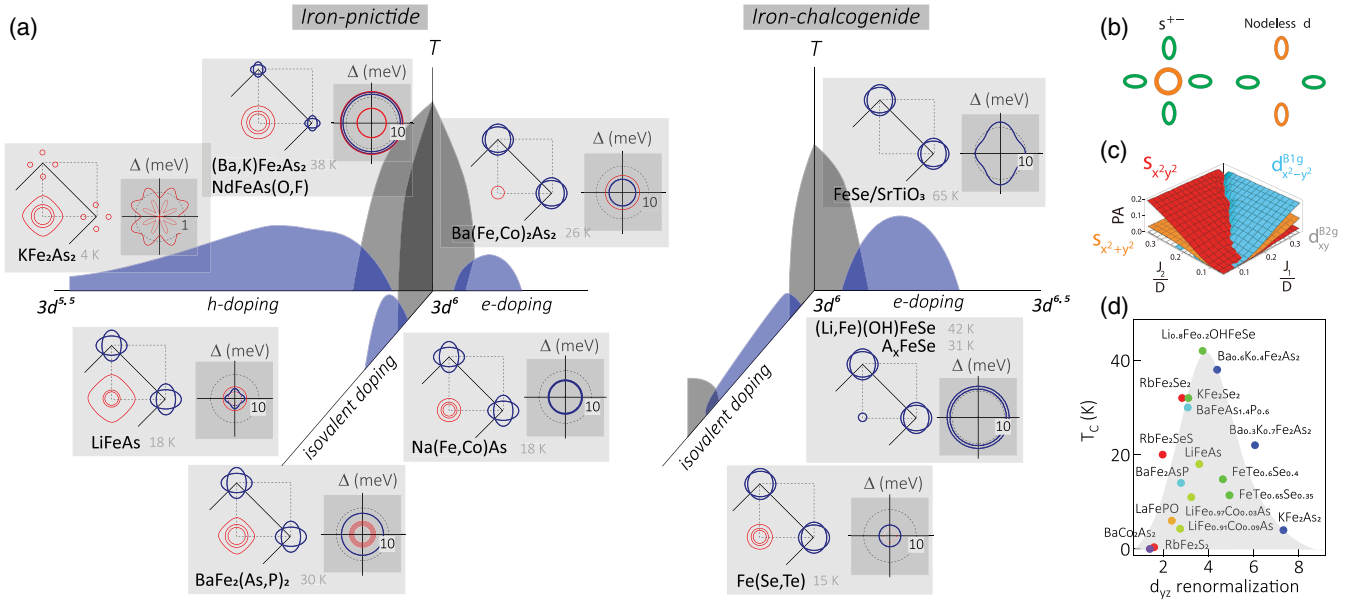
FIG. 27. Superconducting gap symmetry and anisotropy across different families of FeSCs. (a) Extended temperature-doping phase diagram with corresponding Fermi surfaces and the gap structures in various FeSCs. The thin red circle represents hole pockets, and thick blue represents electron pockets. Polar plots of the gap amplitude on the hole and electron Fermi surface sheet obey the same color coding, respectively. The dashed circles are grid lines for size references. Red shading indicates substantial k_z dependence of the gap when projected onto the x-y plane. (b) Proposed interpocket pairing mechanisms for (left panel) $s^{\pm}$-wave and (right panel) d-wave symmetry. Colors indicate different signs of the order parameter. Adapted from Hirschfeld, Korshunov, and Mazin, 2011, and Hirschfeld, 2016. (c) Pairing amplitude computation based on coexisting electron and hole pockets. Different colors represent different symmetries as a function of nearest-neighbor and next-nearest-neighbor exchange couplings J_1 and J_2. Adapted from Si, Yu, and Abrahams, 2016. (d) Dependence of superconducting transition temperature T_c on the d_{yz} orbital renormalization strength. The same doping series of materials are represented by markers of the same color.

and the M electron pockets possess opposing order parameter signs, as suggested by the existence of a strong (π, π) spin resonance at $T < T_c$ in neutron scattering (Christianson et al., 2008; Qiu et al., 2009; Shamoto et al., 2010). This is necessitated by stronger Coulomb repulsion for interpocket channels than intrapocket channels, made possible by the antiferromagnetic spin fluctuation (A. Wang et al., 2013; Chubukov and Hirschfeld, 2015; Hirschfeld, 2016). ARPES finds nodeless superconducting gaps in Co- or K-doped Ba-122, NaFeAs (Ding et al., 2008; Lin et al., 2008; Z.-H. Liu et al., 2011), and undoped and intercalated bulk FeSe (Mou et al., 2011; Wang, Qian et al., 2011; M. Xu et al., 2012) on all Fermi surface sheets (Fig. 27). Accidental or symmetry enforced nodes may still appear in systems with both electron and hole pockets (Wang, Yang et al., 2011), as suggested in bulk FeSe (D. Liu et al., 2018), P-doped Ba-122 and KFe₂As₂ systems (Fig. 27) (Okazaki et al., 2012; Ye et al., 2012).

Meanwhile, when the system is heavily electron or hole doped, the intrapocket repulsion regains dominance due to either increased interpocket screening or complete removal of Γ hole pockets, and d-wave pairing amplitude may be increased [Fig. 27(b), right panel] (Hirschfeld, Korshunov, and Mazin, 2011; Lee, 2018). While nodeless anisotropic gaps are consistently observed in the monolayer system and its bulk counterparts (Liu et al., 2012; Lee et al., 2014; Niu et al., 2015; Y. Zhang, Lee et al., 2016; Zhao et al., 2016; Du et al., 2018), both s-wave and d-wave symmetry remain viable possibilities, as the proposed nodal direction does not always

intercept with a Fermi surface (Fan et al., 2015; Du et al., 2018; Ge et al., 2019). However, in heavily electron-doped A_xFeSe systems, nodeless superconducting gaps have been reported at both the zone center and the zone corner electron pockets (Mou et al., 2011; Y. Zhang et al., 2011; X.-P. Wang et al., 2012b; M. Xu et al., 2012). Recently pairing symmetry that breaks time-reversal symmetry was suggested in heavily hole-doped (Ba, K)Fe₂As₂ (Grinenko et al., 2020), although a related ARPES study is lacking.

Orbital-selective pairing is considered relevant in nematic FeSe systems, where the highly anisotropic C_2 gap function on the electron pocket is rooted in the inequivalence of d_{xz} and d_{yz} orbitals (D. Liu et al., 2018). In the meantime, the gap anisotropy in underdoped Na(Fe,Co)As has been interpreted either as varying d_{xy} orbital content along the Fermi surface (Zhang et al., 2013) or as a result of momentum-dependent competition with a SDW (Ge et al., 2013). A detailed temperature-dependent study of both the superconducting gap and the SDW gap does indicate a competition between the two, even though the two gaps are substantially separated in energy (Ge et al., 2013; M. Yi et al., 2014). The role of the d_{xy} orbital in FeSe, on the other hand, is suggested to either have extremely weak spectral coherence (Sprau et al., 2017) or move above E_F due to nematic splitting and band hybridization at low temperatures or both (Yi et al., 2019; Huh et al., 2020). Electronic correlation is considered central to the superconductivity in FeSCs, and the superconducting T_c is shown to be maximized for systems with intermediate
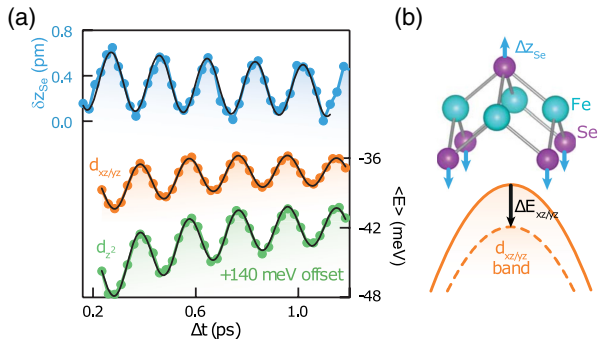
FIG. 28. Coherent A_{1g} phonon in FeSe. (a) The lattice displacement (top) and band energy shifts (bottom) are resolved by time-resolved x-ray diffraction and trARPES, respectively. (b) Schematic of the lattice (top) and band (bottom) modulation due to the coherently excited mode. From Gerber *et al.*, 2017.

electronic correlation strength across different families and dopings [Fig. 27(d)]. However, the impact from the highly family-dependent low-energy electronic structures should not be overlooked, because small doping changes can often drive dramatic Fermi surface topology change in FeSCs. The superconductivity in FeSCs also shows a wide range of family-dependent isotope effects, indicating complex lattice involvement amid the highly intertwined orbital, magnetic and electronic degrees of freedom.

E. Coupled lattice and electronic effects

On top of the rich electronic effects, the role of the lattice remains intriguing in FeSCs. The superconducting transition temperature T_c shows systematic dependence on the iron chalcogen bond angle, as reflected in the T_c enhancement from 8 to 37 K and the corresponding phonon frequency change under modest pressure in FeSe (Mizuguchi *et al.*, 2008; Margadonna *et al.*, 2009; Medvedev *et al.*, 2009; Huang *et al.*, 2010). In addition, T_c depends sensitively on the pnictogen height, in a fashion similar to its dependence on the band renormalization factor in Fig. 27(d) (Yi *et al.*, 2017). This suggests an intimate relation between the electronic and lattice degrees of freedom that impact T_c. Such relation is further reenforced by family- and doping-dependent iron isotope effects for both superconducting T_c and the SDW in some FeSC systems (R. Liu *et al.*, 2009; Shirage *et al.*, 2009; Khasanov *et al.*, 2010). From an ARPES perspective, the close relationship between band renormalization and local lattice structure and the polaronic behavior in FeTe are discussed in Sec. V.B.1. This section focuses on electron-phonon coupling effects in FeSe systems.

1. Correlation-enhanced electron-phonon interaction

Electron-phonon coupling in bulk FeSe was recently shown to far exceed that predicted by DFT, highlighting the enhancing role of electron correlations for the electron-phonon coupling (Gerber *et al.*, 2017). An ultrafast laser pulse was used to excite a coherent A_{1g} phonon in a bulklike FeSe film (see Fig. 28), enabling a precision terahertz lock-in

measurement of electronic and lattice structure oscillations. The experiment combined FEL-based time-resolved x-ray diffraction and laser-based trARPES for direct measurement of the deformation potential associated with the coherent mode. This aspect of the electron-phonon interaction was rarely discussed in earlier theoretical assessments of the phonon contribution to superconductivity.

2. Interfacial superconductivity in thin-film FeSe

Monolayer FeSe film grown epitaxially on a $SrTiO_3$ substrate is evidenced to show superconducting T_c above 50 K (Q.-Y. Wang *et al.*, 2012). Given the maximum T_c of 8 K (37 K under pressure) in bulk FeSe (Hsu *et al.*, 2008; Medvedev *et al.*, 2009) and the expectation of stronger phase fluctuations in low-dimensional thin films, this initially came as a surprise.

ARPES shows evidence of interfacial electron transfer from the substrate into the FeSe monolayer, indicated by the lack of a nematic order reconstructed Fermi surface [Fig. 29(a), left], the completely occupied Γ hole bands, and the absence of an anisotropic nematic band shift that would have broken the C_4 symmetry [Fig. 29(b), left column] (Liu *et al.*, 2012; S. He *et al.*, 2013; Tan *et al.*, 2013; X. Liu *et al.*, 2014). The absence of Γ hole pockets challenges the aforementioned interpocket pairing mechanism. Increasing the layer number to two and three readily negates the electron-doping effect, and clear consequences from compensated charge carriers and restored nematic order under twinning can be seen [Figs. 29(a) and 29(b), middle and right columns]. A superconducting gap measurement at the M point shows BCS-type gap-closing behavior, with the $2\Delta/T_c$ ratio around the intermediate coupling value of 5 [Figs. 29(c) and 29(d)] (Liu *et al.*, 2012; Lee *et al.*, 2014).

Unlike the optimally electron-doped bulk $K_{0.8}Fe_2Se_2$ ($T_c \sim 30$ K) (Y. Zhang *et al.*, 2011; Ying *et al.*, 2012) and $Li_{0.8}Fe_{0.2}(OH)FeSe$ ($T_c \sim 41$ K) (Zhao *et al.*, 2016), a cascade of "shakeoff" replica electron bands at the M point have been observed in monolayer FeSe/$SrTiO_3$. These exist in both the normal and superconducting states [Figs. 30(a) and 30(b)] (Lee *et al.*, 2014). This has been interpreted either as evidence for intrinsic coupling to the ~ 92 meV $SrTiO_3$ LO4 optical phonon (Coh, Cohen, and Louie, 2015; Li *et al.*, 2016; S. Zhang *et al.*, 2016; Lee, 2018) or due to the electron's postemission interaction with the surface Fuchs-Kliewer phonons (Li and Sawatzky, 2018; Jandke *et al.*, 2019). The energetic separation between the shakeoff and primary bands probed by ARPES is shown to be larger than the surface optical phonon energy probed by EELS (Li, Devereaux, and Lee, 2019; Song *et al.*, 2019). It is also found that a change up to a factor of 4 in the substrate charge carrier density does not change the replica band behavior (Jia *et al.*, 2021). These observations are consistent with the strong electron-phonon coupling effect in the initial states.

FeSe films grown on an orthorhombic rutile-TiO_2 substrate are shown to have similar superconducting gaps, T_c, and shakeoff bands to those grown on $SrTiO_3$ (Rebec *et al.*, 2017). This and other substrate-dependent experiments rule out the putative role of nematicity and strain-induced structural distortion in determining the superconducting T_c
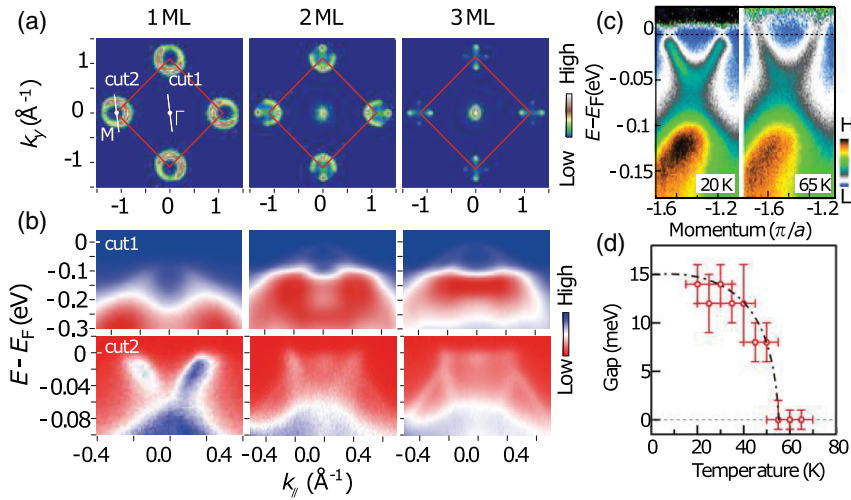
FIG. 29.   Layer and temperature dependence of the FeSe/SrTiO$_3$ thin film. (a) Fermi surface of monolayer, two-layer, and three-layer FeSe films at low temperature (left to right). (b) The corresponding energy-momentum cuts through high-symmetry points: cut 1 at M and cut 2 at M. Adapted from Tan *et al.*, 2013. (c) The M pocket at 20 K (left) and 65 K (right). (d) Temperature dependence of the superconducting gap on the M pocket. Adapted from Liu *et al.*, 2012.
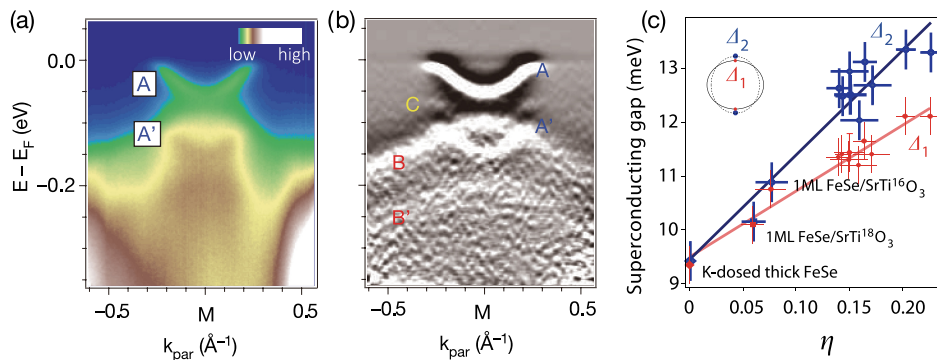
FIG. 30.   Interfacial electron-phonon coupling in FeSe monolayer film. (a) Γ-M energy-momentum cut in FeSe/SrTiO$_3$, with the main electron pocket and its shakeoff labeled A and A', respectively. (b) Second energy-derivative-enhanced plot of (a). Adapted from Lee *et al.*, 2014. (c) Superconducting gap sizes on two intercepting M pockets from one K-dosed bulk FeSe (diamonds) and seven FeSe/SrTiO$_3$ samples, containing ^{16}O (circles) and ^{18}O (squares). η is the extracted electron-phonon interaction strength. Adapted from Song *et al.*, 2019.

(Z. Huang *et al.*, 2016; Rebec *et al.*, 2017). A positive correlation between the electron-phonon coupling strength η and the superconducting gap size Δ are observed [Fig. 30(c)], lending support to an interfacial electron-phonon coupling enhanced pairing mechanism (Song *et al.*, 2019). In the meantime, proposals and evidence also exist for a cooperative relationship between 2D-enhanced electron-electron correlation and electron-phonon coupling (He *et al.*, 2014; Mandal *et al.*, 2017; Zhao *et al.*, 2018), reminiscent of similar correlation-enhanced electron-phonon coupling in bulk FeSe and cuprates.

F. Outlook

Iron-based superconductors are emerging as an archetypal platform to understand and control multiorbital correlated physics. ARPES will continue to investigate the rich physics in this Hunds-Mott model system, including superconductivity, magnetism, orbital-selective physics, and nematicity. Unification of the itinerant-local perspectives will be further pursued, with an appreciation for the key role played by the Hund's coupling. With the large number of FeSC families realized via highly systematic and versatile chemical substitution, universal single-particle properties of both the quantum critical phenomena (magnetic and/or nematic) and the correlation effects can be extracted. Interfacial engineering of superconductivity, particularly instigated by the thin-film iron chalcogenides, will also continue to grow into broader material systems based on the methodology developed and still developing in the FeSCs.

VI. LOW-DIMENSIONAL SYSTEMS

A. Overview

Low-dimensional systems have garnered increasing research interest over the past two decades, in part fueled
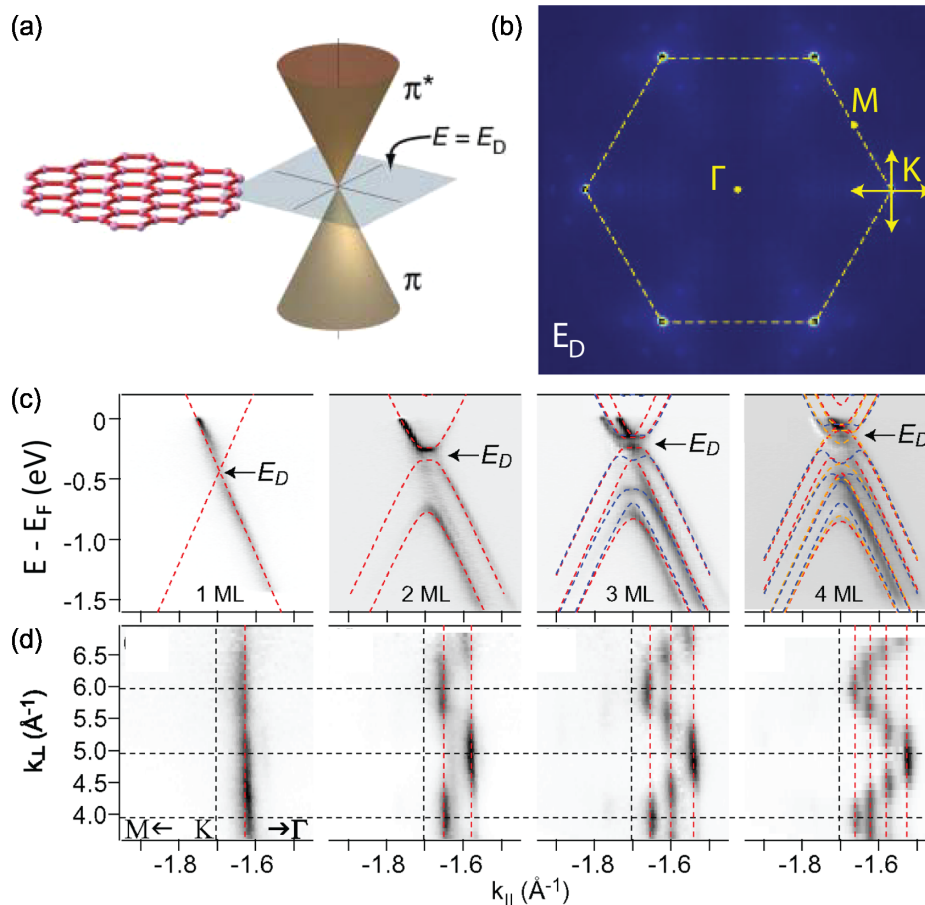
FIG. 31. Band structure of graphene. (a) Monolayer graphene and its computed Dirac cone band structure at the Brillouin zone corner. (b) Measured isoenergy contour at the Dirac point energy E_D of monolayer graphene. Adapted from Ohta *et al.*, 2006. (c) Band structure near the Dirac point and (d) $k_{||} - k_z$ Fermi surface maps for monolayer to four-layer graphene. Adapted from Ohta *et al.*, 2007.

by the discovery of graphene and its half-integer quantum Hall effect at room temperature (Novoselov *et al.*, 2004; Zhang *et al.*, 2005; Castro Neto *et al.*, 2009). Because of the spatial confinement and symmetry reduction, interactions of types and strengths that are uncommon in three dimensions become possible, giving rise to a wealth of new material properties ranging from interfacial electron gasses to the high-temperature quantum spin Hall effect (Shkolnikov *et al.*, 2002; Ohtomo and Hwang, 2004; Wu *et al.*, 2018). Operationally, device fabrication and measurements on low-dimensional systems directly benefit from mature technologies (Schaibley *et al.*, 2016; Waldrop, 2016; Rhodes *et al.*, 2019). Unparalleled chemical and physical tunability here also kick-start a new era of synthesis-oriented quantum materials research.

Because of the substantially reduced material volume relative to bulk single crystals, traditional thermodynamic (heat capacity, thermal transport) and x-ray and neutron scattering probes face challenges in the study of low-dimensional materials.[14] Meanwhile, electrical transport,

optical spectroscopy, and various microscopies remain the major tools to investigate often micron-sized, few-layer-thick samples and devices. Taking advantage of the large interaction cross section between deep UV light and matter, ARPES has emerged as a powerful technique in quasi-1D and quasi-2D material studies (Mo, 2017; Cattelan and Fox, 2018). Reciprocally, the demand to probe on the length scale of typical low-dimensional devices is also spurring the rapid development of ARPES light sources with ∼10 μm- to ∼100 nm-sized beam spots (Sec. III.B).

Here we emphasize the unique role that ARPES has played in (1) graphitic systems and their correlation effects, (2) spin-orbit coupling, charge order, and Mott-ness in transition metal dichalcogenides, (3) 2D electron gases and strong coupling effects in complex oxides and their interfaces, and (4) spin-charge separation in quasi-1D systems. *In situ* MBE-ARPES studies on FeSe and complex oxide films are covered in Secs. V.E.2 and VIII. For a detailed discussion on quantum confinement in topological systems, see Sec. VII.B.3.

B. Graphene and other single-element monolayers

Graphene is a single layer of carbon atoms arranged in a honeycomb lattice via covalent bonding. This lattice structure results in a peculiar low-energy electronic structure consisting

---

[14]For x-ray and neutron scattering on thin-film samples, proper choice of geometry on selected elements with a large scattering cross section can still yield a good signal (Need *et al.*, 2018) even down to the monolayer limit (Fang *et al.*, 2017).

mainly of carbon p_z electrons (π band), with two sets of doubly degenerate Dirac cones (valleys) alternately residing on the six Brillouin zone corners (Castro Neto *et al.*, 2009; Vafek and Vishwanath, 2014). Such low-energy electronic structure also evinces fundamental topological concepts such as the nonzero Berry's phase (Novoselov *et al.*, 2005). Unlike quantum well states in typical semiconductors, low-energy charge carriers in graphene exhibit electron-hole degeneracy, vanishing effective mass toward charge neutrality, and negligible spin-orbit coupling ($\sim 10^{-3}$ meV) and approximately follow the Dirac equation of motion (Geim and Novoselov, 2007). Therefore, in addition to its many intriguing physical properties, graphene is a solid-state platform to interrogate relativistic concepts and phenomena at the thermal energy scale (Stander, Huard, and Goldhaber-Gordon, 2009). Photoemission played a crucial role in determining its electronic structure, dimensional crossover behavior, and various electronic interaction effects.

Synchrotron-based ARPES first confirmed the existence of Dirac cone-shaped bands in single-layer and bilayer graphene using the former method [Figs. 31(a)–31(c)] (Ohta *et al.*, 2006, 2007). Similar Dirac electrons are also observed in bulk graphite (Zhou *et al.*, 2006). In particular, adding one or more layers results in energy splitting of the Dirac cone, rounding out the energy-momentum dispersion from linear to hyperbolic and giving rise to massive Dirac fermions

(Ohta *et al.*, 2006). Surface charge doping via potassium adsorption is demonstrated to continuously modify the band structure near the Dirac point, which is interpreted as a result of broken symmetry between the top and bottom graphene layers (Ohta *et al.*, 2006). Further addition of graphene layers gradually restores the Dirac band's k_z dispersion from 0 to ~ 1 eV via a discrete k_z point addition in accordance with the layer numbers [Figs. 31(c) and 31(d)] (Zhou, Gweon, and Lanzara, 2006; Ohta *et al.*, 2007).

In contrast to the early impression of graphene being a purely noninteracting system, a cascade of strong band distortions is observed in doped graphene. Along with thermal, optical, and electrical transport measurements, ARPES provides the momentum-resolved single-particle evidence for a hierarchy of quasiparticle dynamics. Figure 32(a) shows a series of dispersion anomalies around the K point at different carrier concentrations (Bostwick *et al.*, 2007). At ~ 200 meV below E_F, electron-phonon coupling as strong as $\lambda \sim 0.3$ is observed to disrupt the otherwise linear dispersion. Between 0.5 and 1.0 eV below E_F, signatures of plasmaron formation are manifested through doubling of the Dirac cones (Bostwick *et al.*, 2010). Electronic correlation effects are also revealed through interlayer coupling to different substrates [Figs. 32(b) and 32(c)]. Here the Dirac cone can be renormalized differently from what one would expect from a mode-coupling induced band renormalization (Hwang *et al.*, 2012), or even
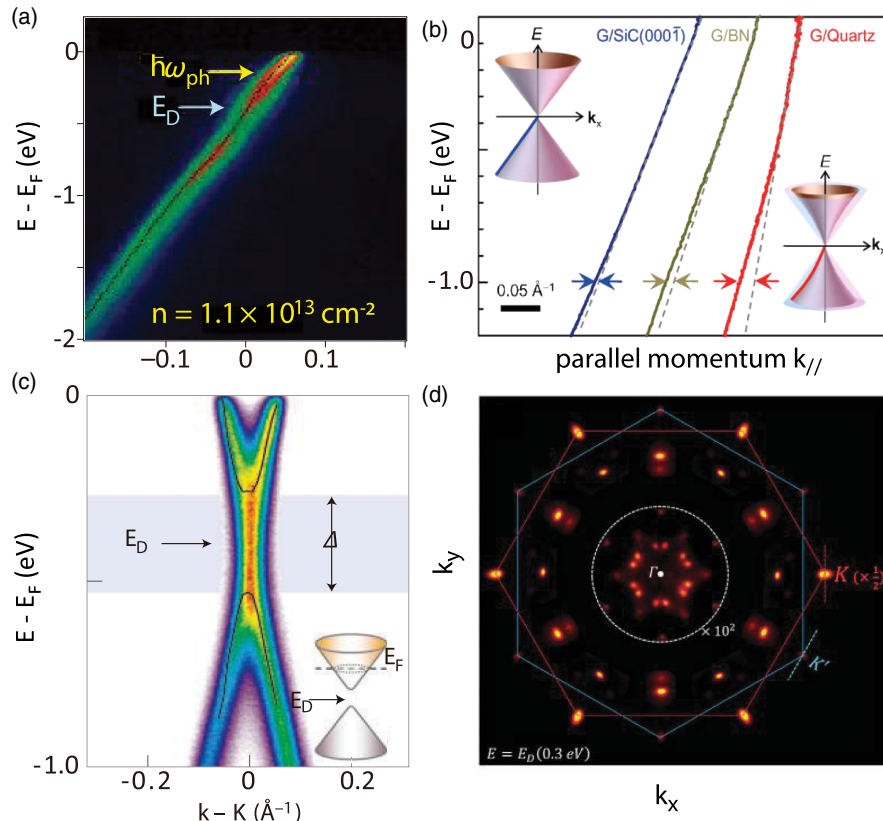
FIG. 32. Interaction effects in graphene systems. (a) Low-energy dispersion anomalies in doped graphene. Adapted from Bostwick *et al.*, 2007. (b) Substrate effect causing band renormalization in graphene. Adapted from Hwang *et al.*, 2012. (c) Substrate induced gap opening on the Dirac point for graphene-6H SiC heterostructure. Adapted from Zhou, Gweon *et al.*, 2007. (d) Removal of translational symmetry and the formation of dodecagonal Dirac electron replicas in 30° twisted bilayer graphene. Adapted from Ahn *et al.*, 2018.

gapped out (Zhou, Gweon *et al.*, 2007). Interactions in graphene have also been studied in trARPES via the photo-excited population dynamics, which can be modeled to evaluate the relative contributions of Auger scattering and impact ionization (Gierz *et al.*, 2013; Johannsen *et al.*, 2013).

Graphene-based heterostructures, especially those formed with thin-film transition metal dichalcogenides and those with an interlayer twisting angle, are also receiving more investigation with the rising interest in superlattice ("Moiré") engineering on 2D platforms. For example, the superlattice potential between *h*-BN, ruthenium, or iridium and graphene is shown to induce both low-energy and high-energy band gaps on the Dirac band (Pletikosić *et al.*, 2009; Enderlein *et al.*, 2010; Y. Liu *et al.*, 2010; E. Wang *et al.*, 2016). Twisting two graphene layers relative to each other at small angles has proven to be effective in tuning the bandwidth via interlayer band hybridization (Peng *et al.*, 2017). When the angle is exactly 30°, the rotational symmetry remains while the translational symmetry is removed, resembling a quasicrystal [Fig. 32(d)]. Anomalously strong interlayer potential is shown to scatter Brillouin zone corner Dirac electrons toward the zone center, forming replicas with dodecagonal rotational symmetry (Ahn *et al.*, 2018).

In addition to graphene, borophene (monolayer boron), all of group IV, and group V (with the exception of nitrogen) single-element monolayer systems have been synthesized, covering an extremely diverse set of physical phenomena ranging from the theoretically predicted robust quantum spin Hall insulator (Liu, Jiang, and Yao, 2011; Y. Xu *et al.*, 2013) to a tunable band gap semiconductor (Kim *et al.*, 2015). Photoemission studies in these systems have mostly focused on eV-scale band structure identification (Vogt *et al.*, 2012; Zhu, Chen *et al.*, 2015; Feng *et al.*, 2016, 2017; Mo, 2017), with the major limiting factor being sample stability and availability, especially toward the less metallic side. Molten monolayer lead on Cu(111) was used to pioneer the study of the single-particle spectral function in a liquid (Baumberger *et al.*, 2004).

C. Transition metal dichalcogenides

Many of graphene's intriguing properties come from its low-energy Dirac electrons and weak spin-orbit coupling, which makes it a near-zero-gap semiconductor. However, transistors for a logic circuit utilize "on-and-off" switching behavior, requiring a nonzero energy gap. Transition metal dichalcogenides (TMDCs) are a family of similarly layered van der Waals materials that contain semiconductors with tunable eV-scale band gaps, and sometimes substantial spin-orbit coupling. ARPES, especially when combined with *in situ* MBE or a microfocused beam spot, often provides critical electronic evidence and microscopic guidance for 2D TMDC engineering (Mo, 2017).

Following the discovery of up to a factor of 10^4 enhancement in luminescence quantum efficiency of monolayer 2*H*-MoX$_2$ (*X* = S, Se) compared to its bulk form (Mak *et al.*, 2010; Splendiani *et al.*, 2010), ARPES observed an indirect-to-direct band gap transition going from multilayer to monolayer films (Fig. 33) (Jin *et al.*, 2013;
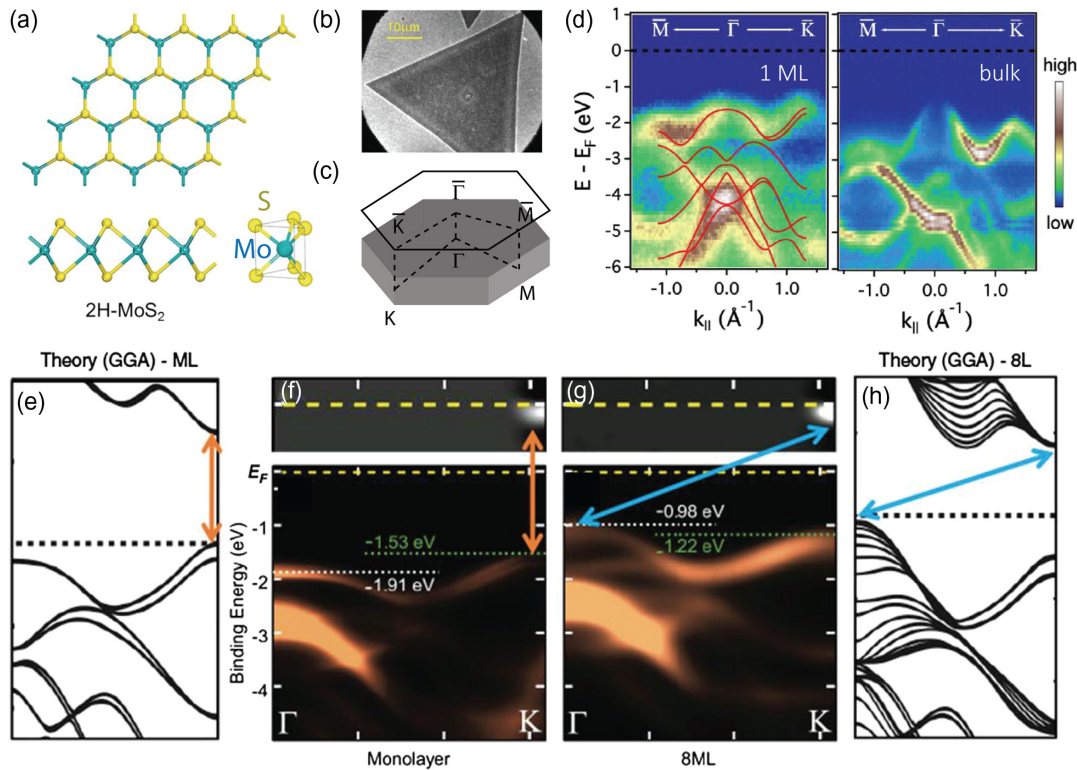
FIG. 33. Lattice and electronic structure of layer-dependent 2*H*-MoX$_2$ (*X* = S, Se). (a) Top and side views of the lattice structure. (b) PEEM image of a CVD grown flake. (c) Brillouin zone and high-symmetry points. (d) Microspot ARPES results on monolayer flake and bulk MoS$_2$. Adapted from Jin *et al.*, 2013. (e),(f) DFT calculation and experimental measurements of monolayer and (g),(h) eight-layer band structures of MoSe$_2$. Unoccupied states are achieved via surface dosing. Adapted from Y. Zhang *et al.*, 2014.
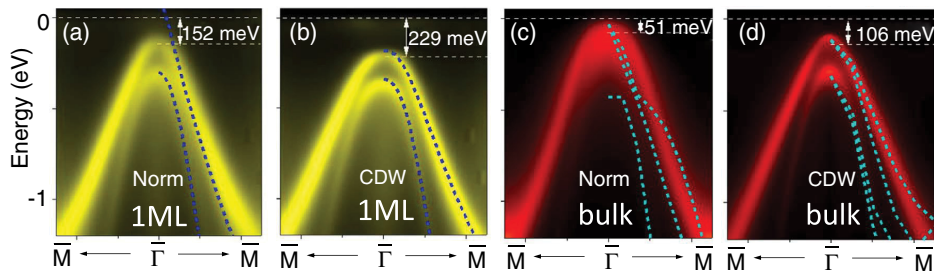
FIG. 34. Layer-dependent CDW order revealed by band folding in $1T$-TiSe$_2$. Single-particle spectra in (a),(c) the normal-state and (b),(d) the CDW state of $1T$-TiSe$_2$. (a),(b) Monolayer thin film grown *in situ* on bilayer graphene. (c),(d) Bulk material. Adapted from Chen, Chan *et al.*, 2015.

Y. Zhang *et al.*, 2014; Yuan *et al.*, 2016). In particular, this was shown to be caused by a rapid rise of the K-point valence band top. In the meantime, the lack of inversion symmetry in the monolayer (or odd number of layers) $2H$ phase implies spin splitting of the energy bands. Indeed, 140–500 meV spin-orbit splitting of the valence band is observed in monolayer $(Mo/W)(S/Se)_2$ (Alidoust *et al.*, 2014; Y. Zhang *et al.*, 2014), providing direct electronic evidence for the mechanism of valley-selective optical excitations via circularly polarized light observed via photoluminescence (Mak *et al.*, 2012; Zeng *et al.*, 2012) as well as trARPES (Bertoni *et al.*, 2016). Spin-resolved ARPES also reports evidence for spin polarization on the split valence bands in MoSe$_2$ and WSe$_2$, with a strong dependence on light polarization and geometry, as discussed in Sec. II.E (Mo *et al.*, 2016). Spin-orbit coupling also gives rise to topological phases such as the quantum spin Hall state, as discussed in Sec. VII.

Thin-film TMDCs and their associated heterostructures also strongly interact with light, hosting excitons with up to ∼30 ns radiative lifetime at room temperature (Liu *et al.*, 2015; Mak and Shan, 2016; Mohamed *et al.*, 2018). Direct determination of the exciton binding energies in monolayer MoS$_2$ and WSe$_2$ on both insulating and conductive substrates is achieved via the combination of optical reflectivity, ARPES, and angle-resolved inverse photoemission measurements (Park *et al.*, 2018). The exciton binding energy is substantially reduced due to screening on a metallic substrate. Microspot ARPES is also utilized to determine interlayer band alignments and exciton binding energies in MoSe$_2$/WSe$_2$ heterostructures (Wilson *et al.*, 2017). Time resolved ARPES has recently measured the wave function of excitons in WSe$_2$ (Man *et al.*, 2020) and revealed the spectroscopic signature of their creation and relaxation processes (Madéo *et al*, 2020).

ARPES also plays an important role in the study of superconductivity and charge order phenomena in Ti-, Zr-, V-, Nb-, and Ta-based TMDCs and their thin films. With the exception of $2H$-NbS$_2$, the superconductivity here always occurs in a CDW ordered state. In these systems, electron-phonon coupling usually imprints strongly on the ARPES spectra (Rahn *et al.*, 2012), and the reduction of layer number can modify the system symmetry (Xu *et al.*, 2018), usually leading to a lower superconducting transition temperature and a higher CDW order temperature (Xi *et al.*, 2015; Ugeda *et al.*, 2016; Duvjir *et al.*, 2018; Ryu *et al.*, 2018). At best, simple Fermi surface nesting scenarios can

explain a few instances of incommensurate CDW phases such as in VSe$_2$ (Borisenko *et al.*, 2008; Shen *et al.*, 2008; Li, Jiang *et al.*, 2018) but are not universally applicable in TMDCs (Johannes and Mazin, 2008; Zhu, Cao *et al.*, 2015; Nakata *et al.*, 2018). For instance, ARPES on $1T$-TiSe$_2$ shows band folding in the CDW state born out of a fully gapped normal state, disfavoring a nesting scenario that would require a Fermi surface to begin with (Chen, Chan *et al.*, 2015). The associated ordering temperature and energy gap are considerably larger in the monolayer limit than in the bulk (Fig. 34) (Chen, Chan *et al.*, 2015). Band folding in bulk crystals has also been studied using trARPES, where the timescale for the disappearance of band folding has been taken as evidence for an excitonic CDW mechanism (Rohwer *et al.*, 2011; Hellmann *et al.*, 2012). This appears to be supported by simultaneously softened phonon and plasmon modes at the charge ordering wave vector probed with momentum-resolved EELS (Kogar *et al.*, 2017). Meanwhile, the insulating behavior and CDW order in monolayer $1T$-NbSe$_2$ and bulk $1T$-TaS/Se$_2$ are attributed to strong electronic correlation ("Mott-ness"), where the low-energy spectra are ubiquitously gapped without any sign of coherent quasiparticles (Lahoud *et al.*, 2014; Nakata *et al.*, 2016; Chen *et al.*, 2020).

D. 2DEG in transition metal oxides

Complex transition metal oxides behave quite differently than other chalcogenides, mostly because of the exceptionally strong electron negativity of oxygen atoms. As a result, they possess highly ionic bonding (between metal and oxygen ions), much stronger charge transfer (between layers), and a greater tendency to form dangling bonds and oxygen vacancies (on the surface and interface). Each trait contributes uniquely to the peculiar properties of a 2D electron gas (2DEG) that appears on their surfaces, and to interfacial coupling on many surfaces and interfaces.

Following the seminal discovery of a high mobility 2D electron gas at the interface between two insulating perovskites, LaAlO$_3$ and SrTiO$_3$ (Ohtomo and Hwang, 2004), similar 2D conductive states were subsequently discovered and demonstrated by ARPES on SrTiO$_3$ (110), (111), and (001) surfaces [Fig. 35(b)] (Meevasana *et al.*, 2011; Santander-Syro *et al.*, 2011; King *et al.*, 2014; Rödel *et al.*, 2014; Walker *et al.*, 2014, 2015; Wang *et al.*, 2014), and on KTaO$_3$ (100) polar surfaces (King *et al.*, 2012;
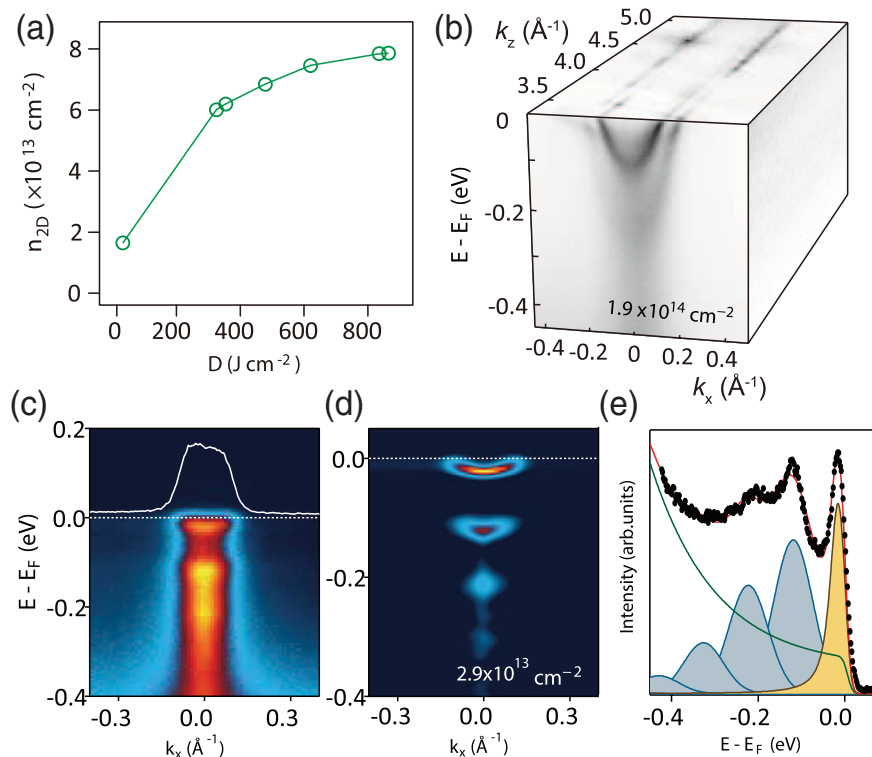
FIG. 35. Surface 2D electron gas in $SrTiO_3$. (a) 2DEG carrier density vs UV irradiation dosage on the $SrTiO_3$ (001) surface. Adapted from Meevasana *et al.*, 2011. (b) Electronic structure of the 2DEG on the $SrTiO_3$ (001) surface. Note the high in-plane dispersion and the lack of k_z dispersion. (c) Strong polaronic shakeoff on the 2DEG surface state at low carrier concentrations. (d) Maximum curvature plot of (c) to highlight the shakeoff bands. (e) EDC fitting of the shakeoff band consisting of multiple phonon sidebands. Adapted from Z. Wang *et al.*, 2016.

Bruno *et al.*, 2019).[15] The initial photoemission evidence was from the $SrTiO_3$ (001) surface via either bulk crystal cleaving (Santander-Syro *et al.*, 2011) or progressive UV irradiation [Fig. 35(a)] (Meevasana *et al.*, 2011). When one combines surface atomic oxygen treatment with photoemission from oxygen vacancy states, it is revealed that the surface 2DEG comes from UV-induced oxygen vacancies (Walker *et al.*, 2014, 2015) and is mostly of Ti-$3d_{xy}$ character (Plumb *et al.*, 2014). The surface states also show quantum confinement effects due to surface band bending, with renormalization effects on the d_{xz} and d_{yz} bands (Meevasana *et al.*, 2011; Santander-Syro *et al.*, 2011; King *et al.*, 2014). In the wake of surface-enhanced superconductivity on monolayer–FeSe/$SrTiO_3$ heterostructures (Lee *et al.*, 2014), strong electron-phonon coupling–induced polaronic shakeoff spectra were retrospectively noticed on the $SrTiO_3$ surface state at low carrier concentrations [Figs. 35(c)–35(e)] (Chen, Avila *et al.*, 2015; Z. Wang *et al.*, 2016). Such strong coupling is interpreted as a consequence of an exceptionally large Born effective charge associated with the Ti—O bond stretching from the LO4 optical phonon vibration (Lee *et al.*, 2014).

In an effort to overcome the surface sensitivity and lack of access to buried interfaces, soft-x-ray ARPES at Ti L_3 and L_2 edges (~460 eV) is employed to penetrate through an 18-Å-thick $LaAlO_3$ overlayer and probe the interfacial 2DEG on a $LaAlO_3$/$SrTiO_3$ heterostructure (Cancellieri *et al.*, 2016). With a 40 meV energy resolution, both the surface states and their polaronic shakeoff can be identified. When the soft-x-ray photon energy is tuned to match the depth profile of the heterostructure so as to form a standing wave, layer selectivity may be achieved at the antinode of the photon field (Gray *et al.*, 2010, 2013).

We note that 2D surface states also frequently exist on semiconductor and metal surfaces (LaShell, McDougall, and Jensen, 1996; Bianchi *et al.*, 2010; Tamai *et al.*, 2013; Jovic *et al.*, 2017). Because of the inherent broken inversion symmetry on the surface, large spin splitting may be observed if spin-orbit coupling is also strong (LaShell, McDougall, and Jensen, 1996; Tamai *et al.*, 2013).

E. Quasi-1D systems

Further dimensional confinement leads to quasi-1D materials with even greater electronic instability and a breakdown of the Landau quasiparticle description. Experimentally, these systems either are bona fide nanowires or are effectively 1D because of highly anisotropic valence electronic interactions. The former category requires a carefully self-assembled or

---

[15]Metallic states can also be created on the anatase TiO_2 (001) surface. But this state shows strong k_z dispersion, implying a 3D nature (Moser *et al.*, 2013).
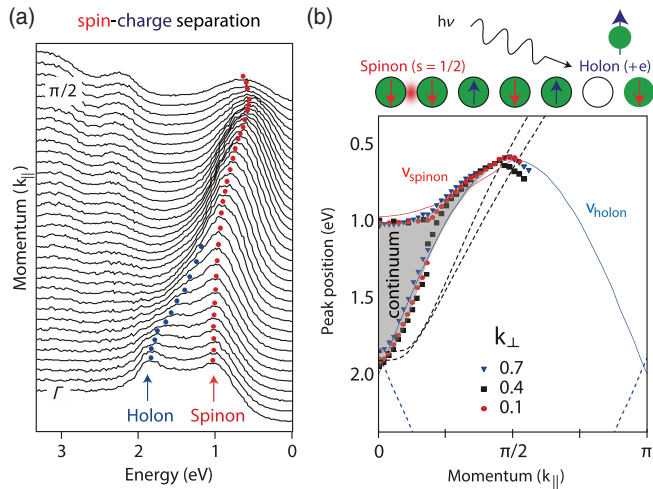
FIG. 36. Evidence for spin-charge separation in the 1D chain compound $SrCuO_2$. (a) Raw energy distribution curves for the bifurcated single-particle excitation consisting of spinon (red) and holon (blue) branches. (b) Fitted dispersions collapsed from different perpendicular momenta. The dashed lines are band theory calculations, while the red and blue solid lines are analytical fits to the spinon and holon dispersions. Adapted from Kim *et al.*, 2006.

self-aligned nanowire array (Ahn *et al.*, 2004; Schäfer *et al.*, 2008) or, otherwise, nanospot ARPES at synchrotron facilities (Arango *et al.*, 2016) (see also Sec. III.B). The latter are bulk crystals including Luttinger liquid candidate purple bronze $Li_{0.9}Mo_6O_{17}$ (Wang *et al.*, 2006, 2009; Dudy *et al.*, 2013),[16] copper spin chain compounds $LiCu_2O_2$ (Papagno *et al.*, 2006), $SrCuO_2$ (Kim *et al.*, 1996, 2006; Suga *et al.*, 2004), organic chain compounds $[Ni(chxn)_2Br]Br_2$ (Fujimori *et al.*, 2002), and doped vanadium oxides β-$Na_{1/3}V_2O_5$ (Okazaki *et al.*, 2004) and V_6O_{13} (Suga *et al.*, 2004).

One main feature of a 1D Luttinger liquid is the fractionalized excitation of a photohole into its charge (holon) and spin (spinon) parts: a phenomenon known as spin-charge separation [Fig. 36(a)] (Nozieres and Pines, 1999; Giamarchi, 2003). In particular, photoemission on $SrCuO_2$ does show evidence for two separate branches of excitation on the single-particle spectrum along the chain direction, bounding a region of excitation continuum in between (Kim *et al.*, 2006). Both branches are nondispersive perpendicular to the chain direction [Fig. 36(b)], reaffirming the 1D nature of the electronic structure. The dispersions of the two branches are governed by the charge hopping t (holon), and the spin exchange J (spinon). The fitted value of $J = 0.27$ eV agrees with respective optical and inelastic neutron scattering results (Kim *et al.*, 2006).

---

[16]A close cousin in the molybdenum purple bronze family is $K/Na_{0.9}Mo_6O_{17}$, which has higher symmetry (C_3 rotation) by forming three equivalent chain directions in plane (Foury and Pouget, 1993). This difference causes the system to have a bulk charge order at 115 K, and a separate quasi-2D surface charge order at 220 K (Mou *et al.*, 2016).

F. Outlook

Low-dimensional materials have produced one of the most prosperous quantum material research scenes in the past decade, with probes tried and tested in graphene research rapidly spilling over to new material systems such as TMDCs and oxide films and interfaces. New device technology has enabled new platforms, such as Moiré systems and free-standing oxide films, that will likely continue to spur new diversification in ARPES sample environments and light sources, such as higher level integration of micro-ARPES and *in situ* device manufacturing with electrical characterizations. Low-dimensional systems are expected to help shed light on traditionally hard correlation physics problems thanks to their excellent optical, mechanical, electrical, and magnetic tunability. With this ease of optimization, they will expand investigations in dimensionality-specific topics such as those in quantum confinement, exotic topological states of matter, and enhanced or stabilized order compared to 3D counterparts.

VII. TOPOLOGICAL MATERIALS

A. Overview

One of the cornerstones of condensed matter physics is the classification of matter into distinct phases, which is conventionally done by considering spontaneously broken symmetries. In the 1980s a new paradigm emerged in which matter began to be classified according to the notion of topological invariants (Thouless *et al.*, 1982; Wen, 1995). In mathematics, a topological invariant is a property that is maintained through smooth deformations of an object. Analogously, topological properties of a material are insensitive to smooth deformations of the system's Hamiltonian. (Here "smooth" refers to an adiabatic perturbation that does not close an energy gap.) Thus, identifying the topological invariants of a material gives robust predictive power for its physical properties.

Some of the most illustrative examples include the quantum Hall insulator, the quantum spin Hall insulator (QSHI), and the quantum anomalous Hall insulator, all of which have been regarded as milestones in promoting our understanding of the topological classification of matter (Haldane, 2017). In these systems, the transport properties around the sample edge are quantized up to 1 ppb (von Klitzing, 2005). This exact quantization, independent of material details, is a reflection of the fact that the transport is a topologically invariant property. This also exemplifies a general principle known as "bulk-boundary correspondence," which guarantees the existence of gapless conducting states at the interface where a topological invariant changes (Hasan and Kane, 2010).

A complete discussion on the topological classification of matter is beyond the scope of this review and is discussed in detail elsewhere (Hasan and Kane, 2010; Qi and Zhang, 2011; Haldane, 2017). We instead give a brief conceptual overview, then focus on developments in which ARPES played a pivotal role in discovering or understanding topological phases by identifying nontrivial topological electronic structures (Zhang *et al.*, 2020). As we later see, the power of ARPES lies in its

capability to measure electronic states both in the bulk and at the boundary. In the bulk, ARPES can directly resolve the energetic sequence of bands and whether they exhibit inversion; on the boundary, ARPES can directly resolve electronic states localized at the interface. The influence of spin-orbit coupling is revealed through spin-resolved ARPES measurements, while the role of time reversal (and other symmetries) is explored by material synthesis and modification via doping or substitution.

B. Topological insulators

1. 3D strong TIs

The 3D strong topological insulator (TI) can be understood as a three-dimensional analog to the previously described QSHI (Fu, Kane, and Mele, 2007; Moore and Balents, 2007; Qi, Hughes, and Zhang, 2008). Conceptually, one begins by considering a trivial insulator with bulk valence and conduction bands of opposite parity separated by an energy gap. In a 3D TI, the spin-orbit interaction causes the bands to become inverted; see Fig. 37. If this inversion occurs at an odd number of points in the Brillouin zone, the material becomes topological (characterized by the so-called $\mathbb{Z}_2$ invariant) and classified as a strong TI. Owing to the bulk-boundary correspondence, a strong TI exhibits gapless surface states that are robust against any perturbation that maintains time-reversal symmetry. As a consequence, both the 2D surface states of a 3D TI and the 1D edge states of a 2D QSHI are said to be protected by time-reversal symmetry. The distinctive signatures of a 3D TI are encoded in quantized magnetoelectric responses (Qi, Hughes, and Zhang, 2008; Essin, Moore,
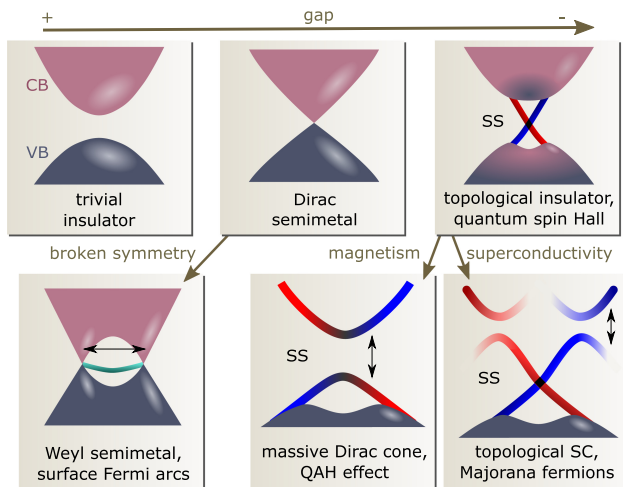
FIG. 37. A simplified view of the band structure evolution in topological states of matter studied by ARPES. A trivial insulator has a finite band gap between a conduction band (CB) and a valence band (VB). Closure of the gap can produce a Dirac semimetal with linear dispersion. Continued evolution of the gap results in band inversion, which can produce a topological insulator with surface states (SSs) bridging the gap. The Dirac semimetal becomes a Weyl semimetal if either time-reversal or spatial-inversion symmetries are broken, whereas the topological insulator exhibits exotic phenomena when coupled with superconductivity and magnetism.

and Vanderbilt, 2009) detectable in a high-precision optical measurement (Wu *et al.*, 2016). Unlike for the 2D QSHI, the transport signature of 3D TIs is subtle (Hasan and Kane, 2010), making ARPES an important tool for identifying 3D TI materials.

Following a theoretical prediction (Fu and Kane, 2007), the first experimentally observed 3D TI was the $Bi_{1-x}Sb_x$ alloy (Hsieh *et al.*, 2008). Both Bi and Sb are semimetals with negative indirect gaps, but finite direct gaps throughout their entire Brillouin zones. In Sb, the valence and conduction bands are inverted at the three equivalent L points, but the absence of a global band gap precludes it from being classified as a TI [Figs. 38(a) and 38(c)]. However, there is a small range ($0.07 < x < 0.22$) in which the alloy is a direct band gap semiconductor at the L points and still retains the band inversion of Sb, as shown in Fig. 38(b). ARPES experiments identified surface states, as verified by their lack of k_z dispersion (Hsieh *et al.*, 2008). Confirmation of their topological origin was based on two criteria: (1) the bands cross E_F an odd number of times between the two time-reversal invariant momenta $\bar{\Gamma}$ and $\bar{M}$ [Fig. 38(e)], and (2) the bands are spin polarized and thus nondegenerate, as confirmed by spin-resolved ARPES (Hsieh *et al.*, 2009b). These observations, summarized in Fig. 38(d), together indicate that the surface bands cannot be eliminated by any perturbation that maintains time-reversal symmetry.

The next 3D TIs to be theoretically predicted and experimentally discovered were Bi_2Se_3 and Bi_2Te_3 (Y. J. Chen *et al.*, 2009; Xia *et al.*, 2009; Zhang *et al.*, 2009). The advantages of these materials over $Bi_{1-x}Sb_x$ are that they are free of alloying disorder and exhibit an exceptionally clean electronic structure with a single Dirac cone surface state. As shown in Figs. 39(a) and 39(b) for Bi_2Se_3 and Bi_2Te_3, respectively, the bulk bands are semiconducting with a gap >200 meV, while the surface states bridge the gap near the Γ point [Fig. 39(d)] and do not disperse with k_z (Y. J. Chen *et al.*, 2009; Xia *et al.*, 2009). As shown in Fig. 39(c), the Fermi surface of Bi_2Te_3 consists of a hexagonally warped pocket from the surface state and a bulk pocket from the conduction band that can be tuned away from E_F by doping (Y. J. Chen *et al.*, 2009). Spin-resolved ARPES measurements confirmed that the surface state of these materials has the requisite helical spin texture, with spins oriented predominantly in plane and tangential to the Fermi surface (Hsieh *et al.*, 2009a). Bi_2Se_3 and Bi_2Te_3 have been the key material platforms to much of the recent work on topological materials, including the discovery of the quantum anomalous Hall effect in $Cr_{0.15}(Bi_{0.1}Sb_{0.9})_{1.85}Te_3$ (C.-Z. Chang *et al.*, 2013) and therefore appear prominently in this review despite the abundance of newer materials.

2. Topological protection and spin polarization

While it is difficult to establish unambiguous proof, ARPES does provide compelling evidence for the unusual robustness of the topological surface state. Trivial surface states are often found to be exquisitely sensitive to disorder and surface adsorbates (Damascelli *et al.*, 2000; Yang *et al.*, 2005; Noh *et al.*, 2009). In contrast, the surface states of Bi_2Se_3 have been observed in ARPES even after exposure to the atmosphere
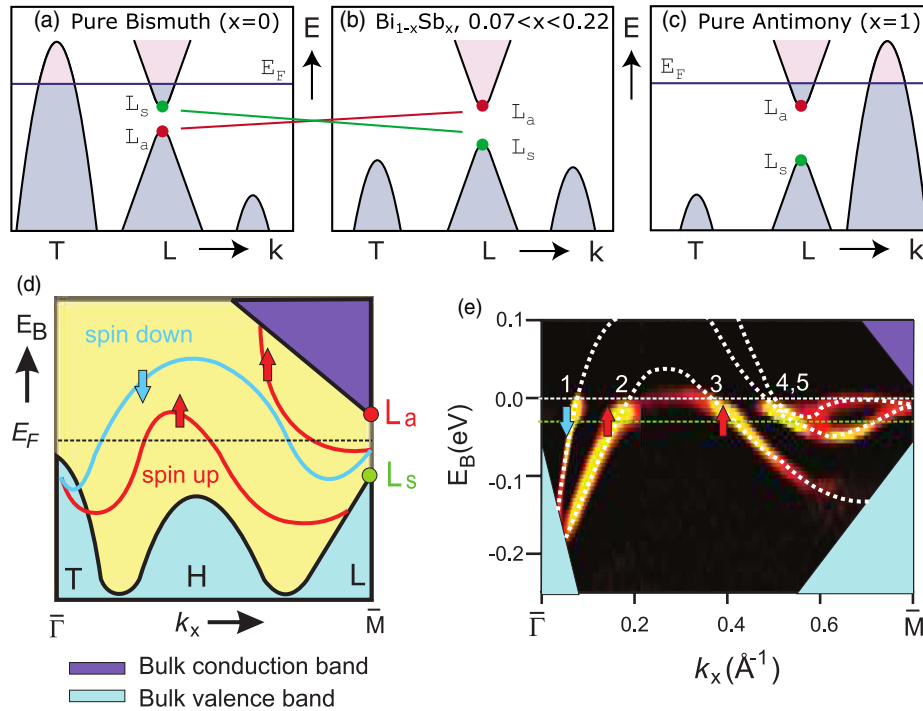
FIG. 38. $Bi_{1-x}Sb_x$ as the first 3D topological insulator. (a)–(c) Electronic structure for pure Bi, the alloy, and pure Sb, respectively. The band arrangement in pure Bi is trivial, while the bands at the L point of pure Sb are inverted. Within a critical doping range, the alloy becomes a direct band gap semiconductor while retaining the topologically nontrivial band inversion. Adapted from Hasan and Kane, 2010. (d) Sketch and (e) ARPES measurement of the surface state dispersion of $Bi_{0.91}Sb_{0.09}$ showing five Fermi-level crossings. The arrows denote the spin polarization of the bands, as verified by spin-resolved ARPES measurements. Adapted from Hsieh et al., 2009b.

(Benia et al., 2011; Chen et al., 2012). More aggressive disorder, such as the removal of atoms by sputtering, causes the surface state to migrate toward the deeper unperturbed layers (Queiroz et al., 2016). While these results are interesting, we caution that these demonstrations of robustness cannot be taken as definitive proof of the topological nature of the bands.

The robustness of the topological surface state is only one aspect of a notion known as "topological protection." Another consequence is the fact that nonmagnetic backscattering from momenta $\mathbf{k}$ to $-\mathbf{k}$ on the surface state is suppressed due to the fact that these states have opposing spin orientations (Roushan et al., 2009). However, scattering to any state other than the one at exactly $-\mathbf{k}$ is still permitted. Via self-energy analysis, ARPES has detected signatures of interband scattering with bulk states (Park et al., 2010) as well as intraband electron-phonon scattering, with reported coupling strengths ranging from $\lambda = 0.076$ up to $\lambda \sim 3$ (Hatch et al., 2011; Pan et al., 2012; Chen et al., 2013; Kondo et al., 2013), with the disparate results likely attributed to differing experimental resolution and sensitivities. Interband and intraband scattering processes have also been documented in the time domain using trARPES (Sobota et al., 2012; Y. H. Wang et al., 2012).

Another important consideration for the scattering properties of the surface state is its deviation from the ideal helical spin texture shown in Fig. 40(a). The dispersion of the surface states of Bi_2Te_3 is hexagonally warped at energies away from the Dirac point [see Fig. 39(c)], which opens scattering channels associated with out-of-plane components of the spin polarization (Fu, 2009; Alpichshev et al., 2010).

The out-of-plane spin was directly measured by spin-resolved ARPES in Bi_2Te_3 (Souma et al., 2011) and subsequently deduced by circular-dichroism ARPES in Bi_2Se_3 (see Sec. II.D for a discussion of the relationship between spin
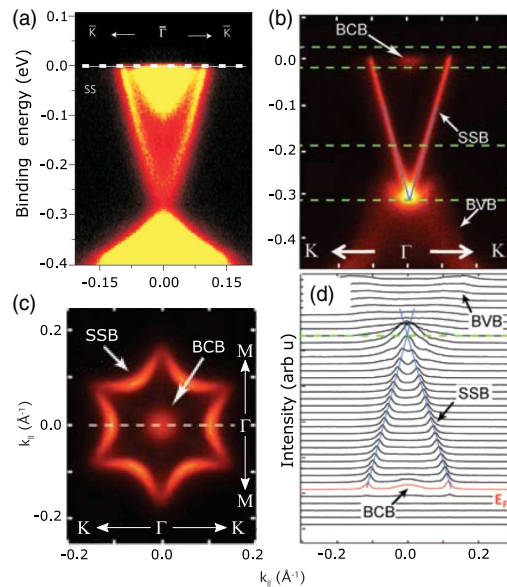
FIG. 39. ARPES measurements of the 3D topological insulators (a) Bi_2Se_3 and (b)–(d) Bi_2Te_3. (a) Adapted from Xia et al., 2009. The topological surface state is observed linearly dispersing across the bulk band gap. (c) Fermi surface of Bi_2Te_3 showing the anisotropic dispersion of the surface state. (d) MDCs of the cut shown in (b). Adapted from Y. J. Chen et al., 2009.
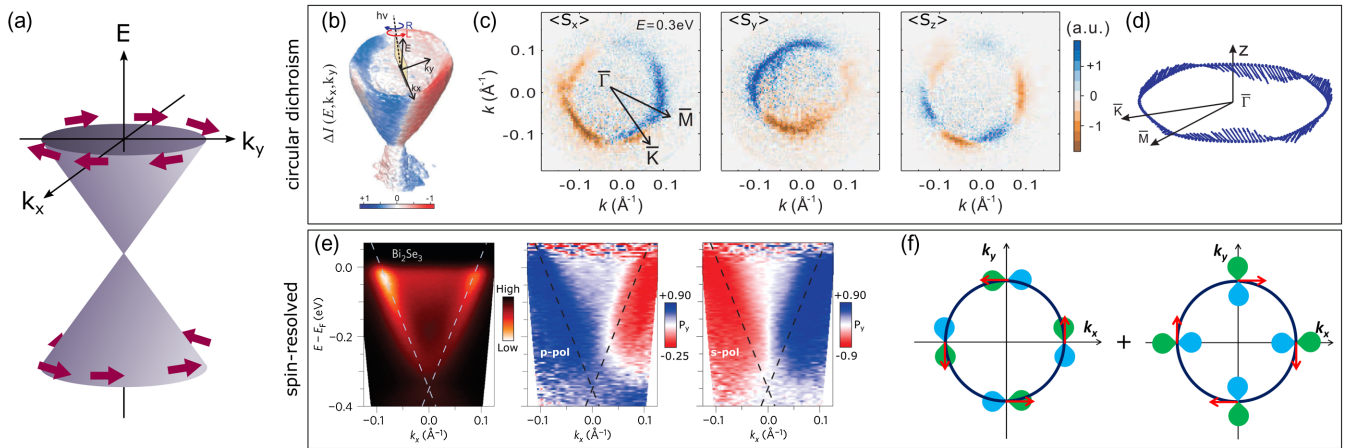
FIG. 40. Deviations from an ideal helical spin texture in 3D TIs. The ideal texture, shown in (a), consists of 100% polarized in-plane spins tangentially oriented along an isotropic Dirac cone. Top row: circular-dichroism ARPES on Bi_2Se_3. (b) Difference in photoemission intensity between left-hand and right-hand circularly polarized light. (c) By modeling matrix elements in a spin-orbit coupled system, all three components of the spin polarization can be calculated from the data. (d) Summary of the deduced spin polarization, including an out-of-plane component associated with hexagonal warping. Adapted from Wang, Hsieh et al., 2011. Bottom row: Spin-orbital texture of Bi_2Se_3. (e) Spin polarization measured by spin-resolved ARPES reverses sign when the light polarization is rotated. Adapted from Jozwiak et al., 2013. (f) This is because the eigenstates are linear combinations of spin (arrows) and orbital (blue and green shapes) components. The experiment measures the spin polarization associated with the orbital component photoemitted by the incident light polarization. Adapted from Zhang, Liu, and Zhang, 2013.

polarization and circular dichroism) (Wang, Hsieh et al., 2011), as shown in the top row of Fig. 40.

An additional deviation from the ideal helical texture is its partial spin polarization (<100%) due to the substantial spin-orbit coupling in these materials (Yazyev, Moore, and Louie, 2010). Early spin-resolved ARPES measurements reported polarizations ranging from 25% (Souma et al., 2011) to 75% (Pan et al., 2011), although subsequent theory work showed that the photoelectron spin polarization is not equivalent to that of the initial state (Park and Louie, 2012). In fact, later experiments showed that the measured spin polarization could be reversed or even rotated out of plane by controlling the excitation photon polarization (Jozwiak et al., 2013; Sánchez-Barriga et al., 2014; Xie et al., 2014; Zhu et al., 2014), as shown in Fig. 40(e). This is explained by the effect of spin-orbit coupling: since spin is not a good quantum number, the eigenstates are linear combinations of spin and orbital components, as shown in Fig. 40(f) (Cao et al., 2013; Zhang, Liu, and Zhang, 2013). These experiments highlight the inherent complexity of a spin-resolved ARPES measurement, as expounded upon in Sec. II.E; here the measurement is sensitive only to the spin polarization of the photoemitted orbital component, which is controlled by light polarization due to matrix elements. Hence, caution is required to deduce the topological nature of a state from its measured spin polarization.

3. Quantum confinement

The short mean free path for photoelectrons allows ARPES to probe phenomena that occur exclusively at the surface. For example, the chemical potential probed by ARPES deviates from that measured in bulk-sensitive transport measurements due to a band-bending potential near the surface, as determined from a comparison to quantum oscillations

(Analytis et al., 2010). This potential continues to evolve after cleaving due to residual adsorbates in the UHV environment (Bianchi et al., 2010) and can be accelerated due to a deposition of impurities (King et al., 2011b; Wray et al., 2011). In both cases, sufficient band bending leads to quantum confinement of the bulk wave function near the sample surface, which manifests as a 2DEG degenerate with the bulk bands (Chiang, 2000). As shown in Fig. 41, the 2DEGs form a series of quantum well states that are spatially localized in the band-bending potential well. Moreover, due to the strong spin-orbit coupling in the system, the 2DEGs exhibit Rashba splitting with a predominantly in-plane spin texture, as verified by spin-resolved ARPES measurements (King et al., 2011b). This splitting is significantly larger than that observed in semiconductor heterostructure 2DEGs and Au(111) surface
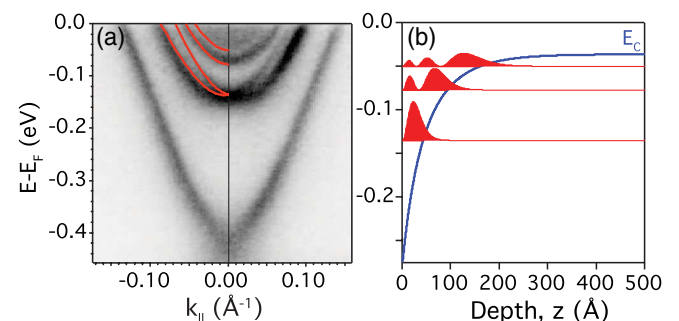
FIG. 41. (a) Series of three 2DEG states on a Bi_2Se_3 surface contaminated with adsorbates. The lowest subband exhibits Rashba splitting due to strong spin-orbit coupling. (b) Model for the formation of 2DEGs. The conduction band energy E_c is subject to a band-bending potential near the surface, leading to quantum confinement of the bulk wave function. Adapted from King et al., 2011b.
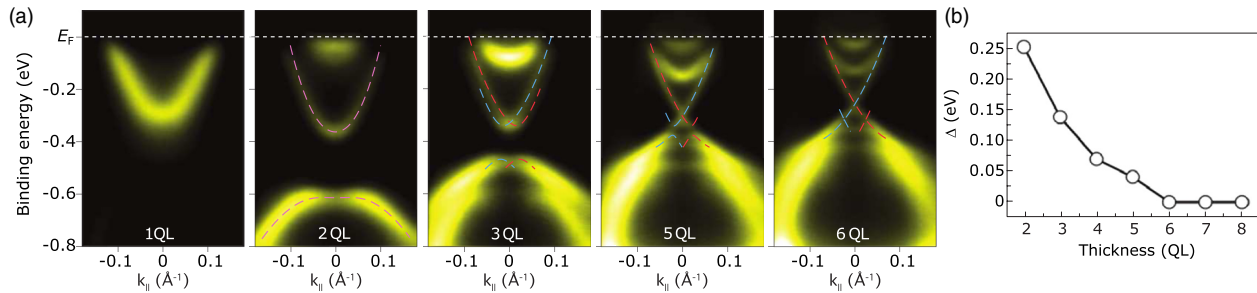
FIG. 42. (a) ARPES spectra of Bi_2Se_3 thin films synthesized to the thickness shown (QL, quintuple layer). There is no Dirac cone observed for sufficiently thin samples. (b) Gap at the Dirac point extracted as a function of film thickness. The gapless topological surface state recovers for thicknesses of more than six QLs. Adapted from Zhang et al., 2010.

states (King et al., 2011b), and comparable to the giant Rashba-type splitting observed for bulk bands in noncentrosymmetric semiconductors (Ishizaka et al., 2011). In addition to their potential application to spintronics, these 2DEGs need to be considered when interpreting transport measurements in TIs since they can contribute 2D conduction channels in addition to the topological surface state (Bansal et al., 2012).

Quantum confinement can also be induced by exfoliation or by fabricating thin-film samples via layer-by-layer growth using molecular beam epitaxy. It was theoretically predicted that, for a sufficiently thin film, a 3D TI will transition to a 2D QSHI in an oscillatory fashion as a function of the film thickness (C.-X. Liu et al., 2010; Lu et al., 2010). This is because the surface state wave functions on opposite sides of the sample begin to overlap and hybridize, opening up a gap at the Dirac point. ARPES measurements on Bi_2Se_3 have displayed this gapped Dirac point for film thicknesses with fewer than six quintuple layers (QLs), as shown in Fig. 42, while at the same time the bulk band structure is quantized into a series of quantum well states due to the spatial confinement (Sakamoto et al., 2010; Zhang et al., 2010). The oscillatory behavior was not observed, possibly because the oscillations dominantly manifest in the sign rather than the magnitude of the gap (C.-X. Liu et al., 2010).

4. Magnetic topological insulators

A 3D TI subject to broken time-reversal symmetry is associated with nontrivial magnetoelectric effects such as image magnetic monopoles and topological Kerr and Faraday rotations (Qi, Hughes, and Zhang, 2008; Essin, Moore, and Vanderbilt, 2009; Wu et al., 2016). When reduced to the 2D limit, magnetic TIs become a platform for studying the quantum anomalous Hall effect (Yu et al., 2010), as was experimentally demonstrated in thin films of Cr-doped $(Bi, Sb)_2Te_3$ (C.-Z. Chang et al., 2013) and $MnBi_2Te_4$ (Deng et al., 2020).

In ARPES, a signature of broken time-reversal symmetry in a 3D TI is the opening of a gap at the Dirac point, as shown in the bottom row of Fig. 37 (Q. Liu et al., 2009). Experimentally this has been investigated by both bulk doping (Chen et al., 2010) and surface doping (Wray et al., 2011) of magnetic impurities. As shown in Fig. 43, a spectral weight suppression is observed at the Dirac point of Bi_2Se_3 when Fe dopants are introduced to the bulk, even in the absence of bulk

ferromagnetic order (Chen et al., 2010). Subsequent work on Mn-doped Bi_2Se_3 thin films revealed a gap derived from out-of-plane ferromagnetic order, as demonstrated by closure of the gap above the Curie temperature. Further evidence for the magnetic nature of the gap was provided by spin-resolved ARPES, which revealed an out-of-plane component of the spin polarization at the Γ point. No out-of-plane spin component was observed for systems doped with nonmagnetic impurities (S.-Y. Xu et al., 2012b).

Despite these positive observations, there remain a number of important uncertainties on how Dirac cones are gapped in the presence of magnetism, and even in how gapped Dirac cones should be interpreted in general. First, in certain circumstances it has been demonstrated that Dirac point gapping may be completely unrelated to the existence of magnetism (Bianchi et al., 2011; Sánchez-Barriga et al., 2016). At the same time it remains unclear under which conditions magnetism is sufficient to open a gap since other groups have reported that surface deposition of magnetic impurities does not open a gap (Scholz et al., 2012; Valla et al., 2012; Schlenk et al., 2013). A recent development that promises to shed light on this issue was the prediction of $MnBi_2Te_4$ as an antiferromagnetic TI (J. Li et al., 2019; Otrokov et al., 2019; D. Zhang et al., 2019), with the first published ARPES results reporting a gap of ~100 meV (Lee et al., 2019; Vidal et al., 2019; Zeugner et al., 2019). However, a series of works contradicted this claim with
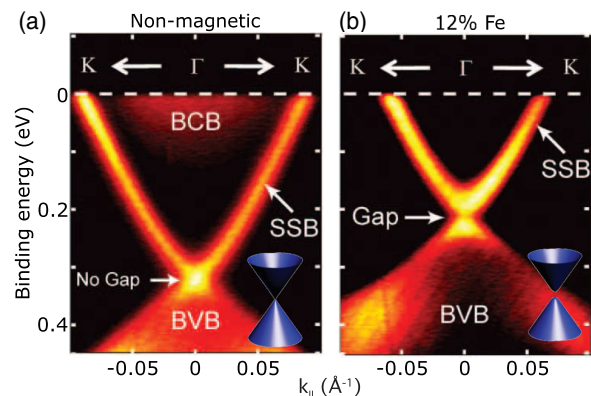
FIG. 43. Magnetically doped topological insulator. (a) Ungapped Dirac cone of Bi_2Se_3. (b) Gapped Dirac cone of Fe-doped Bi_2Se_3. Adapted from Chen et al., 2010.

reports of a gapless surface state (B. Chen et al., 2019; Y. J. Chen et al., 2019; Hao et al., 2019; H. Li et al., 2019; Swatek et al., 2020). It seems likely that these discrepant results are attributed to an $h\nu$-dependent photoemission cross section for the surface states (B. Chen et al., 2019; Hao et al., 2019). If it indeed proves to be the case that the surface state is gapless, it may imply that the antiferromagnetic order is modified, that multiple types of magnetic orders coexist, or that the magnetism is disordered near the surface (Hao et al., 2019).

5. Topological phase transitions

A topological phase transition can be driven by continuously tuning a material parameter through a range that results in band inversion. Unlike a conventional phase transition, this process does not involve a broken symmetry; instead, the phase transition is characterized by a change in the topological invariant. A classic example of a topological phase transition is the crossing of a Landau level in a 2DEG under a changing magnetic field, as in the quantum Hall effect (Hasan and Kane, 2010). In the context of 3D TIs, the most widely studied system by ARPES is $TlBi(S_{1-x}Se_x)_2$, with the chemical substitution x varied to tune both the spin-orbit interaction strength and the lattice parameter. For $x = 0$ the material is a trivial semiconductor, while for $x = 1$ it is a 3D TI. As shown in Fig. 44, at the intermediate value $x \sim 0.6$ the band gap closes and inverts, and a spin-polarized topological surface state emerges (Xu et al., 2011). Multiple groups have reported that despite the band inversion the surface state remains gapped up to $x \sim 1$, an observation that is difficult to reconcile with its topological classification. Potential explanations given by these groups include the roles of spontaneously broken symmetry (Sato et al., 2011), surface termination (Niu et al., 2012), bulk-surface scattering (Souma et al., 2012), or surface disorder (Pielmeier et al., 2015), although comprehensive understanding is still lacking. Another open issue is whether the surface states appear discontinuously with x or evolve smoothly through the phase transition. ARPES measurements near the topological critical point suggest the latter possibility,

as a gapped, spin-polarized surface state begins to develop spectral weight even on the trivial side of the phase transition (S.-Y. Xu et al., 2015e). In Bi_2Se_3, a signature of this trivial surface state remains a spin-polarized surface-localized state degenerate with the bulk bands deep into the topological phase (Jozwiak et al., 2016).

Another platform for studying topological phase transitions is provided by the $Pb_{1-x}Sn_xY$ ($Y = $ Se, Te) class of topological crystalline insulators (TCIs). TCIs represent a distinct topological phase from TIs because they are protected by the point-group symmetry of the crystal structure, in contrast to time reversal as in the case of TIs (Fu, 2011). SnTe was predicted to be a TCI protected by mirror symmetry, endowing the high-symmetry surfaces with an even number of Dirac cones, in contrast to the odd number required for $\mathbb{Z}_2$ TIs. PbTe and PbSe were predicted to be topologically trivial but susceptible to band inversion by application of pressure, strain, or alloying (Hsieh et al., 2012). Indeed, as shown in Fig. 45, $Pb_{1-x}Sn_xSe$ ($x = 0.23$) undergoes a topological phase transition due to a temperature-dependent inversion of the bulk bands (Dziawa et al., 2012). Unlike the earlier example of $TlBi(S_{1-x}Se_x)_2$, here the bulk bands are resolved on both sides of the transition. ARPES has also verified TCI phases in SnTe (Tanaka et al., 2012) and $Pb_{1-x}Sn_xTe$ (S.-Y. Xu et al., 2012a).

6. The quantum spin Hall effect revisited

Some of the first 2D topological systems studied included QSHIs such as HgTe quantum wells at millikelvin temperatures (Konig et al., 2007). Recently there has been a renewed search for QSHIs that are not dependent on a heterostructured design and that exhibit a larger band gap suitable for application at higher temperature. Such a model system could help reconcile some of the experimentally puzzling aspects that remain for the HgTe quantum wells (Ma et al., 2015; Nichele et al., 2016). One notable development was the prediction of the quantum spin Hall effect in monolayer transition metal dichalcogenides (Qian et al., 2014). ARPES
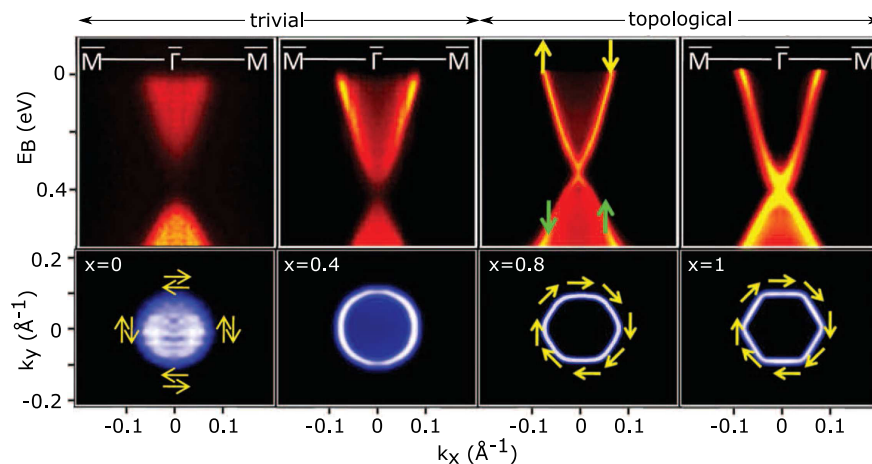
FIG. 44. Topological phase transition driven by chemical substitution in $TlBi(S_{1-x}Se_x)_2$. The top row shows cuts through $k_y = 0$, and the bottom row shows Fermi surface maps, with the doping level x indicated. For $x \lesssim 0.6$ the material is a trivial semiconductor, while for $x \gtrsim 0.6$ the band gap becomes inverted and a topological surface states forms. Adapted from Xu et al., 2011.
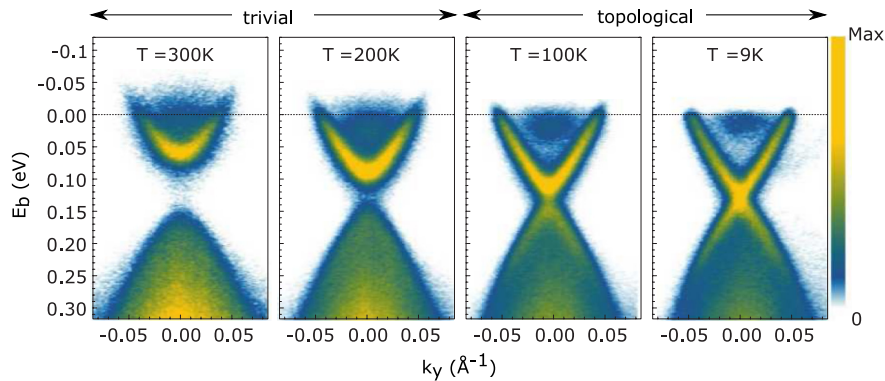
FIG. 45. Topological phase transition driven by temperature in the crystalline topological insulator $Pb_{1-x}Sn_xSe$ ($x = 0.23$). At a temperature between 100 and 200 K the bulk band gap inverts, leading to the formation of topological surface states. From Dziawa et al., 2012.

work on monolayers of $1T'$-WTe_2 synthesized by molecular beam epitaxy supported this prediction by measuring an inverted band gap of 45 meV, as shown in Fig. 46 (Tang et al., 2017), with simultaneous reports of edge conduction in exfoliated films (Fei et al., 2017). The quantum spin Hall effect, including quantized edge conduction, was subsequently confirmed up to 100 K in transport measurements (Wu et al., 2018). In later experiments, the gap of monolayer $1T'$-WSe_2 was found to be up to 130 meV (Chen et al., 2018; Ugeda et al., 2018). Other systems promising room-temperature applications include ultrathin Na_3Bi (Collins et al., 2018), bismuthene on SiC (Reis et al., 2017), and stanene on Cu (Deng et al., 2018). These discoveries lie at the intersection of 2D and topological materials research fields and make quantum spin Hall platforms more readily available.

A closely related phase is the 3D "weak" TI, which can be regarded as a stack of QSHI layers (Fu and Kane, 2007; Fu, Kane, and Mele, 2007). For a bulk crystal one expects the top and bottom surfaces to be insulating, and the side surfaces to exhibit 1D surface states. Experimental verification by ARPES has been hindered by the difficulty in measuring photoelectrons from the side surfaces of cleaved crystals. For candidate materials such as $ZrTe_5$, much of the supporting evidence has been limited to showing that the top surfaces
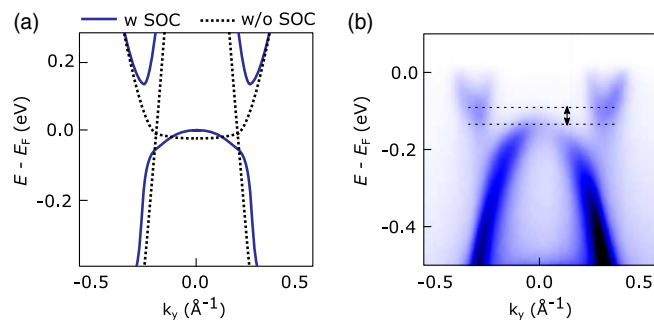
are insulating (Xiong et al., 2017), although such reports have been controversial due to the small gap (Manzoni et al., 2016). Possible indications of the side surface states have manifested as one-dimensional features superposing the spectrum, possibly attributed to photoemission from the edges of cracks in the sample surface (Y. Zhang et al., 2017). Nano-ARPES with sub–1 μm spatial resolution has been utilized to separately resolve the signal from the top (001) and side (100) surfaces of β-Bi_4I_4, revealing a 1D state associated solely with the side surface (Noguchi et al., 2019). This is suggestive of a one-dimensional edge state, but as it is the first measurement of its kind follow-up work is required to confirm that this is indeed an incontrovertible hallmark of a weak TI.

7. Topological superconductors

The theory of topological superconductors is analogous to that of TIs, with the role of the insulating band gap replaced by the particle-hole symmetric superconducting gap (Schnyder et al., 2009; Qi and Zhang, 2011). Similarly, the gapless edge modes of TIs are replaced by gapless Majorana states in topological superconductors, with the form of the wave function constrained by the particle-hole symmetry of the Bogoliubov–de Gennes Hamiltonian. An interesting situation arises when one of these states is bound to the interface between normal and superconducting regions at a vortex. This state, known as a Majorana zero mode, is an equal admixture of electrons and holes, represents a quasiparticle that is charge neutral, has exactly zero energy, and is its own antiparticle. It is therefore analogous to the Majorana fermion, which has been hypothesized as a elementary particle in nature but has not yet been experimentally observed (Hasan and Kane, 2010; Qi and Zhang, 2011). In contrast, Majorana zero modes are nonfermionic since they obey non-Abelian statistics, which allows them to form the basis for the field of topological quantum computation (Nayak et al., 2008).

The simplest theoretical proposal for a system exhibiting Majorana zero modes involves a superconductor with spinless $p_x + ip_y$ pairing. It was later realized that the non-spin-degenerate bands of a 3D TI surface state, if driven to superconduct, would resemble a spinless $p_x + ip_y$ superconductor that maintains time-reversal symmetry (Fu and Kane, 2008).

FIG. 46. Monolayer $1T'$-WTe_2 as a quantum spin Hall insulator. (a) Calculated band structure showing the band inversion enabled by spin-orbit coupling. (b) ARPES measurement revealing a 45 meV band gap, as indicated by the horizontal dashed lines. Adapted from Tang et al., 2017.

Many efforts have focused on inducing superconductivity in TIs via the proximity effect. For example, scanning tunneling spectroscopy measurements on Bi_2Se_3 thin films fabricated on superconducting $NbSe_2$ revealed a superconducting gap >0.5 meV for film thickness less than three QLs, although complementary ARPES experiments showed that the Dirac cone features a sizable hybridization gap (M.-x Wang *et al.*, 2012). Further experiments showed that even the hybridization-gapped Dirac cone hosts spin-polarized carriers and exhibits a superconducting gap of ∼0.5 meV up to $T_c \sim 7$ K, with the superconducting gap size decreasing with film thickness (S.-Y. Xu *et al.*, 2014). In a related development, superconducting gaps were demonstrated in up to ten QL Bi_2Se_3 films on polycrystalline Nb substrates (Flötotto *et al.*, 2018). Finally, we mention that superconducting gaps of up to 15 meV were reported up to 60 K in Bi_2Se_3 films grown on a cuprate superconductor (E. Wang *et al.*, 2013), although follow-up studies brought this observation into question, citing unfavorable conditions due to mismatched Fermi surface topologies, incompatible lattice symmetries, and a short coherence length (S.-Y. Xu, Liu *et al.*, 2014; Yilmaz *et al.*, 2014).

Another approach is to identify superconducting materials that intrinsically exhibit topological surface states. An intensely investigated potential platform is the iron-based superconductor $FeTe_{1-x}Se_x$ ($x = 0.45$), where ARPES revealed possible signatures of a topological surface state crossing the gap between bulk bands near the Γ point. These states are spin polarized and exhibit an isotropic superconducting gap up to 1.8 meV with $T_c = 14.5$ K (Zhang *et al.*, 2018). Scanning tunneling spectroscopy measurements discovered a zero bias peak in vortex cores, which is a necessary but not sufficient condition for establishing a Majorana bound state (Wang *et al.*, 2018). Similar ARPES observations have been reported in other materials in the iron-based superconductor family (Q. Liu *et al.*, 2018; P. Zhang *et al.*, 2019; W. Liu *et al.*, 2020). In all of these materials, the identification of the topological surface state is not as unambiguous as in the Bi_2Se_3 family due to small bulk gaps and nearly overlapping bulk bands, and considerable controversy in the interpretation of the ARPES data remains (Borisenko *et al.*, 2020). Recently topological surface states were also suggested in superconducting MgB_2 (X. Zhou *et al.*, 2019), $TaSe_3$ (Nie *et al.*, 2018), and $2M$-WS_2 (Fang *et al.*, 2019), which all remain to be further scrutinized.

8. Topological Kondo insulator candidates

In a topological Kondo insulator, the role of a bulk insulating gap is played by the hybridization gap between itinerant carriers and localized f electrons in a heavy fermion material (see Sec. VIII.F) (Dzero *et al.*, 2010). These materials are noteworthy in that electron correlations play a central role in the formation of the inverted band structure. One prominent yet controversial example is SmB_6. Some measures of the Fermi surface, such as quantum oscillations, provide evidence for two-dimensional states (Li *et al.*, 2014), although additional signals attributed to the bulk indicate that much is not yet understood about quantum oscillations in a Kondo insulator (Tan *et al.*, 2015). Several ARPES works have

supported the existence of topological states with the observation of surface states within the bulk Kondo gap (Jiang *et al.*, 2013; Neupane *et al.*, 2013; N. Xu *et al.*, 2013), which are spin polarized (N. Xu *et al.*, 2014). However, doubts have been raised about the interpretation of these features, especially due to the role of surface termination (Zhu, Nicolaou *et al.*, 2013), bending of the chemical potential in the near-surface region (Frantzeskakis *et al.*, 2013), and coexistence of topologically trivial Rashba-split surface states (Hlawenka *et al.*, 2018). Because of these and other open questions (Dzero *et al.*, 2016), it remains unclear as to whether SmB_6 can be considered a topological Kondo insulator.

9. Other TIs

Several dozen TIs have been experimentally studied in the years following the initial discovery of $Bi_{1-x}Sb_x$ in 2008 (Ando, 2013). trARPES has been a useful tool for its ability to resolve topological states even when they are unoccupied in equilibrium (Niesner *et al.*, 2012; Sobota *et al.*, 2013b; Yan, Stadtmüller *et al.*, 2015; P. Zhang *et al.*, 2017). It is now recognized that topological materials are not nearly as rare as one might expect: large-scale theoretical searches have predicted thousands of topological materials, estimating that up to 30% of materials in nature are topologically nontrivial, with ∼12% being TIs (Tang *et al.*, 2019; Vergniory *et al.*, 2019; T. Zhang *et al.*, 2019). These studies have published freely accessible, searchable databases, thus bringing to an end the era in which topological materials are evaluated on a case-by-case basis.

10. Platform for Floquet physics

TIs have served as a platform for studying nonequilibrium Floquet-Bloch states using trARPES; see Fig. 11(e). These states follow from the Floquet theorem, which shows that a periodic perturbation with period T leads to quasistatic eigenstates that are evenly spaced in energy by $2\pi\hbar/T$ (Shirley, 1965). In a trARPES experiment, the periodic perturbation is applied by the electric field of the pump pulse.

Floquet-Bloch bands were first demonstrated for the topological surface states of Bi_2Se_3 excited with a midinfrared pump. Replica bands were observed, with avoided-crossing gaps between neighboring Floquet states. In addition, it was shown that dressing of the Dirac cone with circularly polarized light broke time-reversal symmetry and thus opened a gap at the Dirac point (Y. H. Wang *et al.*, 2013). One subtlety in studying Floquet-Bloch states is that they are difficult to distinguish from laser-assisted photoemission (LAPE), in which the photoelectron emits or absorbs photons into so-called Volkov states. Both effects lead to replica bands spaced by the photon energy; the distinction is that Floquet-Bloch states are dressed in the solid, while Volkov states are dressed in the vacuum. The polarization dependence of the intensities and avoided-crossing gaps allows for discriminating these effects, and even suppressing the Volkov states; see Fig. 47 (Mahmood *et al.*, 2016). We note that LAPE at photoexcited surfaces is quite generic (Miaja-Avila *et al.*, 2006); therefore, observation of replica features alone is insufficient for identifying Floquet-Bloch states, and hybridization between the sidebands must be observed (Mahmood *et al.*, 2016).
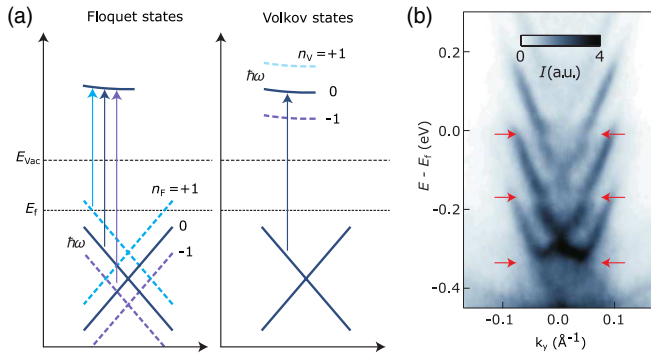
FIG. 47. (a) Distinction between Floquet states and Volkov states, which are dressing of electronic states in the solid and vacuum, respectively. Both states can exist simultaneously. (b) Experimental measurement of Floquet-Bloch bands on Bi_2Se_3. Red arrows highlight avoided crossings between neighboring Floquet states. Adapted from Mahmood et al., 2016.

FIG. 48. Dirac semimetals. (a) Sketch of the band-inversion mechanism of Dirac semimetal formation. If two 3D bands of opposite parity are driven to invert, and are symmetry forbidden from mixing, they will necessarily form a pair of fourfold degenerate Dirac nodes that disperse linearly as a function of k_x, k_y, and k_z. (b) Experimental realization in Cd_3As_2. The 3D Fermi surface consists of a pair of nodal points. A cut through a node reveals a linear band dispersion (iv). Adapted from Z. K. Liu et al., 2014a.

The subgap photon energy and clean Dirac structure is what made Bi_2Se_3 an ideal platform for demonstrating this distinctly nonequilibrium phenomenon, although we note that the topological property itself was not strictly relevant.

C. Topological semimetals

Since the discovery of TIs, it has been recognized that the topological classification of matter can be extended to semimetals. The first example we discuss is the Dirac semimetal, which hosts a point of fourfold degeneracy about which the bands disperse linearly in all three momenta dimensions; see Fig. 37, upper row. If inversion or time-reversal symmetry is broken, the nodal point splits into two doubly degenerate nodes separated in momentum space, creating what is known as a Weyl semimetal (Fig. 37, bottom row). We discuss the basic concepts underlying the topology of these phases and highlight the role of ARPES in identifying the phases and their characteristic surface states. Turner and Vishwanath (2013) and Armitage, Mele, and Vishwanath (2018) provided comprehensive reviews on these topics.

1. Dirac semimetals

Dirac semimetals are realized at the topological phase transition in 3D TIs, when the bulk band gap closes and a fourfold degeneracy occurs. However, this degeneracy is accidental since an infinitesimal change of the tuning parameter will reopen the gap. The question arises as to whether a Dirac semimetal can be realized as a more robust electronic state. Indeed, it can happen when a band inversion occurs between two bands that cannot be mixed due to symmetry, as shown in Fig. 48(a). Note that the fourfold degeneracies necessarily appear in pairs and can be gapped by breaking additional symmetries (Yang and Nagaosa, 2014; Armitage, Mele, and Vishwanath, 2018).

Dirac semimetals were first observed using ARPES in Na_3Bi (Z. K. Liu et al., 2014b) and Cd_3As_2 (Borisenko et al., 2014; Z. K. Liu et al., 2014a; Neupane et al., 2014), with the salient features summarized in Fig. 48(b). In both cases, the band crossings are protected by bulk c-axis rotational

symmetries. By mapping the electronic structure as a function of k_x, k_y, and k_z, the experiments confirm that the Fermi surface consists of a pair of nodes, while the bands disperse linearly along all three momenta directions. We note that while topological surface states have been observed in Dirac semimetals (S.-Y. Xu et al., 2015d; H. Yi et al., 2014), they do not enjoy the same level of protection as in Weyl semimetals due to the fact that the surfaces can break the spatial symmetries that preserve the crossings in the bulk (Potter, Kimchi, and Vishwanath, 2014; Kargarian, Randeria, and Lu, 2016).

2. Weyl semimetals

As mentioned, a Weyl semimetal is created when a Dirac semimetal is subjected to broken inversion and/or time-reversal symmetry. Each Weyl node is associated with an integer-valued topological index known as chirality. Since chirality is conserved, a Weyl node is stable unless annihilated with a node of opposite chirality (Turner and Vishwanath, 2013; Armitage, Mele, and Vishwanath, 2018). Thus, Weyl nodes are intrinsically more robust than Dirac nodes, which are chirality neutral and therefore depend on additional symmetries to protect against gapping.

Like TIs, Weyl semimetals are associated with topological surface states, but they have the unusual property that their Fermi surfaces form arcs in momentum space. These arcs must connect Weyl points of opposite chirality and are therefore topologically protected as long as the Weyl points avoid annihilation by remaining separated. Viewed as a geometrical construct, a Fermi surface must be a closed

contour, so the existence of a Fermi arc appears anomalous. The key here is that the surface states are not isolated, since they merge into the bulk at the Weyl points. In fact, the Fermi surface contour is globally closed if one considers the arcs on opposite sides of the sample (Wan *et al.*, 2011; Turner and Vishwanath, 2013; Armitage, Mele, and Vishwanath, 2018). This is analogous to a real-space lattice dislocation that propagates to opposite sides of a crystal.

The first Weyl semimetals discovered were associated with broken inversion symmetry. In this case the Weyl nodes exist in multiples of four because time-reversal symmetry maps a node at **k** onto a node at −**k** with the same chirality; thus, another pair must exist to achieve net zero chirality, as shown in Fig. 49(a). The first materials studied using ARPES include TaAs (Lv *et al.*, 2015; S.-Y. Xu *et al.*, 2015b; L. X. Yang *et al.*, 2015), NbAs (S.-Y. Xu *et al.*, 2015a), and TaP (S.-Y. Xu *et al.*, 2015c; Liu *et al.*, 2016). A band-mapping of the bulk and surface bands is shown in Fig. 49(b), with enlargements of the Weyl nodes and surface Fermi arcs displayed in Figs. 49(c)

and 49(d) (L. X. Yang *et al.*, 2015). To verify the bulk and surface assignment of these features, Fig. 49(e) shows an overlay of Fermi surfaces from surface-sensitive low-energy ARPES with bulk-sensitive soft-x-ray ARPES. The Weyl node structure is associated with the bulk, while the arcs are associated with the surface [Fig. 49(f)] (S.-Y. Xu *et al.*, 2015b). There have been some discrepancies in the identification and interpretation of the Fermi arcs between various groups; this may be because only their existence is topologically protected, while the dispersion can be highly sensitive to the surface condition (Sun, Wu, and Yan, 2015; H. F. Yang *et al.*, 2019).

In the case of broken time-reversal symmetry the Weyl nodes are created in pairs of opposite helicity [Fig. 49(a)]. The experimental evidence for Weyl semimetals with broken time-reversal symmetry has been more elusive (Kuroda *et al.*, 2017), although recently there was compelling evidence from ARPES and STM that $Co_3Sn_2S_2$ is a ferromagnetic Weyl semimetal with three pairs of Weyl nodes (Liu *et al.*, 2019; Morali *et al.*, 2019). Similarly, Co_2MnGa was found to be a magnetic Weyl semimetal, exhibiting so-called line nodes rather than nodal points (Belopolski *et al.*, 2019). For all these materials, to date only measurements in the ferromagnetic phase have been reported.

For the Weyl node semimetals discussed thus far, the Weyl fermions feature closed, nearly circular constant-energy contours with vanishing density of states at the node. If the dispersion around the Weyl node tilts sufficiently, the constant-energy contours become open, and there is a finite density of states at the energy of the node. These two cases have been classified as type I and type II. While type II Weyl semimetals have been reported in ARPES measurements (Deng *et al.*, 2016; L. Huang *et al.*, 2016), subsequent work has shown that unambiguous identification is not straightforward, since the distinction between topologically trivial and nontrivial Fermi arcs in the ARPES data can be subtle (Bruno *et al.*, 2016). Just as in the case for type I semimetals, measurements on a time-reversal symmetry breaking type II Weyl semimetal have recently been reported (Borisenko *et al.*, 2019).

Finally, we emphasize that this is not an exhaustive review of topological semimetallic states. Other exotic states, including drumhead surface states in line-node semimetals (Burkov, Hook, and Balents, 2011; Belopolski *et al.*, 2019) and helicoid surface bands in chiral semimetals (Fang *et al.*, 2016; Sanchez *et al.*, 2019; Schröter *et al.*, 2019), continue to be experimentally investigated, with ARPES playing the leading role in characterizing their nontrivial band topology.

D. Outlook

The pace of research on topological materials in just over a decade has been rapid, with ARPES playing a central role not only in mapping their band dispersions but also in projecting out the spin-orbital components of their wave functions. In the near term, there will continue to be a strong effort toward identifying magnetic topological materials with unequivocal Dirac point gapping. The development of small-spot ARPES will pave the way to discovering novel topological physics at edge channels and domain walls. The pursuit of a robust

FIG. 49. Weyl semimetals. (a) The simplest inversion symmetry breaking Weyl semimetal has four Weyl nodes, and the simplest time-reversal symmetry breaking Weyl semimetal has two Weyl nodes. (b) Band mapping of the inversion symmetry-breaking Weyl semimetal TaAs, with (c) a close-up of the surface Fermi arcs compared to (d) a calculation. Adapted from L. X. Yang *et al.*, 2015. (e) Fermi surface mapping of TaAs combining low-energy, surface-sensitive ARPES (green) with soft-x-ray, bulk-sensitive ARPES (orange). The soft-x-ray measurements isolate the bulk Weyl nodes, while the low-energy measurements reveal the surface Fermi arcs connecting them. (f) Schematic of this electronic structure, including the bulk Weyl nodes and surface Fermi arcs. Adapted from S.-Y. Xu *et al.*, 2015b.

topological superconductor will continue, with ARPES not only evidencing the topological surface states and superconducting gap but also measuring the dispersion of the elusive Majorana quasiparticles. Finally, investigations will increasingly advance beyond systems described by single-particle theory, with an emphasis on the relationship between topological phenomena and strong correlations (Rachel, 2018).

VIII. OTHER MATERIALS

To demonstrate the breadth of ARPES's impact in condensed matter physics, we now provide an overview of how ARPES has facilitated a microscopic understanding of various other material families. These families include metals and semimetals with noteworthy transport properties, superconductors, f-electron systems exhibiting Kondo physics, and charge density wave systems. This section is primarily organized by physical phenomenon, although material families that share similar compositions are grouped where appropriate.

A. Conventional superconductors

With the advent of high-resolution (~ 70 μeV) low-temperature (subkelvin) small-spot (~ 100 nm to 1 μm) laser- and synchrotron-based ARPES, spectroscopic features in superconductors with T_c's at single digit kelvins begin to receive more investigations. This includes superconducting boron-doped diamond ($\Delta_{sc} = 0.78$ meV, $T_c = 6.6$ K) (Ishizaka et al., 2007), β-pyrochlore superconductor KOs_2O_6 ($\Delta_{sc} = 1.63$ meV, $T_c = 9.6$ K) (Shimojima et al., 2007), and Sn ($\Delta_{sc} = 0.52$ meV, $T_c = 3.7$ K) (Okazaki et al., 2012). We focus here on a collection of such superconducting systems, with an emphasis on the determination of superconducting gap size and momentum structure.

1. MgB$_2$ and graphite intercalation compounds

MgB_2 with $T_c = 39$ K holds the T_c record for any binary compound under ambient pressure (Nagamatsu et al., 2001). It has an isotope effect that is dominated by the boron atoms (Bud'Ko et al., 2001), and the electronic structure is characterized by bands associated with highly covalent in-plane σ bonds and out-of-plane π bonds (Belashchenko, van Schilfgaarde, and Antropov, 2001). The superconductivity is postulated to be attributed to the highly anharmonic E_{2g} optical phonon involving mainly boron motion (Hinks, Claus, and Jorgensen, 2001; Yildirim et al., 2001). These observations indicate that MgB_2 is a conventional phonon-mediated multiband superconductor.

Early momentum-integrated superconducting gap measurements indicated a wide range of gap values (Rubio-Bollinger, Suderow, and Vieira, 2001; Sharoni, Felner, and Millo, 2001; Takahashi et al., 2001), which were later realized to contain contributions from both the σ and π bands (Buzea and Yamashita, 2001; Sologubenko et al., 2002; Yelland et al., 2002). ARPES first reported direct measurement of both σ and π bands (Uchiyama et al., 2002) and their respective superconducting gaps: 5.5–6 meV on the σ band and a nearby

surface band, and 1.5–2.2 meV on the π band (Souma et al., 2003; Tsuda et al., 2003). Subsequently, interband pairing was considered to play a significant role in determining the coupling strength and T_c (Choi et al., 2002; Dolgov et al., 2009). With laser ARPES, detailed doping, angle, and isotope substitution dependence of the superconducting gaps were subsequently examined in great detail near the Brillouin zone center (Tsuda et al., 2005; Mou et al., 2015; Mou, Manni et al., 2016). The σ bands exhibit an isotropic superconducting gap and a strong mode-coupling feature around 66.5 meV ($Mg^{11}B_2$) and 70 meV ($Mg^{10}B_2$).

A closely related material family includes graphite intercalated compounds such as CaC_6 and YbC_6 (Emery et al., 2005). In analogy to MgB_2, these are multiband superconductors but with 2D π bands derived from stacked graphite sheets, and 3D free-electron-like interlayer bands derived from the s orbitals of the intercalant atoms. The superconductivity was theoretically proposed to be a result of electron-phonon interactions between the π and interlayer bands (Calandra and Mauri, 2005; Boeri et al., 2007; Sanna et al., 2007). Early ARPES work reported mode coupling on the graphite bands (Valla et al., 2009) and evidence for the existence of the interlayer bands (Sugawara, Sato, and Takahashi, 2009), with later work evidencing the interband electron-phonon coupling and superconducting gap on both bands (Yang et al., 2014). More recently, similar mechanisms have been invoked to explain superconductivity in decorated monolayer graphene (Fedorov et al., 2014; Ludbrook et al., 2015).

2. Bismuthates

Bismuthate superconductors, most in the doped forms of $Ba_{1-x}K_xBiO_3$ and $BaPb_{1-x}Bi_xO_3$, have the highest T_c (34 and 13 K, respectively) of all oxide superconductors predating the cuprates (Cava et al., 1988; Sleight, Gillson, and Bierstedt, 1993). The low-energy electronic structure of $BaBiO_3$ is predominately composed of O $2p$ electrons, where a band gap in excess of 0.4 eV is seen by ARPES on *in situ* grown thin films (Plumb et al., 2016). Strong k_z dispersion and an isotropic three-dimensional single Fermi surface are observed in a slightly K-overdoped bulk compound ($T_c = 22$ K), where long-range Coulomb interaction is postulated to account for the expanded bandwidth and enhanced electron-phonon coupling (Wen et al., 2018). Superconducting gap measurements also show a highly isotropic momentum structure; a $2\Delta/k_BT_c$ ratio at the s-wave BCS limit is observed. Strong electron-phonon coupling causes a dispersion anomaly at around 50 meV binding energy, with $\lambda \sim 1.3$ (Wen et al., 2018). Taking into account moderate electronic correlation enhancement, recent GW perturbation theory calculations successfully reproduced such a strong electron-phonon coupling constant, thus ascribing the superconducting mechanism to conventional phonon-mediated s-wave BCS type (Wen et al., 2018; Z. Li et al., 2019).

B. Cobaltates and rhodates

Cobaltates and rhodates exhibit many symmetry-breaking phases in their temperature-doping phase diagrams, but they

are most well known for their thermoelectric properties (Foo *et al.*, 2004). In contrast to the conventional explanation of large spin-orbital entropy, direct ARPES measurement of the quasiparticle dispersion instead shows that the Seeback coefficient is attributed to the combined effects of a peculiar flat electron band top, with electronic correlation–induced and electron-phonon coupling–induced mass renormalization (Kuroki and Arita, 2007; S.-D. Chen *et al.*, 2017). In particular, by comparing the fully occupied t_{2g} bandwidths between the more strongly correlated sodium cobaltate and the more weakly correlated potassium rhodates, the electronic correlation is shown to double the Seebeck coefficient from the rhodates to the cobaltates (S.-D. Chen *et al.*, 2017). Via similar approaches, the presence of well-defined quasiparticles in Sr_2RhO_4 also enabled a direct quantitative derivation of thermodynamic properties from low-energy single-particle spectra (Baumberger *et al.*, 2006).

The doping evolution of the Fermi surface shape and volume in Na_xCoO_2 also highlights various many-body effects. Single-particle hopping as small as 10 meV and strong band renormalization have been argued for in the Curie-Weiss metallic phase (Hasan *et al.*, 2004; Yang *et al.*, 2004), although the total bandwidth is observed to be much larger. At $x = 1/3$ doping, the hexagonal Fermi surface is shown to exhibit a strong CDW instability at a nesting wave vector that corresponds to the cobalt sublattice (Qian *et al.*, 2006; Yang, Wang, and Ding, 2007). At the actual charge ordered doping $x = 1/2$, the Fermi surface has been argued to better trace the low-temperature-ordered sodium sublattice (Qian *et al.*, 2006). Measurements of both the nonsuperconducting variant and a hydrated superconducting variant indicate a single large Fermi surface originating from cobalt's a_{1g} band, whereas the zone corner e_g' band always remains below, although near, the chemical potential (Hasan *et al.*, 2004; Shimojima *et al.*, 2006). A similar observation was also made in the more weakly correlated potassium rhodates (S.-D. Chen *et al.*, 2017). The missing e_g' pocket has since been suggested as an extrinsic surface termination artifact (Pillay, Johannes, and Mazin, 2008), a disorder effect (Singh and Kasinathan, 2006), and a correlation effect (Bourgeois, Aligia, and Rozenberg, 2009), but no consensus has been reached.

C. Ruthenates

In contrast to $3d$ transition metal compounds which are dominated by electronic correlation effects, the heavier and more orbitally extended $4d$ and $5d$ transition metal compounds have a moderate Coulomb interaction U at a scale comparable to the Hund's coupling J_H and spin-orbit coupling λ. As one prominent example, ruthenates have driven the development of new experimental techniques since their discovery (Maeno *et al.*, 1994). Sr_2RuO_4 exhibits putative unconventional superconductivity that is highly tunable by strain (Ishida *et al.*, 1998; Hicks *et al.*, 2014; Steppke *et al.*, 2017; Pustogow *et al.*, 2019), has one of the cleanest two-dimensional Fermi liquid normal states up to ~25 K (Mackenzie *et al.*, 1996), a strange high-temperature phase that overshoots the Mott-Ioffe-Regel limit (Tyler *et al.*, 1998; Cao *et al.*, 2004), and a strong spin-orbit interaction (Mackenzie and Maeno, 2003).
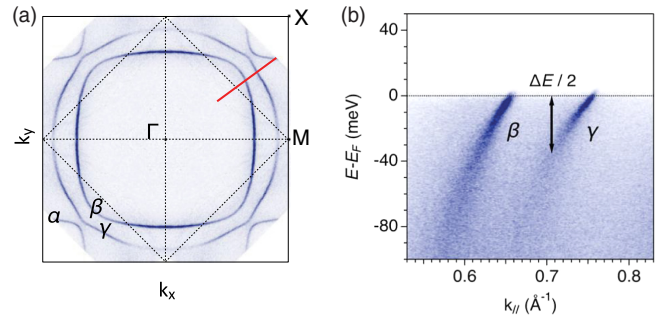
FIG. 50. High-resolution laser ARPES on Sr_2RuO_4. (a) Fermi surface on CO passivated Sr_2RuO_4. (b) Spectral intensity on the energy-momentum cut along the red line in (a), where the band splitting is used to extract the spin-orbit coupling strength. From Tamai *et al.*, 2019.

Early photoemission experiments observed a rather complicated Fermi surface in *in situ* cleaved Sr_2RuO_4 single crystals. Not fully accounted for within the quantum oscillation results, some of the Fermi pockets were later recognized as surface reconstruction effects (Okuda *et al.*, 1998; Damascelli *et al.*, 2001; Ding *et al.*, 2001; Shan-Yu *et al.*, 2012). After deliberate surface passivation, the surface states disappear and three sharpened bulk bands, α, β, and γ [Figs. 50(a) and 50(b)], remain (Tamai *et al.*, 2019). A cascade of low-energy dispersion anomalies are identified between 15 and 80 meV on both the α and β bands (Aiura *et al.*, 2004; Ingle *et al.*, 2005; Iwasawa *et al.*, 2005; C. Kim *et al.*, 2011), and a cupratelike high-energy anomaly at 700–800 meV also signals the presence of electronic correlation effects (Iwasawa *et al.*, 2012). High-resolution ARPES measurements enabled by a new generation of deep UV laser light source allow for detailed band structure measurement and full Fermi surface mapping covering almost the entire Brillouin zone (Y. He *et al.*, 2016; Tamai *et al.*, 2019). This makes it possible to perform full momentum extraction of the electronic self-energy via a band-orbital basis transformation, leading to the revelation that the anisotropic self-energy is mainly a result of momentum-dependent orbital content mixing (Haverkort *et al.*, 2008; Tamai *et al.*, 2019). This is further supported by spin-resolved ARPES measurements on all three bulk bands, where the apparent spin-orbit coupling strength λ is estimated to be ~130 ± 30 meV (Veenstra *et al.*, 2014). By comparing the energy and momentum splitting of β and γ bands with DFT and dynamic mean-field theory (DMFT) calculations, λ is reevaluated at 200 meV, accounting for both electronic correlation enhancement and quasiparticle coherence factor renormalization (Haverkort *et al.*, 2008; Kim *et al.*, 2018; Tamai *et al.*, 2019). We point out that, due to the momentum independence of the spin-orbit self-energy in an orbital basis, this also offers an ideal material platform to benchmark DMFT.

The physical properties of the ruthenate family are also heavily influenced by a low-lying van Hove point, in both Sr_2RuO_4 (Shen *et al.*, 2007) and $Sr_3Ru_2O_7$ (Tamai *et al.*, 2008). Tunneling and ARPES experiments consistently identify high electron densities within ~6 meV of the Fermi level, which is interpreted as heavy Ru $4d_{xy}$ electrons

(Iwaya *et al.*, 2007; Lee *et al.*, 2009; Allan *et al.*, 2013). In Sr$_2$RuO$_4$, the γ band van Hove singularity near the zone boundary was first predicted, then observed to cross the Fermi level when subjected to strain applied via a substrate lattice mismatch on thin-film samples (Burganov *et al.*, 2016) or mechanically strained bulk crystals (Sunko *et al.*, 2019). *In situ* tuning of compressive strain up to -4.1% on the closely related $(Ca, Pr)_2RuO_4$ single crystal also causes the quasiparticles to appear on the Fermi surface, inducing an insulator-to-metal transition (Riccò *et al.*, 2018); see Fig. 8(c).

D. Iridates

The Ruddlesden-Popper (RP) series iridate Sr/Ba$_{n+1}$Ir$_n$O$_{3n+1}$ with perovskite structure attracted great research interest due to its variety of exotic magnetic and electronic phases. The single-layer compound ($n = 1$) is considered a spin-orbit coupled Mott insulator. The system antiferromagnetically orders at 240 K (with Sr) or 230 K (with Ba) with a total angular momentum $J_{\text{eff}} = 1/2$ (Kim *et al.*, 2008, 2009; Moon *et al.*, 2008; Moser *et al.*, 2014; Uchida *et al.*, 2014). As a system that also defies expected metallicity and possesses correlation-induced antiferromagnetism, Sr$_2$IrO$_4$ has been widely considered as a second gateway to illuminate the cuprate high-T_c problem (Wang and Senthil, 2011; Watanabe, Shirakawa, and Yunoki, 2013). The bilayer compound ($n = 2$) is a semiconductor that forms c-axis collinear antiferromagnetic order at 285 K with a weak ordering moment (Cao *et al.*, 2002). And at $n = \infty$, as with the ruthenate and manganite RP series, the system develops metallicity and becomes a correlated metal (Moon *et al.*, 2008; Nie *et al.*, 2015; Cao and Schlottmann, 2018). While its magnetism has been investigated mainly with resonant x-ray scattering and neutron scattering techniques (Kim, Daghofer *et al.*, 2014; Rau, Lee, and Kee, 2016), photoemission plays an important role in revealing the corresponding evolution in electronic structures.

Large incoherent spectral gaps are observed in both stoichiometric Sr$_2$IrO$_4$ and stoichiometric Sr$_3$Ir$_2$O$_7$, which may possess topologically nontrivial surface states after *in situ* sample cleaving (Wojek *et al.*, 2012; de la Torre *et al.*, 2014; C. Liu *et al.*, 2014; Brouet *et al.*, 2015). Doping La on the Sr site or Rh on the Ir site drives a metal-insulator transition (Ge *et al.*, 2011; Li *et al.*, 2013; X. Chen *et al.*, 2015) during which low-energy quasiparticle spectral weight develops (de la Torre *et al.*, 2014; 2015; Brouet *et al.*, 2015; He *et al.*, 2015a) [Fig. 51(b)]. The stabilizing role of spin-orbit coupling in the Mott insulating state was recently disentangled from the doping effect via controlled Ru and Rh doping and careful analysis of orbital contents (Zwartsenberg *et al.*, 2020). The Fermi surface develops a band folding that coincides with both the antiferromagnetic ordering wave vector and a structural distortion due to IrO$_6$ octahedron rotation. The latter also exists in nonmagnetic isostructural rhodates [Fig. 51(a)] (Baumberger *et al.*, 2006; de la Torre *et al.*, 2014; 2015; He *et al.*, 2015a). This folded Fermi surface manifests as an arclike feature that resembles the Fermi arc in cuprates; see Sec. IV.D (de la Torre *et al.*, 2014; Kim, Krupin *et al.*, 2014; He *et al.*, 2015a). With either bulk or surface carrier doping, the low-energy spectra indeed exhibit an
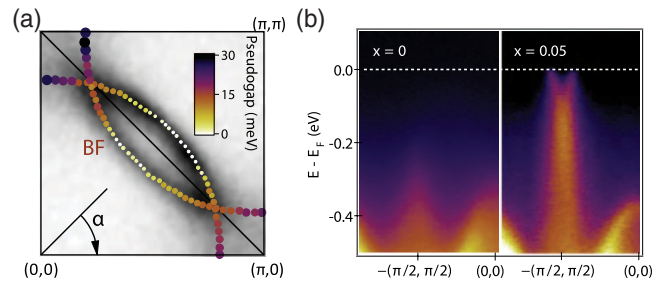
FIG. 51. Fermi surface and development of quasiparticles in iridates. (a) Fermi surface overlaid with the anisotropic energy gap (colored dots) in Sr$_2$IrO$_4$. (b) Emergence of quasiparticles with electron doping in Sr$_2$IrO$_4$. Adapted from de la Torre *et al.*, 2015.

anisotropic energy gap that lacks clear quasiparticles, prompting comparison to the pseudogap phenomenon or even superconductivity in the cuprates [Fig. 51(b)] (de la Torre *et al.*, 2015; Yan, Ren *et al.*, 2015; Kim *et al.*, 2016; Battisti *et al.*, 2017). Measurements above the Néel temperature show no sign of spectral gap closing, which indicates the Mott insulating nature of the system (Moser *et al.*, 2014). The electronic correlation may also give rise to negative electronic compressibility: a lowering chemical potential with electron addition providing a potential microscopic explanation for the tendency toward phase separation in doped iridates (X. Chen *et al.*, 2015; He *et al.*, 2015b).

Another major iridate family Ln$_2$Ir$_2$O$_7$ (Ln = lanthanide series or Bi) is of the pyrochlore structure. ARPES experiments in this family remain challenging, due mainly to the lack of an easy cleaving plane. In the metallic compound Pr$_2$Ir$_2$O$_7$, a cubic and time-reversal symmetry-protected Fermi node is observed by ARPES, supporting the system as a correlated topological material (Wan *et al.*, 2011; Kondo *et al.*, 2015). Further temperature-dependent experiments on the all-in-all-out spin ordered compound Nd$_2$Ir$_2$O$_7$ shows a highly three-dimensional metallic normal state with a similar Fermi node (Guo, Ritter, and Komarek, 2016; Nakayama *et al.*, 2016). However, while the single-particle gap opens only below the magnetic transition, the quasiparticle also gradually loses spectral coherence approaching zero temperature. This indicates successive transitions from a metal to a Slater insulator, then to a Mott insulator (Nakayama *et al.*, 2016).

Quantum spin liquid candidate honeycomb iridates Na$_2$IrO$_3$ and α-Li$_2$IrO$_3$ are formed by edge-sharing IrO$_6$ octahedra. While most of the focus remains on the magnetic degrees of freedom, photoemission confirms that the size of the Mott gap ($\sim$340 meV) is comparable to the spin-orbit coupling strength ($\sim$500 meV) (Comin *et al.*, 2012).

E. Delafossite oxides

The materials PdCoO$_2$, PtCoO$_2$, and PdCrO$_2$ are anisotropic metals with high in-plane conductivity. The conduction occurs in the Pd/Pt layers separated by insulating CoO$_2$/CrO$_2$ layers; see Mackenzie (2017) for a comprehensive review. The bulk electronic structure as measured by ARPES consists of a single 2D band crossing the Fermi level with a hexagonal cross section that exhibits weak correlation effects

(Kushwaha *et al.*, 2015). This unusually clean electronic structure makes these materials an excellent model system for studying electronic interactions using ARPES.

The cleaved surface is polar, leading to a formation of surface states that is visible in ARPES. They are not protected as in topological materials, as evidenced by the relative ease with which they can be removed by disorder (Noh *et al.*, 2009; Sobota *et al.*, 2013a). The surface states of $PtCoO_2$ exhibit a large Rashba-like spin splitting attributed to the atomic spin-orbit coupling of the relatively lightweight Co, which is unlocked by the unusually large magnitude of inversion symmetry breaking at the CoO_2-terminated surface (Sunko *et al.*, 2017). Another interesting aspect of the surface states is that they can host ferromagnetic order (Mazzola *et al.*, 2018). Independently, the bulk of these materials can also exhibit magnetic order: in $PdCrO_2$, the localized Cr^{3+} ions ($S = 3/2$) exhibit a 120° spin structure, making it possible to study the interaction of itinerant electrons with a localized antiferromagnetic structure (Takatsu *et al.*, 2009). In ARPES this interaction manifests as a folding of the itinerant Pd bands with respect to the antiferromagnetic zone boundary, which vanishes above the Néel temperature $T_N = 37.5$ K (Noh *et al.*, 2014). This folding was proposed to arise from a novel mechanism that convolves the ARPES spectrum of the itinerant layer with the spin-spin correlation function of the AFM layer (Sunko *et al.*, 2020).

F. Heavy fermion systems

Heavy fermion systems are typically rare-earth metals or actinides with partially filled $4f$ or $5f$ orbitals, in which the charge carriers exhibit an effective mass up to 3 orders of magnitude larger than that of a bare electron. The essential physics can be described in terms of a lattice of localized f-electron moments interacting with an interpenetrating sea of conduction electrons. Mediated by coherent Kondo scattering, the local moments form a many-body spin singlet with the conduction electrons. This results in the formation of a composite quasiparticle that inherits the mass of the f electrons and is expected to increase the Fermi surface volume due to incorporation of the f degrees of freedom. At the same time, the interplay between Ruderman-Kittel-Kasuya-Yosida interactions and Kondo screening leads to an antiferromagnetic quantum critical point, often accompanied by unconventional superconductivity (Hewson, 1993; Si and Steglich, 2010). Since the antiferromagnetism and superconductivity manifest at relatively low (<10 K) temperature scales, these phases and their associated quantum criticality have been extensively studied by transport and thermodynamics measurements, while ARPES has focused on higher-energy physics such as the degree of f-d hybridization.

Since the f-electron cross section is strongly $h\nu$ dependent, with diminishing intensity below ∼50 eV (Yeh and Lindau, 1985), $h\nu > 100$ eV is routinely employed to exploit the enhanced f-electron signal. Moreover, soft-x-ray (>500 eV) ARPES has been useful for suppressing the contribution of surface states and achieving true bulk sensitivity, albeit at the cost of compromised energy resolution (Yano *et al.*, 2007). Another technical yet important limitation is imposed by safety protocols concerning transuranic compounds, which

spurred the development of separate dedicated ARPES facilities for these materials (Graham, Joyce, and Durakiewicz, 2013).

Much of the ARPES work on f-d hybridization has centered around $4f$ Ce- and Yb-based compounds. For these materials, the spectral function is generally well described by the periodic Anderson model: the binding energy of the bare f electrons is renormalized by correlations, forming a nondispersive band near E_F (also known as the Kondo resonance) that then hybridizes with the dispersive d-electron bands (Denlinger *et al.*, 2001). One advantage of Yb compounds over Ce compounds for ARPES is that the Kondo resonance is below E_F (Fujimori, 2016). Figures 52(a) and 52(b) show the ARPES spectrum of a prototypical heavy fermion material $YbRh_2Si_2$ together with a sketch of the periodic Anderson model: the $4f$ Kondo resonance below E_F (shaded red) is incorporated into the Fermi surface by hybridizing with the Rh $4d$ bands (shaded blue) (Danzenbächer *et al.*, 2011). Here a multitude of flatbands are observed due to crystal-field splitting of the $4f$ levels (Vyalikh *et al.*, 2010). One of the central questions concerns the temperature scale associated with the f-d hybridization. ARPES measurements on $YbRh_2Si_2$ found no significant changes from 1 to 100 K (Kummer *et al.*, 2015), while measurements on $CeCoIn_5$ suggest that dehybridization occurs above ∼200 K (Q. Y. Chen *et al.*, 2017; Jang *et al.*, 2020). These values vastly exceed the temperature scales for coherent Kondo scattering inferred from resistivity measurements (Trovarelli *et al.*, 2000; Petrovic *et al.*, 2001). Further understanding is required to reconcile temperature-dependent thermodynamic and transport properties with the single-particle spectral function measured by ARPES.

$5f$ electrons have been studied in U-based compounds. While some materials, such as UPd_3, UGe_2, and USb_2, do seem to be well described by the periodic Anderson model (Beaux *et al.*, 2011), other materials, such as $UFeGa_5$, are better understood in an itinerant $5f$-electron model (Fujimori *et al.*, 2006). One U compound that has attracted significant attention is URu_2Si_2 due to the observation of a phase transition in the specific heat at $T_{HO} = 17.5$ K (Palstra *et al.*, 1985). Although apparently of magnetic origin, this has come to be known as the "hidden-order" phase since magnetic order remains mysteriously unobserved (Durakiewicz, 2014). ARPES revealed the emergence of a flatband near E_F in the
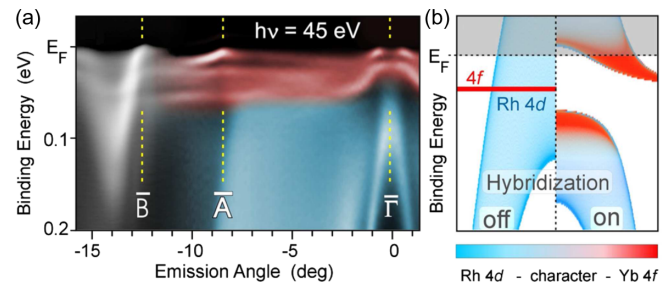
FIG. 52. (a) ARPES spectrum from the heavy fermion system $YbRh_2Si_2$, and (b) sketch of the spectral function as described by the periodic Anderson model. The renormalized f level, or Kondo resonance, exists below E_F and hybridizes with the dispersive Rh $4d$ conduction electrons. From Danzenbächer *et al.*, 2011.

hidden-order phase (Santander-Syro *et al.*, 2009) and attributed it to a doubling of the unit cell along the *c* axis that folds the Γ point to the *Z* point (Yoshida *et al.*, 2010) and leads to dramatic Fermi surface reconstruction (Bareille *et al.*, 2014). Other recent results suggest that these flatbands already exist at higher temperatures, but below T_{HO} they rapidly hybridize with the conduction electrons to form sharp spectral features (Chatterjee *et al.*, 2013). This contrasts sharply with the previously discussed high-temperature gradual onset of hybridization in 4*f* systems, and therefore appears to be a distinct signature of the hidden-order transition.

G. Extreme magnetoresistance semimetals

Since 2014 there has been a surge of research on semimetals that exhibit large magnetoresistance such as WTe$_2$ (Ali *et al.*, 2014), Cd$_3$As$_2$ (Liang *et al.*, 2015), LaSb (Tafti *et al.*, 2016), and others in related families. This effect has been termed extreme magnetoresistance (XMR) due to the large magnitude ($>10^4$) and nonsaturating behavior up to high magnetic fields. The mechanism for XMR has been under some debate; with many of these materials exhibiting some form of topological order, some works have suggested that the XMR is associated with the lifting of topological protection by the external magnetic field (Liang *et al.*, 2015; Shekhar *et al.*, 2015; Tafti *et al.*, 2016). Others have argued for a conventional carrier-compensation picture (Pippard, 1989), in which the XMR derives from a nearly equal concentration of electrons and holes such as in WTe$_2$ (Pletikosić *et al.*, 2014) and LaSb (Zeng *et al.*, 2016). In topologically trivial materials such as YSb, the XMR is explained in terms of imbalanced carrier concentrations complemented with substantially different electron and hole mobilities (J. He *et al.*, 2016). More evidence against an ostensible clean role of topology is provided by a comparative ARPES study of La*X* (*X* = Bi, Sb, As) that showed that these materials belong to different topological classes despite all exhibiting XMR (Nummy *et al.*, 2018). On the other hand, the carrier concentrations were shown to be strongly imbalanced in the topologically nontrivial LaBi (Jiang *et al.*, 2018), further raising questions about whether universal conclusions can be drawn on the relative roles of topology and carrier compensation in this class of materials.

H. Rare-earth tritellurides

The CDW is a prototypical ordering phenomenon in condensed matter that exemplifies the role of electron-lattice interactions. In a canonical Peierls scenario, the electronic energy gain of a lattice distortion overwhelms the elastic energy cost, leading to a divergence of the electronic susceptibility at the wave vector that nests the Fermi surface ($q = 2k_F$) and an accompanying inter-unit-cell charge modulation (Grüner, 1994). However, doubts have been raised as to whether this concept of "Fermi surface nesting" can be applied to real materials with finite temperature, scattering rates, and imperfect nesting geometries; instead, the *q*-dependent electron-phonon coupling for all occupied states must be considered (Johannes and Mazin, 2008). We further note that strong electronic correlation effects can also give rise to exotic valence electron CDW or excitonic insulating states, which have a less pronounced influence on the lattice than the aforementioned mechanisms; see Secs. IV and VI.C.

The rare-earth tritellurides (*R*Te$_3$) have been a model system for ARPES to study CDWs. Structural studies have revealed an incommensurate CDW in a broad range of materials (*R* = La, Sm, Gd, Tb, Dy, Ho, Er, Tm) with transition temperatures in the range ~240–420 K (DiMasi *et al.*, 1995; Ru *et al.*, 2008). The normal-state electronic structure is well described by a tight-binding model with weakly hybridized quasi-1D p_x and p_z orbitals; see Fig. 53(a). Upon entering the CDW state, ARPES shows that the bands are folded by q_{CDW}, leading to gapping of the Fermi surface and the formation of shadow bands (Gweon *et al.*, 1998; Brouet *et al.*, 2004, 2008; Moore *et al.*, 2010). Although many of these results are discussed in a canonical nesting-driven scenario, it has been pointed out that *q*-dependent electron-phonon coupling can make important contributions to determining q_{CDW} (Eiter *et al.*, 2013; Maschek *et al.*, 2015).

trARPES has been extensively employed to investigate the dynamics of the order parameter (Schmitt *et al.*, 2008; Rettig *et al.*, 2014; Leuenberger *et al.*, 2015). Figure 53(b) shows a
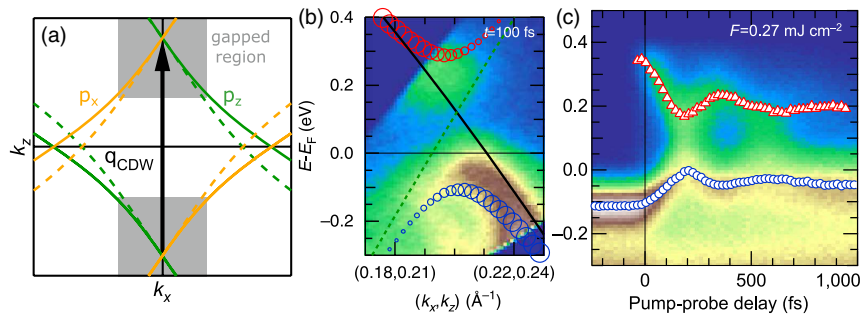
FIG. 53. trARPES studies on the CDW in *R*Te$_3$. (a) Tight-binding Fermi surface for DyTe$_3$ consisting of the p_x and p_z orbitals, as indicated. Dashed lines represent the folded shadow bands. The CDW ordering vector q_{CDW} and gapped region are indicated. (b) Cut through the gapped region after pumping showing the gap and shadow bands. Because of photoexcitation of carriers, both upper and lower bands are visible. Markers indicate the band dispersion in a tight-binding model. (c) Spectrum in the gap region as a function of pump-probe delay. Markers indicate the peak positions of the upper and lower CDW bands, which reveal a partial closure and oscillation of the gap amplitude. Adapted from Rettig *et al.*, 2016.

cut through the gapped region after pumping, where the normally unoccupied side of the gap (above E_F) is visible due to a nonequilibrium population of electrons. As shown in Fig. 53(c), the gap not only reduces in magnitude but also oscillates, reflecting a coherent modulation of the order parameter known as the amplitude mode. It has been suggested that the nesting conditions themselves are dynamically modified, raising the prospect of stabilizing order using ultrafast excitations (Rettig *et al.*, 2016).

I. Manganese oxides

The manganese oxides (manganites) have been the subject of intense investigation because they exhibit colossal magnetoresistance, in which the conductivity changes by orders of magnitude upon application of a magnetic field (Ramirez, 1997). Unlike the XMR effect in semimetals, this phenomenon is a manifestation of the competition between many-body interactions including structural, orbital, and spin degrees of freedom, resulting in a complex phase diagram that hosts a variety of magnetic phases. Several ARPES studies have focused on both the single-layer $La_{1-x}Sr_xMnO_3$ (Lev *et al.*, 2015; Horiba *et al.*, 2016) and the bilayer manganite $La_{2-2x}Sr_{1+2x}Mn_2O_7$ (Mannella *et al.*, 2005) in the doping range of $x \sim 0.4$, which is a ferromagnetic metal below $T_c \sim 120$ K and a paramagnetic insulator above T_c. Many of the microscopic ingredients are generally agreed upon: the ferromagnetic state is mediated by double-exchange interactions between Mn moments that simultaneously favor electron delocalization. In the high-temperature paramagnetic state, the electrons undergo self-trapping due to the strong electron-phonon interaction, forming small polarons with a tendency to become localized at impurities. The fact that a magnetic field can tip the balance between these states is the origin of the colossal magnetoresistance (Millis, 1998). There is, however, some controversy concerning the role of polarons. Early ARPES work on the $x = 0.4$ doping reported a pseudogapped Fermi surface with well-defined quasiparticle peaks only in the $(0,0)$-(π,π) direction below T_c, suggesting a common phenomenology with the Fermi arc state in cuprates (Mannella *et al.*, 2005). The incoherent spectral weight was assigned to localized polarons, while the sharp peaks were taken as evidence for a "polaronic metal" in which polaron condensation acts in concert with double-exchange interactions to foster metallic conductivity. This hypothesis was supported by a direct correlation between the quasiparticle spectral weight and the dc conductivity (Mannella *et al.*, 2007). However, the universality of this observation was challenged by other experiments for $x = 0.36 - 0.38$ reporting quasiparticle peaks in the $(\pi,0)$ direction persisting well above T_c (Sun *et al.*, 2006, 2007; de Jong *et al.*, 2007). More recently a combined STM-ARPES study argued that the intrinsic Fermi surface is gapped throughout k space both below and above T_c in the broad doping range $x = 0.3 - 0.425$. Quasiparticle peaks were observed in ARPES only for $<5\%$ of the cleaved surface and were assigned to regions with stacking-fault intergrowths as separately observed in STM measurements (Massee *et al.*, 2011). Because of the reported phase separation, the Fermi surface volume is an important metric for evaluating the purity of the phase being measured. While a unifying picture is still lacking in this class of materials, the spectral signatures of highly polaronic physics are robust.

IX. CONCLUSION AND OUTLOOK

Over the past decade, ARPES has emerged as the key tool for condensed matter physics research, exemplified by its impact on strongly correlated cuprate superconductors, Hund's metal iron superconductors, 2D materials, and topological matter. It is rapidly evolving from a stand-alone characterization technique toward a platform for discovering and controlling new quantum phenomena. Conventional ARPES as a technique has matured to the point that complete-system solutions are now commercially available, which will fast-track the popularization of its basic functionalities to the broader materials research community as well as to industry (Shallenberger *et al.*, 1998; Cabuil *et al.*, 2007). Given the rapidly growing volume of research, standardization of data acquisition, open-source data analysis routines, and data storage is imminently desirable. At the same time, from the instrumentation point of view, we foresee a major impact due to the continued development of light sources. Fourth generation synchrotrons, quasicontinuous and ultrafast lasers, and x-ray FELs will enable precision experiments with previously unattainable spatial, temporal, and chemical specificity. On the photoelectron spectrometer side, multiplexing detectors will play an increasingly prominent role, especially in the domain of spin-resolved ARPES, where these efficiency gains will be used to routinely map the spin and orbital parts of wave functions, with great sensitivity to local symmetries. Meanwhile, in sync with the deepening understanding of photoemission theory, expansion of single photoemission to a multiparticle probe via interference effects and multielectron emission will spearhead the effort to directly address many-body correlation and entanglement effects (Kouzakov and Berakdar, 2003; Huth *et al.*, 2014; Trützschler *et al.*, 2017). On the sample side, *in situ* synthesis and environment tuning will permit access to phases previously thought to be beyond the scope of an ARPES experiment (Shen, Yang, and Liu, 2017; Trotochaud *et al.*, 2017; Cattelan and Fox, 2018; Yamane *et al.*, 2019). Enabled by the in-lens deflector of modern electron spectrometers, the combination of an electrified sample environment with nanoscale spatial resolution will unlock a new era of *in operando* studies of fabricated devices and exfoliated heterostructures. The pace of concerted scientific and technique codevelopment will continue, with the rate accelerating with more rapid iteration between experiment and theory.

ARPES will continue to be a leading tool pushing the frontier of quantum materials research, helping to set the intellectual agenda by testing new ideas, discovering surprises, and challenging orthodoxies. There is little doubt that this technique is going to be at the focal point of the necessary debates leading to new paradigms of physics.

ACKNOWLEDGMENTS

REFERENCES

Abbamonte, P., A. Rusydi, S. Smadici, G. Gu, G. Sawatzky, and D. Feng, 2005, Nat. Phys. **1**, 155.

Åberg, T., 1967, Phys. Rev. **156**, 35.

Ahn, J., J. Byun, H. Koh, E. Rotenberg, S. Kevan, and H. Yeom, 2004, Phys. Rev. Lett. **93**, 106401.

Ahn, S. J., et al., 2018, Science **361**, 782.

Ai, P., et al., 2019, Chin. Phys. Lett. **36**, 067402.

Aiura, Y., Y. Yoshida, I. Hase, S. Ikeda, H. Higashiguchi, X. Cui, K. Shimada, H. Namatame, M. Taniguchi, and H. Bando, 2004, Phys. Rev. Lett. **93**, 117005.

Ali, M. N., et al., 2014, Nature (London) **514**, 205.

Alidoust, N., et al., 2014, Nat. Commun. **5**, 4673.

Allan, M. P., et al., 2013, New J. Phys. **15**, 063029.

Allen, J., et al., 1990, Phys. Rev. Lett. **64**, 595.

Alloul, H., T. Ohno, and P. Mendels, 1989, Phys. Rev. Lett. **63**, 1700.

Alpichshev, Z., J. G. Analytis, J.-H. Chu, I. R. Fisher, Y. L. Chen, Z. X. Shen, A. Fang, and A. Kapitulnik, 2010, Phys. Rev. Lett. **104**, 016401.

Analytis, J. G., J.-H. Chu, Y. Chen, F. Corredor, R. D. McDonald, Z. X. Shen, and I. R. Fisher, 2010, Phys. Rev. B **81**, 205407.

Anderson, P. W., 1959, Phys. Rev. **115**, 2.

Anderson, P. W., 1987, Science **235**, 1196.

Ando, Y., 2013, J. Phys. Soc. Jpn. **82**, 102001.

Ando, Y., Y. Hanaki, S. Ono, T. Murayama, K. Segawa, N. Miyamoto, and S. Komiya, 2000, Phys. Rev. B **61**, R14956.

Ando, Y., S. Komiya, K. Segawa, S. Ono, and Y. Kurita, 2004, Phys. Rev. Lett. **93**, 267001.

Anzai, H., M. Arita, H. Namatame, M. Taniguchi, M. Ishikado, K. Fujita, S. Ishida, S. Uchida, and A. Ino, 2017, Sci. Rep. **7**, 4830.

Anzai, H., A. Ino, M. Arita, H. Namatame, M. Taniguchi, M. Ishikado, K. Fujita, S. Ishida, and S. Uchida, 2013, Nat. Commun. **4**, 1815.

Anzai, H., et al., 2010, Phys. Rev. Lett. **105**, 227002.

Arango, Y. C., L. Huang, C. Chen, J. Avila, M. C. Asensio, D. Grützmacher, H. Lüth, J. G. Lu, and T. Schäpers, 2016, Sci. Rep. **6**, 29493.

Armitage, N., P. Fournier, and R. Greene, 2010, Rev. Mod. Phys. **82**, 2421.

Armitage, N., et al., 2001, Phys. Rev. Lett. **86**, 1126.

Armitage, N., et al., 2002, Phys. Rev. Lett. **88**, 257001.

Armitage, N., et al., 2003, Phys. Rev. B **68**, 064517.

Armitage, N. P., E. J. Mele, and A. Vishwanath, 2018, Rev. Mod. Phys. **90**, 015001.

Arpiainen, V., A. Bansil, and M. Lindroos, 2009, Phys. Rev. Lett. **103**, 067005.

Ashcroft, N. W., and N. D. Mermin, 1976, Solid State Physics, Science: Physics (Thomson Learning, Stamford, CT).

Atkinson, W., J. D. Bazak, and B. M. Andersen, 2012, Phys. Rev. Lett. **109**, 267004.

Avci, S., et al., 2012, Phys. Rev. B **85**, 184507.

Avci, S., et al., 2014, Nat. Commun. **5**, 3845.

Avigo, I., et al., 2013, J. Phys. Condens. Matter **25**, 094003.

Bachrach, R. Z., 2012, Synchrotron Radiation Research: Advances in Surface and Interface Science Techniques, Vol. 1 (Springer Science+Business Media, New York), Chap. 11.

Badoux, S., et al., 2016, Nature (London) **531**, 210.

Baek, S., D. Efremov, J. Ok, J. Kim, J. Van Den Brink, and B. Büchner, 2015, Nat. Mater. **14**, 210.

Balakirev, F. F., J. B. Betts, A. Migliori, S. Ono, Y. Ando, and G. S. Boebinger, 2003, Nature (London) **424**, 912.

Balasubramanian, T., E. Jensen, X. L. Wu, and S. L. Hulbert, 1998, Phys. Rev. B **57**, R6866.

Balatsky, A. V., W. Lee, and Z. Shen, 2009, Phys. Rev. B **79**, 020505.

Bang, Y., and G. Stewart, 2017, J. Phys. Condens. Matter **29**, 123003.

Bansal, N., Y. S. Kim, M. Brahlek, E. Edrey, and S. Oh, 2012, Phys. Rev. Lett. **109**, 116804.

Bardeen, J., L. N. Cooper, and J. R. Schrieffer, 1957, Phys. Rev. **108**, 1175.

Bardyszewski, W., and L. Hedin, 1985, Phys. Scr. **32**, 439.

Bareille, C., F. L. Boariu, H. Schwab, P. Lejay, F. Reinert, and A. F. Santander-Syro, 2014, Nat. Commun. **5**, 4326.

Barrett, N., K. Winkler, B. Krömker, and E. Conrad, 2013, Ultramicroscopy **130**, 94.

Barton, J., C. Bahr, Z. Hussain, S. Robey, J. Tobin, L. Klebanoff, and D. Shirley, 1983, Phys. Rev. Lett. **51**, 272.

Barton, J., S. Robey, C. Bahr, and D. Shirley, 1985, in The Structure of Surfaces (Springer, New York), pp. 191–198.

Bartynski, R. A., R. H. Gaylord, T. Gustafsson, and E. W. Plummer, 1986, Phys. Rev. B **33**, 3644.

Batlogg, B., H. Hwang, H. Takagi, R. J. Cava, H. Kao, and J. Kwo, 1994, Physica (Amsterdam) **235C–240C**, 130.

Batterman, B. W., 1964, Phys. Rev. **133**, A759.

Battisti, I., et al., 2017, Nat. Phys. **13**, 21.

Baumberger, F., W. Auwärter, T. Greber, and J. Osterwalder, 2004, Science **306**, 2221.

Baumberger, F., N. Ingle, W. Meevasana, K. Shen, D. Lu, R. Perry, A. Mackenzie, Z. Hussain, D. Singh, and Z.-X. Shen, 2006, Phys. Rev. Lett. **96**, 246402.

Beaux, M., et al., 2011, J. Electron Spectrosc. Relat. Phenom. **184**, 517.

Bechtel, J. H., 1975, J. Appl. Phys. **46**, 1585.

Bednorz, J. G., and K. A. Müller, 1986, Z. Phys. B **64**, 189.

Bednorz, J. G., and K. A. Müller, 1988, Rev. Mod. Phys. **60**, 585.

Belashchenko, K. D., M. van Schilfgaarde, and V. P. Antropov, 2001, Phys. Rev. B **64**, 092503.

Belopolski, I., *et al.*, 2019, Science **365**, 1278.

Benia, H. M., C. Lin, K. Kern, and C. R. Ast, 2011, Phys. Rev. Lett. **107**, 177602.

Berakdar, J., 1998, Phys. Rev. B **58**, 9808.

Berglund, C. N., and W. E. Spicer, 1964, Phys. Rev. **136**, A1030.

Berntsen, M. H., O. Götberg, and O. Tjernberg, 2011, Rev. Sci. Instrum. **82**, 095113.

Bertoni, R., *et al.*, 2016, Phys. Rev. Lett. **117**, 277201.

Bianchi, M., D. Guan, S. Bao, J. Mi, B. B. Iversen, P. D. King, and P. Hofmann, 2010, Nat. Commun. **1**, 128.

Bianchi, M., R. C. Hatch, J. Mi, B. B. Iversen, and P. Hofmann, 2011, Phys. Rev. Lett. **107**, 086802.

Bilbro, L., R. V. Aguilar, G. Logvenov, O. Pelleg, I. Bozović, and N. Armitage, 2011, Nat. Phys. **7**, 298.

Blackburn, E., J. Chang, A. Said, B. Leu, R. Liang, D. Bonn, W. Hardy, E. Forgan, and S. Hayden, 2013, Phys. Rev. B **88**, 054506.

Boeri, L., G. B. Bachelet, M. Giantomassi, and O. K. Andersen, 2007, Phys. Rev. B **76**, 064510.

Böhmer, A., T. Arai, F. Hardy, T. Hattori, T. Iye, T. Wolf, H. v. Löhneysen, K. Ishida, and C. Meingast, 2015, Phys. Rev. Lett. **114**, 027001.

Bok, J. M., J. J. Bae, H.-Y. Choi, C. M. Varma, W. Zhang, J. He, Y. Zhang, L. Yu, and X. Zhou, 2016, Sci. Adv. **2**, e1501329.

Bok, J. M., J. H. Yun, H.-Y. Choi, W. Zhang, X. Zhou, and C. M. Varma, 2010, Phys. Rev. B **81**, 174516.

Bonifacio, R., C. Pellegrini, and L. M. Narducci, 1984, AIP Conf. Proc. **118**, 236.

Borisenko, S., V. Bezguba, A. Fedorov, Y. Kushnirenko, V. Voroshnin, M. Sturza, S. Aswartham, and A. Yaresko, 2020, npj Quantum Mater. **5**, 67.

Borisenko, S., Q. Gibson, D. Evtushinsky, V. Zabolotnyy, B. Büchner, and R. J. Cava, 2014, Phys. Rev. Lett. **113**, 027603.

Borisenko, S., A. Kordyuk, T. Kim, A. Koitzsch, M. Knupfer, J. Fink, M. Golden, M. Eschrig, H. Berger, and R. Follath, 2003, Phys. Rev. Lett. **90**, 207001.

Borisenko, S., *et al.*, 2006, Phys. Rev. Lett. **96**, 117004.

Borisenko, S., *et al.*, 2008, Phys. Rev. Lett. **100**, 196402.

Borisenko, S., *et al.*, 2010, Phys. Rev. Lett. **105**, 067002.

Borisenko, S., *et al.*, 2016, Nat. Phys. **12**, 311.

Borisenko, S., *et al.*, 2019, Nat. Commun. **10**, 3424.

Borisenko, S. V., A. A. Kordyuk, A. Koitzsch, T. K. Kim, K. A. Nenkov, M. Knupfer, J. Fink, C. Grazioli, S. Turchini, and H. Berger, 2004, Phys. Rev. Lett. **92**, 207001.

Boschini, F., H. Hedayat, C. Dallera, P. Farinello, C. Manzoni, A. Magrez, H. Berger, G. Cerullo, and E. Carpene, 2014, Rev. Sci. Instrum. **85**, 123903.

Boschini, F., *et al.*, 2018, Nat. Mater. **17**, 416.

Bostwick, A., T. Ohta, T. Seyller, K. Horn, and E. Rotenberg, 2007, Nat. Phys. **3**, 36.

Bostwick, A., F. Speck, T. Seyller, K. Horn, M. Polini, R. Asgari, A. H. MacDonald, and E. Rotenberg, 2010, Science **328**, 999.

Bourgeois, A., A. Aligia, and M. J. Rozenberg, 2009, Phys. Rev. Lett. **102**, 066402.

Bovensiepen, U., and P. Kirchmann, 2012, Laser Photonics Rev. **6**, 589.

Božović, I., X. He, J. Wu, and A. Bollinger, 2016, Nature (London) **536**, 309.

Braun, J., 1996, Rep. Prog. Phys. **59**, 1267.

Breznay, N. P., I. M. Hayes, B. Ramshaw, R. D. McDonald, Y. Krockenberger, A. Ikeda, H. Irie, H. Yamamoto, and J. G. Analytis, 2016, Phys. Rev. B **94**, 104514.

Brisk, M. A., and A. Baker, 1975, J. Electron Spectrosc. Relat. Phenom. **7**, 197.

Brouet, V., M. F. Jensen, P.-H. Lin, A. Taleb-Ibrahimi, P. Le Fèvre, F. Bertran, C.-H. Lin, W. Ku, A. Forget, and D. Colson, 2012, Phys. Rev. B **86**, 075123.

Brouet, V., D. LeBoeuf, P.-H. Lin, J. Mansart, A. Taleb-Ibrahimi, P. Le Fèvre, F. Bertran, A. Forget, and D. Colson, 2016, Phys. Rev. B **93**, 085137.

Brouet, V., W. L. Yang, X. J. Zhou, Z. Hussain, N. Ru, K. Y. Shin, I. R. Fisher, and Z. X. Shen, 2004, Phys. Rev. Lett. **93**, 126405.

Brouet, V., *et al.*, 2008, Phys. Rev. B **77**, 235104.

Brouet, V., *et al.*, 2015, Phys. Rev. B **92**, 081117.

Bruno, F. Y., S. McKeown Walker, S. Riccò, A. de la Torre, Z. Wang, A. Tamai, T. K. Kim, M. Hoesch, M. S. Bahramy, and F. Baumberger, 2019, Adv. Electron. Mater. **5**, 1800860.

Bruno, F. Y., *et al.*, 2016, Phys. Rev. B **94**, 121112.

Bud'Ko, S., G. Lapertot, C. Petrovic, C. Cunningham, N. Anderson, and P. Canfield, 2001, Phys. Rev. Lett. **86**, 1877.

Bulut, N., and D. Scalapino, 1996, Phys. Rev. B **54**, 14971.

Burganov, B., *et al.*, 2016, Phys. Rev. Lett. **116**, 197003.

Burkov, A. A., M. D. Hook, and L. Balents, 2011, Phys. Rev. B **84**, 235126.

Buss, J. H., *et al.*, 2019, Rev. Sci. Instrum. **90**, 023105.

Buzea, C., and T. Yamashita, 2001, Supercond. Sci. Technol. **14**, R115.

Cabuil, N., *et al.*, 2007, AIP Conf. Proc., **931**, 191.

Calandra, M., and F. Mauri, 2005, Phys. Rev. Lett. **95**, 237002.

Campuzano, J., *et al.*, 1999, Phys. Rev. Lett. **83**, 3709.

Cancellieri, C., A. S. Mishchenko, U. Aschauer, A. Filippetti, C. Faber, O. Barišić, V. Rogalev, T. Schmitt, N. Nagaosa, and V. N. Strocov, 2016, Nat. Commun. **7**, 10386.

Cao, G., and P. Schlottmann, 2018, Rep. Prog. Phys. **81**, 042502.

Cao, G., W. Song, Y. Sun, and X. Lin, 2004, Solid State Commun. **131**, 331.

Cao, G., Y. Xin, C. Alexander, J. Crow, P. Schlottmann, M. Crawford, R. Harlow, and W. Marshall, 2002, Phys. Rev. B **66**, 214412.

Cao, Y., *et al.*, 2013, Nat. Phys. **9**, 499.

Cardona, M., and L. Ley, 1978, Eds., *Photoemission in Solids I: General Principles*, Topics in Applied Physics Vol. 26 (Springer, Berlin).

Caroli, C., D. Lederer-Rozenblatt, B. Roulet, and D. Saint-James, 1973, Phys. Rev. B **8**, 4552.

Castro Neto, A., F. Guinea, N. M. Peres, K. S. Novoselov, and A. K. Geim, 2009, Rev. Mod. Phys. **81**, 109.

Cattelan, M., and N. A. Fox, 2018, Nanomaterials **8**, 284.

Cava, R. J., B. Batlogg, J. Krajewski, R. Farrow, L. Rupp, Jr., A. White, K. Short, W. Peck, and T. Kometani, 1988, Nature (London) **332**, 814.

Chaix, L., *et al.*, 2017, Nat. Phys. **13**, 952.

Chang, C.-Z., *et al.*, 2013, Science **340**, 167.

Chang, J., M. Maansson, S. Pailhes, T. Claesson, O. Lipscombe, S. Hayden, L. Patthey, O. Tjernberg, and J. Mesot, 2013, Nat. Commun. **4**, 2559.

Chang, Y. J., G. Khalsa, L. Moreschini, A. L. Walter, A. Bostwick, K. Horn, A. H. MacDonald, and E. Rotenberg, 2013, Phys. Rev. B **87**, 115212.

Chatterjee, S., J. Trinckauf, T. Hänke, D. E. Shai, J. W. Harter, T. J. Williams, G. M. Luke, K. M. Shen, and J. Geck, 2013, Phys. Rev. Lett. **110**, 186401.

Chatterjee, U., *et al.*, 2011, Proc. Natl. Acad. Sci. U.S.A. **108**, 9346.

Chen, B., *et al.*, 2019, Nat. Commun. **10**, 4469.

Chen, C., J. Avila, E. Frantzeskakis, A. Levy, and M. C. Asensio, 2015, Nat. Commun. **6**, 8585.

Chen, C., *et al.*, 2012, Proc. Natl. Acad. Sci. U.S.A. **109**, 3694.

Chen, C., *et al.*, 2013, Sci. Rep. **3**, 2411.

Chen, H., *et al.*, 2009, Europhys. Lett. **85**, 17006.

Chen, H.-D., O. Vafek, A. Yazdani, and S.-C. Zhang, 2004, Phys. Rev. Lett. **93**, 187002.

Chen, P., Y.-H. Chan, X.-Y. Fang, Y. Zhang, M.-Y. Chou, S.-K. Mo, Z. Hussain, A.-V. Fedorov, and T.-C. Chiang, 2015, Nat. Commun. **6**, 8943.

Chen, P., W. W. Pai, Y.-H. Chan, W.-L. Sun, C.-Z. Xu, D.-S. Lin, M. Y. Chou, A.-V. Fedorov, and T.-C. Chiang, 2018, Nat. Commun. **9**, 2003.

Chen, Q. Y., *et al.*, 2017, Phys. Rev. B **96**, 045107.

Chen, S.-D., *et al.*, 2017, Phys. Rev. B **96**, 081109.

Chen, S.-D., *et al.*, 2019, Science **366**, 1099.

Chen, T., Z. Tesanovic, R. Liu, X. Chen, and C. Chien, 2008, Nature (London) **453**, 1224.

Chen, W., G. Khaliullin, and O. P. Sushkov, 2009, Phys. Rev. B **80**, 094519.

Chen, X., P. Dai, D. Feng, T. Xiang, and F.-C. Zhang, 2014, Natl. Sci. Rev. **1**, 371.

Chen, X., T. Wu, G. Wu, R. Liu, H. Chen, and D. Fang, 2008, Nature (London) **453**, 761.

Chen, X., *et al.*, 2015, Phys. Rev. B **92**, 075125.

Chen, Y., *et al.*, 2020, Nat. Phys. **16**, 218.

Chen, Y. J., *et al.*, 2019, Phys. Rev. X **9**, 041040.

Chen, Y. L., *et al.*, 2009, Science **325**, 178.

Chen, Y. L., *et al.*, 2010, Science **329**, 659.

Chiang, C.-T., M. Huth, A. Trützschler, F. O. Schumann, J. Kirschner, and W. Widdra, 2015, J. Electron Spectrosc. Relat. Phenom. **200**, 15.

Chiang, C.-T., A. Trützschler, M. Huth, R. Kamrla, F. O. Schumann, and W. Widdra, 2020, Prog. Surf. Sci. **95**, 100572.

Chiang, T. C., J. A. Knapp, M. Aono, and D. E. Eastman, 1980, Phys. Rev. B **21**, 3513.

Chiang, T.-C., 2000, Surf. Sci. Rep. **39**, 181.

Chiang, T.-C., J. Knapp, D. Eastman, and M. Aono, 1979, Solid State Commun. **31**, 917.

Choi, H. J., D. Roundy, H. Sun, M. L. Cohen, and S. G. Louie, 2002, Nature (London) **418**, 758.

Christianson, A., *et al.*, 2008, Nature (London) **456**, 930.

Chu, J.-H., J. G. Analytis, K. De Greve, P. L. McMahon, Z. Islam, Y. Yamamoto, and I. R. Fisher, 2010, Science **329**, 824.

Chu, J.-H., H.-H. Kuo, J. G. Analytis, and I. R. Fisher, 2012, Science **337**, 710.

Chuang, Y.-D., A. Gromko, A. Fedorov, Y. Aiura, K. Oka, Y. Ando, M. Lindroos, R. Markiewicz, A. Bansil, and D. Dessau, 2004, Phys. Rev. B **69**, 094515.

Chubukov, A., 2012, Annu. Rev. Condens. Matter Phys. **3**, 57.

Chubukov, A. V., and P. J. Hirschfeld, 2015, Phys. Today **68**, No. 6, 46.

Cilento, F., A. Crepaldi, G. Manzoni, A. Sterzi, M. Zacchigna, P. Bugnon, H. Berger, and F. Parmigiani, 2016, J. Electron Spectrosc. Relat. Phenom. **207**, 7.

Citrin, P. H., G. K. Wertheim, and Y. Baer, 1977, Phys. Rev. B **16**, 4256.

Coh, S., M. L. Cohen, and S. G. Louie, 2015, New J. Phys. **17**, 073027.

Collins, J. L., *et al.*, 2018, Nature (London) **564**, 390.

Colombier, E., S. Budko, N. Ni, and P. Canfield, 2009, Phys. Rev. B **79**, 224518.

Comin, R., *et al.*, 2012, Phys. Rev. Lett. **109**, 266406.

Cooper, R., *et al.*, 2009, Science **323**, 603.

Corder, C., P. Zhao, J. Bakalis, X. Li, M. D. Kershis, A. R. Muraca, M. G. White, and T. K. Allison, 2018, Struct. Dyn. **5**, 054301.

Cucchi, I., *et al.*, 2019, Nano Lett. **19**, 554.

Cuk, T., *et al.*, 2004, Phys. Rev. Lett. **93**, 117003.

Cvetkovic, V., and Z. Tesanovic, 2009, Europhys. Lett. **85**, 37002.

Dagotto, E., 2013, Rev. Mod. Phys. **85**, 849.

Dagotto, E., R. Joynt, A. Moreo, S. Bacci, and E. Gagliano, 1990, Phys. Rev. B **41**, 9049.

Dahm, T., V. Hinkov, S. Borisenko, A. Kordyuk, V. Zabolotnyy, J. Fink, B. Büchner, D. Scalapino, W. Hanke, and B. Keimer, 2009, Nat. Phys. **5**, 217.

Dai, P., 2015, Rev. Mod. Phys. **87**, 855.

Dai, P., J. Hu, and E. Dagotto, 2012, Nat. Phys. **8**, 709.

Dai, Y., *et al.*, 2015, Phys. Rev. X **5**, 031035.

Dallera, C., L. Duo, L. Braicovich, G. Panaccione, G. Paolicelli, B. Cowie, and J. Zegenhagen, 2004, Appl. Phys. Lett. **85**, 4532.

Damascelli, A., Z. Hussain, and Z.-X. Shen, 2003, Rev. Mod. Phys. **75**, 473.

Damascelli, A., *et al.*, 2000, Phys. Rev. Lett. **85**, 5194.

Damascelli, A., *et al.*, 2001, J. Electron Spectrosc. Relat. Phenom. **114**–**116**, 641.

Danzenbächer, S., *et al.*, 2011, Phys. Rev. Lett. **107**, 267601.

da Silva Neto, E. H., *et al.*, 2016, Sci. Adv. **2**, e1600782.

Davis, J. S., and D.-H. Lee, 2013, Proc. Natl. Acad. Sci. U.S.A. **110**, 17623.

Day, R., *et al.*, 2018, Phys. Rev. Lett. **121**, 076401.

Day, R. P., B. Zwartsenberg, I. S. Elfimov, and A. Damascelli, 2019, npj Quantum Mater. **4**, 54.

de Jong, S., Y. Huang, I. Santoso, F. Massee, R. Follath, O. Schwarzkopf, L. Patthey, M. Shi, and M. S. Golden, 2007, Phys. Rev. B **76**, 235117.

de la Torre, A., E. Hunter, A. Subedi, S. M. Walker, A. Tamai, T. Kim, M. Hoesch, R. S. Perry, A. Georges, and F. Baumberger, 2014, Phys. Rev. Lett. **113**, 256402.

de la Torre, A., *et al.*, 2015, Phys. Rev. Lett. **115**, 176402.

Deng, J., *et al.*, 2018, Nat. Mater. **17**, 1081.

Deng, K., *et al.*, 2016, Nat. Phys. **12**, 1105.

Deng, Y., Y. Yu, M. Z. Shi, Z. Guo, Z. Xu, J. Wang, X. H. Chen, and Y. Zhang, 2020, Science **367**, 895.

Denlinger, J., G.-H. Gweon, J. Allen, C. Olson, M. Maple, J. Sarrao, P. Armstrong, Z. Fisk, and H. Yamagami, 2001, J. Electron Spectrosc. Relat. Phenom. **117-118**, 347.

Dessau, D., B. Wells, Z.-X. Shen, W. Spicer, A. Arko, R. List, D. Mitzi, and A. Kapitulnik, 1991, Phys. Rev. Lett. **66**, 2160.

Devereaux, T., T. Cuk, Z.-X. Shen, and N. Nagaosa, 2004, Phys. Rev. Lett. **93**, 117004.

Dil, J. H., 2009, J. Phys. Condens. Matter **21**, 403001.

DiMasi, E., M. C. Aronson, J. F. Mansfield, B. Foran, and S. Lee, 1995, Phys. Rev. B **52**, 14516.

Ding, H., S.-C. Wang, H.-B. Yang, T. Takahashi, J. Campuzano, and Y. Maeno, 2001, Physica (Amsterdam) **364C-365C**, 594.

Ding, H., T. Yokoya, J. Campuzano, T. Takahashi, M. Randeria, M. Norman, T. Mochiku, K. Kadowaki, and J. Giapintzakis, 1996, Nature (London) **382**, 51.

Ding, H., *et al.*, 1995, Phys. Rev. Lett. **74**, 2784.

Ding, H., *et al.*, 2008, Europhys. Lett. **83**, 47001.

Ding, Y., *et al.*, 2019, Chin. Phys. Lett. **36**, 017402.

Dolgov, O. V., I. I. Mazin, D. Parker, and A. A. Golubov, 2009, Phys. Rev. B **79**, 060502.

Dong, C., H. Wang, Q. Mao, R. Khan, X. Zhou, C. Li, J. Yang, B. Chen, and M. Fang, 2013, J. Phys. Condens. Matter 25, 385701.

Dose, V., 1977, Appl. Phys. 14, 117.

Dose, V., 1985, Surf. Sci. Rep. 5, 337.

Douglas, J. F., et al., 2007, Nature (London) 446, E5.

Drachuck, G., E. Razzoli, G. Bazalitski, A. Kanigel, C. Niedermayer, M. Shi, and A. Keren, 2014, Nat. Commun. 5, 3390.

Drozdov, I. K., I. Pletikosić, C.-K. Kim, K. Fujita, G. Gu, J. S. Davis, P. Johnson, I. Božović, and T. Valla, 2018, Nat. Commun. 9, 5210.

Du, Z., et al., 2018, Nat. Phys. 14, 134.

Dudy, L., J. Denlinger, J. Allen, F. Wang, J. He, D. Hitchcock, A. Sekiyama, and S. Suga, 2013, J. Phys. Condens. Matter 25, 014007.

Durakiewicz, T., 2014, Philos. Mag. 94, 3723.

Duvjir, G., et al., 2018, Nano Lett. 18, 5432.

Dynes, R., V. Narayanamurti, and J. P. Garno, 1978, Phys. Rev. Lett. 41, 1509.

Dzero, M., K. Sun, V. Galitski, and P. Coleman, 2010, Phys. Rev. Lett. 104, 106408.

Dzero, M., J. Xia, V. Galitski, and P. Coleman, 2016, Annu. Rev. Condens. Matter Phys. 7, 249.

Dziawa, P., et al., 2012, Nat. Mater. 11, 1023.

Echenique, P., R. Berndt, E. Chulkov, T. Fauster, A. Goldmann, and U. Höfer, 2004, Surf. Sci. Rep. 52, 219.

Edkins, S. D., et al., 2019, Science 364, 976.

Eisaki, H., N. Kaneko, D. Feng, A. Damascelli, P. Mang, K. Shen, Z.-X. Shen, and M. Greven, 2004, Phys. Rev. B 69, 064512.

Eiter, H.-M., M. Lavagnini, R. Hackl, E. A. Nowadnick, A. F. Kemper, T. P. Devereaux, J.-H. Chu, J. G. Analytis, I. R. Fisher, and L. Degiorgi, 2013, Proc. Natl. Acad. Sci. U.S.A. 110, 64.

Elmers, H. J., et al., 2016, Phys. Rev. B 94, 201403.

Emery, N., C. Hérold, M. dAstuto, V. Garcia, C. Bellin, J. Marêché, P. Lagrange, and G. Loupias, 2005, Phys. Rev. Lett. 95, 087003.

Emery, V., 1987, Phys. Rev. Lett. 58, 2794.

Emery, V., and S. Kivelson, 1995, Nature (London) 374, 434.

Enderlein, C., Y. Kim, A. Bostwick, E. Rotenberg, and K. Horn, 2010, New J. Phys. 12, 033014.

Eriksson, M., J. F. van der Veen, and C. Quitmann, 2014 J. Synchrotron Radiat. 21, 837.

Essin, A. M., J. E. Moore, and D. Vanderbilt, 2009, Phys. Rev. Lett. 102, 146805.

Fadley, C. S., 2005, Nucl. Instrum. Methods Phys. Res., Sect. A 547, 24.

Fadley, C. S., 2013, J. Electron Spectrosc. Relat. Phenom. 190, 165.

Fan, Q., et al., 2015, Nat. Phys. 11, 946.

Fang, C., L. Lu, J. Liu, and L. Fu, 2016, Nat. Phys. 12, 936.

Fang, X.-Y., H. Hong, P. Chen, and T.-C. Chiang, 2017, Phys. Rev. B 95, 201409.

Fang, Y., et al., 2019, Adv. Mater. 31, 1901942.

Fauster, T., and W. Steinmann, 1995, in Photonic Probes of Surfaces, edited by P. Halevi (North-Holland, Amsterdam), pp. 347–411.

Fedorov, A., T. Valla, P. Johnson, Q. Li, G. Gu, and N. Koshizuka, 1999, Phys. Rev. Lett. 82, 2179.

Fedorov, A. V., et al., 2014, Nat. Commun. 5, 3257.

Fei, Z., T. Palomaki, S. Wu, W. Zhao, X. Cai, B. Sun, P. Nguyen, J. Finney, X. Xu, and D. H. Cobden, 2017, Nat. Phys. 13, 677.

Feibelman, P. J., and D. E. Eastman, 1974, Phys. Rev. B 10, 4932.

Fellner-Feldegg, H., U. Gelius, B. Wannberg, A. Nilsson, E. Basilier, and K. Siegbahn, 1974, J. Electron Spectrosc. Relat. Phenom. 5, 643.

Feng, B., et al., 2017, Phys. Rev. Lett. 118, 096401.

Feng, Y., et al., 2016, Proc. Natl. Acad. Sci. U.S.A. 113, 14656.

Fernandes, R. M., A. E. Böhmer, C. Meingast, and J. Schmalian, 2013, Phys. Rev. Lett. 111, 137001.

Fernandes, R. M., and A. V. Chubukov, 2017, Rep. Prog. Phys. 80, 014503.

Fernandes, R. M., A. V. Chubukov, and J. Schmalian, 2014, Nat. Phys. 10, 97.

Filipkowski, M., J. Budnick, and Z. Tan, 1990, Physica (Amsterdam) 167C, 35.

Flötotto, D., Y. Ota, Y. Bai, C. Zhang, K. Okazaki, A. Tsuzuki, T. Hashimoto, J. N. Eckstein, S. Shin, and T.-C. Chiang, 2018, Sci. Adv. 4, eaar7214.

Fominykh, N., J. Berakdar, J. Henk, and P. Bruno, 2002, Phys. Rev. Lett. 89, 086402.

Foo, M. L., Y. Wang, S. Watauchi, H. Zandbergen, T. He, R. J. Cava, and N. P. Ong, 2004, Phys. Rev. Lett. 92, 247001.

Fournier, D., et al., 2010, Nat. Phys. 6, 905.

Foury, P., and J. Pouget, 1993, Int. J. Mod. Phys. B 07, 3973.

Fradkin, E., S. A. Kivelson, and J. M. Tranquada, 2015, Rev. Mod. Phys. 87, 457.

Frantzeskakis, E., et al., 2013, Phys. Rev. X 3, 041024.

Franz, M., and A. Millis, 1998, Phys. Rev. B 58, 14572.

Fu, L., 2009, Phys. Rev. Lett. 103, 266801.

Fu, L., 2011, Phys. Rev. Lett. 106, 106802.

Fu, L., C. Kane, and E. Mele, 2007, Phys. Rev. Lett. 98, 106803.

Fu, L., and C. L. Kane, 2007, Phys. Rev. B 76, 045302.

Fu, L., and C. L. Kane, 2008, Phys. Rev. Lett. 100, 096407.

Fujimori, S.-i., 2016, J. Phys. Condens. Matter 28, 153002.

Fujimori, S.-i., A. Ino, T. Okane, A. Fujimori, K. Okada, T. Manabe, M. Yamashita, H. Kishida, and H. Okamoto, 2002, Phys. Rev. Lett. 88, 247601.

Fujimori, S.-i., et al., 2006, Phys. Rev. B 73, 125109.

Fukuzumi, Y., K. Mizuhashi, K. Takenaka, and S. Uchida, 1996, Phys. Rev. Lett. 76, 684.

Garrett, G. A., T. F. Albrecht, J. F. Whitaker, and R. Merlin, 1996, Phys. Rev. Lett. 77, 3661.

Gauthier, A., J. A. Sobota, N. Gauthier, K.-J. Xu, H. Pfau, C. R. Rotundu, Z.-X. Shen, and P. S. Kirchmann, 2020, J. Appl. Phys. 128, 093101.

Gauzzi, A., et al., 2016, Phys. Rev. B 94, 180509.

Gay, T. J., and F. B. Dunning, 1992, Rev. Sci. Instrum. 63, 1635.

Gazier, C., and J. Prescott, 1970, Phys. Lett. 32A, 425.

Ge, M., T. Qi, O. Korneta, D. De Long, P. Schlottmann, W. Crummett, and G. Cao, 2011, Phys. Rev. B 84, 100402.

Ge, Q., et al., 2013, Phys. Rev. X 3, 011020.

Ge, Z., C. Yan, H. Zhang, D. Agterberg, M. Weinert, and L. Li, 2019, Nano Lett. 19, 2497.

Geim, A., and K. Novoselov, 2007, Nat. Mater. 6, 183.

Gelius, U., B. Wannberg, P. Baltzer, H. Fellner-Feldegg, G. Carlsson, C.-G. Johansson, J. Larsson, P. Münger, and G. Vegerfors, 1990 J. Electron Spectrosc. Relat. Phenom. 52, 747.

Georges, A., L. de Medici, and J. Mravlje, 2013, Annu. Rev. Condens. Matter Phys. 4, 137.

Gerber, S., et al., 2017, Science 357, 71.

Ghiringhelli, G., et al., 2012, Science 337, 821.

Giamarchi, T., 2003, Quantum Physics in One Dimension, International Series of Monographs on Physics Vol. 121 (Clarendon, Oxford).

Gierz, I., M. Lindroos, H. Höchst, C. R. Ast, and K. Kern, 2012, Nano Lett. 12, 3900.

Gierz, I., J. C. Petersen, M. Mitrano, C. Cacho, I. C. E. Turcu, E. Springate, A. Stöhr, A. Köhler, U. Starke, and A. Cavalleri, 2013, Nat. Mater. 12, 1119.

Gierz, I., *et al.*, 2015, Phys. Rev. Lett. **114**, 125503.

Gollisch, H., N. v. Schwartzenberg, and R. Feder, 2006, Phys. Rev. B **74**, 075407.

Gomes, K. K., A. N. Pasupathy, A. Pushp, S. Ono, Y. Ando, and A. Yazdani, 2007, Nature (London) **447**, 569.

Gor'kov, L., 1958, Sov. Phys. JETP **34**, 505, http://jetp.ac.ru/cgi-bin/dn/e_007_03_0505.pdf.

Gotlieb, K., C.-Y. Lin, M. Serbyn, W. Zhang, C. L. Smallwood, C. Jozwiak, H. Eisaki, Z. Hussain, A. Vishwanath, and A. Lanzara, 2018, Science **362**, 1271.

Graf, J., C. Jozwiak, C. L. Smallwood, H. Eisaki, R. A. Kaindl, D.-H. Lee, and A. Lanzara, 2011, Nat. Phys. **7**, 805.

Graf, J., *et al.*, 2007, Phys. Rev. Lett. **98**, 067004.

Graham, K. S., J. J. Joyce, and T. Durakiewicz, 2013, Rev. Sci. Instrum. **84**, 093902.

Gray, A., *et al.*, 2010, Phys. Rev. B **82**, 205116.

Gray, A., *et al.*, 2013, Europhys. Lett. **104**, 17004.

Gray, A. X., 2014, J. Electron Spectrosc. Relat. Phenom. **195**, 399.

Gray, A. X., *et al.*, 2011, Nat. Mater. **10**, 759.

Greene, R. L., P. R. Mandal, N. R. Poniatowski, and T. Sarkar, 2020, Annu. Rev. Condens. Matter Phys. **11**, 213.

Grinenko, V., *et al.*, 2020, Nat. Phys. **16**, 789.

Gromko, A., A. Fedorov, Y.-D. Chuang, J. Koralek, Y. Aiura, Y. Yamaguchi, K. Oka, Y. Ando, and D. Dessau, 2003, Phys. Rev. B **68**, 174520.

Gros, C., B. Edegger, V. Muthukumar, and P. Anderson, 2006, Proc. Natl. Acad. Sci. U.S.A. **103**, 14298.

Grüner, G., 1994, *Density Waves in Solids* (Perseus, Cambridge, MA).

Guo, H., C. Ritter, and A. Komarek, 2016, Phys. Rev. B **94**, 161102.

Gurvitch, M., and A. Fiory, 1987, Phys. Rev. Lett. **59**, 1337.

Gutzwiller, M. C., 1963, Phys. Rev. Lett. **10**, 159.

Gweon, G.-H., J. D. Denlinger, J. A. Clack, J. W. Allen, C. G. Olson, E. DiMasi, M. C. Aronson, B. Foran, and S. Lee, 1998, Phys. Rev. Lett. **81**, 886.

Gweon, G.-H., T. Sasagawa, S. Zhou, J. Graf, H. Takagi, D.-H. Lee, and A. Lanzara, 2004, Nature (London) **430**, 187.

Haight, R., 1995, Surf. Sci. Rep. **21**, 275.

Haight, R., and D. R. Peale, 1994, Rev. Sci. Instrum. **65**, 1853.

Haldane, F. D. M., 2017, Rev. Mod. Phys. **89**, 040502.

Hamidian, M., *et al.*, 2016, Nature (London) **532**, 343.

Hand, M., H. Wang, S. S. Dhesi, and K. Sawhney, 2016, J. Synchrotron Radiat. **23**, 176.

Hao, Y.-J., *et al.*, 2019, Phys. Rev. X **9**, 041038.

Hardy, F., *et al.*, 2010, Europhys. Lett. **91**, 47008.

Hardy, W., D. Bonn, D. Morgan, R. Liang, and K. Zhang, 1993, Phys. Rev. Lett. **70**, 3999.

Harris, J., Y. Yan, P. Matl, N. P. Ong, P. Anderson, T. Kimura, and K. Kitazawa, 1995, Phys. Rev. Lett. **75**, 1391.

Hartnoll, S., A. Lucas, and S. Sachdev, 2018, *Holographic Quantum Matter* (MIT Press, Cambridge, MA).

Hasan, M., *et al.*, 2004, Phys. Rev. Lett. **92**, 246402.

Hasan, M. Z., and C. L. Kane, 2010, Rev. Mod. Phys. **82**, 3045.

Hashimoto, M., I. M. Vishik, R.-H. He, T. P. Devereaux, and Z.-X. Shen, 2014, Nat. Phys. **10**, 483.

Hashimoto, M., *et al.*, 2008, Phys. Rev. B **77**, 094516.

Hashimoto, M., *et al.*, 2010, Nat. Phys. **6**, 414.

Hashimoto, M., *et al.*, 2011, Phys. Rev. Lett. **106**, 167003.

Hashimoto, M., *et al.*, 2015, Nat. Mater. **14**, 37.

Hatch, R. C., M. Bianchi, D. Guan, S. Bao, J. Mi, B. B. Iversen, L. Nilsson, L. Hornekær, and P. Hofmann, 2011, Phys. Rev. B **83**, 241303.

Haule, K., and G. Kotliar, 2009, New J. Phys. **11**, 025021.

Haverkort, M. W., I. S. Elfimov, L. H. Tjeng, G. A. Sawatzky, and A. Damascelli, 2008, Phys. Rev. Lett. **101**, 026406.

He, J., *et al.*, 2013, Phys. Rev. Lett. **111**, 107005.

He, J., *et al.*, 2014, Proc. Natl. Acad. Sci. U.S.A. **111**, 18501.

He, J., *et al.*, 2015a, Sci. Rep. **5**, 8533.

He, J., *et al.*, 2015b, Nat. Mater. **14**, 577.

He, J., *et al.*, 2016, Phys. Rev. Lett. **117**, 267201.

He, J., *et al.*, 2019, Proc. Natl. Acad. Sci. U.S.A. **116**, 3449.

He, R.-H., *et al.*, 2009, Nat. Phys. **5**, 119.

He, R.-H., *et al.*, 2011a, Science **331**, 1579.

He, R.-H., *et al.*, 2011b, New J. Phys. **13**, 013031.

He, S., *et al.*, 2013, Nat. Mater. **12**, 605.

He, Y., Y. Wang, and Z.-X. Shen, 2017, Rev. Sci. Instrum. **88**, 073903.

He, Y., *et al.*, 2016, Rev. Sci. Instrum. **87**, 011301.

He, Y., *et al.*, 2018a, Science **362**, 62.

He, Y., *et al.*, 2018b, Phys. Rev. B **98**, 035102.

He, Y., *et al.*, 2020, arXiv:2009.10932.

Hedin, L., and J. Lee, 2002, J. Electron Spectrosc. Relat. Phenom. **124**, 289.

Heinzmann, U., and J. H. Dil, 2012, J. Phys. Condens. Matter **24**, 173001.

Hellmann, S., K. Rossnagel, M. Marczynski-Bühlow, and L. Kipp, 2009, Phys. Rev. B **79**, 035402.

Hellmann, S., *et al.*, 2010, Phys. Rev. Lett. **105**, 187401.

Hellmann, S., *et al.*, 2012, New J. Phys. **14**, 013062.

Hengsberger, M., F. Baumberger, H. J. Neff, T. Greber, and J. Osterwalder, 2008, Phys. Rev. B **77**, 085425.

Hengsberger, M., R. Frésard, D. Purdie, P. Segovia, and Y. Baer, 1999, Phys. Rev. B **60**, 10796.

Hewson, A. C., 1993, *The Kondo Problem to Heavy Fermions* (Cambridge University Press, Cambridge, England).

Hicks, C. W., *et al.*, 2014, Science **344**, 283.

Hillebrecht, F. U., *et al.*, 2002, Rev. Sci. Instrum. **73**, 1229.

Himpsel, F., 1990, Surf. Sci. Rep. **12**, 3.

Himpsel, F. J., and D. E. Eastman, 1978, Phys. Rev. B **18**, 5236.

Himpsel, F. J., and D. E. Eastman, 1980, Phys. Rev. B **21**, 3207.

Himpsel, F. J., and I. Lindau, 2009, in *Digital Encyclopedia of Applied Physics* (Wiley-VCH, Weinheim), pp. 285–318.

Hinks, D., H. Claus, and J. Jorgensen, 2001, Nature (London) **411**, 457.

Hirschfeld, P., M. Korshunov, and I. Mazin, 2011, Rep. Prog. Phys. **74**, 124508.

Hirschfeld, P. J., 2016, C.R. Phys. **17**, 197.

Hlawenka, P., *et al.*, 2018, Nat. Commun. **9**, 517.

Hofmann, S., 2013, *Auger- and X-Ray Photoelectron Spectroscopy in Materials Science*, Springer Series in Surface Sciences Vol. 49 (Springer, Berlin).

Hong, S. H., J. M. Bok, W. Zhang, J. He, X. Zhou, C. M. Varma, and H.-Y. Choi, 2014, Phys. Rev. Lett. **113**, 057001.

Hopkinson, J., J. Pendry, and D. Titterington, 1980, Comput. Phys. Commun. **19**, 69.

Horiba, K., M. Kitamura, K. Yoshimatsu, M. Minohara, E. Sakai, M. Kobayashi, A. Fujimori, and H. Kumigashira, 2016, Phys. Rev. Lett. **116**, 076401.

Horio, M., *et al.*, 2016, Nat. Commun. **7**, 10567.

Horio, M., *et al.*, 2018, Phys. Rev. Lett. **121**, 077004.

Horio, M., *et al.*, 2019, Phys. Rev. B **100**, 054517.

Hosono, H., A. Yamamoto, H. Hiramatsu, and Y. Ma, 2018, Mater. Today **21**, 278.

Hossain, M., *et al.*, 2008, Nat. Phys. **4**, 527.

Hsieh, D., D. Qian, L. Wray, Y. Xia, Y. S. Hor, R. J. Cava, and M. Z. Hasan, 2008, Nature (London) **452**, 970.

Hsieh, D., *et al.*, 2009a, Nature (London) **460**, 1101.

Hsieh, D., *et al.*, 2009b, Science **323**, 919.

Hsieh, T. H., H. Lin, J. Liu, W. Duan, A. Bansil, and L. Fu, 2012, Nat. Commun. **3**, 982.

Hsu, F.-C., *et al.*, 2008, Proc. Natl. Acad. Sci. U.S.A. **105**, 14262.

Huang, L., *et al.*, 2016, Nat. Mater. **15**, 1155.

Huang, Q., Y. Qiu, W. Bao, M. Green, J. Lynn, Y. Gasparovic, T. Wu, G. Wu, and X. Chen, 2008, Phys. Rev. Lett. **101**, 257003.

Huang, T.-W., C.-M. Lin, H.-S. Sheu, T.-L. Hung, K.-W. Yeh, P.-C. Hsu, Y.-L. Huang, F.-C. Hsu, and M.-K. Wu, 2010, Physica (Amsterdam) **470C**, S502.

Huang, Z., and K.-J. Kim, 2007, Phys. Rev. ST Accel. Beams **10**, 034801.

Huang, Z., Y. Pu, H. Xu, D. Xu, Q. Song, X. Lou, C. Wen, R. Peng, and D. Feng, 2016, 2D Mater. **3**, 014005.

Hubbard, J., 1963, Proc. R. Soc. A **276**, 238.

Hüfner, S., 2003, *Photoelectron Spectroscopy*, Advanced Texts in Physics (Springer, Berlin).

Huh, S., *et al.*, 2020, Commun. Phys. **3**, 52.

Hussey, N., J. Buhot, and S. Licciardello, 2018, Rep. Prog. Phys. **81**, 052501.

Hussey, N., R. Cooper, X. Xu, Y. Wang, I. Mouzopoulou, B. Vignolle, and C. Proust, 2011, Phil. Trans. R. Soc. A **369**, 1626.

Huth, M., C.-T. Chiang, A. Trützschler, F. O. Schumann, J. Kirschner, and W. Widdra, 2014, Appl. Phys. Lett. **104**, 061602.

Hwang, C., D. A. Siegel, S.-K. Mo, W. Regan, A. Ismach, Y. Zhang, A. Zettl, and A. Lanzara, 2012, Sci. Rep. **2**, 590.

Hwang, H., B. Batlogg, H. Takagi, H. Kao, J. Kwo, R. J. Cava, J. Krajewski, and W. Peck, Jr., 1994, Phys. Rev. Lett. **72**, 2636.

Ideta, S., *et al.*, 2013, J. Phys. Conf. Ser. **428**, 012039.

Imada, M., A. Fujimori, and Y. Tokura, 1998, Rev. Mod. Phys. **70**, 1039.

Imai, T., C. Slichter, K. Yoshimura, M. Katoh, and K. Kosuge, 1993, Phys. Rev. Lett. **71**, 1254.

Ingle, N., *et al.*, 2005, Phys. Rev. B **72**, 205114.

Ino, A., C. Kim, M. Nakamura, T. Yoshida, T. Mizokawa, A. Fujimori, Z.-X. Shen, T. Kakeshita, H. Eisaki, and S. Uchida, 2002, Phys. Rev. B **65**, 094504.

Irmer, N., F. Frentzen, R. David, P. Stoppmanns, B. Schmiedeskamp, and U. Heinzmann, 1995, Surf. Sci. **331–333**, 1147.

Ishida, K., H. Mukuda, Y. Kitaoka, K. Asayama, Z. Mao, Y. Mori, and Y. Maeno, 1998, Nature (London) **396**, 658.

Ishida, Y., and S. Shin, 2018, Rev. Sci. Instrum. **89**, 043903.

Ishizaka, K., *et al.*, 2007, Phys. Rev. Lett. **98**, 047003.

Ishizaka, K., *et al.*, 2011, Nat. Mater. **10**, 521.

Iwasawa, H., P. Dudin, K. Inui, T. Masui, T. K. Kim, C. Cacho, and M. Hoesch, 2019, Phys. Rev. B **99**, 140510.

Iwasawa, H., E. F. Schwier, M. Arita, A. Ino, H. Namatame, M. Taniguchi, Y. Aiura, and K. Shimada, 2017, Ultramicroscopy **182**, 85.

Iwasawa, H., H. Takita, K. Goto, W. Mansuer, T. Miyashita, E. F. Schwier, A. Ino, K. Shimada, and Y. Aiura, 2018, Sci. Rep. **8**, 1.

Iwasawa, H., Y. Yoshida, I. Hase, K. Shimada, H. Namatame, M. Taniguchi, and Y. Aiura, 2012, Phys. Rev. Lett. **109**, 066404.

Iwasawa, H., Y. Yoshida, I. Hase, K. Shimada, H. Namatame, M. Taniguchi, and Y. Aiura, 2013, Sci. Rep. **3**, 1930.

Iwasawa, H., *et al.*, 2005, Phys. Rev. B **72**, 104514.

Iwasawa, H., *et al.*, 2007, Physica (Amsterdam) **463C–465C**, 52.

Iwasawa, H., *et al.*, 2008, Phys. Rev. Lett. **101**, 157005.

Iwaya, K., *et al.*, 2007, Phys. Rev. Lett. **99**, 057208.

Jandke, J., F. Yang, P. Hlobil, T. Engelhardt, D. Rau, K. Zakeri, C. Gao, J. Schmalian, and W. Wulfhekel, 2019, Phys. Rev. B **100**, 020503.

Jang, S., J. D. Denlinger, J. W. Allen, V. S. Zapf, M. B. Maple, J. N. Kim, B. G. Jang, and J. H. Shim, 2020, Proc. Natl. Acad. Sci. U.S.A. **117**, 23467.

Ji, F., T. Shi, M. Ye, W. Wan, Z. Liu, J. Wang, T. Xu, and S. Qiao, 2016, Phys. Rev. Lett. **116**, 177601.

Jia, T., Z. Chen, S. N. Rebec, M. Hashimoto, D. Lu, T. P. Devereaux, D.-H. Lee, R. G. Moore, and Z.-X. Shen, 2021 Adv. Sci. (in press), 10.1002/advs.202003454.

Jiang, J., *et al.*, 2013, Nat. Commun. **4**, 3010.

Jiang, J., *et al.*, 2018, Phys. Rev. Mater. **2**, 024201.

Jiang, S., H. Xing, G. Xuan, C. Wang, Z. Ren, C. Feng, J. Dai, Z. Xu, and G. Cao, 2009, J. Phys. Condens. Matter **21**, 382203.

Jin, W., *et al.*, 2013, Phys. Rev. Lett. **111**, 106801.

Johannes, M., and I. Mazin, 2008, Phys. Rev. B **77**, 165135.

Johannsen, J. C., *et al.*, 2013, Phys. Rev. Lett. **111**, 027403.

Johnson, P., and J. Davenport, 1985, Phys. Rev. B **31**, 7521.

Johnson, P., H.-B. Yang, J. Rameau, G. Gu, Z.-H. Pan, T. Valla, M. Weinert, and A. Fedorov, 2015, Phys. Rev. Lett. **114**, 167001.

Johnston, D. C., 2010, Adv. Phys. **59**, 803.

Johnston, S., F. Vernay, B. Moritz, Z.-X. Shen, N. Nagaosa, J. Zaanen, and T. Devereaux, 2010, Phys. Rev. B **82**, 064513.

Johnston, S., I. Vishik, W. Lee, F. Schmitt, S. Uchida, K. Fujita, S. Ishida, N. Nagaosa, Z. Shen, and T. Devereaux, 2012, Phys. Rev. Lett. **108**, 166404.

Jovic, V., *et al.*, 2017, Nano Lett. **17**, 7339.

Joynt, R., 1999, Science **284**, 777.

Jozwiak, C., J. Graf, G. Lebedev, N. Andresen, A. K. Schmid, A. V. Fedorov, F. El Gabaly, W. Wan, A. Lanzara, and Z. Hussain, 2010, Rev. Sci. Instrum. **81**, 053904.

Jozwiak, C., J. A. Sobota, K. Gotlieb, A. F. Kemper, C. R. Rotundu, R. J. Birgeneau, Z. Hussain, D.-H. Lee, Z.-X. Shen, and A. Lanzara, 2016, Nat. Commun. **7**, 13143.

Jozwiak, C., *et al.*, 2011, Phys. Rev. B **84**, 165113.

Jozwiak, C., *et al.*, 2013, Nat. Phys. **9**, 293.

Julien, M.-H., 2003, Physica (Amsterdam) **329B–333B**, 693.

Jung, W., *et al.*, 2011, Phys. Rev. B **84**, 245435.

Kamihara, Y., H. Hiramatsu, M. Hirano, R. Kawamura, H. Yanagi, T. Kamiya, and H. Hosono, 2006, J. Am. Chem. Soc. **128**, 10012.

Kamihara, Y., T. Watanabe, M. Hirano, and H. Hosono, 2008, J. Am. Chem. Soc. **130**, 3296.

Kaminski, A., and H. M. Fretwell, 2005, New J. Phys. **7**, 98.

Kaminski, A., T. Kondo, T. Takeuchi, and G. Gu, 2015, Philos. Mag. **95**, 453.

Kaminski, A., S. Rosenkranz, H. Fretwell, Z. Li, H. Raffy, M. Randeria, M. Norman, and J. Campuzano, 2003, Phys. Rev. Lett. **90**, 207003.

Kaminski, A., S. Rosenkranz, H. Fretwell, M. Norman, M. Randeria, J. Campuzano, J. Park, Z. Li, and H. Raffy, 2006, Phys. Rev. B **73**, 174511.

Kaminski, A., S. Rosenkranz, M. R. Norman, M. Randeria, Z. Z. Li, H. Raffy, and J. C. Campuzano, 2016, Phys. Rev. X **6**, 031040.

Kaminski, A., *et al.*, 2002, Nature (London) **416**, 610.

Kampf, A. P., and J. Schrieffer, 1990, Phys. Rev. B **42**, 7967.

Kanamori, J., 1963, Prog. Theor. Phys. **30**, 275.

Kanigel, A., *et al.*, 2006, Nat. Phys. **2**, 447.

Kargarian, M., M. Randeria, and Y.-M. Lu, 2016, Proc. Natl. Acad. Sci. U.S.A. **113**, 8648.

Karkare, S., W. Wan, J. Feng, T. C. Chiang, and H. A. Padmore, 2017, Phys. Rev. B **95**, 075439.

Kartsovnik, M., *et al.*, 2011, New J. Phys. **13**, 015001.

Kasahara, S., *et al.*, 2010, Phys. Rev. B **81**, 184519.

Kasahara, S., *et al.*, 2012, Nature (London) **486**, 382.

Kastl, C., *et al.*, 2019, ACS Nano **13**, 1284.

Kastner, M., R. Birgeneau, G. Shirane, and Y. Endoh, 1998, Rev. Mod. Phys. **70**, 897.

Keimer, B., S. A. Kivelson, M. R. Norman, S. Uchida, and J. Zaanen, 2015, Nature (London) **518**, 179.

Keimer, B., *et al.*, 1992, Phys. Rev. B **46**, 14034.

Kemper, A. F., O. Abdurazakov, and J. K. Freericks, 2018, Phys. Rev. X **8**, 041009.

Kessler, J., 1985, *Polarized Electrons* (Springer, Berlin).

Kevan, S., D. Rosenblatt, D. Denley, B.-C. Lu, and D. Shirley, 1978, Phys. Rev. Lett. **41**, 1565.

Khasanov, A., S. C. Bhargava, J. G. Stevens, J. Jiang, J. D. Weiss, E. E. Hellstrom, and A. Nath, 2011, J. Phys. Condens. Matter **23**, 202201.

Khasanov, R., M. Bendele, A. Bussmann-Holder, and H. Keller, 2010, Phys. Rev. B **82**, 212505.

Kim, B., H. Ohsumi, T. Komesu, S. Sakai, T. Morita, H. Takagi, and T.-h. Arima, 2009, Science **323**, 1329.

Kim, B., *et al.*, 2006, Nat. Phys. **2**, 397.

Kim, B., *et al.*, 2008, Phys. Rev. Lett. **101**, 076402.

Kim, C., A. Matsuura, Z.-X. Shen, N. Motoyama, H. Eisaki, S. Uchida, T. Tohyama, and S. Maekawa, 1996, Phys. Rev. Lett. **77**, 4054.

Kim, C., *et al.*, 2011, J. Phys. Chem. Solids **72**, 556.

Kim, J., S. S. Baik, S. H. Ryu, Y. Sohn, S. Park, B.-G. Park, J. Denlinger, Y. Yi, H. J. Choi, and K. S. Kim, 2015, Science **349**, 723.

Kim, J., M. Daghofer, A. Said, T. Gog, J. Van den Brink, G. Khaliullin, and B. Kim, 2014, Nat. Commun. **5**, 4453.

Kim, M., J. Mravlje, M. Ferrero, O. Parcollet, and A. Georges, 2018, Phys. Rev. Lett. **120**, 126401.

Kim, S.-K., and J. Kortright, 2001, Phys. Rev. Lett. **86**, 1347.

Kim, Y., *et al.*, 2011, Phys. Rev. B **83**, 064509.

Kim, Y. K., O. Krupin, J. Denlinger, A. Bostwick, E. Rotenberg, Q. Zhao, J. Mitchell, J. Allen, and B. Kim, 2014, Science **345**, 187.

Kim, Y. K., N. Sung, J. Denlinger, and B. Kim, 2016, Nat. Phys. **12**, 37.

King, D., D. Dessau, A. Loeser, Z. Shen, and B. Wells, 1995, J. Phys. Chem. Solids **56**, 1865.

King, P., S. M. Walker, A. Tamai, A. De La Torre, T. Eknapakul, P. Buaphet, S.-K. Mo, W. Meevasana, M. Bahramy, and F. Baumberger, 2014, Nat. Commun. **5**, 3414.

King, P., *et al.*, 2012, Phys. Rev. Lett. **108**, 117602.

King, P. D. C., *et al.*, 2011a, Phys. Rev. Lett. **106**, 127005.

King, P. D. C., *et al.*, 2011b, Phys. Rev. Lett. **107**, 096802.

Kirschner, J., 1985, *Polarized Electrons at Surfaces*, 1st ed., Springer Tracts in Modern Physics (Springer-Verlag, Berlin).

Kiss, T., T. Shimojima, K. Ishizaka, A. Chainani, T. Togashi, T. Kanai, X.-Y. Wang, C.-T. Chen, S. Watanabe, and S. Shin, 2008, Rev. Sci. Instrum. **79**, 023106.

Klintberg, E. L., S. K. Goh, S. Kasahara, Y. Nakai, K. Ishida, M. Sutherland, T. Shibauchi, Y. Matsuda, and T. Terashima, 2010, J. Phys. Soc. Jpn. **79**, 123706.

Klitzing, K. v., G. Dorda, and M. Pepper, 1980, Phys. Rev. Lett. **45**, 494.

Kogar, A., *et al.*, 2017, Science **358**, 1314.

Kohno, M., 2012, Phys. Rev. Lett. **108**, 076401.

Koitzsch, A., S. Borisenko, A. Kordyuk, T. Kim, M. Knupfer, J. Fink, H. Berger, and R. Follath, 2004, Phys. Rev. B **69**, 140507.

Koitzsch, A., *et al.*, 2004, Phys. Rev. B **69**, 220505.

Kondo, T., Y. Hamaya, A. D. Palczewski, T. Takeuchi, J. Wen, Z. Xu, G. Gu, J. Schmalian, and A. Kaminski, 2011, Nat. Phys. **7**, 21.

Kondo, T., R. Khasanov, T. Takeuchi, J. Schmalian, and A. Kaminski, 2009, Nature (London) **457**, 296.

Kondo, T., W. Malaeb, Y. Ishida, T. Sasagawa, H. Sakamoto, T. Takeuchi, T. Tohyama, and S. Shin, 2015, Nat. Commun. **6**, 7699.

Kondo, T., Y. Nakashima, W. Malaeb, Y. Ishida, Y. Hamaya, T. Takeuchi, and S. Shin, 2013, Phys. Rev. Lett. **110**, 217006.

Kondo, T., A. D. Palczewski, Y. Hamaya, T. Takeuchi, J. Wen, Z. Xu, G. Gu, and A. Kaminski, 2013, Phys. Rev. Lett. **111**, 157003.

Kondo, T., T. Takeuchi, T. Yokoya, S. Tsuda, S. Shin, and U. Mizutani, 2004, J. Electron Spectrosc. Relat. Phenom. **137**–**140**, 663.

Kondo, T., *et al.*, 2010, Phys. Rev. B **81**, 060507.

Kondo, T., *et al.*, 2013, Phys. Rev. Lett. **110**, 217601.

Kondo, T., *et al.*, 2015, Nat. Commun. **6**, 10042.

Konig, M., S. Wiedmann, C. Brune, A. Roth, H. Buhmann, L. W. Molenkamp, X.-L. Qi, and S.-C. Zhang, 2007, Science **318**, 766.

Kontani, H., T. Saito, and S. Onari, 2011, Phys. Rev. B **84**, 024528.

Koralek, J. D., J. F. Douglas, N. C. Plumb, J. D. Griffith, S. T. Cundiff, H. C. Kapteyn, M. M. Murnane, and D. S. Dessau, 2007, Rev. Sci. Instrum. **78**, 053905.

Koralek, J. D., *et al.*, 2006, Phys. Rev. Lett. **96**, 017005.

Kordyuk, A., S. Borisenko, M. Knupfer, and J. Fink, 2003, Phys. Rev. B **67**, 064504.

Kordyuk, A. A., S. V. Borisenko, A. Koitzsch, J. Fink, M. Knupfer, and H. Berger, 2005, Phys. Rev. B **71**, 214513.

Kotsugi, M., W. Kuch, F. Offi, L. I. Chelaru, and J. Kirschner, 2003, Rev. Sci. Instrum. **74**, 2754.

Kouzakov, K. A., and J. Berakdar, 2003, Phys. Rev. Lett. **91**, 257007.

Krömker, B., M. Escher, D. Funnemann, D. Hartung, H. Engelhard, and J. Kirschner, 2008, Rev. Sci. Instrum. **79**, 053702.

Kummer, K., *et al.*, 2015, Phys. Rev. X **5**, 011028.

Kunisada, S., *et al.*, 2020, Science **369**, 833.

Kuroda, K., *et al.*, 2017, Nat. Mater. **16**, 1090.

Kuroki, K., and R. Arita, 2007, J. Phys. Soc. Jpn. **76**, 083707.

Kushwaha, P., *et al.*, 2015, Sci. Adv. **1**, e1500692.

Kutnyakhov, D., *et al.*, 2020, Rev. Sci. Instrum. **91**, 013109.

Kuzmicheva, T. E., S. A. Kuzmichev, M. Mikheev, Y. G. Ponomarev, S. Tchesnokov, V. M. Pudalov, E. P. Khlybov, and N. Zhigadlo, 2014, Phys. Usp. **57**, 819.

Lahoud, E., O. N. Meetei, K. Chaska, A. Kanigel, and N. Trivedi, 2014, Phys. Rev. Lett. **112**, 206402.

Lai, K., A. Takemori, S. Miyasaka, F. Engetsu, H. Mukuda, and S. Tajima, 2014, Phys. Rev. B **90**, 064504.

Lambropoulos, P., 1974, Phys. Rev. A **9**, 1992.

Lanzara, A., *et al.*, 2001, Nature (London) **412**, 510.

LaShell, S., B. McDougall, and E. Jensen, 1996, Phys. Rev. Lett. **77**, 3419.

Lebegue, S., 2007, Phys. Rev. B **75**, 035110.

Lee, C.-C., W.-G. Yin, and W. Ku, 2009, Phys. Rev. Lett. **103**, 267001.

Lee, D.-H., 2018, Annu. Rev. Condens. Matter Phys. **9**, 261.

Lee, J., M. Allan, M. Wang, J. Farrell, S. Grigera, F. Baumberger, J. Davis, and A. Mackenzie, 2009, Nat. Phys. **5**, 800.

Lee, J., *et al.*, 2014, Nature (London) **515**, 245.

Lee, P. A., 2014, Phys. Rev. X **4**, 031017.

Lee, P. A., N. Nagaosa, and X.-G. Wen, 2006, Rev. Mod. Phys. **78**, 17.

Lee, S. H., *et al.*, 2019, Phys. Rev. Research **1**, 012011.

Lee, W., W. Meevasana, S. Johnston, D. Lu, I. Vishik, R. Moore, H. Eisaki, N. Kaneko, T. Devereaux, and Z. Shen, 2008, Phys. Rev. B **77**, 140504.

Lee, W., I. Vishik, K. Tanaka, D. Lu, T. Sasagawa, N. Nagaosa, T. Devereaux, Z. Hussain, and Z.-X. Shen, 2007, Nature (London) **450**, 81.

Legros, A., *et al.*, 2019, Nat. Phys. **15**, 142.

Leong, Z., C. Setty, K. Limtragool, and P. W. Phillips, 2017, Phys. Rev. B **96**, 205101.

Le Tacon, M., A. Bosak, S. Souliou, G. Dellea, T. Loew, R. Heid, K. Bohnen, G. Ghiringhelli, M. Krisch, and B. Keimer, 2014, Nat. Phys. **10**, 52.

Leuenberger, D., J. A. Sobota, S.-L. Yang, A. F. Kemper, P. Giraldo-Gallo, R. G. Moore, I. R. Fisher, P. S. Kirchmann, T. P. Devereaux, and Z.-X. Shen, 2015, Phys. Rev. B **91**, 201106.

Lev, L., *et al.*, 2015, Phys. Rev. Lett. **114**, 237601.

Levinson, H. J., E. W. Plummer, and P. J. Feibelman, 1979, Phys. Rev. Lett. **43**, 952.

Li, F., and G. A. Sawatzky, 2018, Phys. Rev. Lett. **120**, 237001.

Li, G., *et al.*, 2014, Science **346**, 1208.

Li, H., X. Zhou, S. Parham, T. J. Reber, H. Berger, G. B. Arnold, and D. S. Dessau, 2018, Nat. Commun. **9**, 26.

Li, H., *et al.*, 2018, arXiv:1809.02194.

Li, H., *et al.*, 2019, Phys. Rev. X **9**, 041039.

Li, J., Y. Li, S. Du, Z. Wang, B.-L. Gu, S.-C. Zhang, K. He, W. Duan, and Y. Xu, 2019, Sci. Adv. **5**, eaaw5685.

Li, J., *et al.*, 2012, Phys. Rev. B **85**, 214509.

Li, L., P. Kong, T. Qi, C. Jin, S. Yuan, L. E. DeLong, P. Schlottmann, and G. Cao, 2013, Phys. Rev. B **87**, 235127.

Li, W., *et al.*, 2019, Proc. Natl. Acad. Sci. U.S.A. **116**, 12156.

Li, Y., J. Jiang, H. Yang, D. Prabhakaran, Z. Liu, L. Yang, and Y. Chen, 2018, Phys. Rev. B **97**, 115118.

Li, Z., G. Antonius, M. Wu, F. H. da Jornada, and S. G. Louie, 2019, Phys. Rev. Lett. **122**, 186402.

Li, Z.-X., T. Devereaux, and D.-H. Lee, 2019, Phys. Rev. B **100**, 241101.

Li, Z.-X., F. Wang, H. Yao, and D.-H. Lee, 2016, Sci. Bull. **61**, 925.

Liang, T., Q. Gibson, M. N. Ali, M. Liu, R. J. Cava, and N. P. Ong, 2015, Nat. Mater. **14**, 280.

Liebsch, A., 1974, Phys. Rev. Lett. **32**, 1203.

Lin, C.-H., T. Berlijn, L. Wang, C.-C. Lee, W.-G. Yin, and W. Ku, 2011, Phys. Rev. Lett. **107**, 257001.

Lin, Z., *et al.*, 2008, Chin. Phys. Lett. **25**, 4402.

Lindroos, M., 1982, Phys. Scr. **25**, 788.

Liu, C., *et al.*, 2011, Phys. Rev. B **84**, 020509.

Liu, C., *et al.*, 2014, Phys. Rev. B **90**, 045127.

Liu, C.-C., H. Jiang, and Y. Yao, 2011, Phys. Rev. B **84**, 195430.

Liu, C.-X., H. Zhang, B. Yan, X.-L. Qi, T. Frauenheim, X. Dai, Z. Fang, and S.-C. Zhang, 2010, Phys. Rev. B **81**, 041307.

Liu, D., *et al.*, 2012, Nat. Commun. **3**, 931.

Liu, D., *et al.*, 2018, Phys. Rev. X **8**, 031033.

Liu, D. F., *et al.*, 2019, Science **365**, 1282.

Liu, G., *et al.*, 2008, Rev. Sci. Instrum. **79**, 023105.

Liu, G., *et al.*, 2009, Phys. Rev. B **80**, 134519.

Liu, Q., C.-X. Liu, C. Xu, X.-L. Qi, and S.-C. Zhang, 2009, Phys. Rev. Lett. **102**, 156603.

Liu, Q., *et al.*, 2018, Phys. Rev. X **8**, 041056.

Liu, R., *et al.*, 2009, Nature (London) **459**, 64.

Liu, T., *et al.*, 2010, Nat. Mater. **9**, 718.

Liu, W., *et al.*, 2020, Nat. Commun. **11**, 5688.

Liu, X., T. Galfsky, Z. Sun, F. Xia, E.-c. Lin, Y.-H. Lee, S. Kéna-Cohen, and V. M. Menon, 2015, Nat. Photonics **9**, 30.

Liu, X., *et al.*, 2014, Nat. Commun. **5**, 5047.

Liu, Y., L. Zhang, M. Brinkley, G. Bian, T. Miller, and T.-C. Chiang, 2010, Phys. Rev. Lett. **105**, 136804.

Liu, Y., *et al.*, 2020, Rev. Sci. Instrum. **91**, 013102.

Liu, Z., *et al.*, 2013, Phys. Rev. Lett. **110**, 037003.

Liu, Z. K., *et al.*, 2014a, Nat. Mater. **13**, 677.

Liu, Z. K., *et al.*, 2014b, Science **343**, 864.

Liu, Z. K., *et al.*, 2016, Nat. Mater. **15**, 27.

Liu, Z.-H., *et al.*, 2011, Phys. Rev. B **84**, 064519.

Loeser, A., Z.-X. Shen, D. Dessau, D. Marshall, C. Park, P. Fournier, and A. Kapitulnik, 1996, Science **273**, 325.

Longo, J., and P. Raccah, 1973, J. Solid State Chem. **6**, 526.

Lorek, E., E. W. Larsen, C. M. Heyl, S. Carlström, D. Paleček, D. Zigmantas, and J. Mauritsson, 2014, Rev. Sci. Instrum. **85**, 123106.

Lu, D., I. M. Vishik, M. Yi, Y. Chen, R. G. Moore, and Z.-X. Shen, 2012, Annu. Rev. Condens. Matter Phys. **3**, 129.

Lu, D., *et al.*, 2008, Nature (London) **455**, 81.

Lu, H.-Z., W.-Y. Shan, W. Yao, Q. Niu, and S.-Q. Shen, 2010, Phys. Rev. B **81**, 115407.

Lu, Y.-M., T. Xiang, and D.-H. Lee, 2014, Nat. Phys. **10**, 634.

Lubashevsky, Y., E. Lahoud, K. Chashka, D. Podolsky, and A. Kanigel, 2012, Nat. Phys. **8**, 309.

Ludbrook, B., *et al.*, 2015, Proc. Natl. Acad. Sci. U.S.A. **112**, 11795.

Luetkens, H., *et al.*, 2009, Nat. Mater. **8**, 305.

Luttinger, J., 1960, Phys. Rev. **119**, 1153.

Lv, B. Q., *et al.*, 2015, Phys. Rev. X **5**, 031013.

Lv, W., J. Wu, and P. Phillips, 2009, Phys. Rev. B **80**, 224506.

Lynch, D. W., and C. G. Olson, 2005, *Photoemission Studies of High-Temperature Superconductors* (Cambridge University Press, Cambridge, England).

Ma, E. Y., *et al.*, 2015, Nat. Commun. **6**, 7252.

Mackenzie, A., S. Julian, A. Diver, G. McMullan, M. Ray, G. Lonzarich, Y. Maeno, S. Nishizaki, and T. Fujita, 1996, Phys. Rev. Lett. **76**, 3786.

Mackenzie, A. P., 2017, Rep. Prog. Phys. **80**, 032501.

Mackenzie, A. P., and Y. Maeno, 2003, Rev. Mod. Phys. **75**, 657.

Madéo, J., *et al.*, 2020, Science **370**, 1199.

Maeno, Y., H. Hashimoto, K. Yoshida, S. Nishizaki, T. Fujita, J. Bednorz, and F. Lichtenberg, 1994, Nature (London) **372**, 532.

Maesaka, H., 2015, in *Proceedings of the 6th International Particle Accelerator Conference (IPAC '15), Richmond, VA, 2015*, edited by S. Henderson, T. Satogata, and V. R. W. Schaa (JACoW, Geneva), pp. 3657–3661.

Mahan, G. D., 1970, Phys. Rev. B **2**, 4334.

Mahan, G. D., 2000, *Many-Particle Physics* (Springer, Boston).

Mahmood, F., C.-K. Chan, Z. Alpichshev, D. Gardner, Y. Lee, P. A. Lee, and N. Gedik, 2016, Nat. Phys. **12**, 306.

Maier, T. A., T. Berlijn, and D. J. Scalapino, 2019, Phys. Rev. B **99**, 224515.

Mak, K. F., K. He, J. Shan, and T. F. Heinz, 2012, Nat. Nanotechnol. **7**, 494.

Mak, K. F., C. Lee, J. Hone, J. Shan, and T. F. Heinz, 2010, Phys. Rev. Lett. **105**, 136805.

Mak, K. F., and J. Shan, 2016, Nat. Photonics **10**, 216.

Man, M. K. L., *et al.*, 2020, arXiv:2011.13104.

Mandal, S., P. Zhang, S. Ismail-Beigi, and K. Haule, 2017, Phys. Rev. Lett. **119**, 067004.

Mannella, N., W. L. Yang, X. J. Zhou, H. Zheng, J. F. Mitchell, J. Zaanen, T. P. Devereaux, N. Nagaosa, Z. Hussain, and Z.-X. Shen, 2005, Nature (London) **438**, 474.

Mannella, N., *et al.*, 2007, Phys. Rev. B **76**, 233102.

Mans, A., *et al.*, 2006, Phys. Rev. Lett. **96**, 107007.

Manzoni, G., *et al.*, 2016, Phys. Rev. Lett. **117**, 237601.

Margadonna, S., Y. Takabayashi, Y. Ohishi, Y. Mizuguchi, Y. Takano, T. Kagayama, T. Nakagawa, M. Takata, and K. Prassides, 2009, Phys. Rev. B **80**, 064506.

Markiewicz, R., 1997, J. Phys. Chem. Solids **58**, 1179.

Marshall, D., *et al.*, 1996, Phys. Rev. Lett. **76**, 4841.

Mårtensson, N., P. Baltzer, P. Brühwiler, J.-O. Forsell, A. Nilsson, A. Stenborg, and B. Wannberg, 1994, J. Electron Spectrosc. Relat. Phenom. **70**, 117.

Martin, S., A. Fiory, R. Fleming, L. Schneemeyer, and J. Waszczak, 1990, Phys. Rev. B **41**, 846.

Martinez, G., and P. Horsch, 1991, Phys. Rev. B **44**, 317.

Maschek, M., S. Rosenkranz, R. Heid, A. H. Said, P. Giraldo-Gallo, I. R. Fisher, and F. Weber, 2015, Phys. Rev. B **91**, 235146.

Massee, F., *et al.*, 2011, Nat. Phys. **7**, 978.

Matsui, H., T. Sato, T. Takahashi, S.-C. Wang, H.-B. Yang, H. Ding, T. Fujii, T. Watanabe, and A. Matsuda, 2003, Phys. Rev. Lett. **90**, 217002.

Matsui, H., K. Terashima, T. Sato, T. Takahashi, M. Fujita, and K. Yamada, 2005, Phys. Rev. Lett. **95**, 017003.

Matsuura, K., *et al.*, 2017, Nat. Commun. **8**, 1143.

Matt, C. E., *et al.*, 2018, Nat. Commun. **9**, 972.

Mattheiss, L., 1987, Phys. Rev. Lett. **58**, 1028.

Mazzola, F., *et al.*, 2018, Proc. Natl. Acad. Sci. U.S.A. **115**, 12956.

Medvedev, S., *et al.*, 2009, Nat. Mater. **8**, 630.

Meevasana, W., F. Baumberger, K. Tanaka, F. Schmitt, W. Dunkel, D. Lu, S.-K. Mo, H. Eisaki, and Z.-X. Shen, 2008, Phys. Rev. B **77**, 104506.

Meevasana, W., P. King, R. He, S. Mo, M. Hashimoto, A. Tamai, P. Songsiriritthigul, F. Baumberger, and Z. Shen, 2011, Nat. Mater. **10**, 114.

Meevasana, W., *et al.*, 2006, Phys. Rev. Lett. **96**, 157003.

Meng, J., *et al.*, 2009, Nature (London) **462**, 335.

Miaja-Avila, L., C. Lei, M. Aeschlimann, J. L. Gland, M. M. Murnane, H. C. Kapteyn, and G. Saathoff, 2006, Phys. Rev. Lett. **97**, 113604.

Miao, H., *et al.*, 2016, Phys. Rev. B **94**, 201109.

Michon, B., *et al.*, 2019, Nature (London) **567**, 218.

Miller, T., W. E. McMahon, and T.-C. Chiang, 1996, Phys. Rev. Lett. **77**, 1167.

Miller, T. L., *et al.*, 2015, Phys. Rev. B **91**, 085109.

Millis, A. J., 1998, Nature (London) **392**, 147.

Mills, A. K., S. Zhdanovich, F. Boschini, M. Na, M. Schneider, P. Dosanjh, D. Wong, G. Levy, A. Damascelli, and D. J. Jones, 2017, in *Conference on Lasers and Electro-Optics*, Vol. 37 (OSA, Washington, DC), p. STu1I.2.

Minár, J., J. Braun, S. Mankovsky, and H. Ebert, 2011, J. Electron Spectrosc. Relat. Phenom. **184**, 91.

Mino, L., E. Borfecchia, J. Segura-Ruiz, C. Giannini, G. Martinez-Criado, and C. Lamberti, 2018, Rev. Mod. Phys. **90**, 025007.

Mirhosseini, H., and J. Henk, 2012, Phys. Rev. Lett. **109**, 036803.

Mishchenko, A., and N. Nagaosa, 2004, Phys. Rev. Lett. **93**, 036402.

Mizuguchi, Y., F. Tomioka, S. Tsuda, T. Yamaguchi, and Y. Takano, 2008, Appl. Phys. Lett. **93**, 152505.

Mo, S.-K., 2017, Nano Convergence **4**, 6.

Mo, S.-K., C. Hwang, Y. Zhang, M. Fanciulli, S. Muff, J. H. Dil, Z.-X. Shen, and Z. Hussain, 2016, J. Phys. Condens. Matter **28**, 454001.

Mohamed, N. B., H. E. Lim, F. Wang, S. Koirala, S. Mouri, K. Shinokita, Y. Miyauchi, and K. Matsuda, 2018, Appl. Phys. Express **11**, 015201.

Moon, S., *et al.*, 2008, Phys. Rev. Lett. **101**, 226402.

Moore, J. E., and L. Balents, 2007, Phys. Rev. B **75**, 121306.

Moore, R. G., V. Brouet, R. He, D. H. Lu, N. Ru, J.-H. Chu, I. R. Fisher, and Z.-X. Shen, 2010, Phys. Rev. B **81**, 073102.

Morali, N., R. Batabyal, P. K. Nag, E. Liu, Q. Xu, Y. Sun, B. Yan, C. Felser, N. Avraham, and H. Beidenkopf, 2019, Science **365**, 1286.

Moritz, B., S. Johnston, and T. Devereaux, 2010, J. Electron Spectrosc. Relat. Phenom. **181**, 31.

Morozov, A., J. Berakdar, S. Samarin, F. Hillebrecht, and J. Kirschner, 2002, Phys. Rev. B **65**, 104425.

Moser, S., 2017, J. Electron Spectrosc. Relat. Phenom. **214**, 29.

Moser, S., *et al.*, 2013, Phys. Rev. Lett. **110**, 196403.

Moser, S., *et al.*, 2014, New J. Phys. **16**, 013008.

Motoyama, E., G. Yu, I. Vishik, O. Vajk, P. Mang, and M. Greven, 2007, Nature (London) **445**, 186.

Mott, N., 1968, Rev. Mod. Phys. **40**, 677.

Mou, D., R. Jiang, V. Taufour, S. Bud'ko, P. Canfield, and A. Kaminski, 2015, Phys. Rev. B **91**, 214519.

Mou, D., S. Manni, V. Taufour, Y. Wu, L. Huang, S. Bud'ko, P. Canfield, and A. Kaminski, 2016, Phys. Rev. B **93**, 144504.

Mou, D., *et al.*, 2011, Phys. Rev. Lett. **106**, 107001.

Mou, D., *et al.*, 2016, Phys. Rev. Lett. **116**, 196401.

Nagamatsu, J., N. Nakagawa, T. Muranaka, Y. Zenitani, and J. Akimitsu, 2001, Nature (London) **410**, 63.

Nakata, Y., K. Sugawara, S. Ichinokura, Y. Okada, T. Hitosugi, T. Koretsune, K. Ueno, S. Hasegawa, T. Takahashi, and T. Sato, 2018, npj 2D Mater. Appl. **2**, 12.

Nakata, Y., K. Sugawara, R. Shimizu, Y. Okada, P. Han, T. Hitosugi, K. Ueno, T. Sato, and T. Takahashi, 2016, NPG Asia Mater. **8**, e321.

Nakayama, K., Y. Miyata, G. Phan, T. Sato, Y. Tanabe, T. Urata, K. Tanigaki, and T. Takahashi, 2014, Phys. Rev. Lett. **113**, 237001.

Nakayama, K., *et al.*, 2006, Phys. Rev. B **74**, 054505.

Nakayama, M., *et al.*, 2016, Phys. Rev. Lett. **117**, 056403.

Nambu, Y., 1960, Phys. Rev. **117**, 648.

Nandi, S., *et al.*, 2010, Phys. Rev. Lett. **104**, 057006.

Nayak, C., S. H. Simon, A. Stern, M. Freedman, and S. Das Sarma, 2008, Rev. Mod. Phys. **80**, 1083.

Nazarenko, A., K. Vos, S. Haas, E. Dagotto, and R. Gooding, 1995, J. Supercond. **8**, 671.

Need, R. F., P. B. Marshall, E. Kenney, A. Suter, T. Prokscha, Z. Salman, B. J. Kirby, S. Stemmer, M. J. Graf, and S. D. Wilson, 2018, npj Quantum Mater. **3**, 7.

Neupane, M., P. Richard, Z.-H. Pan, Y.-M. Xu, R. Jin, D. Mandrus, X. Dai, Z. Fang, Z. Wang, and H. Ding, 2009, Phys. Rev. Lett. **103**, 097001.

Neupane, M., *et al.*, 2013, Nat. Commun. **4**, 2991.

Neupane, M., *et al.*, 2014, Nat. Commun. **5**, 3786.

Nguyen, P. V., *et al.*, 2019, Nature (London) **572**, 220.

Nichele, F., *et al.*, 2016, New J. Phys. **18**, 083005.

Nicholson, C. W., A. Lücke, W. G. Schmidt, M. Puppin, L. Rettig, R. Ernstorfer, and M. Wolf, 2018, Science **362**, 821.

Nie, S., L. Xing, R. Jin, W. Xie, Z. Wang, and F. B. Prinz, 2018, Phys. Rev. B **98**, 125143.

Nie, Y. F., *et al.*, 2015, Phys. Rev. Lett. **114**, 016401.

Niesner, D., *et al.*, 2012, Phys. Rev. B **86**, 205403.

Nijboer, B., 1946, Physica (Amsterdam) **12**, 461.

Niu, C., Y. Dai, Y. Zhu, J. Lu, Y. Ma, and B. Huang, 2012, Appl. Phys. Lett. **101**, 182101.

Niu, X., *et al.*, 2015, Phys. Rev. B **92**, 060504.

Niu, X., *et al.*, 2016, Phys. Rev. B **93**, 054516.

Noguchi, R., *et al.*, 2019, Nature (London) **566**, 518.

Noh, H.-J., J. Jeong, J. Jeong, E.-J. Cho, S. Kim, K. Kim, B. Min, and H.-D. Kim, 2009, Phys. Rev. Lett. **102**, 256404.

Noh, H.-J., *et al.*, 2014, Sci. Rep. **4**, 3680.

Norman, M., M. Randeria, H. Ding, and J. Campuzano, 1998, Phys. Rev. B **57**, R11093.

Norman, M., M. Randeria, B. Janko, and J. Campuzano, 2000, Phys. Rev. B **61**, 14742.

Norman, M. R., H. Ding, H. Fretwell, M. Randeria, and J. C. Campuzano, 1999, Phys. Rev. B **60**, 7585.

Norman, M. R., M. Eschrig, A. Kaminski, and J. C. Campuzano, 2001, Phys. Rev. B **64**, 184508.

Novoselov, K. S., A. K. Geim, S. Morozov, D. Jiang, M. I. Katsnelson, I. Grigorieva, S. Dubonos, and A. A. Firsov, 2005, Nature (London) **438**, 197.

Novoselov, K. S., A. K. Geim, S. V. Morozov, D. Jiang, Y. Zhang, S. V. Dubonos, I. V. Grigorieva, and A. A. Firsov, 2004, Science **306**, 666.

Nozieres, P., and D. Pines, 1999, *Theory of Quantum Liquids*, Advanced Books Classics (Avalon Publishing, New York).

Nummy, T. J., J. A. Waugh, S. P. Parham, Q. Liu, H.-Y. Yang, H. Li, X. Zhou, N. C. Plumb, F. F. Tafti, and D. S. Dessau, 2018, npj Quantum Mater. **3**, 24.

Ohta, T., A. Bostwick, J. L. McChesney, T. Seyller, K. Horn, and E. Rotenberg, 2007, Phys. Rev. Lett. **98**, 206802.

Ohta, T., A. Bostwick, T. Seyller, K. Horn, and E. Rotenberg, 2006, Science **313**, 951.

Ohtomo, A., and H. Hwang, 2004, Nature (London) **427**, 423.

Okawa, M., *et al.*, 2009, Phys. Rev. B **79**, 144528.

Okazaki, K., A. Fujimori, T. Yamauchi, and Y. Ueda, 2004, Phys. Rev. B **69**, 140506.

Okazaki, K., *et al.*, 2012, Science **337**, 1314.

Okuda, T., 2017, J. Phys. Condens. Matter **29**, 483001.

Okuda, T., H. Daimon, M. Kotsugi, K. Nakatsuji, M. Fujikawa, S. Suga, Y. Tezuka, S. Shin, M. Kasai, and Y. Tokura, 1998, J. Electron Spectrosc. Relat. Phenom. **88–91**, 473.

Oloff, L.-P., M. Oura, A. Chainani, and K. Rossnagel, 2016, in *Hard X-Ray Photoelectron Spectroscopy (HAXPES)*, edited by J. Woicik (Springer International Publishing, Cham, Switzerland), pp. 555–568.

Oloff, L.-P., *et al.*, 2014, New J. Phys. **16**, 123045.

Osterwalder, J., 2006, in *Magnetism: A Synchrotron Radiation Approach*, edited by E. Beaurepaire, H. Bulou, F. Scheurer, and J.-P. Kappler (Springer, Berlin), pp. 95–120.

Osterwalder, J., T. Greber, E. Wetli, J. Wider, and H. Neff, 2000, Prog. Surf. Sci. **64**, 65.

Otrokov, M. M., I. P. Rusinov, M. Blanco-Rey, M. Hoffmann, A. Y. Vyazovskaya, S. V. Eremeev, A. Ernst, P. M. Echenique, A. Arnau, and E. V. Chulkov, 2019, Phys. Rev. Lett. **122**, 107202.

Ovsyannikov, R., P. Karlsson, M. Lundqvist, C. Lupulescu, W. Eberhardt, A. Föhlisch, S. Svensson, and N. Mårtensson, 2013, J. Electron Spectrosc. Relat. Phenom. **191**, 92.

Paglione, J., and R. L. Greene, 2010, Nat. Phys. **6**, 645.

Palstra, T. T. M., A. A. Menovsky, J. van den Berg, A. J. Dirkmaat, P. H. Kes, G. J. Nieuwenhuys, and J. A. Mydosh, 1985, Phys. Rev. Lett. **55**, 2727.

Pan, Z.-H., A. V. Fedorov, D. Gardner, Y. S. Lee, S. Chu, and T. Valla, 2012, Phys. Rev. Lett. **108**, 187001.

Pan, Z.-H., E. Vescovo, A. V. Fedorov, D. Gardner, Y. S. Lee, S. Chu, G. D. Gu, and T. Valla, 2011, Phys. Rev. Lett. **106**, 257004.

Papagno, M., D. Pacilé, G. Caimi, H. Berger, L. Degiorgi, and M. Grioni, 2006, Phys. Rev. B **73**, 115120.

Papalazarou, E., *et al.*, 2012, Phys. Rev. Lett. **108**, 256808.

Parham, S., H. Li, T. J. Nummy, J. A. Waugh, X. Q. Zhou, J. Griffith, J. Schneeloch, R. D. Zhong, G. D. Gu, and D. S. Dessau, 2017, Phys. Rev. X **7**, 041013.

Park, C.-H., and S. G. Louie, 2012, Phys. Rev. Lett. **109**, 097601.

Park, J.-H., C. H. Kim, J.-W. Rhim, and J. H. Han, 2012, Phys. Rev. B **85**, 195401.

Park, S., N. Mutz, T. Schultz, S. Blumstengel, A. Han, A. Aljarb, L.-J. Li, E. J. List-Kratochvil, P. Amsalem, and N. Koch, 2018, 2D Mater. **5**, 025003.

Park, S. R., W. S. Jung, C. Kim, D. J. Song, C. Kim, S. Kimura, K. D. Lee, and N. Hur, 2010, Phys. Rev. B **81**, 041405.

Park, S. R., D. Song, C. Leem, C. Kim, C. Kim, B. Kim, and H. Eisaki, 2008, Phys. Rev. Lett. **101**, 117006.

Parker, D. R., M. J. Smith, T. Lancaster, A. J. Steele, I. Franke, P. J. Baker, F. L. Pratt, M. J. Pitcher, S. J. Blundell, and S. J. Clarke, 2010, Phys. Rev. Lett. **104**, 057007.

Pendry, J., 1969, J. Phys. C **2**, 1215.

Peng, H., *et al.*, 2017, Adv. Mater. **29**, 1606741.

Peng, H., *et al.*, 2020, Rev. Sci. Instrum. **91**, 033905.

Peng, Y., *et al.*, 2013, Nat. Commun. **4**, 2459.

Perfetti, L., P. A. Loukakos, M. Lisowski, U. Bovensiepen, H. Berger, S. Biermann, P. S. Cornaglia, A. Georges, and M. Wolf, 2006, Phys. Rev. Lett. **97**, 067402.

Petek, H., and S. Ogawa, 1997, Prog. Surf. Sci. **56**, 239.

Petrovic, C., P. G. Pagliuso, M. F. Hundley, R. Movshovich, J. L. Sarrao, J. D. Thompson, Z. Fisk, and P. Monthoux, 2001, J. Phys. Condens. Matter **13**, L337.

Pfau, H., *et al.*, 2019, Phys. Rev. Lett. **123**, 066402.

Pickett, W. E., 1989, Rev. Mod. Phys. **61**, 433.

Pielmeier, F., *et al.*, 2015, New J. Phys. **17**, 023067.

Pierce, D. T., and F. Meier, 1976, Phys. Rev. B **13**, 5484.

Pietzsch, A., *et al.*, 2008, New J. Phys. **10**, 033004.

Pillay, D., M. Johannes, and I. Mazin, 2008, Phys. Rev. Lett. **101**, 246808.

Pillo, T., R. Zimmermann, P. Steiner, and S. Hüfner, 1997, J. Phys. Condens. Matter **9**, 3987.

Pines, D., and P. Nozières, 1966, *The Theory of Quantum Liquids* (Benjamin, New York).

Pippard, A., 1989, *Magnetoresistance in Metals* (Cambridge University Press, Cambridge, England).

Pitaevskii, L., and S. Stringari, 2016, *Bose-Einstein Condensation and Superfluidity*, Vol. 164 (Oxford University Press, New York).

Platé, M., *et al.*, 2005, Phys. Rev. Lett. **95**, 077001.

Pletikosić, I., M. N. Ali, A. V. Fedorov, R. J. Cava, and T. Valla, 2014, Phys. Rev. Lett. **113**, 216601.

Pletikosić, I., M. Kralj, P. Pervan, R. Brako, J. Coraux, A. Ndiaye, C. Busse, and T. Michely, 2009, Phys. Rev. Lett. **102**, 056808.

Plumb, N., *et al.*, 2014, Phys. Rev. Lett. **113**, 086801.

Plumb, N., *et al.*, 2016, Phys. Rev. Lett. **117**, 037002.

Plummer, E. W., and W. Eberhardt, 2007, in *Advances in Chemical Physics*, edited by S. A. Rice (John Wiley & Sons, New York), pp. 533–656.

Potter, A. C., I. Kimchi, and A. Vishwanath, 2014, Nat. Commun. **5**, 5161.

Presland, M., J. Tallon, R. Buckley, R. Liu, and N. Flower, 1991, Physica (Amsterdam) **176C**, 95.

Pringle, D., G. Williams, and J. Tallon, 2000, Phys. Rev. B **62**, 12527.

Proust, C., E. Boaknin, R. Hill, L. Taillefer, and A. Mackenzie, 2002, Phys. Rev. Lett. **89**, 147003.

Pu, Y., Z. Huang, H. Xu, D. Xu, Q. Song, C. Wen, R. Peng, and D. Feng, 2016, Phys. Rev. B **94**, 115146.

Puppin, M., *et al.*, 2019, Rev. Sci. Instrum. **90**, 023104.

Pustogow, A., *et al.*, 2019, Nature (London) **574**, 72.

Pustovit, Y. V., and A. Kordyuk, 2016, Low Temp. Phys. **42**, 995.

Qi, X.-L., T. L. Hughes, and S.-C. Zhang, 2008, Phys. Rev. B **78**, 195424.

Qi, X.-L., and S.-C. Zhang, 2011, Rev. Mod. Phys. **83**, 1057.

Qian, D., *et al.*, 2006, Phys. Rev. Lett. **96**, 046407.

Qian, X., J. Liu, L. Fu, and J. Li, 2014, Science **346**, 1344.

Qiu, Y., *et al.*, 2009, Phys. Rev. Lett. **103**, 067008.

Queiroz, R., *et al.*, 2016, Phys. Rev. B **93**, 165409.

Rachel, S., 2018, Rep. Prog. Phys. **81**, 116501.

Rahn, D., S. Hellmann, M. Kalläne, C. Sohrt, T. Kim, L. Kipp, and K. Rossnagel, 2012, Phys. Rev. B **85**, 224532.

Rameau, J. D., J. Smedley, E. M. Muller, T. E. Kidd, and P. D. Johnson, 2011, Phys. Rev. Lett. **106**, 137602.

Rameau, J. D., *et al.*, 2014, Phys. Rev. B **89**, 115115.

Rameau, J. D., *et al.*, 2016, Nat. Commun. **7**, 13761.

Ramirez, A. P., 1997, J. Phys. Condens. Matter **9**, 8171.

Ran, Y., F. Wang, H. Zhai, A. Vishwanath, and D.-H. Lee, 2009, Phys. Rev. B **79**, 014505.

Randeria, M., H. Ding, J. Campuzano, A. Bellman, G. Jennings, T. Yokoya, T. Takahashi, H. Katayama-Yoshida, T. Mochiku, and K. Kadowaki, 1995, Phys. Rev. Lett. **74**, 4951.

Rau, J. G., E. K.-H. Lee, and H.-Y. Kee, 2016, Annu. Rev. Condens. Matter Phys. **7**, 195.

Razzoli, E., G. Drachuck, A. Keren, M. Radovic, N. Plumb, J. Chang, Y.-B. Huang, H. Ding, J. Mesot, and M. Shi, 2013, Phys. Rev. Lett. **110**, 047004.

Razzoli, E., *et al.*, 2010, New J. Phys. **12**, 125003.

Rebec, S., T. Jia, C. Zhang, M. Hashimoto, D.-H. Lu, R. Moore, and Z.-X. Shen, 2017, Phys. Rev. Lett. **118**, 067002.

Reber, T., N. Plumb, J. Waugh, and D. Dessau, 2014, Rev. Sci. Instrum. **85**, 043907.

Reber, T., *et al.*, 2012, Nat. Phys. **8**, 606.

Reber, T., *et al.*, 2019, Nat. Commun. **10**, 5737.

Reimann, J., *et al.*, 2018, Nature (London) **562**, 396.

Reis, F., G. Li, L. Dudy, M. Bauernfeind, S. Glass, W. Hanke, R. Thomale, J. Schäfer, and R. Claessen, 2017, Science **357**, 287.

Renner, C., B. Revaz, J.-Y. Genoud, K. Kadowaki, and Ø. Fischer, 1998, Phys. Rev. Lett. **80**, 149.

Rettig, L., J.-H. Chu, I. R. Fisher, U. Bovensiepen, and M. Wolf, 2014, Faraday Discuss. **171**, 299.

Rettig, L., R. Cortés, J.-H. Chu, I. R. Fisher, F. Schmitt, R. G. Moore, Z.-X. Shen, P. S. Kirchmann, M. Wolf, and U. Bovensiepen, 2016, Nat. Commun. **7**, 10459.

Reutzel, M., A. Li, and H. Petek, 2019, Phys. Rev. X **9**, 011044.

Reznik, D., B. Keimer, F. Dogan, and I. A. Aksay, 1995, Phys. Rev. Lett. **75**, 2396.

Rhodes, D., S. H. Chae, R. Ribeiro-Palau, and J. Hone, 2019, Nat. Mater. **18**, 541.

Riccò, S., *et al.*, 2018, Nat. Commun. **9**, 4535.

Rice, T. M., K.-Y. Yang, and F.-C. Zhang, 2011, Rep. Prog. Phys. **75**, 016502.

Richard, P., *et al.*, 2010, Phys. Rev. Lett. **104**, 137001.

Rienks, E., M. Ärrälä, M. Lindroos, F. Roth, W. Tabis, G. Yu, M. Greven, and J. Fink, 2014, Phys. Rev. Lett. **113**, 137001.

Riley, J. M., *et al.*, 2014, Nat. Phys. **10**, 835.

Rinott, S., K. Chashka, A. Ribak, E. D. Rienks, A. Taleb-Ibrahimi, P. Le Fevre, F. Bertran, M. Randeria, and A. Kanigel, 2017, Sci. Adv. **3**, e1602372.

Rödel, T., *et al.*, 2014, Phys. Rev. Applied **1**, 051002.

Rohde, G., A. Hendel, A. Stange, K. Hanff, L.-P. Oloff, L. X. Yang, K. Rossnagel, and M. Bauer, 2016, Rev. Sci. Instrum. **87**, 103102.

Rohwer, T., *et al.*, 2011, Nature (London) **471**, 490.

Rösch, O., and O. Gunnarsson, 2004, Phys. Rev. Lett. **92**, 146403.

Rossbach, J., J. R. Schneider, and W. Wurth, 2019, Phys. Rep. **808**, 1.

Rotter, M., M. Tegel, and D. Johrendt, 2008, Phys. Rev. Lett. **101**, 107006.

Rotundu, C., D. Keane, B. Freelon, S. Wilson, A. Kim, P. Valdivia, E. Bourret-Courchesne, and R. Birgeneau, 2009, Phys. Rev. B **80**, 144517.

Roushan, P., J. Seo, C. V. Parker, Y. S. Hor, D. Hsieh, D. Qian, A. Richardella, M. Z. Hasan, R. J. Cava, and A. Yazdani, 2009, Nature (London) **460**, 1106.

Rowell, J., and L. Kopf, 1965, Phys. Rev. **137**, A907.

Ru, N., C. L. Condron, G. Y. Margulis, K. Y. Shin, J. Laverock, S. B. Dugdale, M. F. Toney, and I. R. Fisher, 2008, Phys. Rev. B **77**, 035114.

Rubio-Bollinger, G., H. Suderow, and S. Vieira, 2001, Phys. Rev. Lett. **86**, 5582.

Ryu, H., *et al.*, 2018, Nano Lett. **18**, 689.

Sakakibara, H., H. Usui, K. Kuroki, R. Arita, and H. Aoki, 2012, Phys. Rev. B **85**, 064501.

Sakamoto, H., T. Kondo, S. Shin, M. Matsunami, H. Ikuta, and T. Takeuchi, 2017, J. Electron Spectrosc. Relat. Phenom. **220**, 54.

Sakamoto, H., K. Ogawa, T. Kondo, S. Shin, M. Matsunami, H. Ikuta, and T. Takeuchi, 2016, J. Phys. Soc. Jpn. **85**, 104710.

Sakamoto, Y., T. Hirahara, H. Miyazaki, S.-i. Kimura, and S. Hasegawa, 2010, Phys. Rev. B **81**, 165432.

Saldin, D. K., and J. C. H. Spence, 1994, Ultramicroscopy **55**, 397.

Samarin, S., O. Artamonov, A. Sergeant, J. Kirschner, A. Morozov, and J. Williams, 2004, Phys. Rev. B **70**, 073403.

Sanchez, D. S., *et al.*, 2019, Nature (London) **567**, 500.

Sánchez-Barriga, J., *et al.*, 2014, Phys. Rev. X **4**, 011046.

Sánchez-Barriga, J., *et al.*, 2016, Nat. Commun. **7**, 10559.

Sandvik, A., D. Scalapino, and N. Bickers, 2004, Phys. Rev. B **69**, 094523.

Sanna, A., G. Profeta, A. Floris, A. Marini, E. K. U. Gross, and S. Massidda, 2007, Phys. Rev. B **75**, 020511.

Santander-Syro, A., *et al.*, 2011, Nature (London) **469**, 189.

Santander-Syro, A. F., M. Klein, F. L. Boariu, A. Nuber, P. Lejay, and F. Reinert, 2009, Nat. Phys. **5**, 637.

Sato, T., K. Segawa, K. Kosaka, S. Souma, K. Nakayama, K. Eto, T. Minami, Y. Ando, and T. Takahashi, 2011, Nat. Phys. **7**, 840.

Sawatzky, G., and J. Allen, 1984, Phys. Rev. Lett. **53**, 2339.

Scalapino, D. J., 1995, Phys. Rep. **250**, 329.

Scalapino, D. J., 2012, Rev. Mod. Phys. **84**, 1383.

Schäfer, J., C. Blumenstein, S. Meyer, M. Wisniewski, and R. Claessen, 2008, Phys. Rev. Lett. **101**, 236802.

Schaibley, J. R., H. Yu, G. Clark, P. Rivera, J. S. Ross, K. L. Seyler, W. Yao, and X. Xu, 2016, Nat. Rev. Mater. **1**, 16055.

Schaich, W., and N. Ashcroft, 1971, Phys. Rev. B **3**, 2452.

Schlenk, T., *et al.*, 2013, Phys. Rev. Lett. **110**, 126804.

Schmitt, F., *et al.*, 2008, Science **321**, 1649.

Schneider, C. M., and J. Kirschner, 1995, Crit. Rev. Solid State Mater. Sci. **20**, 179.

Schnyder, A. P., S. Ryu, A. Furusaki, and A. W. W. Ludwig, 2009, AIP Conf. Proc. **1134**, 10.

Scholz, M. R., J. Sánchez-Barriga, D. Marchenko, A. Varykhalov, A. Volykhov, L. V. Yashina, and O. Rader, 2012, Phys. Rev. Lett. **108**, 256810.

Scholz, M. R., *et al.*, 2013, Phys. Rev. Lett. **110**, 216801.

Schönhense, G., K. Medjanik, and H.-J. Elmers, 2015, J. Electron Spectrosc. Relat. Phenom. **200**, 94.

Schönhense, G., A. Oelsner, O. Schmidt, G. Fecher, V. Mergel, O. Jagutzki, and H. Schmidt-Böcking, 2001, Surf. Sci. **480**, 180.

Schröter, N. B. M., *et al.*, 2019, Nat. Phys. **15**, 759.

Schumann, F., C. Winkler, G. Kerherve, and J. Kirschner, 2006, Phys. Rev. B **73**, 041404.

Schumann, F., C. Winkler, and J. Kirschner, 2007, Phys. Rev. Lett. **98**, 257604.

Schumann, F., C. Winkler, and J. Kirschner, 2009, Phys. Status Solidi (b) **246**, 1483.

Seah, M. P., and W. A. Dench, 1979, Surf. Interface Anal. **1**, 2.

Sensarma, R., M. Randeria, and N. Trivedi, 2007, Phys. Rev. Lett. **98**, 027004.

Shallenberger, J., D. Cole, D. Downey, S. Falk, and Zhiyong Zhao, 1998, in *Proceedings of the 1998 International Conference on Ion Implantation Technology, Kyoto, Japan, 1998*, Vol. 1, edited by J. Matsuo, G. Takaoka, and I. Yamada (IEEE, New York), pp. 566–569.

Shamoto, S.-i., M. Ishikado, A. D. Christianson, M. D. Lumsden, S. Wakimoto, K. Kodama, A. Iyo, and M. Arai, 2010, Phys. Rev. B **82**, 172508.

Shan-Yu, L., *et al.*, 2012, Chin. Phys. Lett. **29**, 067401.

Sharoni, A., I. Felner, and O. Millo, 2001, Phys. Rev. B **63**, 220508(R).

Shekhar, C., *et al.*, 2015, Nat. Phys. **11**, 645.

Shen, D., H. Yang, and Z. Liu, 2017, in *Modern Technologies for Creating the Thin-Film Systems and Coatings*, edited by N. N. Nikitenkov (IntechOpen, London), p. 59.

Shen, D., *et al.*, 2008, Phys. Rev. Lett. **101**, 226406.

Shen, K., N. Kikugawa, C. Bergemann, L. Balicas, F. Baumberger, W. Meevasana, N. Ingle, Y. Maeno, Z.-X. Shen, and A. Mackenzie, 2007, Phys. Rev. Lett. **99**, 187001.

Shen, K., *et al.*, 2004, Phys. Rev. Lett. **93**, 267002.

Shen, Z.-X., and G. Sawatzky, 1999, Phys. Status Solidi (b) **215**, 523.

Shen, Z.-X., W. Spicer, D. King, D. Dessau, and B. Wells, 1995, Science **267**, 343.

Shen, Z.-X., *et al.*, 1993, Phys. Rev. Lett. **70**, 1553.

Shi, J., *et al.*, 2004, Phys. Rev. Lett. **92**, 186401.

Shibauchi, T., A. Carrington, and Y. Matsuda, 2014, Annu. Rev. Condens. Matter Phys. **5**, 113.

Shimojima, T., K. Ishizaka, S. Tsuda, T. Kiss, T. Yokoya, A. Chainani, S. Shin, P. Badica, K. Yamada, and K. Togano, 2006, Phys. Rev. Lett. **97**, 267003.

Shimojima, T., K. Okazaki, and S. Shin, 2015, J. Phys. Soc. Jpn. **84**, 072001.

Shimojima, T., *et al.*, 2007, Phys. Rev. Lett. **99**, 117003.

Shimojima, T., *et al.*, 2010, Phys. Rev. Lett. **104**, 057002.

Shimojima, T., *et al.*, 2014, Phys. Rev. B **90**, 121111.

Shirage, P. M., K. Kihou, K. Miyazawa, C.-H. Lee, H. Kito, H. Eisaki, T. Yanagisawa, Y. Tanaka, and A. Iyo, 2009, Phys. Rev. Lett. **103**, 257003.

Shirley, J. H., 1965, Phys. Rev. **138**, B979.

Shkolnikov, Y., E. De Poortere, E. Tutuc, and M. Shayegan, 2002, Phys. Rev. Lett. **89**, 226805.

Si, Q., and F. Steglich, 2010, Science **329**, 1161.

Si, Q., R. Yu, and E. Abrahams, 2016, Nat. Rev. Mater. **1**, 16017.

Sie, E. J., T. Rohwer, C. Lee, and N. Gedik, 2019, Nat. Commun. **10**, 3535.

Sing, M., *et al.*, 2009, Phys. Rev. Lett. **102**, 176805.

Singh, D. J., 2008, Phys. Rev. B **78**, 094511.

Singh, D. J., and D. Kasinathan, 2006, Phys. Rev. Lett. **97**, 016404.

Sleight, A. W., J. Gillson, and P. Bierstedt, 1993, Solid State Commun. **88**, 841.

Smallwood, C. L., J. P. Hinton, C. Jozwiak, W. Zhang, J. D. Koralek, H. Eisaki, D.-H. Lee, J. Orenstein, and A. Lanzara, 2012, Science **336**, 1137.

Smallwood, C. L., R. A. Kaindl, and A. Lanzara, 2016, Europhys. Lett. **115**, 27001.

Smith, K. E., and S. D. Kevan, 1991, Prog. Solid State Chem. **21**, 49.

Smith, N. V., 1988, Rep. Prog. Phys. **51**, 1227.

Smith, N. V., and M. M. Traum, 1975, Phys. Rev. B **11**, 2087.

Sobota, J. A., S. Yang, J. G. Analytis, Y. L. Chen, I. R. Fisher, P. S. Kirchmann, and Z.-X. Shen, 2012, Phys. Rev. Lett. **108**, 117403.

Sobota, J. A., *et al.*, 2013a, Phys. Rev. B **88**, 125109.

Sobota, J. A., *et al.*, 2013b, Phys. Rev. Lett. **111**, 136802.

Sologubenko, A., J. Jun, S. Kazakov, J. Karpinski, and H. Ott, 2002, Phys. Rev. B **66**, 014504.

Song, D., *et al.*, 2012, Phys. Rev. B **86**, 144520.

Song, D., *et al.*, 2017, Phys. Rev. Lett. **118**, 137001.

Song, Q., *et al.*, 2019, Nat. Commun. **10**, 758.

Souma, S., M. Komatsu, M. Nomura, T. Sato, A. Takayama, T. Takahashi, K. Eto, K. Segawa, and Y. Ando, 2012, Phys. Rev. Lett. **109**, 186804.

Souma, S., K. Kosaka, T. Sato, M. Komatsu, A. Takayama, T. Takahashi, M. Kriener, K. Segawa, and Y. Ando, 2011, Phys. Rev. Lett. **106**, 216803.

Souma, S., *et al.*, 2003, Nature (London) **423**, 65.

Spałek, J., 2007, Acta Phys. Pol. A **111**, 409.

Splendiani, A., L. Sun, Y. Zhang, T. Li, J. Kim, C.-Y. Chim, G. Galli, and F. Wang, 2010, Nano Lett. **10**, 1271.

Sprau, P. O., A. Kostin, A. Kreisel, A. E. Böhmer, V. Taufour, P. C. Canfield, S. Mukherjee, P. J. Hirschfeld, B. M. Andersen, and J. S. Davis, 2017, Science **357**, 75.

Stander, N., B. Huard, and D. Goldhaber-Gordon, 2009, Phys. Rev. Lett. **102**, 026807.

Steppke, A., *et al.*, 2017, Science **355**, eaaf9398.

Stewart, G., 2011, Rev. Mod. Phys. **83**, 1589.

Strocov, V., 2003, J. Electron Spectrosc. Relat. Phenom. **130**, 65.

Strocov, V., X. Wang, M. Shi, M. Kobayashi, J. Krempasky, C. Hess, T. Schmitt, and L. Patthey, 2014, J. Synchrotron Radiat. **21**, 32.

Su, Y., and C. Zhang, 2020, Phys. Rev. B **101**, 205110.

Su, Y., *et al.*, 2009, Phys. Rev. B **79**, 064504.

Suga, S., and C. Tusche, 2015, J. Electron Spectrosc. Relat. Phenom. **200**, 119.

Suga, S., *et al.*, 2004, Phys. Rev. B **70**, 155106.

Sugawara, K., T. Sato, and T. Takahashi, 2009, Nat. Phys. **5**, 40.

Sun, Y., S.-C. Wu, and B. Yan, 2015, Phys. Rev. B **92**, 115428.

Sun, Z., J. F. Douglas, A. V. Fedorov, Y.-D. Chuang, H. Zheng, J. F. Mitchell, and D. S. Dessau, 2007, Nat. Phys. **3**, 248.

Sun, Z., *et al.*, 2006, Phys. Rev. Lett. **97**, 056401.

Sunko, V., *et al.*, 2017, Nature (London) **549**, 492.

Sunko, V., *et al.*, 2019, npj Quantum Mater. **4**, 46.

Sunko, V., *et al.*, 2020, Sci. Adv. **6**, eaaz0611.

Suzuki, Y., *et al.*, 2015, Phys. Rev. B **92**, 205117.

Swatek, P., Y. Wu, L.-L. Wang, K. Lee, B. Schrunk, J. Yan, and A. Kaminski, 2020 Phys. Rev. B **101**, 161109.

Sze, S., and K. K. Ng, 2006, *Physics of Semiconductor Devices* (John Wiley & Sons, Hoboken, NJ).

Tafti, F. F., Q. D. Gibson, S. K. Kushwaha, N. Haldolaarachchige, and R. J. Cava, 2016, Nat. Phys. **12**, 272.

Takagi, H., S. Uchida, and Y. Tokura, 1989, Phys. Rev. Lett. **62**, 1197.

Takahashi, T., T. Sato, H. Matsui, and K. Terashima, 2005, New J. Phys. **7**, 105.

Takahashi, T., T. Sato, S. Souma, T. Muranaka, and J. Akimitsu, 2001, Phys. Rev. Lett. **86**, 4915.

Takatsu, H., H. Yoshizawa, S. Yonezawa, and Y. Maeno, 2009, Phys. Rev. B **79**, 104424.

Takeuchi, T., T. Kondo, T. Kitao, H. Kaga, H. Yang, H. Ding, A. Kaminski, and J. C. Campuzano, 2005, Phys. Rev. Lett. **95**, 227004.

Tallon, J., R. Islam, J. Storey, G. Williams, and J. Cooper, 2005, Phys. Rev. Lett. **94**, 237002.

Tallon, J., J. Storey, and J. Loram, 2011, Phys. Rev. B **83**, 092502.

Tamai, A., W. Meevasana, P. King, C. Nicholson, A. De La Torre, E. Rozbicki, and F. Baumberger, 2013, Phys. Rev. B **87**, 075113.

Tamai, A., *et al.*, 2008, Phys. Rev. Lett. **101**, 026407.

Tamai, A., *et al.*, 2019, Phys. Rev. X **9**, 021048.

Tan, B. S., *et al.*, 2015, Science **349**, 287.

Tan, S., *et al.*, 2013, Nat. Mater. **12**, 634.

Tanaka, K., *et al.*, 2006, Science **314**, 1910.

Tanaka, Y., Z. Ren, T. Sato, K. Nakayama, S. Souma, T. Takahashi, K. Segawa, and Y. Ando, 2012, Nat. Phys. **8**, 800.

Tanatar, M., *et al.*, 2010, Phys. Rev. B **81**, 184508.

Tang, F., H. C. Po, A. Vishwanath, and X. Wan, 2019, Nature (London) **566**, 486.

Tang, S., *et al.*, 2017, Nat. Phys. **13**, 683.

Thompson, A., and D. Vaughan, 2001, *X-Ray Data Booklet*, 2nd ed. (Center for X-Ray Optics and Advanced Light Source, Berkeley, CA).

Thomsen, C., M. Cardona, B. Gegenheimer, R. Liu, and A. Simon, 1988, Phys. Rev. B **37**, 9860.

Thouless, D. J., M. Kohmoto, M. P. Nightingale, and M. den Nijs, 1982, Phys. Rev. Lett. **49**, 405.

Timusk, T., and B. Statt, 1999, Rep. Prog. Phys. **62**, 61.

Tomić, M., H. O. Jeschke, R. M. Fernandes, and R. Valentí, 2013, Phys. Rev. B **87**, 174503.

Tranquada, J., B. Sternlieb, J. Axe, Y. Nakamura, and S. Uchida, 1995, Nature (London) **375**, 561.

Trebino, R., 2000, *Frequency-Resolved Optical Gating: The Measurement of Ultrashort Laser Pulses* (Springer, Boston).

Trotochaud, L., A. R. Head, O. Karslıoğlu, L. Kyhl, and H. Bluhm, 2017, J. Phys. Condens. Matter **29**, 053002.

Trovarelli, O., C. Geibel, S. Mederle, C. Langhammer, F. M. Grosche, P. Gegenwart, M. Lang, G. Sparn, and F. Steglich, 2000, Phys. Rev. Lett. **85**, 626.

Trützschler, A., M. Huth, C.-T. Chiang, R. Kamrla, F. O. Schumann, J. Kirschner, and W. Widdra, 2017, Phys. Rev. Lett. **118**, 136401.

Tsuda, S., T. Yokoya, Y. Takano, H. Kito, A. Matsushita, F. Yin, J. Itoh, H. Harima, and S. Shin, 2003, Phys. Rev. Lett. **91**, 127001.

Tsuda, S., *et al.*, 2005, Phys. Rev. B **72**, 064527.

Tsuei, C., and J. Kirtley, 2000, Rev. Mod. Phys. **72**, 969.

Tsuei, C., J. R. Kirtley, C. Chi, L. S. Yu-Jahnes, A. Gupta, T. Shaw, J. Sun, and M. Ketchen, 1994, Phys. Rev. Lett. **73**, 593.

Turner, A. M., and A. Vishwanath, 2013, in *Topological Insulators*, Contemporary Concepts of Condensed Matter Science Vol. 6, edited by M. Franz, and L. Molenkamp (Elsevier, New York), pp. 293–324.

Tusche, C., A. Krasyuk, and J. Kirschner, 2015, Ultramicroscopy **159**, 520.

Tyler, A., A. Mackenzie, S. NishiZaki, and Y. Maeno, 1998, Phys. Rev. B **58**, R10107.

Uchida, M., Y. Nie, P. King, C. Kim, C. Fennie, D. Schlom, and K. Shen, 2014, Phys. Rev. B **90**, 075142.

Uchiyama, H., K. Shen, S. Lee, A. Damascelli, D. Lu, D. Feng, Z.-X. Shen, and S. Tajima, 2002, Phys. Rev. Lett. **88**, 157002.

Ugeda, M. M., *et al.*, 2016, Nat. Phys. **12**, 92.

Ugeda, M. M., *et al.*, 2018, Nat. Commun. **9**, 3401.

Unguris, J., A. Seiler, R. Celotta, D. T. Pierce, P. Johnson, and N. Smith, 1982, Phys. Rev. Lett. **49**, 1047.

Vafek, O., and A. Vishwanath, 2014, Annu. Rev. Condens. Matter Phys. **5**, 83.

Valla, T., J. Camacho, Z.-H. Pan, A. V. Fedorov, A. C. Walters, C. A. Howard, and M. Ellerby, 2009, Phys. Rev. Lett. **102**, 107007.

Valla, T., A. Fedorov, P. Johnson, and S. Hulbert, 1999, Phys. Rev. Lett. **83**, 2085.

Valla, T., A. V. Fedorov, P. D. Johnson, B. O. Wells, S. L. Hulbert, Q. Li, G. D. Gu, and N. Koshizuka, 1999, Science **285**, 2110.

Valla, T., Z.-H. Pan, D. Gardner, Y. S. Lee, and S. Chu, 2012, Phys. Rev. Lett. **108**, 117601.

Van Veenendaal, M., G. Sawatzky, and W. Groen, 1994, Phys. Rev. B **49**, 1407.

Varma, C., S. Schmitt-Rink, and E. Abrahams, 1987, Solid State Commun. **62**, 681.

Veenstra, C. N., *et al.*, 2014, Phys. Rev. Lett. **112**, 127002.

Vergniory, M. G., L. Elcoro, C. Felser, N. Regnault, B. A. Bernevig, and Z. Wang, 2019, Nature (London) **566**, 480.

Vershinin, M., S. Misra, S. Ono, Y. Abe, Y. Ando, and A. Yazdani, 2004, Science **303**, 1995.

Vidal, R. C., *et al.*, 2019, Phys. Rev. B **100**, 121104.

Vignolle, B., A. Carrington, R. Cooper, M. French, A. Mackenzie, C. Jaudet, D. Vignolles, C. Proust, and N. Hussey, 2008, Nature (London) **455**, 952.

Vishik, I., 2018, Rep. Prog. Phys. **81**, 062501.

Vishik, I., W. Lee, R. He, M. Hashimoto, Z. Hussain, T. Devereaux, and Z. Shen, 2010, New J. Phys. **12**, 105008.

Vishik, I., *et al.*, 2012, Proc. Natl. Acad. Sci. U.S.A. **109**, 18332.

Vishik, I., *et al.*, 2014, Phys. Rev. B **89**, 195141.

Vogt, P., P. De Padova, C. Quaresima, J. Avila, E. Frantzeskakis, M. C. Asensio, A. Resta, B. Ealet, and G. Le Lay, 2012, Phys. Rev. Lett. **108**, 155501.

von Klitzing, K., 2005, Phil. Trans. R. Soc. A **363**, 2203.

Voss, S., M. Tia, S. Schößler, A. Czasch, and O. Jagutzki, 2020, J. Electron Spectrosc. Relat. Phenom. **241**, 146875.

Vyalikh, D. V., *et al.*, 2010, Phys. Rev. Lett. **105**, 237601.

Waldrop, M. M., 2016, Nature (London) **530**, 144.

Walker, S. M., A. De La Torre, F. Y. Bruno, A. Tamai, T. Kim, M. Hoesch, M. Shi, M. Bahramy, P. King, and F. Baumberger, 2014, Phys. Rev. Lett. **113**, 177601.

Walker, S. M., *et al.*, 2015, Adv. Mater. **27**, 3894.

Wallauer, R., *et al.*, 2012, Rev. Sci. Instrum. **83**, 103905.

Wan, X., A. M. Turner, A. Vishwanath, and S. Y. Savrasov, 2011, Phys. Rev. B **83**, 205101.

Wang, A., J. Lin, P. Cheng, G. Ye, F. Chen, J. Ma, X. Lu, B. Lei, X. Luo, and X. Chen, 2013, Phys. Rev. B **88**, 094516.

Wang, D., *et al.*, 2018, Science **362**, 333.

Wang, E., *et al.*, 2013, Nat. Phys. **9**, 621.

Wang, E., *et al.*, 2016, Nat. Phys. **12**, 1111.

Wang, F., J. Alvarez, J. Allen, S.-K. Mo, J. He, R. Jin, D. Mandrus, and H. Höchst, 2009, Phys. Rev. Lett. **103**, 136401.

Wang, F., J. Alvarez, S.-K. Mo, J. Allen, G.-H. Gweon, J. He, R. Jin, D. Mandrus, and H. Höchst, 2006, Phys. Rev. Lett. **96**, 196403.

Wang, F., and T. Senthil, 2011, Phys. Rev. Lett. **106**, 136402.

Wang, F., F. Yang, M. Gao, Z.-Y. Lu, T. Xiang, and D.-H. Lee, 2011, Europhys. Lett. **93**, 57003.

Wang, M.-x., *et al.*, 2012, Science **336**, 52.

Wang, Q., *et al.*, 2016, Nat. Commun. **7**, 12182.

Wang, Q.-Y., *et al.*, 2012, Chin. Phys. Lett. **29**, 037402.

Wang, X.-P., T. Qian, P. Richard, P. Zhang, J. Dong, H.-D. Wang, C.-H. Dong, M.-H. Fang, and H. Ding, 2011, Europhys. Lett. **93**, 57001.

Wang, X.-P., *et al.*, 2012a, Phys. Rev. B **85**, 214518.

Wang, X.-P., *et al.*, 2012b, Europhys. Lett. **99**, 67001.

Wang, Y., K. Wohlfeld, B. Moritz, C. J. Jia, M. van Veenendaal, K. Wu, C.-C. Chen, and T. P. Devereaux, 2015, Phys. Rev. B **92**, 075119.

Wang, Y. H., D. Hsieh, D. Pilon, L. Fu, D. R. Gardner, Y. S. Lee, and N. Gedik, 2011, Phys. Rev. Lett. **107**, 207602.

Wang, Y. H., D. Hsieh, E. J. Sie, H. Steinberg, D. R. Gardner, Y. S. Lee, P. Jarillo-Herrero, and N. Gedik, 2012, Phys. Rev. Lett. **109**, 127401.

Wang, Y. H., H. Steinberg, P. Jarillo-Herrero, and N. Gedik, 2013, Science **342**, 453.

Wang, Z., *et al.*, 2014, Proc. Natl. Acad. Sci. U.S.A. **111**, 3933.

Wang, Z., *et al.*, 2016, Nat. Mater. **15**, 835.

Wannberg, B., 2009, Nucl. Instrum. Methods Phys. Res., Sect. A **601**, 182.

Watanabe, H., T. Shirakawa, and S. Yunoki, 2013, Phys. Rev. Lett. **110**, 027002.

Watson, M., *et al.*, 2015, Phys. Rev. B **91**, 155106.

Watson, M. D., P. Dudin, L. C. Rhodes, D. V. Evtushinsky, H. Iwasawa, S. Aswartham, S. Wurmehl, B. Büchner, M. Hoesch, and T. K. Kim, 2019, npj Quantum Mater. **4**, 36.

Weinelt, M., 2002, J. Phys. Condens. Matter **14**, R1099.

Wells, B., Z.-X. Shen, A. Matsuura, D. King, M. Kastner, M. Greven, and R. Birgeneau, 1995, Phys. Rev. Lett. **74**, 964.

Wen, C., *et al.*, 2018, Phys. Rev. Lett. **121**, 117002.

Wen, X.-G., 1995, Adv. Phys. **44**, 405.

Wilson, N. R., *et al.*, 2017, Sci. Adv. **3**, e1601832.

Wojek, B. M., M. Berntsen, S. Boseggia, A. Boothroyd, D. Prabhakaran, D. McMorrow, H. Rønnow, J. Chang, and O. Tjernberg, 2012, J. Phys. Condens. Matter **24**, 415602.

Wollman, D., D. J. Van Harlingen, W. Lee, D. Ginsberg, and A. J. Leggett, 1993, Phys. Rev. Lett. **71**, 2134.

Woodruff, D., D. Norman, B. Holland, N. Smith, H. Farrell, and M. Traum, 1978, Phys. Rev. Lett. **41**, 1130.

Wray, L. A., S.-Y. Xu, Y. Xia, D. Hsieh, A. V. Fedorov, Y. S. Hor, R. J. Cava, A. Bansil, H. Lin, and M. Z. Hasan, 2011, Nat. Phys. **7**, 32.

Wu, L., M. Salehi, N. Koirala, J. Moon, S. Oh, and N. P. Armitage, 2016, Science **354**, 1124.

Wu, S., V. Fatemi, Q. D. Gibson, K. Watanabe, T. Taniguchi, R. J. Cava, and P. Jarillo-Herrero, 2018, Science **359**, 76.

Wu, Y.-M., A. Abanov, Y. Wang, and A. V. Chubukov, 2019, Phys. Rev. B **99**, 144512.

Xi, F., T. Shi, Q. Fan, S. Prestemon, W. Wan, Z. An, and S. Qiao, 2013, J. Synchrotron Radiat. **20**, 145.

Xi, X., L. Zhao, Z. Wang, H. Berger, L. Forró, J. Shan, and K. F. Mak, 2015, Nat. Nanotechnol. **10**, 765.

Xia, Y., *et al.*, 2009, Nat. Phys. **5**, 398.

Xie, Z., *et al.*, 2014, Nat. Commun. **5**, 3382.

Xiong, H., *et al.*, 2017, Phys. Rev. B **95**, 195119.

Xu, C., M. Müller, and S. Sachdev, 2008, Phys. Rev. B **78**, 020501.

Xu, C.-Z., Y. Liu, R. Yukawa, L.-X. Zhang, I. Matsuda, T. Miller, and T.-C. Chiang, 2015, Phys. Rev. Lett. **115**, 016801.

Xu, C.-Z., X. Wang, P. Chen, D. Flötotto, J. A. Hlevyack, M.-K. Lin, G. Bian, S.-K. Mo, and T.-C. Chiang, 2018, Phys. Rev. Mater. **2**, 064002.

Xu, M., *et al.*, 2012, Phys. Rev. B **85**, 220504.

Xu, N., *et al.*, 2013, Phys. Rev. B **88**, 121102.

Xu, N., *et al.*, 2014, Nat. Commun. **5**, 4566.

Xu, S.-Y., C. Liu, A. Richardella, I. Belopolski, N. Alidoust, M. Neupane, G. Bian, N. Samarth, and M. Z. Hasan, 2014, Phys. Rev. B **90**, 085128.

Xu, S.-Y., *et al.*, 2011, Science **332**, 560.

Xu, S.-Y., *et al.*, 2012a, Nat. Commun. **3**, 1192.

Xu, S.-Y., *et al.*, 2012b, Nat. Phys. **8**, 616.

Xu, S.-Y., *et al.*, 2014, Nat. Phys. **10**, 943.

Xu, S.-Y., *et al.*, 2015a, Nat. Phys. **11**, 748.

Xu, S.-Y., *et al.*, 2015b, Science **349**, 613.

Xu, S.-Y., *et al.*, 2015c, Sci. Adv. **1**, e1501092.

Xu, S.-Y., *et al.*, 2015d, Science **347**, 294.

Xu, S.-Y., *et al.*, 2015e, Nat. Commun. **6**, 6870.

Xu, Y., B. Yan, H.-J. Zhang, J. Wang, G. Xu, P. Tang, W. Duan, and S.-C. Zhang, 2013, Phys. Rev. Lett. **111**, 136804.

Yamane, H., F. Matsui, T. Ueba, T. Horigome, S. Makita, K. Tanaka, S. Kera, and N. Kosugi, 2019, Rev. Sci. Instrum. **90**, 093102.

Yan, B., B. Stadtmüller, N. Haag, S. Jakobs, J. Seidel, D. Jungkenn, S. Mathias, M. Cinchetti, M. Aeschlimann, and C. Felser, 2015, Nat. Commun. **6**, 10167.

Yan, Y. J., M. Q. Ren, H. C. Xu, B. P. Xie, R. Tao, H. Y. Choi, N. Lee, Y. J. Choi, T. Zhang, and D. L. Feng, 2015, Phys. Rev. X **5**, 041018.

Yang, B.-J., and N. Nagaosa, 2014, Nat. Commun. **5**, 4898.

Yang, H., Z. Wang, and H. Ding, 2007, J. Phys. Condens. Matter **19**, 355004.

Yang, H. F., *et al.*, 2019, Nat. Commun. **10**, 3478.

Yang, H.-B., J. Rameau, Z.-H. Pan, G. Gu, P. Johnson, H. Claus, D. Hinks, and T. Kidd, 2011, Phys. Rev. Lett. **107**, 047003.

Yang, H.-B., *et al.*, 2004, Phys. Rev. Lett. **92**, 246403.

Yang, H.-B., *et al.*, 2005, Phys. Rev. Lett. **95**, 146401.

Yang, L. X., *et al.*, 2015, Nat. Phys. **11**, 728.

Yang, S.-H., B. Mun, A. Kay, S.-K. Kim, J. Kortright, J. Underwood, Z. Hussain, and C. Fadley, 2000, Surf. Sci. **461**, L557.

Yang, S.-L., J. Sobota, C. Howard, C. Pickard, M. Hashimoto, D. Lu, S.-K. Mo, P. Kirchmann, and Z.-X. Shen, 2014, Nat. Commun. **5**, 3493.

Yang, S.-L., J. A. Sobota, Y. He, D. Leuenberger, H. Soifer, H. Eisaki, P. S. Kirchmann, and Z.-X. Shen, 2019, Phys. Rev. Lett. **122**, 176403.

Yang, S.-L., J. A. Sobota, D. Leuenberger, Y. He, M. Hashimoto, D. H. Lu, H. Eisaki, P. S. Kirchmann, and Z.-X. Shen, 2015, Phys. Rev. Lett. **114**, 247001.

Yano, M., A. Sekiyama, H. Fujiwara, T. Saita, S. Imada, T. Muro, Y. Onuki, and S. Suga, 2007, Phys. Rev. Lett. **98**, 036405.

Yao, W., *et al.*, 2018, Proc. Natl. Acad. Sci. U.S.A. **115**, 6928.

Yazyev, O. V., J. E. Moore, and S. G. Louie, 2010, Phys. Rev. Lett. **105**, 266806.

Ye, Z., Y. Zhang, M. Xu, Q. Ge, F. Chen, J. Jiang, B. Xie, J. Hu, and D. Feng, 2012, Phys. Rev. B **86**, 035136.

Ye, Z., *et al.*, 2014, Phys. Rev. X **4**, 031041.

Yeh, J., and I. Lindau, 1985, At. Data Nucl. Data Tables **32**, 1.

Yelland, E., J. Cooper, A. Carrington, N. Hussey, P. Meeson, S. Lee, A. Yamamoto, and S. Tajima, 2002, Phys. Rev. Lett. **88**, 217002.

Yi, H., *et al.*, 2014, Sci. Rep. **4**, 6106.

Yi, M., Y. Zhang, Z.-X. Shen, and D. Lu, 2017, npj Quantum Mater. **2**, 57.

Yi, M., *et al.*, 2009, Phys. Rev. B **80**, 174510.

Yi, M., *et al.*, 2011, Proc. Natl. Acad. Sci. U.S.A. **108**, 6878.

Yi, M., *et al.*, 2013, Phys. Rev. Lett. **110**, 067003.

Yi, M., *et al.*, 2014, Nat. Commun. **5**, 3711.

Yi, M., *et al.*, 2015, Nat. Commun. **6**, 7777.

Yi, M., *et al.*, 2019, Phys. Rev. X **9**, 041049.

Yildirim, T., *et al.*, 2001, Phys. Rev. Lett. **87**, 037001.

Yilmaz, T., I. Pletikosić, A. P. Weber, J. T. Sadowski, G. D. Gu, A. N. Caruso, B. Sinkovic, and T. Valla, 2014, Phys. Rev. Lett. **113**, 067003.

Ying, T., X. Chen, G. Wang, S. Jin, T. Zhou, X. Lai, H. Zhang, and W. Wang, 2012, Sci. Rep. **2**, 426.

Ying-Ying, P., *et al.*, 2013, Chin. Phys. Lett. **30**, 067402.

Yoshida, H., 2012, Chem. Phys. Lett. **539-540**, 180.

Yoshida, R., *et al.*, 2010, Phys. Rev. B **82**, 205108.

Yoshida, T., M. Hashimoto, I. M. Vishik, Z.-X. Shen, and A. Fujimori, 2012, J. Phys. Soc. Jpn. **81**, 011006.

Yoshida, T., *et al.*, 2007, J. Phys. Condens. Matter **19**, 125209.

Yu, J., A. J. Freeman, and J.-H. Xu, 1987, Phys. Rev. Lett. **58**, 1035.

Yu, R., W. Zhang, H.-J. Zhang, S.-C. Zhang, X. Dai, and Z. Fang, 2010, Science **329**, 61.

Yu, T., C. E. Matt, F. Bisti, X. Wang, T. Schmitt, J. Chang, H. Eisaki, D. Feng, and V. N. Strocov, 2020, npj Quantum Mater. **5**, 46.

Yuan, H., *et al.*, 2016, Nano Lett. **16**, 4738.

Yusof, Z., B. Wells, T. Valla, A. Fedorov, P. Johnson, Q. Li, C. Kendziora, S. Jian, and D. Hinks, 2002, Phys. Rev. Lett. **88**, 167006.

Zaanen, J., Y. Liu, Y.-W. Sun, and K. Schalm, 2015, *Holographic Duality in Condensed Matter Physics* (Cambridge University Press, Cambridge, England).

Zaanen, J., G. Sawatzky, and J. Allen, 1985, Phys. Rev. Lett. **55**, 418.

Zabolotnyy, V. B., *et al.*, 2007a, Phys. Rev. B **76**, 064519.

Zabolotnyy, V. B., *et al.*, 2007b, Phys. Rev. B **76**, 024502.

Zeng, H., J. Dai, W. Yao, D. Xiao, and X. Cui, 2012, Nat. Nanotechnol. **7**, 490.

Zeng, L.-K., *et al.*, 2016, Phys. Rev. Lett. **117**, 127204.

Zeugner, A., *et al.*, 2019, Chem. Mater. **31**, 2795.

Zhang, C., Y. Li, D. Pei, Z. Liu, and Y. Chen, 2020, Annu. Rev. Mater. Res. **50**, 131.

Zhang, C., *et al.*, 2013, Phys. Rev. Lett. **111**, 207002.

Zhang, D., M. Shi, T. Zhu, D. Xing, H. Zhang, and J. Wang, 2019, Phys. Rev. Lett. **122**, 206401.

Zhang, F., and T. Rice, 1988, Phys. Rev. B **37**, 3759.

Zhang, H., C.-X. Liu, X.-L. Qi, X. Dai, Z. Fang, and S.-C. Zhang, 2009, Nat. Phys. **5**, 438.

Zhang, H., C.-X. Liu, and S.-C. Zhang, 2013, Phys. Rev. Lett. **111**, 066801.

Zhang, P., P. Richard, T. Qian, Y.-M. Xu, X. Dai, and H. Ding, 2011, Rev. Sci. Instrum. **82**, 043712.

Zhang, P., *et al.*, 2015, Phys. Rev. B **91**, 214503.

Zhang, P., *et al.*, 2017, Phys. Rev. Lett. **118**, 046802.

Zhang, P., *et al.*, 2018, Science **360**, 182.

Zhang, P., *et al.*, 2019, Nat. Phys. **15**, 41.

Zhang, R., D. Gong, X. Lu, S. Li, P. Dai, and H. Luo, 2014, Supercond. Sci. Technol. **27**, 115003.

Zhang, S., *et al.*, 2016, Phys. Rev. B **94**, 081116.

Zhang, T., Y. Jiang, Z. Song, H. Huang, Y. He, Z. Fang, H. Weng, and C. Fang, 2019, Nature (London) **566**, 475.

Zhang, W., *et al.*, 2008a, Phys. Rev. Lett. **101**, 017002.

Zhang, W., *et al.*, 2008b, Phys. Rev. Lett. **100**, 107002.

Zhang, W., *et al.*, 2014, Nat. Commun. **5**, 4959.

Zhang, X., Q. Liu, J.-W. Luo, A. J. Freeman, and A. Zunger, 2014, Nat. Phys. **10**, 387.

Zhang, Y., J. Lee, R. Moore, W. Li, M. Yi, M. Hashimoto, D. Lu, T. Devereaux, D.-H. Lee, and Z.-X. Shen, 2016, Phys. Rev. Lett. **117**, 117001.

Zhang, Y., Y.-W. Tan, H. L. Stormer, and P. Kim, 2005, Nature (London) **438**, 201.

Zhang, Y., *et al.*, 2010, Nat. Phys. **6**, 584.

Zhang, Y., *et al.*, 2011, Nat. Mater. **10**, 273.

Zhang, Y., *et al.*, 2012, Phys. Rev. B **85**, 085121.

Zhang, Y., *et al.*, 2014, Nat. Nanotechnol. **9**, 111.

Zhang, Y., *et al.*, 2016, Phys. Rev. B **94**, 115153.

Zhang, Y., *et al.*, 2017, Nat. Commun. **8**, 15512.

Zhao, J., *et al.*, 2008, Nat. Mater. **7**, 953.

Zhao, L., *et al.*, 2016, Nat. Commun. **7**, 10608.

Zhao, W., M. Li, C.-Z. Chang, J. Jiang, L. Wu, C. Liu, J. S. Moodera, Y. Zhu, and M. H. Chan, 2018, Sci. Adv. **4**, eaao2682.

Zhong, Y.-G., *et al.*, 2018, Phys. Rev. B **98**, 140507.

Zhou, P., L. Chen, Y. Liu, I. Sochnikov, A. T. Bollinger, M.-G. Han, Y. Zhu, X. He, I. Bozović, and D. Natelson, 2019, Nature (London) **572**, 493.

Zhou, S., G.-H. Gweon, J. Graf, A. Fedorov, C. Spataru, R. Diehl, Y. Kopelevich, D.-H. Lee, S. G. Louie, and A. Lanzara, 2006, Nat. Phys. **2**, 595.

Zhou, S., G.-H. Gweon, and A. Lanzara, 2006, Ann. Phys. (Amsterdam) **321**, 1730.

Zhou, S. Y., G.-H. Gweon, A. Fedorov, d. First, PN, W. De Heer, D.-H. Lee, F. Guinea, A. Castro Neto, and A. Lanzara, 2007, Nat. Mater. **6**, 770.

Zhou, X., T. Cuk, T. Devereaux, N. Nagaosa, and Z.-X. Shen, 2007, in *Handbook of High-Temperature Superconductivity* (Springer, New York), pp. 87–144.

Zhou, X., S. He, G. Liu, L. Zhao, L. Yu, and W. Zhang, 2018, Rep. Prog. Phys. **81**, 062101.

Zhou, X., B. Wannberg, W. Yang, V. Brouet, Z. Sun, J. Douglas, D. Dessau, Z. Hussain, and Z.-X. Shen, 2005, J. Electron Spectrosc. Relat. Phenom. **142**, 27.

Zhou, X., *et al.*, 2003, Nature (London) **423**, 398.

Zhou, X., *et al.*, 2005, Phys. Rev. Lett. **95**, 117001.

Zhou, X., *et al.*, 2019, Phys. Rev. B **100**, 184511.

Zhu, F.-f., W.-j. Chen, Y. Xu, C.-l. Gao, D.-d. Guan, C.-h. Liu, D. Qian, S.-C. Zhang, and J.-f. Jia, 2015, Nat. Mater. **14**, 1020.

Zhu, X., Y. Cao, J. Zhang, E. W. Plummer, and J. Guo, 2015, Proc. Natl. Acad. Sci. U.S.A. **112**, 2367.

Zhu, Z.-H., A. Nicolaou, G. Levy, N. P. Butch, P. Syers, X. F. Wang, J. Paglione, G. A. Sawatzky, I. S. Elfimov, and A. Damascelli, 2013, Phys. Rev. Lett. **111**, 216402.

Zhu, Z.-H., C. N. Veenstra, G. Levy, A. Ubaldini, P. Syers, N. P. Butch, J. Paglione, M. W. Haverkort, I. S. Elfimov, and A. Damascelli, 2013, Phys. Rev. Lett. **110**, 216401.

Zhu, Z.-H., *et al.*, 2014, Phys. Rev. Lett. **112**, 076802.

Zwartsenberg, B., *et al.*, 2020, Nat. Phys. **16**, 290.